

DYNAMIC INDUCTIVE POWER TRANSFER SYSTEMS WITH REFLEXIVE
TUNING NETWORKS DESIGNED BY MACHINE LEARNING by

Shuntaro Inoue

A dissertation submitted in partial fulfillment
of the requirements for the degree

of

DOCTOR OF PHILOSOPHY

in

Electrical Engineering

Approved:

Regan Andrew Zane, Ph.D.
Major Professor

Abhilash Kamineni, Ph.D.
Committee Member

Nicholas S. Flann, Ph.D.
Committee Member

Hongjie Wang, Ph.D.
Committee Member

Marv Halling, Ph.D.
Committee Member

D. Richard Cutler, Ph.D.
Vice Provost of Graduate Studies

UTAH STATE UNIVERSITY
Logan, Utah

2023

Copyright © Shuntaro Inoue 2023

All Rights Reserved

ABSTRACT

Dynamic inductive power transfer systems with
reflexive tuning networks designed by machine learning

by

Shuntaro Inoue, Doctor of Philosophy

Utah State University, 2023

Major Professor: Regan Andrew Zane, Ph.D.
Department: Electrical and Computer Engineering

This dissertation proposes and demonstrates a new dynamic inductive power transfer (DIPT) system with a single inverter connected to multiple transmitter coils to make DIPT systems more affordable. Typical DIPT systems have individual inverters for each transmitter coil, which becomes a significant cost factor if the transmitter coils are implemented on roads for a long distance. The proposed reflexive tuning DIPT system utilizes a reflected impedance to allow a single inverter to drive multiple transmitter coils. Using reflexive tuning, the approach naturally achieves high currents only on the transmitter coil that is presently coupled to a receiver coil as a vehicle travels along a DIPT roadway system, while the remaining coils connected to the shared inverter operate with significantly lower currents. A 50 kW prototype is designed by a new optimization method combining neural networks and genetic algorithms. Finally, a 50 kW prototype is demonstrated on both automated rail and vehicle systems. The measured dc-dc efficiency with single and four transmitter coils are 90.0% and 87.9%, respectively.

(216 pages)

PUBLIC ABSTRACT

Dynamic inductive power transfer systems with
reflexive tuning networks designed by machine learning

Shuntaro Inoue

This dissertation proposes a new way to make dynamic wireless charging systems more affordable. Instead of using one inverter for each transmitter coil, as is typically done, the proposed system uses a single inverter that is connected to multiple transmitter coils. This approach is made possible by reflexive tuning, which allows for high currents to be achieved only on the transmitter coil in use. The system was tested with a 50kW prototype, designed using a combination of neural networks and genetic algorithms. The prototype was tested on both automated rail and vehicle systems. The measured dc-dc efficiency with single and four transmitter coils are 90.0% and 87.9%, respectively.

ACKNOWLEDGMENTS

First of all, I would like to thank Professor Regan Andrew Zane for giving me numerous technical advice, organizing appropriate support staff and students, and connecting appropriate people with me at the right time. I was lucky to be involved in the environment when he started ASPIRE. It has been an amazing experience for me. Through the three years and four months at the Utah Power Electronics Laboratory, I learned much about technology, management, and private aspects from him.

I would like to thank Professor Abhilash Kamineni for numerous technical advice. I cannot count how often his suggestions quickly cleared problems I struggled with over a few days. His profound experience in power electronics areas, including IPT technology, affected almost everything in this dissertation.

Furthermore, I am grateful to Professor Nicholas Flann for inspiring my research from the computer science aspect. His presentation at the power laboratory opened my eyes to developing the ANN-based optimization algorithm, and his suggestion in my proposal defense inspired me to develop the ANN- and GA-based optimization algorithms.

I would also like to thank Prof. Hongjie Wang and Prof. Marv Halling for serving on my committee and providing me with valuable advice to improve my project.

I would like to thank Toyota Central R&D labs. Inc. for giving me the opportunity to come to Utah Power Electronics Laboratory to do my Ph.D. project.

Many thanks go to all my Utah Power Electronics Laboratory colleagues for assisting with my research. I want to express my gratitude to Bryce Hesterman and Matt Jones for giving technical advice for my prototypes. I want to thank Dustin Maughan, Andrew Budge, Angie Griffeth, Samantha Tervort, and Evan Hyde for supporting me in experiments. I want to thank Chakridhar R. Teeneti, Reebal Nimri, and Shaju Saha for discussing technical topics with me. Chakri's discussion helped me to come up with the new reflexive tuning topology. Discussion with Reebal led to the development of the superposition method for ANN-based optimization. Discussion and technical help from Shaju led to the development

of the ANN- and GA-based optimization algorithms. I want to thank electrical students Josh Larsen, Dakota Goodrich, Samuel Kiguthi, Jonathan Newman, and Timothy Goodale for working on my projects. Their assistance proceeded my research forward a lot. I want to thank mechanical students Ryan Cook, Alan Peterson, Gabe Gilbert, and Kobe Davis for working on constructing the automated rail and vehicle systems. I am grateful to Benny Varghese, Dorai Yelaverthi, Reza Tavakoli, Mayank Chawla, Mahmoud Mansour, Marium Rasheed, Brian Hobbs, Benjamin Hansen, Mackay Baugh, Tucker Skinner, Conner Sabin, and more for many other supports.

I would like to thank colleagues of Toyota Central R&D Labs., Inc., Shuji Tomura, Goh Teck Chiang, and Masanori Ishigaki. I would also like to thank Leo Liu at Toyota Research Institute, Masato Maemura, Toshiya Hashimoto at Toyota Motor Company, people at ASPIRE Research Center, and many more names I could not list here.

I would like to express my sincere gratitude to my wife, Maiko. She supported and encouraged me during hard times. If I had not had her help, I could not have completed this thesis.

Shuntaro Inoue

CONTENTS

	Page
ABSTRACT	iii
PUBLIC ABSTRACT	iv
ACKNOWLEDGMENTS	v
LIST OF TABLES	x
LIST OF FIGURES	xi
ACRONYMS	xvii
1 INTRODUCTION	1
1.1 Electrification of transportation	2
1.2 Solutions for battery electric vehicles' challenges	3
1.2.1 Extreme fast charging	3
1.2.2 Battery swapping	3
1.2.3 Dynamic wireless power transfer	5
1.3 Types of wireless power transfer	6
1.3.1 Inductive power transfer	6
1.3.2 Capacitive power transfer	6
1.3.3 Microwave power transfer	7
1.4 Key engineering challenges of DIPT	7
1.4.1 Cost	8
1.4.2 Interoperability	9
1.4.3 High efficiency and high power density	10
1.4.4 High tolerance to coil misalignment	10
1.4.5 Low electromagnetic stray fields	10
1.4.6 Foreign object detection	11
1.5 Goals and contributions of the thesis	12
1.6 Outline of the thesis	13
2 An overview of Inductive power transfer systems	15
2.1 Isolated dc-dc converter & inductive power transfer	15
2.2 Basics of IPT tuning technique	19
2.3 Compensation circuit topologies	24
2.3.1 Transmitter side	24
2.3.2 Receiver side	26
2.4 IPT pad topologies	28
2.5 Transmitter side configurations for DIPT Systems	29
2.5.1 Long track type	29
2.5.2 Pads-array type	31

2.6	Summary of the Chapter	36
3	Reflexive tuning IPT systems	38
3.1	Conventional reflexive tuning topology	39
3.2	Proposed reflexive tuning circuit topology	40
3.3	Theoretical analysis of the proposed circuit	41
3.3.1	Uncoupled condition	41
3.3.2	Coupled condition	43
3.3.3	Output power	44
3.3.4	Soft switching analysis	48
3.3.5	Stability of the system	48
3.3.6	Comparison of the Pareto fronts	49
3.3.7	Takeaways of the proposed circuit	50
3.4	Design and Sensitivity Analysis of the proposed circuit	51
3.4.1	Circuit design	51
3.4.2	Sensitivity analysis	55
3.5	Stray field simulation	57
3.6	Experimental verification	59
3.7	Summary of the Chapter	69
4	ANN-based design optimization method	70
4.1	Design Optimization Method for Inductive Power Transfer Systems	70
4.1.1	Finite Element Method	71
4.1.2	Superposition Method	71
4.1.3	Nonlinear Fitting utilizing a Neural Network	72
4.2	Theory of the proposed ANN-based design method	72
4.3	Proposed design optimization method	77
4.4	Optimization process	80
4.5	Experimental verification	84
4.6	Summary of the Chapter	89
5	ANN- and GA-based design optimization method	90
5.1	Intorduction	90
5.2	The proposed design optimization process	93
5.2.1	Assumption of the optimization problem	93
5.2.2	Solution 1: Reduction of ANN training data collection time by superposition of magnetic fields	97
5.2.3	Solution 2: Genetic algorithm to improve the random input	99
5.3	Design optimization	99
5.3.1	Construction of ANN	100
5.3.2	Fitting of ANN	105
5.3.3	Construction of GA	107
5.3.4	The extraction process of an optimized design point	109
5.4	Verification in FEM and circuit simulation	111
5.5	Experimental results	114
5.5.1	Prototype system	114
5.5.2	Measurement methods	115

5.5.3	Experimental results	118
5.6	Conclusion	123
6	High-power reflexive tuning DIPT system optimization	125
6.1	Design of a 50 kW reflexive tuning system	125
6.1.1	ANN- and GA-based design optimization	125
6.1.2	Design comparison of the proposed and conventional reflexive tuning circuits	125
6.1.3	Circuit simulation of transmitter current and output power	128
6.1.4	Circuit simulation for soft-switching analysis	130
6.1.5	Output power sensitivity for the input and output voltages	131
6.2	Coil prototype	132
6.3	50 kW test on the automated rail	132
6.4	60 km/h Vehicle Test	143
6.5	Summary of the Chapter	146
7	Conclusion & Outlook	148
7.1	Results & Conclusions	148
7.1.1	Contribution 1	148
7.1.2	Contribution 2	149
7.1.3	Contribution 3	149
7.1.4	Contribution 4	149
7.2	Future Research Areas	150
7.3	Published papers	151
7.3.1	Conference papers	151
7.3.2	Journals	151
7.3.3	Patent	152
	REFERENCES	153
	APPENDICES	164
A	Python code for the ANN-based design optimization	165
A.1	User input	165
A.2	Define training and validation data	165
A.3	Neural network process	168
A.4	Save the created model	174
A.5	Generate random input	175
A.6	Generate prediction data for random input data	179
A.7	Extraction process	193
	CURRICULUM VITAE	199

LIST OF TABLES

Table		Page
1.1	The details of the cost breakdown of a DIPT system [1], assuming one dollar per euro and 52.5 kW inverter per transmitter coil	9
2.1	The output characteristics of the different receiver compensations [2]	24
2.2	List of IPT pad topologies [3]	28
3.1	Comparison between the proposed and conventional circuit typologies	50
3.2	Design specifications for the proposed circuit	52
3.3	Design conditions for the proposed and conventional circuit	53
3.4	Maxwell simulation conditions	58
3.5	Comparison of the measured and simulation results of the stray magnetic field in the uncoupled condition	67
4.1	Design specifications for the IPT system	80
4.2	Design parameters of the prototype	85
4.3	Measured magnetic parameters	86
4.4	Measured input and output power and the estimated loss distribution	88
5.1	Ranges of ten random input variables for the coil dimensions	94
5.2	Design criteria of extraction process	96
5.3	Design specifications for the DIPT system	106
5.4	Geometry parameters of the optimized coils	112
5.5	Comparison between the ANN prediction and FEM results	113
5.6	Comparison between ANN prediction versus circuit simulation results	113
5.7	Values of the compensation components	117
5.8	Comparison between ANN prediction versus experimental results	123
6.1	Shared design parameters between the proposed and conventional circuits	127
6.2	Separately design parameters for the proposed and conventional circuits	127
6.3	System parameters of the experimental setup	136
6.4	Comparison of the theoretical and experimental total dc-dc efficiencies	141

LIST OF FIGURES

Figure	Page
1.1 The U.S. greenhouse gas emissions by economic sector in 2019	2
1.2 Share of global transport-related greenhouse gas emissions by mode in 2018 [4]	2
1.3 Extream fast charging [5]	4
1.4 Battery swapping [6]	4
1.5 Dynamic wireless power transfer [7]	5
1.6 Inductive type [8]	6
1.7 Capacitive type [8]	7
1.8 Microwave type [9]	7
1.9 Cost breakdown of a DIPT system [1], assuming one dollar per euro	8
2.1 Resonant isolated dc-dc converter	15
2.2 Isolated dc-dc converter	16
2.3 IPT tuning	18
2.4 Generarized resonant circuit model [10]	19
2.5 Thevenin-equivalent circuit that models the receiver side circuit of the resonant circuit	20
2.6 Physical meaning of open circuit voltage and short circuit current	20
2.7 Relationshipt between the amplitude of output voltage and output current [2]	21
2.8 Series tuned receiver circuit	21
2.9 Parallel tuned receiver circuit	23
2.10 Series tuned transmitter circuit	24
2.11 Parallel tuned transmitter circuit	25

2.12 LCC tuned transmitter circuit	26
2.13 Series tuned receiver circuit	26
2.14 Parallel tuned receiver circuit	27
2.15 LCC tuned receiver circuit	27
2.16 Two major configurations of DIPT systems	29
2.17 Segmented long track [11]	31
2.18 Individual inverter type [12]	32
2.19 Bypass switch type [13]	33
2.20 Double-coupler method [14]	33
2.21 Reactive power compensation network by an auxiliary circuit [15]	34
2.22 Reactive power compensation network by an auxiliary circuit [16]	35
2.23 reflexive tuning method [17]	35
3.1 The conceptual diagram of the reflexive tuning approach	39
3.2 Conventional reflexive tuning circuit topology	39
3.3 Proposed reflexive tuning topology	40
3.4 Circuit conversion process to derive theoretical inverter current in the uncoupled condition	41
3.5 Uncoupled transmitter side circuits to derive the equation of the transmitter current	42
3.6 Coupled condition	43
3.7 Equivalent circuit in the coupled condition	44
3.8 ZVS region	49
3.9 Pareto fronts of the proposed and the conventional circuit on the surface of Efficiency versus output power P_{out}	50
3.10 LTspice-simulated waveforms	53
3.11 LTspice-simulated current amplitude and output power	54

3.12	LTspice-simulated sensitivity analysis results with respect to parasitic components	55
3.13	LTspice-simulated sensitivity analysis results with respect to compensation components	56
3.14	Maxwell simulation setup	57
3.15	Maxwell-simulated magnetic field emission. Proposed reflexive tuning circuit versus constant current circuit	60
3.16	Dimension of the prototype system	61
3.17	Experimental prototype of the proposed reflexive tuning dynamic power transfer system	62
3.18	Experimental setup diagram	63
3.19	Experimental waveforms of the proposed prototype	64
3.20	Measured output power and efficiency as the receiver coil moves from the center of L_1 to the center of L_2	65
3.21	Measured amplitude of current as the receiver coil moves from the center of L_1 to the center of L_2	66
3.22	Variance of measured currents in the misalignment condition	67
3.23	Measured output power versus receiver position in the misalignment condition	68
3.24	Measured magnetic field at uncoupled condition	68
3.25	LTspice simulated loss breakdown when output power is 2,022 W, total loss is 678 W, and total efficiency is 74.9%.	68
4.1	The proposed design optimization method	73
4.2	Degree-of-freedom considered for the design optimization of the coils	74
4.3	Root mean square error vs. iterations	81
4.4	Distribution of all data at $P_{\text{out}}=3.3$ kW. The calculation time for both method are the same.	82
4.5	Extracted data from Fig.4.4 (a) and (b), respectively. All the data satisfy $B_{\text{stray}} \leq 10\mu\text{T}$ and $k_{\text{diff}} \leq 20\%$	83
4.6	Schematic diagram of the experimental setup	85

4.7	Photograph of the whole experimental setup	86
4.8	Waveforms at the primary and the secondary side	87
4.9	Measured magnetic field	88
5.1	Challenges with the conventional ANN-based design optimization approach	92
5.2	The coil model and it's design variables to be optimized	94
5.3	The conventional design flow and proposed solutions	95
5.4	3-D FEM simulation model	97
5.5	Solution 1: Calculation method for stray fields	98
5.6	Solution 2: Comparison between the conventional ANN-based method and the proposed ANN and GA-based method	99
5.7	Activation functions	103
5.8	IPT system with the double-sided LCC compensation network	103
5.9	Prediction error with respect to the number of iterative calculations	106
5.10	Prediction error with respect to the number of training data	107
5.11	Proposed flow of the genetic algorithm	108
5.12	Conventional: design extraction process without GA	109
5.13	Proposed: design extraction process with GA	110
5.14	Dimension of the DIPT system designed by the proposed method	111
5.15	Comparison between the ANN prediction and FEM results	112
5.16	Comparison between the ANN prediction and the circuit simulation result .	114
5.17	Overview of the constructed coils	115
5.18	Automated rail system	116
5.19	Schematic diagram for efficiency and stray field measurements	116
5.20	Measurement method of stray fields	117
5.21	Schematic diagram for power ripple and average output power measurements	118

5.22	Top view of the experimental system	119
5.23	Voltage and current waveforms at $P_{\text{out}} = 3 \text{ kW}$	120
5.24	Measured stray magnetic field	121
5.25	Measured output power with respect to the receiver position (Moving speed: 6 km/h)	122
6.1	Design output result after 90 generations of GA	126
6.2	Maxwell simulation model	128
6.3	LTspice simulation model of the proposed circuit	128
6.4	LTspice-simulated waveforms	129
6.5	LTspice-simulated waveforms	130
6.6	Output power sensitivity for the input and output voltages	131
6.7	Detail of the prototype coils	133
6.8	Overveiw of the experimental setup	134
6.9	Circuit diagram of the experiment in the rail setup	134
6.10	Experimental waveforms of the inverter voltage v_{in} and inverter current i_{in}	137
6.11	Series capacitor currents $i_{C1\text{sa}}$, $i_{C2\text{sa}}$, $i_{C3\text{sa}}$, and $i_{C4\text{sa}}$ when the transmitter coil L_3 is active at 50 kW output power	137
6.12	Transmitter coil currents i_{L1} , i_{L2} , i_{L3} , and i_{L4} when the transmitter coil L_3 is active at 50 kW output power	138
6.13	Distribution of transmitter currents, output power, and efficiency at 10 km/h	139
6.14	Comparison between the aligned and misaligned conditions	140
6.15	Estimated loss breakdown when the output power is 50 kW	141
6.16	Theoretical power loss versus number of transmitters with 50 kW design	142
6.17	Schematic diagram of the vehicle test setup	144
6.18	Overview of the vehicle test setup	144
6.19	Photos of the vehicle system	145

6.20	Distribution of transmitter currents and output power with the vehicle test setup	146
A.1	Output of the source code: Prediction error with respect to the number of iterative calculations	175
A.2	Output of the source code: Plot 1	195
A.3	Output of the source code: Plot 2	196
A.4	Output of the source code: Plot 3	197
A.5	Output of the source code: Plot 4	198

ACRONYMS

IPT	Inductive Power Transfer
SIPT	Static Inductive Power Transfer
DIPT	Dynamic Inductive Power Transfer
DWPT	Dynamic Wireless Power Transfer
FEM	Finite Element Method
ZVS	Zero Voltage Switching
ANN	Artificial Neural Network
GA	Genetic Algorithm
ZVS	Zero Voltage Switching
LV	Low Voltage
HV	High Voltage
GP	Geometry Parameter
MP	Magnetic Parameter
ICT	Information and Communications Technology
FOD	Foreign Object Detection

CHAPTER 1

INTRODUCTION

The world's energy sources are shifting from fuel to electrical energy generated by renewable sources [18–20]. There are four major driving forces of electrification:

- Global warming
- Air pollution
- Unstable fuel prices
- Redundancy of energy sources for national security

Especially global warming has been affecting the global energy policy, such as the Kyoto Protocol [21] and the California Zero Emission Vehicle (ZEV) program [22]. The largest driver of global warming is gas emissions that create a greenhouse effect, more than 90% of which are carbon dioxide (CO₂: 72%) and methane (CH₄: 19%) [23]. The total U.S. greenhouse gas emissions by the economic sector in 2019 are shown in Fig. 1.1 [24]. The transportation sector has the largest share of greenhouse gas emissions. Greenhouse gas emissions from transportation primarily come from burning fossil fuels for our cars, trucks, ships, trains, and planes. Electricity production generates the second-largest share of greenhouse gas emissions. Approximately 62 percent of our electricity comes from burning fossil fuels, mostly coal and natural gas. Greenhouse gas emissions from the industry come from burning fossil fuels for energy and generating certain chemical reactions that are necessary to produce goods from raw materials, including steel and cement. Commercial and residential greenhouse gas emissions come primarily from fossil fuels burned for heat, the use of certain products that contain greenhouse gases, and waste treatment. Greenhouse gas emissions from agriculture come from livestock such as cows, agricultural soils, and rice production.

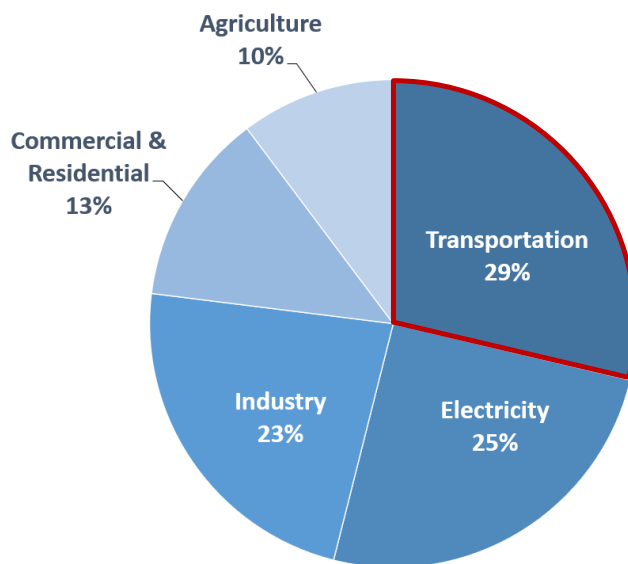


Fig. 1.1: The U.S. greenhouse gas emissions by economic sector in 2019

1.1 Electrification of transportation

Fig. 1.2 shows the share of global transport-related greenhouse gas emissions in 2018 that comes from cars, trucks, planes, ships, and so on [4]. Passenger vehicles (cars, SUVs, motorcycles, etc.) are responsible for almost half the emissions. Medium and heavy-duty vehicles (garbage trucks, buses, semi-trailer trucks, etc.) account for 30 percent.

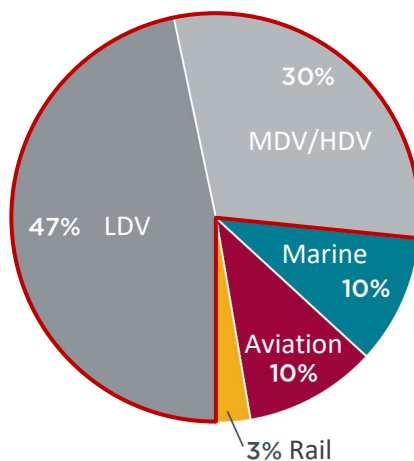


Fig. 1.2: Share of global transport-related greenhouse gas emissions by mode in 2018 [4]

Several solutions have been proposed to solve the problem, including electric vehicles

(EVs), hydrogen, and biofuels [25]. EVs are a solution that is getting a lot of attention [20]. However, EVs have challenges compared to conventional internal combustion engine (ICE) vehicles, such as limited driving range, long charging times, and high prices.

1.2 Solutions for battery electric vehicles' challenges

To overcome these issues, extreme fast charging (XFC) [26], battery swapping [27], and dynamic wireless power transfer (DWPT) systems [28] have been proposed and studied. The details of each solution are described in this section.

1.2.1 Extreme fast charging

Extreme fast charging (XFC) is a concept that charges electric vehicles in a short time close to the fueling time of the engine vehicles. XFC usually means 350 kW and above DC charging. Since XFC is an expanded version of the normal conductive DC charging method, a lot of existing technology can be utilized. However, there are several critical challenges in the approach. First, battery life is often reduced significantly due to the heat if batteries are charged in a short time. Many research projects are ongoing to reduce the heat inside batteries. Second, the electricity grid becomes unstable when the XFC station requires high charging power since the maximum power exceeds 1 MW. To mitigate the effect on the grid, several XFC concepts have been proposed. An example of the XFC's configurations is shown in Fig. 1.3 [5]. The XFC system is connected to a large electric battery that can mitigate the peak required power for the grid. Solar panels are also connected to maximize the benefit of the onsite battery so that the generated electricity can charge the battery or electric vehicles.

1.2.2 Battery swapping

As an alternative to the XFC, battery swapping has been proposed [27], as shown in Fig. 1.4 [6]. The battery swapping station has battery packs stocked in its charging station, and automated mechanical systems detach discharged battery packs and attach charged battery packs to EVs. The obvious benefits of the system are EV charging time

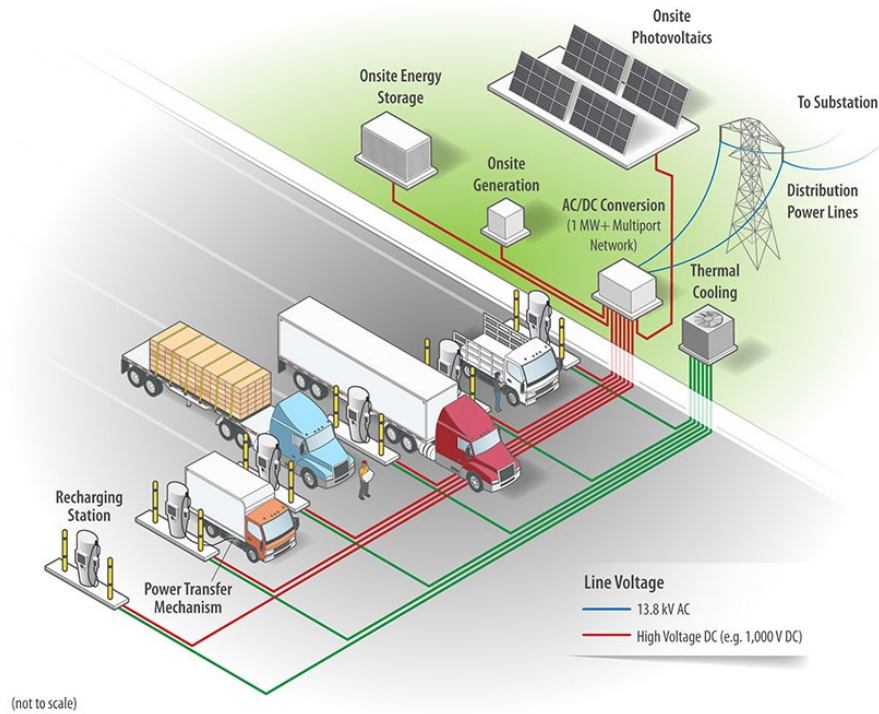


Fig. 1.3: Extream fast charging [5]



Fig. 1.4: Battery swapping [6]

and battery life. The battery swapping time for an electric vehicle can be easily achieved to be almost the same as the fueling time of the engine vehicle. Even though the EV charging time is significantly short, the battery packs stocked in the station are charged with relatively low current, which is helpful for battery life. However, the system has a critical problem; standardization of battery packs. Since battery technology is getting improved

day by day these days, the shape and configuration of battery packs are often upgraded. The situation makes the battery-swapping system difficult to expand the battery-swapping station network globally. Moreover, the system cost, including the charging network, is significantly high since the EVs need mechanical battery swapping architecture, and the charging station needs a lot of battery packs in stock.

1.2.3 Dynamic wireless power transfer

An example of dynamic wireless power transfer systems is shown in Fig. 1.5 [7]. The



Fig. 1.5: Dynamic wireless power transfer [7]

power transmitters embedded in the road deliver electric power wirelessly while the vehicle is running. The system has three benefits; charging time, battery life, and relatively low grid effect. Since the system can charge electric vehicles, the effective waiting time for EV charging becomes zero. The method is good for battery life since the battery charging speed is relatively slower than XFC, which is also good for the grid. Like other methods, the dynamic wireless power transfer method has several challenges, including infrastructure cost and interoperability. The details are described in section 1.4.

1.3 Types of wireless power transfer

Major wireless power transfer technologies used for DWPT systems are categorized into three types: inductive type, capacitive type, and microwave type.

1.3.1 Inductive power transfer

The inductive wireless power transfer type uses induced power with magnetically coupled coils, as shown in Fig. 1.6 [8, 29–39]. The inductive type can typically deliver a high output power of several tens of kilowatts within a gap shorter than the diameter of the transmitter coil itself [40]. At high frequencies such as the megahertz band, there is a problem of high cost, high copper loss, and high core loss due to the windings and the magnetic materials. Therefore, the inductive type uses a frequency up to around 1 MHz [29].

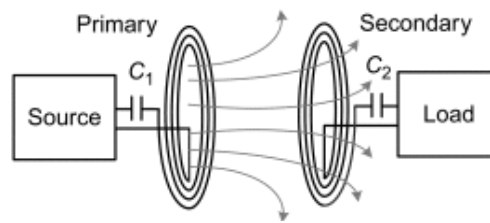


Fig. 1.6: Inductive type [8]

1.3.2 Capacitive power transfer

The capacitive wireless power transfer type uses coupled electrodes, as shown in Fig. 1.7 [8, 41–45]. The power transfer loss of the transmitter and receiver is lower than that of the inductive type at high operating frequencies since no windings or magnetic cores are required. However, it is difficult to obtain sufficient output power because capacitance is quite small in a large gap such as 250 mm. Capacitive power transfer is typically designed at more than 10 times higher frequencies to achieve the same output power level as the inductive type [42]. Eventually, high switching loss of inverters and high conduction loss of tuning inductors and capacitors are big issues for the capacitive type.

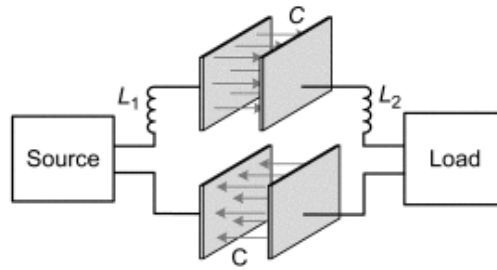


Fig. 1.7: Capacitive type [8]

1.3.3 Microwave power transfer

The microwave wireless power transfer type uses waves with wavelengths approximately 300 mm (1 GHz) to 1 mm (300 GHz), as shown in Fig. 1.8 [9]. For long-distance power transmission, the frequency band is chosen around 2.45 GHz, which is the microwave windows of the atmosphere, and there are abundant practical and low-cost high-efficiency microwave sources and high-efficiency rectifiers for their frequencies [46, 47]. The severe damage microwaves cause to human bodies is the biggest problem of the microwave type.

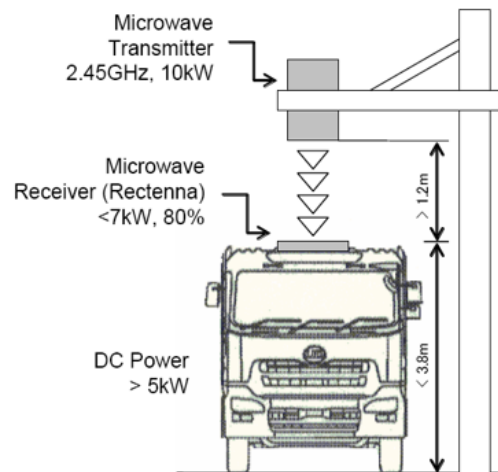


Fig. 1.8: Microwave type [9]

1.4 Key engineering challenges of DIPT

Inductive wireless power transfer is one of the attractive solutions for dynamic wireless

power transfer systems in automotive applications because IPT can offer a high power output of several tens of kilowatts in a gap range of 150 mm to 350 mm [29]. However, to implement the DIPT system broadly on public roads, further investigations are still needed in academic and industrial research. The key engineering challenges for DIPT systems are briefly discussed in this section.

1.4.1 Cost

High infrastructure cost is a challenge for DIPT systems. A cost breakdown of a DIPT system is shown in Fig. 1.9 [1]. The total cost of the DIPT system, including road works,

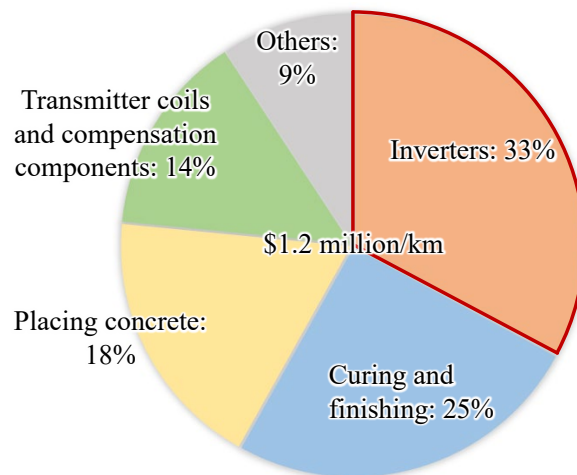


Fig. 1.9: Cost breakdown of a DIPT system [1], assuming one dollar per euro

is about 1.2 million dollars per kilometer. Here, one dollar per euro is assumed since the original analysis was conducted based on the euro. Also, 52.5 kW inverter per transmitter coil is assumed in the calculation. The inverter cost is the highest factor of cost since the inverter is needed for each transmitter coil. Inverter costs account for 33% of the total. The details of the cost breakdown are shown in Table 1.1. 50.2% of the total cost is occupied by electrical components' cost, and the second largest percentage is road works.

Table 1.1: The details of the cost breakdown of a DIPT system [1], assuming one dollar per euro and 52.5 kW inverter per transmitter coil

Category	Item	Item cost [\$/km]	Percentage [%]
Traffic control	Traffic control	34795	2.91
Road works	Milling	38204	3.19
	Placing concrete	220878	18.44
	Curing and finishing	302072	25.23
DIPT electrical and ICT components	MV/LV transformer	12600	1.05
	AC/DC converter	4725	0.39
	DC cables	3571	0.30
	ICT and auxiliary powering cables and pipes	1905	0.16
	Power and data connectors	10000	0.84
	Manholes	5000	0.42
	Inverters	393750	32.88
	Transmitter coils and compensation capacitors	170000	14.20
Total		1197500	100.00

1.4.2 Interoperability

When a DIPT is installed on the road, the system must satisfy the function of delivering power to the different types of vehicles with different heights, output powers, and receiving coil sizes. Maximizing interoperability as much as possible maximizes the utilization of the infrastructure and accelerates the return on investment costs. Therefore, engineers must consider power delivery to vehicles with different air gaps, maximum output power, and receiver coil sizes. It is challenging to increase power volume and weight density to reduce material cost while simultaneously satisfying other design requirements, such as output power, stray magnetic field, misalignment tolerance, and efficiency. The SAE has announced Standard J2954 to simplify the interoperability [48] design. SAEJ2954 specifies wireless transfer standards for stationary charging in three classes: 3.7 kW, 7.7 kW, and 11 kW. A 500 kW standard is also being discussed for heavy-duty vehicles in J2954/2. The standard for DIPT is also being discussed, and charging power levels, geometrical requirements for the transmission coils, communication interfaces, safety features, and test

procedures are planned to be defined.

1.4.3 High efficiency and high power density

Static inductive power transfer (SIPT) systems for stationary EV chargers tend to have lower efficiency and power density than conductive onboard chargers due to the lower coupling coefficient of coils. This trend is further accelerated in the DIPT system since a longer transmitter coil is preferred to reduce the system cost. The longer transmitter coils result in a lower coupling coefficient than the SIPT. The volume of ferrite core and Litz wires for transmitter coils significantly affect the system cost compared to SIPT since the DIPT requires multiple transmitter coils. Therefore, maximizing the power density of transmitter coils is more important than the SIPT system.

1.4.4 High tolerance to coil misalignment

The practical misalignment tolerance of the DIPT is 100-200 mm, although there is still no consensus in academics and industry areas. It is desired to operate under the reduced efficiency caused by misalignment so that charging time is almost unaffected even under misalignment conditions. It is necessary to design the resonant circuit and the inverter with a margin considering the operation where the resonance is shifted. Also, the control system must be stable even when the impedance is shifted due to positional change.

1.4.5 Low electromagnetic stray fields

The high-frequency magnetic and electric fields required for the IPT systems cause safety and electromagnetic compatibility concerns. One of the biggest safety concerns for the IPT system is its effect on the human body. Much research has been done on the safety of high-frequency electromagnetic waves, and strict standards have been established by IEEE, ICNIPR, and SAE [48].

Thermal is also a big issue for the IPT system design. Eddy currents are generated in the metal if a piece of metal is dropped near the IPT system. The metal gets hot and can ignite nearby fallen leaves and paper. To eliminate the risk of ignition, SAE standards

dictate the placement of metal detection sensors or coil surface magnetic fields that do not heat the metal pieces to the ignition temperature.

Electromagnetic waves from the IPT system may affect radios and electronic products. Standards such as SAE have been formulated to prevent these. In the US, frequencies for radio bands and other applications are not allowed for IPT systems. Currently, 79-90 kHz is the main range the IPT system can use, but the extension of the high-frequency band standard is to be considered in the future.

One option for reducing the stray fields around the vehicle is to lower the receiver coil towards the charging platform to cover the transmitter coil. This confines the fields to the active area of the power transfer while simultaneously increasing the efficiency of the power transfer due to the improved magnetic coupling. However, such a solution cannot fully profit from the potential of the technology because movable mechanical parts make the system unreliable and require expensive maintenance costs.

Alternative options include using high-permeability materials for guiding the magnetic flux and electromagnetic shielding. The mixed material of concrete and ferrite is discussed in a company [49].

Several active cancellation schemes have been proposed [50]. Although the leakage magnetic field can be greatly reduced, additional current is required to cancel the magnetic field, increasing system conduction loss. Also, additional windings and components are required, increasing cost and size.

1.4.6 Foreign object detection

DIPT systems need to detect foreign objects to maintain the safety of humans and the systems. However, it is challenging to implement foreign object detection (FOD) sensors for each transmitter coil due to the cost. FOD is categorized into metallic foreign object detection and living object detection [51,52]. Metallic foreign object detection is needed to avoid excessive heat on metal since the excessive heat is dangerous for firing or burning. Living object detection is needed to protect humans from strong magnetic fields. Even though the

frequency range for DIPT systems (79 kHz - 90 kHz) is relatively safer than the further high frequency over the GHz range, the limit is still defined by standard organizations [48].

1.5 Goals and contributions of the thesis

This dissertation research tries to solve the first five key engineering challenges mentioned above. A reflexive tuning circuit is one of the attractive solutions to reduce the cost of inverters, which is the biggest factor of the DIPT system cost. However, the conventional reflexive tuning circuit has less flexibility in that design. As a result, the output power is forced to be small, or the resonance is unstable. This research proposes a new reflexive tuning circuit to overcome the challenge.

Developing a design optimization method for the DIPT system is one of the promised solutions to solve the issue of cost for coils, including winding made with copper and core made with magnetic material, stray field design, high tolerance of misalignment, and wide interoperability. However, the conventional design optimization method for IPT systems relies heavily on FEM simulation. This problem is further compounded for DIPT systems since DIPT requires more calculation points than IPT to know the average output power across the primary coil. Consequently, it is difficult to achieve complete design optimization. To overcome the challenge, this study proposes a new design optimization method for DIPT utilizing a neural network.

This dissertation aims to understand the technical limitations of the proposed reflexive tuning method. As mentioned above, many challenges remain for DIPT. It is necessary to clarify the advantages and disadvantages of technology options that can solve them and understand the technical limitations. This paper develops an ANN- and GA-based DIPT optimization method and clarifies the reflexive tuning circuit's technical limitations for cost reduction.

The main scientific contribution of the thesis is:

The technical limits of the proposed circuit are clarified by proposing a new reflexive tuning circuit and developing a new ANN and GA-based optimal design method. In addition, ANN and GA-based optimization design methods can be expanded to various other applications

that require FEM calculation in their design.

1.6 Outline of the thesis

The content is divided into seven chapters, briefly outlined in the following. Chapter 2 is a general overview of the technologies involved in IPT systems. It covers the fundamental parts of IPT systems and the major tuning techniques, including series and parallel tuning in receiver-side circuits.

In Chapter 3, a new reflexive tuning circuit is investigated. First, the theoretical formula of the proposed circuit is derived based on the conventional reflexive tuning circuit. Validity is verified in the simulation and 2 kW mini experimental system.

ANN-based design optimization method for IPT systems is developed in Chapter 4. First, the fundamental of ANN's nonlinear fitting theory of geometry parameter and magnetic parameters is described. Next, the procedure of the proposed ANN-based design method is explained. The proposed method uses magnetic field superposition to acquire training data time efficiently. The design process is demonstrated for a 3 kW stationary charging system design. We compare the experimental and ANN prediction results in detail and discuss the merits and problems of the proposed method.

In Chapter 5, ANN- and GA-based optimization are considered. It is necessary to extend the ANN-based optimization method developed for stationary charging to DIPT. However, DIPT has more input variables and design requirements, so it is difficult to obtain the optimal design point. We needed a design optimization method to find the optimum design point more effectively. Therefore, we develop an optimization method that combines ANN and GA. A 3 kW DIPT design is shown as an example of how effective input value improvement using GA is. A 3 kW prototype with four transmitter coils is developed with an automated rail to verify the validity of the proposed method. The experimental and prediction results of ANN- and GA-based algorithms are compared, and the merits and demerits of the proposed method are discussed.

In order to integrate the proposed reflexive tuning circuit and the ANN- and GA-based optimization method, a 50 kW reflexive tuning circuit is designed using the method and

constructed in Chapter 6. Efficiency, average output power, and output power ripple at 50 kW output operation are evaluated using the automated rail. Finally, the time response at 60 km/h is evaluated by constructing a vehicle system.

At the end of each chapter, short summaries of the obtained results are given, and the key findings are highlighted. Final conclusions obtained from the presented study are summarized in Chapter 7. The achieved performance of the reflexive tuning circuit is discussed in physical and technical limitations. Finally, the thesis is concluded with suggestions for potential future research areas. Several research findings presented in this thesis have been published at international conferences or in scientific journals. The respective publications have been cited in the document. Additionally, a list of the publications is given at the end of the thesis.

CHAPTER 2

An overview of Inductive power transfer systems

In this section, an overview of inductive power transfer systems is shown. The overview starts with the tuning technique of isolated dc-dc converters to generalize the discussion. Then, the discussion is expanded to the IPT tuning technique as a specific case of an isolated dc-dc converter configuration. Major tuning circuit topologies for the transmitter and receiver sides are explained separately. Finally, the major DIPT configurations are categorized, and each benefit and technical limitation are explained.

2.1 Isolated dc-dc converter & inductive power transfer

Isolated dc-dc converters are commonly used for onboard or offboard conductive chargers for electric vehicles to satisfy the safety requirement. Electrical isolation can protect the grid line if electric vehicle systems have trouble, such as short mode breaks during charging. As one of the configurations of isolated dc-dc converters, resonant isolated dc-dc converters are used, as shown in Fig. 2.1. V_{dc} and V_{bat} represent the dc voltage of the grid and vehicle's battery sides, respectively. V_{dc} is connected with an inverter to convert the dc current I_{dc} to ac current i_{in} . V_{bat} is connected with the diode rectifier to convert the ac current i_{out} to dc current I_{bat} . Transformer windings L_t and L_r are coupled with coupling coefficient k , which is usually strongly coupled with $k > 0.99$.

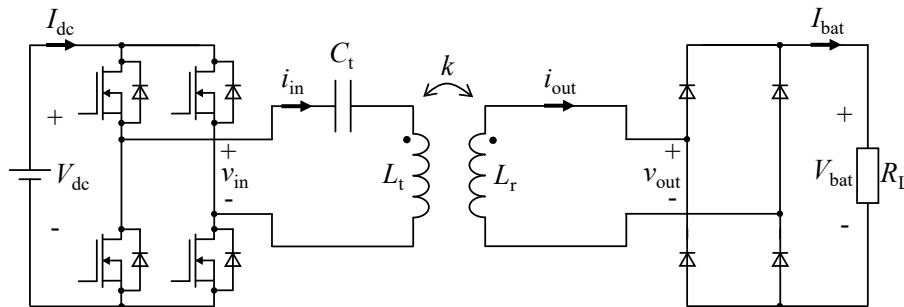


Fig. 2.1: Resonant isolated dc-dc converter

The equivalent circuit of the resonant isolated dc-dc converter is shown in Fig. 2.2. v_{in}

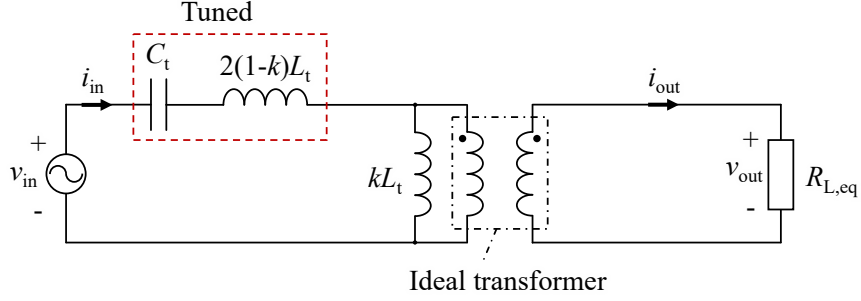


Fig. 2.2: Isolated dc-dc converter

is the inverter output voltage and is a rectangular waveform with a constant 50% duty cycle and 180-degree phase shift. Using the Fourier transfer, v_{in} can be represented as

$$v_{in}(t) = \frac{4V_{dc}}{\pi} \sum_{n=1,3,5,\dots} \frac{1}{n} \sin(n\omega t) \quad (2.1)$$

$$\simeq \frac{4V_{dc}}{\pi} \sin(\omega t) \quad (2.2)$$

where ω is the angular switching frequency of the inverter. The approximation is applied to the rectangular waveform's fundamental frequency ($n = 1$).

$R_{L,eq}$ is the equivalent load resistance. The diode rectifier current i_{out} can be assumed as a sinusoidal waveform. Since the summation of i_{out} in one switching cycle is equal to the battery dc current I_{bat} ,

$$I_{bat} = \frac{1}{T} \int_0^T |i_{out}| dt \quad (2.3)$$

$$= \frac{2}{T} \int_0^{T/2} I_{out} \sin(\omega t + \alpha) dt \quad (2.4)$$

$$= \frac{2}{\pi} I_{out}. \quad (2.5)$$

where α is the phase difference against the inverter voltage v_{in} . Hence, i_{out} can be represented as

$$i_{\text{out}} = I_{\text{out}} \sin(\omega t + \alpha) \quad (2.6)$$

$$= \frac{\pi}{2} I_{\text{bat}} \sin(\omega t + \alpha). \quad (2.7)$$

Since the conduction status of the diode is defined by the direction of the flowing current, the voltage of the diode rectifier v_{out} can be assumed as a rectangular waveform with the same phase as i_{out} . Therefore, the fundamental component of the Fourier series is represented as

$$v_{\text{out}}(t) = \frac{4V_{\text{bat}}}{\pi} \sin(\omega t + \alpha). \quad (2.8)$$

From (2.6) and (2.8), the equivalent load resistance $R_{\text{L,eq}}$ can be represented by the actual load resistance R_{L} as

$$R_{\text{L,eq}} = \frac{v_{\text{out}}}{i_{\text{out}}} \quad (2.9)$$

$$= \left\{ \frac{4}{\pi} V_{\text{bat}} \sin(\omega t + \alpha) \right\} / \left\{ \frac{\pi}{2} I_{\text{bat}} \sin(\omega t + \alpha) \right\} \quad (2.10)$$

$$= \frac{8}{\pi^2} R_{\text{L}}. \quad (2.11)$$

The leakage inductances of the windings L_{t} and L_{r} can be represented as $(1 - k)L_{\text{t}}$ and $(1 - k)L_{\text{r}}$, respectively. The magnetizing inductance of the transformer is represented as kL_{t} . The sum of the leakage inductances $(1 - k)L_{\text{t}}$ and $(1 - k)L_{\text{r}}$ on the transmitter side is represented as

$$L_{\text{leak}} = 2(1 - k)L_{\text{t}}. \quad (2.12)$$

The sum of the leakage inductance L_{leak} is compensated by C_{t} . When the impedance of the magnetizing inductance kL_{t} is large enough compared to the equivalent load resistance $R_{\text{L,eq}}$, the tuned circuit can be assumed that the voltage source v_{in} is directly connected

to a pure resistance. The tuning method can achieve high efficiency because the reactance that the series capacitance needs to compensate for is small in the high coupling coefficient condition. However, the tuning method is sensitive to the coupling coefficient since the resonant condition of the circuit is changed significantly when the leakage inductance is changed. Therefore, the positions of the coil need to be fixed. Additionally, when the coupling coefficient is decreased, and the impedance of magnetizing inductance becomes not large enough compared to the equivalent load resistance, the system efficiency decreases significantly due to the increased circulating current. Even though the resonant method can be applicable to IPT systems, the method is limited to applications with fixed coil positions and small air gaps, such as a rotating spindle [53].

In IPT systems for automotive applications, the coupling coefficient changes dramatically. Therefore, the resonant condition needs to be independent of the coupling coefficient. The tuning method for compensating leakage and magnetizing inductances are shown in Fig. 2.3. The compensation capacitor C_t and C_r compensate the self inductance L_t and L_r ,

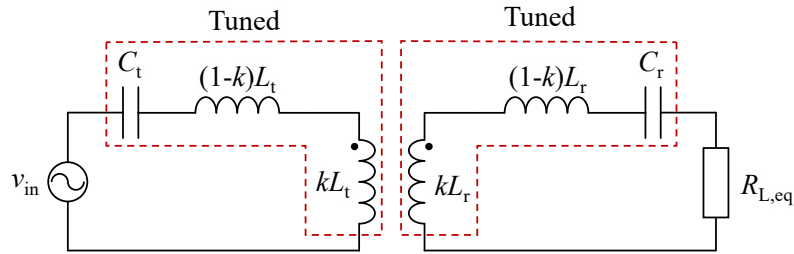


Fig. 2.3: IPT tuning

respectively. As a result, the resonant condition of the IPT system can be independent of the coupling coefficient k . However, the reactive power the compensation capacitor C_t and C_r needs to absorb becomes larger than the conductive charger. Hence, the efficiency of IPT systems is typically reduced compared to conductive chargers.

2.2 Basics of IPT tuning technique

A generalized resonant circuit model is shown in Fig. 2.4. Input and output voltages are

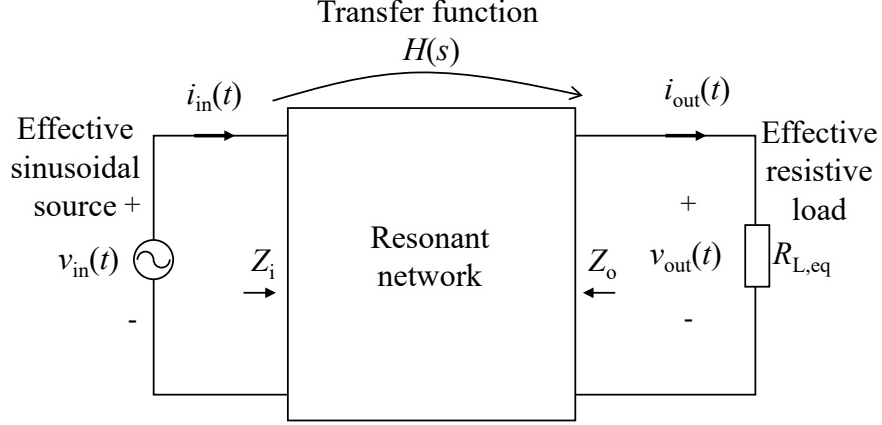


Fig. 2.4: Generarized resonant circuit model [10]

$v_{in}(t)$ and $v_{out}(t)$, respectively. The resonant network is represented with transfer function $H(s)$. The output effective resistive load is $R_{L,eq}$.

$H_{\infty}(s)$ is the open circuit ($R_{L,eq} \rightarrow \infty$) transfer function of the resonant network represented as

$$H_{\infty}(s) = \left. \frac{v_{out}(s)}{v_{in}(s)} \right|_{R_{L,eq}=\infty} \quad (2.13)$$

and Z_{o0} is the output impedance, determined when the input voltage $v_{in}(t)$ is a short circuit. Then, we can model the receiver side's resonant circuit by the Thevenin-equivalent circuit, as shown in Fig. 2.5. Using the derived receiver side model, the output voltage can be represented as

$$v_{out}(s) = H_{\infty}(s)v_{in} \frac{R_{L,eq}}{R_{L,eq} + Z_{o0}(s)} \quad (2.14)$$

Assuming the resonant circuit is purely reactive: any losses or other resistive elements within the resonant circuit are negligible. The equation can be rearranged as

$$\frac{|v_{out}(j\omega)|^2}{V_{oc}^2} + \frac{|i_{out}(j\omega)|^2}{I_{sc}^2} = 1 \quad (2.15)$$

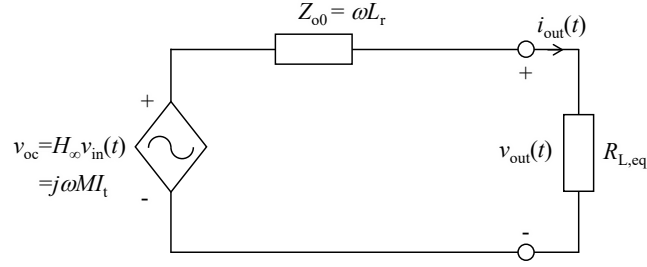


Fig. 2.5: Thevenin-equivalent circuit that models the receiver side circuit of the resonant circuit

where the open circuit voltage V_{oc} and short circuit current I_{sc} are given by

$$V_{oc} = |H_{\infty}(j\omega)| \cdot |v_{in}(j\omega)| \quad (2.16)$$

$$I_{sc} = \frac{|H_{\infty}(j\omega)| \cdot |v_{in}(j\omega)|}{|Z_{o0}(j\omega)|}. \quad (2.17)$$

The physical meaning of open circuit voltage V_{oc} and short circuit current I_{sc} are shown in Fig. 2.6.

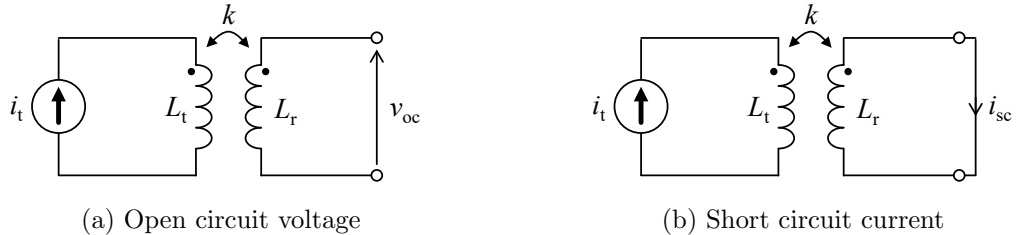


Fig. 2.6: Physical meaning of open circuit voltage and short circuit current

The relationship between the output voltage and current is depicted in Fig. 2.7. The solid line means the trajectory of output power when the reactance Z_{o0} is not compensated. The maximum output power is limited by reactive power caused by Z_{o0} . The dashed lines represent the output power of series compensation and parallel compensation circuits. The output power can be increased dramatically by compensating reactance Z_{o0} .

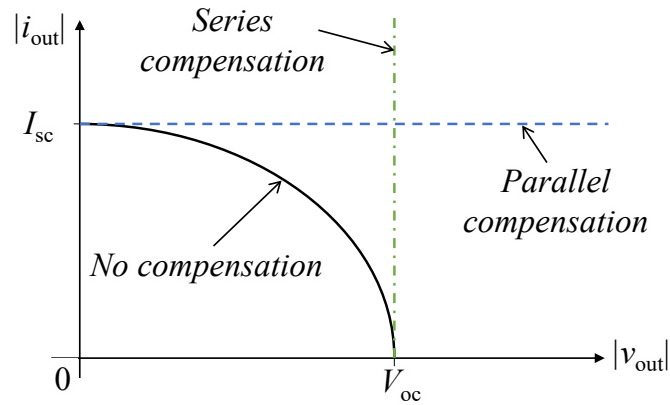


Fig. 2.7: Relationship between the amplitude of output voltage and output current [2]

The equivalent circuits of the series-tuned receiver circuit are shown in Fig. 2.8. The

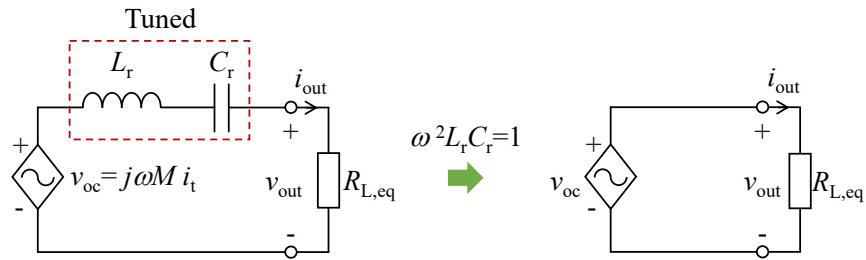


Fig. 2.8: Series tuned receiver circuit

output characteristic becomes constant voltage defined by v_{oc} . Since v_{oc} is the induced voltage by the transmitter current i_t , the amplitude of output voltage v_{out} is represented as

$$V_{out} = V_{oc} \quad (2.18)$$

$$= |H_{\infty}(j\omega)| \cdot |v_{in}(j\omega)| \quad (2.19)$$

$$= \omega M I_t. \quad (2.20)$$

where M is mutual inductance represented as $M = k\sqrt{L_t L_r}$. Hence, the output current is represented as

$$I_{\text{out}} = \frac{V_{\text{oc}}}{R_{\text{L,eq}}} \quad (2.21)$$

$$= \frac{MI_t}{R_{\text{L,eq}}} \quad (2.22)$$

$$= I_{\text{sc}}Q_s \quad (2.23)$$

where I_{sc} is short circuit current represented as

$$I_{\text{sc}} = \frac{|H_{\infty}(j\omega)| \cdot |v_{\text{in}}(j\omega)|}{|Z_{\text{o0}}(j\omega)|} \quad (2.24)$$

$$= \frac{V_{\text{oc}}}{|Z_{\text{o0}}(j\omega)|} \quad (2.25)$$

$$= \frac{V_{\text{oc}}}{\omega L_r} \quad (2.26)$$

$$= \frac{MI_t}{L_r}, \quad (2.27)$$

and Q_s is a load quality factor represented as

$$Q_s = \frac{L_r}{R_{\text{L,eq}}}. \quad (2.28)$$

Therefore, output power P_{out} with the series compensation is

$$P_{\text{out}} = V_{\text{out}}I_{\text{out}} \quad (2.29)$$

$$= V_{\text{oc}}I_{\text{sc}}Q_s. \quad (2.30)$$

The equivalent circuits of the parallel-tuned receiver circuit are shown in Fig. 2.9. The output current I_{out} becomes a constant defined by i_{sc} . Hence, the amplitude of i_{out} is

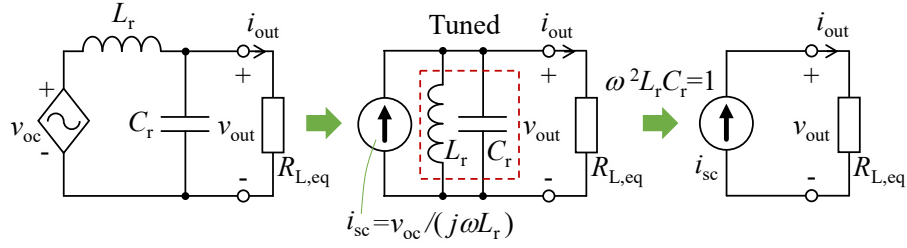


Fig. 2.9: Parallel tuned receiver circuit

represented as

$$I_{\text{out}} = I_{\text{sc}} \quad (2.31)$$

$$= \frac{M I_t}{L_r}. \quad (2.32)$$

Therefore, the amplitude of output voltage v_{out} is represented as

$$V_{\text{out}} = I_{\text{out}} R_{L,\text{eq}} \quad (2.33)$$

$$= \frac{M I_t R_{L,\text{eq}}}{L_r} \quad (2.34)$$

$$= V_{\text{oc}} Q_p \quad (2.35)$$

where Q_p is a load quality factor represented as

$$Q_p = \frac{R_{L,\text{eq}}}{L_r}. \quad (2.36)$$

Finally, the output power P_{out} with parallel compensation is represented as

$$P_{\text{out}} = V_{\text{out}} I_{\text{out}} \quad (2.37)$$

$$= V_{\text{oc}} I_{\text{sc}} Q_p. \quad (2.38)$$

The summary of the driven output voltage V_{out} , output current I_{out} , and output power P_{out} in each compensation circuit is listed in Table 2.1. Typically, Q_s or Q_p are designed around one to eight since an excessively high load quality factor makes the system unstable.

Table 2.1: The output characteristics of the different receiver compensations [2]

Maximum outputs	No compensation (at max power condition)	Series compensa- tion (Fully tuned) $Q_s = \omega_0 L_r / R_{L,eq}$	Parallel compensa- tion (Fully tuned) $Q_p = R_{L,eq} / (\omega_0 L_r)$
Output voltage V_{out}	$V_{oc} / \sqrt{2}$	$V_{oc} = \omega M I_t$	$V_{oc} Q_p$
Output current I_{out}	$I_{sc} / \sqrt{2}$	$I_{sc} Q_s$	$I_{sc} = M I_t / L_r$
Output power P_{out}	$V_{oc} I_{sc} / 2$	$V_{oc} I_{sc} Q_s$	$V_{oc} I_{sc} Q_p$

2.3 Compensation circuit topologies

This section summarizes typical compensation circuits used in IPT systems.

2.3.1 Transmitter side

Series compensation

This is the simplest and most efficient circuit method. However, when the coupling

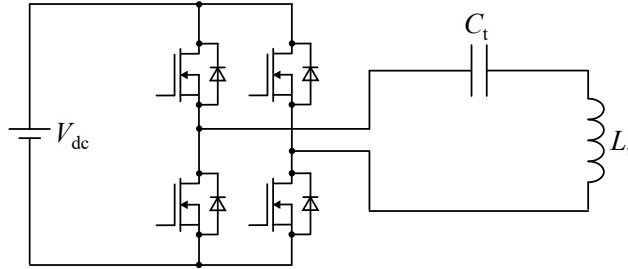


Fig. 2.10: Series tuned transmitter circuit

coefficient is zero, the current in the transmitter coil becomes extremely large. Therefore, the controller must adjust the applied voltage by sensing the current and controlling the phase of the inverter. This circuit method is unsuitable for DIPT applications since the coupling coefficient changes frequently.

Parallel compensation

In order to solve the problem that the power transmission coil becomes extremely large when the coupling coefficient becomes zero, this method uses a parallel configuration of

the resonance capacitors on the power transmission side. The transmitting coil current is

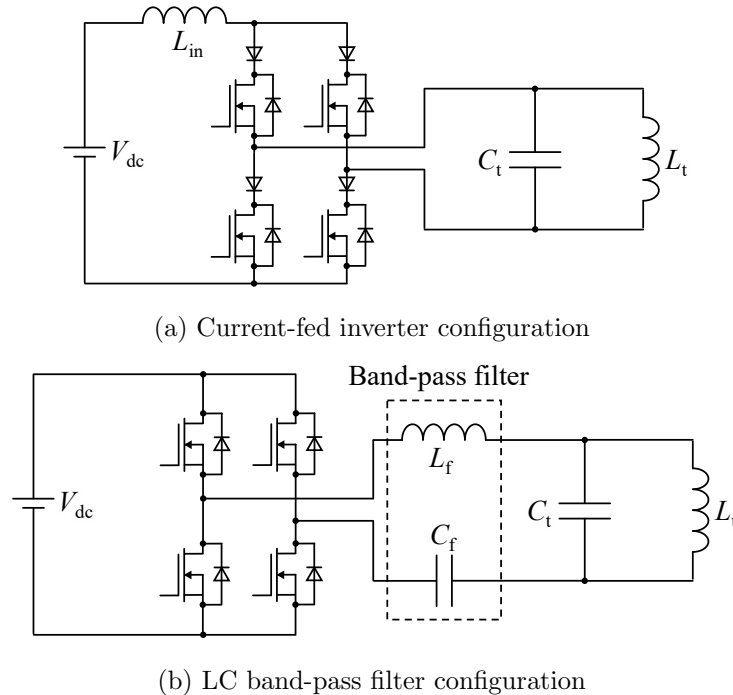


Fig. 2.11: Parallel tuned transmitter circuit

constant regardless of the coupling coefficient. However, the sine wave voltage of the parallel capacitor and the rectangular voltage of the inverter is directly connected in each switching cycle, which causes short-circuit current. Therefore, it is necessary to use a Current-fed inverter instead of a Voltage-fed inverter or insert a band-pass filter between the inverter and the resonance capacitor to pass only the fundamental wave component of the switching frequency.

LCC compensation

Even if the coupling coefficient changes, the current in the power transmission coil remains constant as in the Parallel method. Since the inductor exists in the connection points of the inverter, the inverter configuration becomes simple since a voltage-fed inverter can be used. In general, voltage-fed inverters are preferred over current-fed inverters because

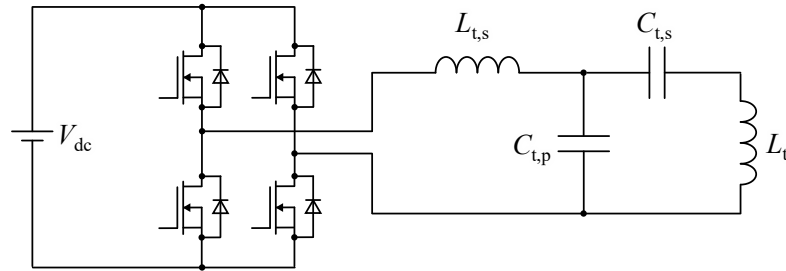


Fig. 2.12: LCC tuned transmitter circuit

they have fewer parts. By adjusting the inductor's value, the transmitter coil's current and voltage can be designed flexibly.

2.3.2 Receiver side

Series compensation

Since it is a constant voltage output, it is not suitable for applications such as batteries that require charging operation with constant current output.

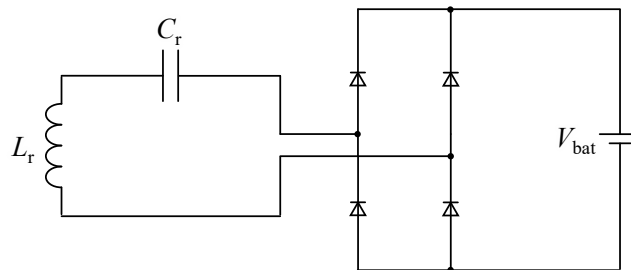


Fig. 2.13: Series tuned receiver circuit

Parallel compensation

The circuit on the power receiving side becomes a constant current output circuit and has characteristics suitable for battery charging. However, an instantaneous current is generated at the timing when the rectangular wave voltage of the rectifier and the sine wave

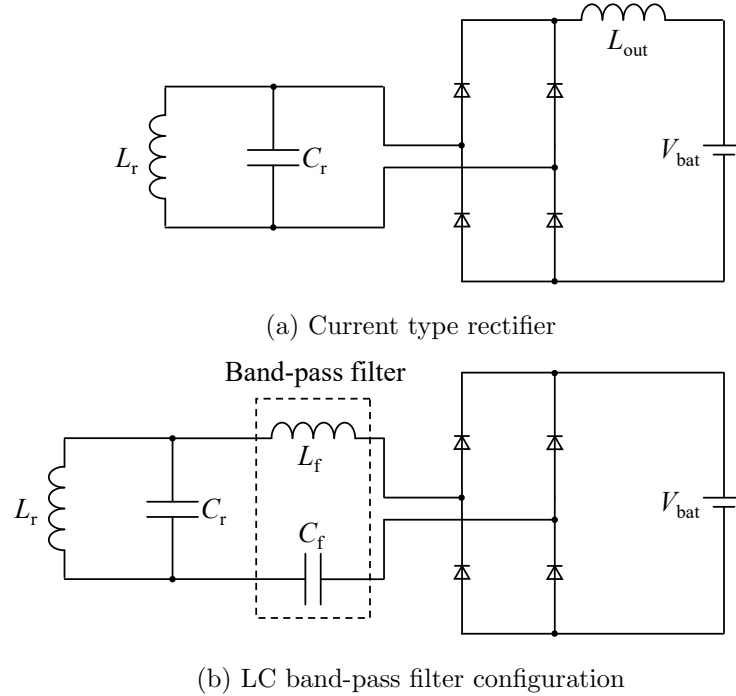


Fig. 2.14: Parallel tuned receiver circuit

voltage of the parallel capacitor on the receiving side is connected in every switching cycle. To prevent this, it is necessary to use a current source rectifier or insert an LC bandpass filter between the resonator and the rectifier.

LCC compensation

Similar to the Parallel method, it has constant current output characteristics, making it suitable for battery charging applications. Since the inductor exists at the connection

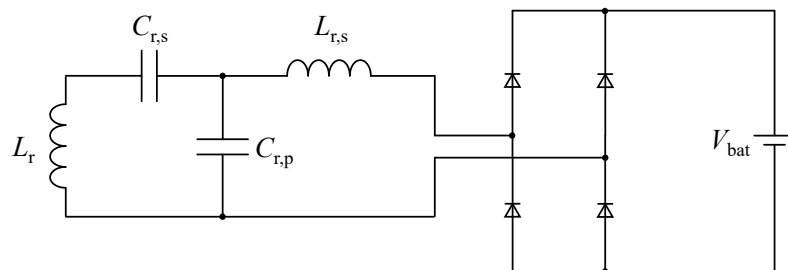
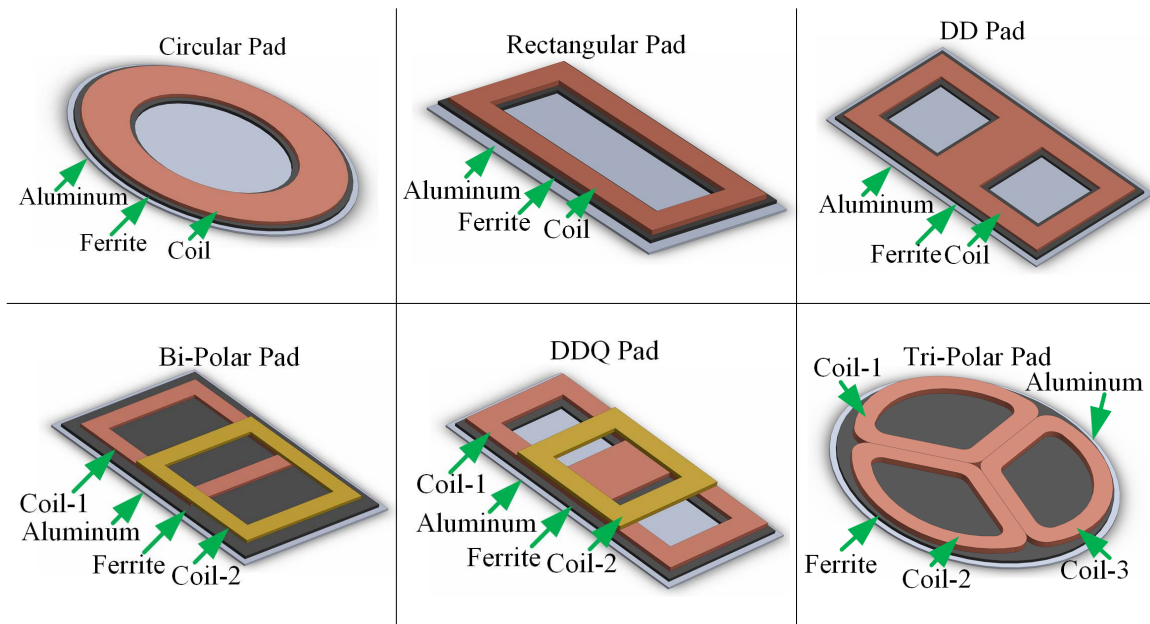


Fig. 2.15: LCC tuned receiver circuit

Table 2.2: List of IPT pad topologies [3]



point of the rectifier circuit, a voltage-type rectifier can be used, and the number of parts can be reduced.

2.4 IPT pad topologies

Table 2.2 shows the list of the IPT pad topologies. The circular pad has the simplest pad structure in this list. It can achieve higher efficiency due to its higher coupling coefficient compared to the rectangular, double D (DD), and DD-quadrature (DDQ) coil topologies [54, 55]. It is the most common pad topology for stationary IPT applications because of its high-efficiency characteristic. The rectangular pad is more cost-effective and compact than the circular pad since the rectangular pad can utilize a larger area than the circular pad to create a magnetic field. Due to its cost-effective and compact characteristics, the topology is the most common pad topology for dynamic IPT applications. The DD pad has a smaller leakage field than the rectangular pad, although it has a similar footprint to the rectangular pad [56]. The bipolar pad has two coils placed so that the two coil's coupling coefficient becomes zero [57–59]. The two coils can be driven independently since the two rectangular coils are magnetically disconnected. If two independent inverters are connected,

the topology is interoperable with the rectangular and DD receiver pads. The topology offers good misalignment tolerance. The DDQ pad consists of the rectangular and DD coil. Similar to the bipolar pad, the two coils are magnetically disconnected [37]. It offers good misalignment tolerance and requires two synchronized inverters for power input if the two coils need to be driven independently. The performances of efficiency and stray field are similar to the bipolar pad. The tripolar pad has a higher coupling coefficient and lower stray magnetic field characteristics than the circular pad [60]. It requires three single-phase synchronized inverters or one three-phase inverter.

2.5 Transmitter side configurations for DIPT Systems

DIPT systems can be categorized into two major types, as shown in Fig. 2.16 [3,61–64]. The first is a long-track configuration, as shown in Fig. 2.16 (a). Continuous power can

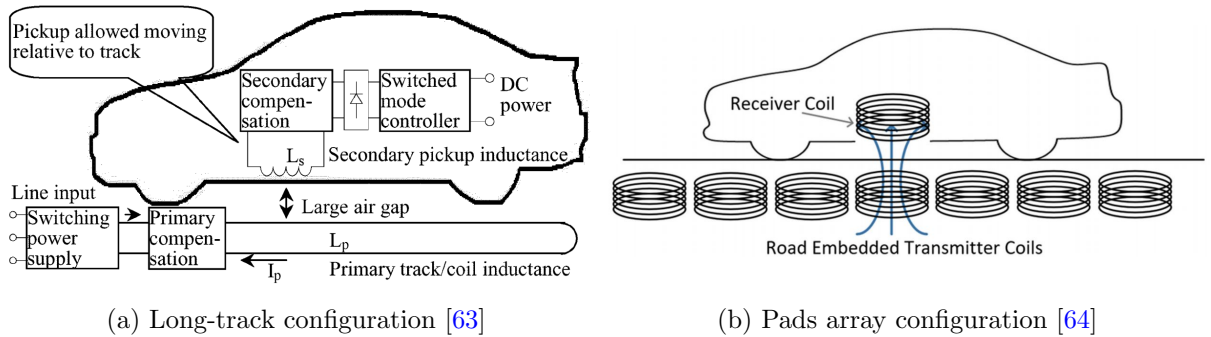


Fig. 2.16: Two major configurations of DIPT systems

be transferred when an EV with a receiver coil runs above the transmitter. The second is a pads-array configuration, as shown in Fig. 2.16 (b). An independent power converter in this configuration can drive each pad. Hence, the transmitters can be selectively excited without a high-frequency common current in the long-track transmitter. The details of each method are discussed in the following sections.

2.5.1 Long track type

Long-track configuration can be further categorized into two types.

Normal long track

The normal long track type simplifies system control and provides a relatively constant coupling coefficient when the vehicle moves in the design space, as already shown in Fig. 2.16 (a) [63, 65–69]. This type can simplify the DIPT system since the number of inverter and compensation circuits is minimized. However, it has three drawbacks [15, 70, 71].

First, the coil generates a stray magnetic field in a large area since a long stretch of road has a coil that is excited with high current, even while a receiver coil only covers a small portion of the transmitter. This results in difficulty maintaining stray fields below the safety limits and achieving high system efficiency [15, 70, 71].

Secondly, the long track design has a higher self-inductance due to the longer coil length, which creates high voltages across the coil terminals. Limiting the coil voltage below the insulation capability of high-frequency power cables, typically up to 5 kV [65] is difficult. The system presented in [72] needed to break up a coil and add a series of capacitors to reduce the coil voltage.

Third, the coupling coefficient becomes quite low due to the large uncoupled area of the transmitter coil. It results in low system efficiency.

Segmental long track

To solve the problems of the normal long-track configuration, the literature [11, 73] proposed segmental long tracks, where the track is made of segmental tracks with a single inverter and a set of switches to select which segmental track should be excited, as shown in Fig. 2.17. The excitation of each segment can be controlled by the ON-OFF state of the switches. The electromagnetic field above the inactive segments is significantly reduced. However, the system needs at least one mechanical relay or bidirectional semiconductor switch per segmental track. The mechanical relay switch makes the reduction of reliability and lifetime of the system, which leads to the system maintenance cost increase. If we use the bidirectional switches, two equivalent numbers of semiconductor switches are needed per bidirectional switch, equal to the number of semiconductor switches for a half-bridge

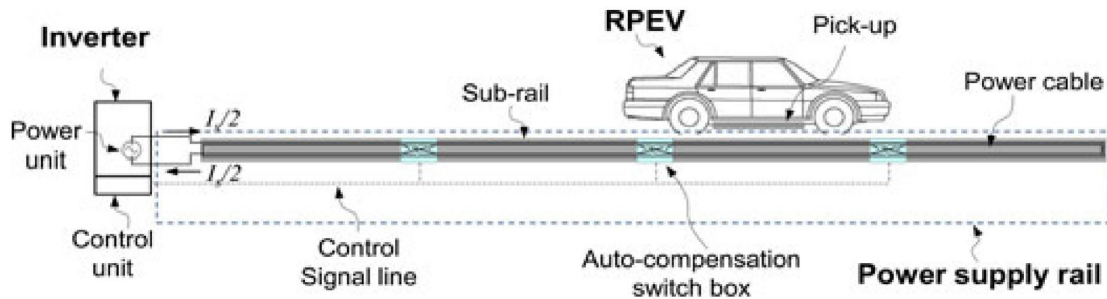


Fig. 2.17: Segmented long track [11]

inverter. Therefore, the segmental long-track configuration often requires significant cost increases compared to the normal long-track configuration.

2.5.2 Pads-array type

The pads-array type can be further categorized into six groups: independent inverter, bypass switch, double coupled method, reactive power compensation by auxiliary circuit, autotuning system by variable self-inductance, and reflexive tuning [61,62]. The type solves the long track type's issues, such as the high stray magnetic field, low coupling coefficient, and large self-inductance on the transmitter side. However, the pads-array design results in a complicated system requiring more inverters to power the coil, additional bypass switches, and receiver position sensors.

Independent Inverter type

In the independent inverter configuration, each pad can be driven by an independent inverter, as shown in Fig. 2.18 [12, 74–76]. Thus, the transmitter can be selectively excited without a high-frequency common current in the long track coil. Moreover, the vehicle covers the energized transmitter, meaning the electromagnetic field is shielded to have a minimum impact on the surrounding environment. Hence, the efficiency and EMI performance could be as good as that in stationary charging. However, the system needs an inverter for each coil. The cost for the system turns out quite expensive compared to the long track

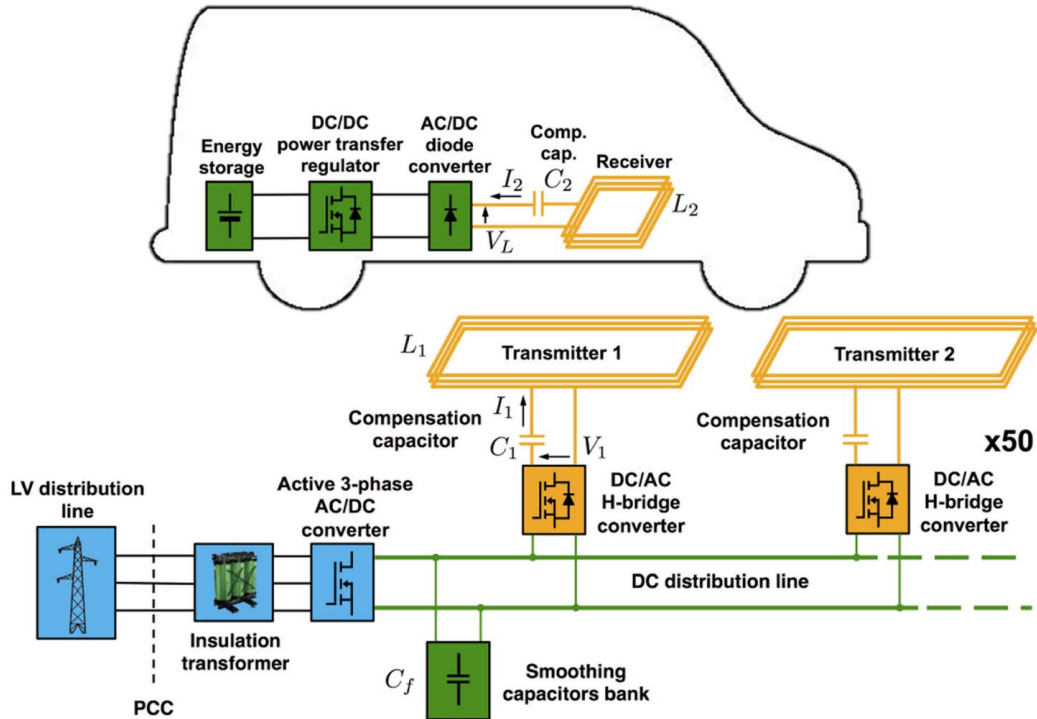


Fig. 2.18: Individual inverter type [12]

configuration. Moreover, the system also needs a position detection sensor to switch the active transmitter coil.

Bypass Switch Type

The bypass switch type uses mechanical relays or bidirectional semiconductor switches to switch circuits to use the same inverter for multiple transmitter coils, as shown in Fig. 2.19 [11, 13, 74, 77–79]. The system switches the coils connected to an inverter according to the position of the receiver coil. The benefit of the system is that it can reduce the number of inverters. However, the system needs at least one mechanical relay or bidirectional semiconductor switch per segmental track, which is the same problem as the segmental track configuration. Additionally, the sensors for each segmented coil are still needed to detect the secondary side coil and switch the bypass switches.

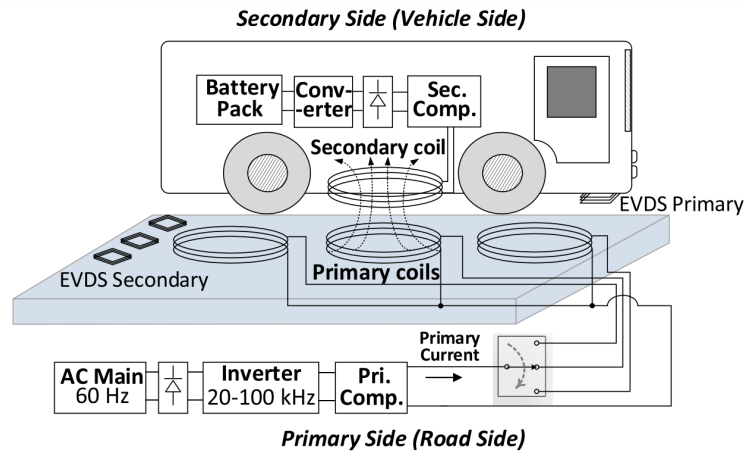


Fig. 2.19: Bypass switch type [13]

Double-coupled method

The double-coupled method has an intermediary coupler and a bidirectional switch per transmitter coil, as shown in Fig. 2.20 [14]. The intermediary couplers are coupled to one

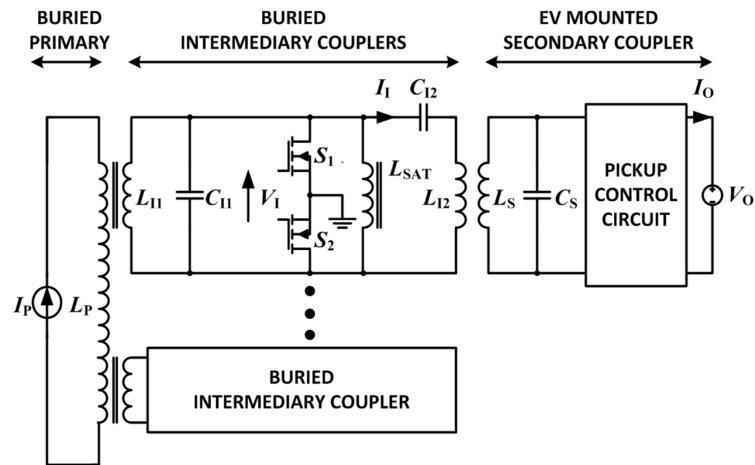


Fig. 2.20: Double-coupler method [14]

transmitter coil on the inverter side. By controlling the ON-OFF time of the switch, the current in each transmitter coil can be controlled. Any transmitter coil can be shut down anytime by the switches. However, the circulating current loss is significantly high since the high-frequency current always circulates in all the intermediary couplers.

Reactive power compensation network by an auxiliary circuit

In the circuit, multiple paralleled transmitter coils are connected to a single inverter. Only the transmitter coil coupled with the receiver coil is activated with a high current, as shown in Fig. 2.21 [15]. An auxiliary LCC network is introduced to regulate the current in

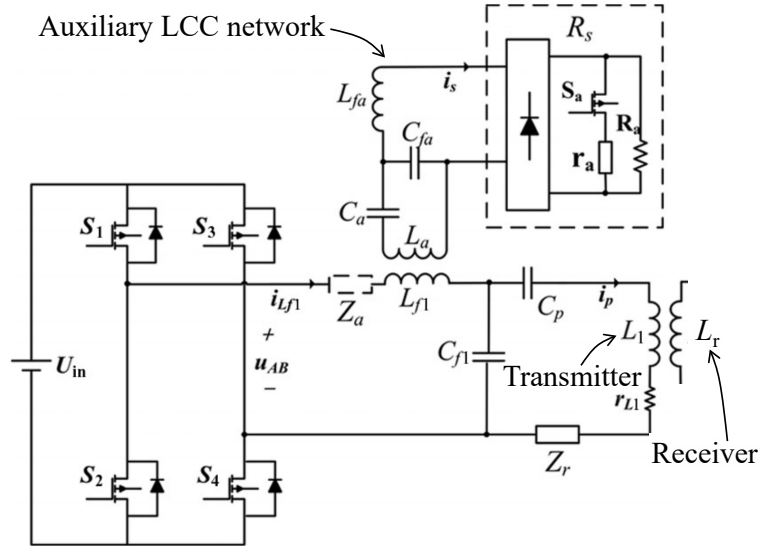


Fig. 2.21: Reactive power compensation network by an auxiliary circuit [15]

the transmitter coil to minimize electromagnetic interference (EMI) and reduce the system's power loss. However, the auxiliary LCC network needs at least one active-controlled power semiconductor and two power diodes per transmitter coil, leading to a decrease in system reliability and a significant cost increase.

Autotuning system by variable self-inductance

The system utilizes the variation of a transmitter coil's self-inductance caused by a receiver coil's ferrite core, as shown in Fig. 2.22 [16]. A transmitter module consists of only passive elements, including series and parallel compensation capacitors. All transmitter modules share a high-frequency ac bus line in parallel without active switches. The current of the coupled transmitter coil increases automatically without any operations, such as controlling the power switches, sensing, or communication as the receiver module approaches.

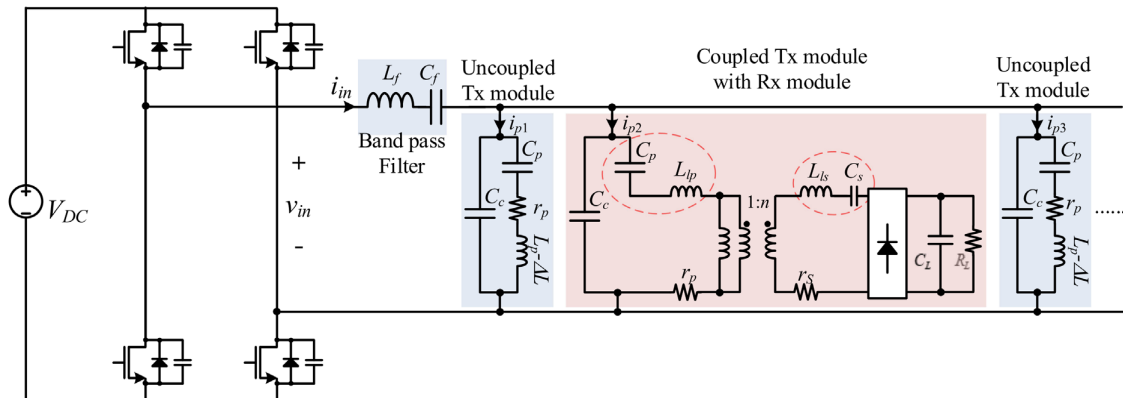


Fig. 2.22: Reactive power compensation network by an auxiliary circuit [16]

Reducing the conduction losses from the uncoupled transmitter modules increases the system's efficiency. Moreover, control becomes simpler because sensors are not required to detect a receiver module. However, the system is unsuitable for vehicle applications because the system needs a small air gap to get enough amount of variation of self-inductance.

Reflexive tuning method

The reflexive tuning method switches resonated transmitter coils utilizing reflected impedance [17, 64]. Fig. 2.23 shows a concept of the reflexive tuning approach. The system

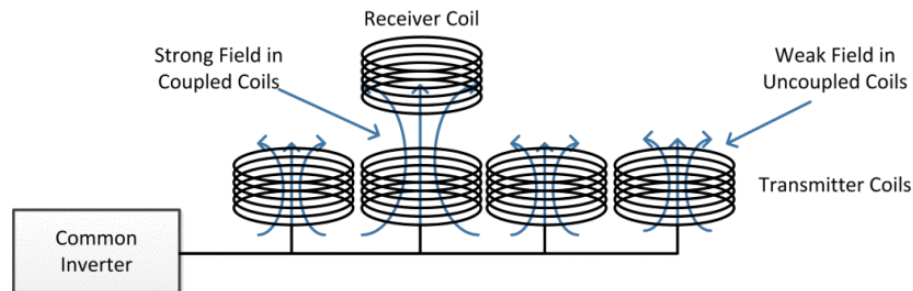


Fig. 2.23: reflexive tuning method [17]

has a common inverter and segmented transmitter coils. The transmitter coil, coupled with the receiver coil, resonates and generates a strong magnetic field. The proposed circuit

topology to achieve the concept uses a reflected impedance. The reflected impedance that appears in the transmitter coils is changed depending on the position of the secondary coil. At particular values of reflected impedance, the primary resonant network will be at resonance, allowing power transfer. As a result, the system can change the amplitude of the current in the transmitter coil automatically. However, the proposed circuit in this literature does not have enough degrees of freedom in its design. Hence it is difficult to achieve the optimized design according to applications. The dissertation research proposes a new magnetic focusing circuit with more degrees of freedom.

2.6 Summary of the Chapter

In this chapter, theoretical equations of IPT systems were derived using a generalized transfer function model. The output voltage, output current, and output power can be represented with simple equations using the open circuit voltage and short circuit current. Second, circuit topologies in actual implementations were discussed. For the transmitter side, the constant current characteristic is suitable for DIPT applications compared to the constant voltage characteristic since a small coupling coefficient causes excessive transmitter current if the transmitter side has a constant voltage characteristic. For the receiver side, the suitable characteristic is also constant current since the battery charging application needs a constant current operation. Considering the constant current characteristic, cost, and design flexibility, double-sided LCC topology is the most typical topology for DIPT applications. Finally, transmitter-side configurations for DIPT systems were discussed, and tradeoffs between long track and pads-array types are explained. Long track type can achieve a relatively low-cost system because fewer inverter and compensation components are required. However, a high stray magnetic field, excessive-high coil voltage, and low system efficiency due to low coupling coefficient and large coils are drawbacks of the system. As a counterpart, the pads-array type is often used for DIPT systems. The system with independent inverters can solve the drawbacks of the long-track system. However, the independent inverter type requires an inverter per transmitter coil, occupying over half of the system cost. Several configurations have been proposed to take both benefits of the

long track type and pad-array type, such as bypass switch type, double-coupled method, and reflexive tuning method. However, each solution cannot simultaneously achieve low cost, low stray field, and high efficiency. The next chapter proposes an improved version of the reflexive tuning method. To verify the limitations of the proposed method, a new optimization method is also developed in this thesis.

CHAPTER 3

Reflexive tuning IPT systems

As mentioned in the previous chapter, dynamic inductive power transfer (DIPT) systems can be categorized into two major types; long track type and array-pads type. Pros of the long track type are simplicity and low cost. Cons are high stray field, low efficiency, and excessive-high transmitter voltage. Array-pads type can be considered as the counterpart of the long track type. The pros of the array-pads type are low stray field, high efficiency, and relatively low transmitter voltage. However, the array-pads type has two cons; complexity and expensive cost. To overcome these tradeoffs between long track type and array-pads type, many different types of DIPT systems have been proposed. As one of the attractive solutions for the issue, the reflexive tuning circuit has been proposed. The system has a simple configuration compared to other solutions since the system switches the active transmitter coil automatically with a passive control. However, the system's cons are the difficulty of designing high-power applications due to the few design parameters. To investigate the further possibility of this approach, a new reflexive tuning circuit is proposed and verified in simulations and an experimental system in this chapter.

The reflexive tuning type can automatically switch an activated transmitter coil utilizing a variation of the reflected reactance [17,64], as shown in Fig. 3.1. The reflexive tuning circuit has a common inverter and arrayed transmitter coils. Each transmitter coil connects to a resonator circuit detuned when a vehicle is not present. As a result, a low current will flow through the coils when no receiver coil is present. When a vehicle is above the top of the transmitter coil, the reflected reactance from the receiver coil will tune the transmitter circuit, allowing a large current to flow through the transmitter coils and transfer power to the vehicle. Each transmitter coil can automatically change the amplitude of the current, even though all the transmitter coils are excited by the same inverter. However, existing reflexive tuning circuits [17,64] do not allow both the power output and gain of the

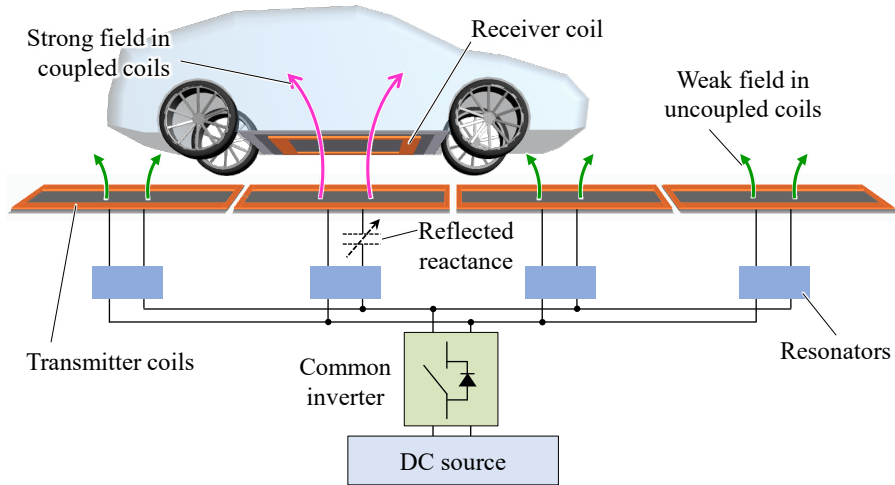


Fig. 3.1: The conceptual diagram of the reflexive tuning approach

transmitter coil to be designed simultaneously due to few design parameters in the compensation circuit. Hence, achieving high output power while maintaining the desired gain of transmitter current is challenging.

3.1 Conventional reflexive tuning topology

The conventional reflexive tuning circuit topology [17, 64], as shown in Fig. 3.2, consists of a bandpass filter formed by L_f and C_f on the inverter side. The purpose of the

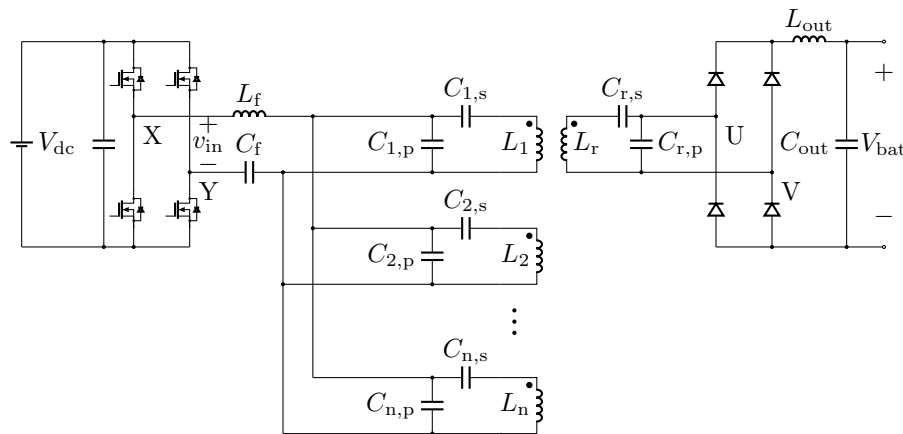


Fig. 3.2: Conventional reflexive tuning circuit topology

bandpass filter is to reduce switching loss due to harmonics in the inverter current from the uncoupled transmitter coil branches. Another benefit of the bandpass filter is eliminating pulse current caused by the rectangular-shaped inverter voltage and the sinusoidal-shaped parallel connected capacitor voltages. Each branch has a parallel compensation capacitor $C_{1,p}$ and a series compensation capacitor $C_{1,s}$. On the receiver side, a series compensation capacitor $C_{r,s}$ and a parallel compensation capacitor $C_{r,p}$ are attached.

The conventional circuit requires an output inductor L_{dc} between the secondary compensation circuit and the output voltage V_{bat} since $C_{r,p}$ can be assumed as a voltage source, and switching action of the diode rectifier creates large current spikes if L_{dc} is not attached between $C_{r,p}$ and V_{bat} .

3.2 Proposed reflexive tuning circuit topology

The proposed reflexive tuning circuit topology is shown in Fig. 3.3. Compared to

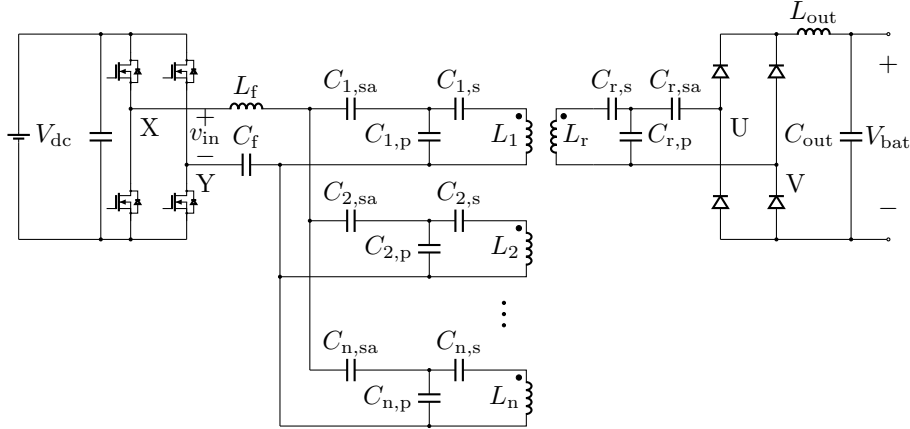


Fig. 3.3: Proposed reflexive tuning topology

the conventional reflexive tuning circuit, each branch has an additional series compensation capacitor $C_{1,sa}$ on the transmitter side and an additional series compensation capacitor $C_{r,sa}$ on the receiver side. $C_{1,sa}$ works as a voltage divider and can reduce the applied voltage to the uncoupled transmitter coils, reducing the uncoupled transmitter currents. $C_{r,sa}$ can

increase the reflected reactance by inserting capacitance in the receiver side unturned loop.

The series compensation capacitor $C_{r,sa}$ on the receiver side can increase the reflected reactance for the reflexive tuning function. The additional compensation capacitor $C_{r,sa}$ solves the problem that the conventional reflexive tuning circuit needs to design output power and reflected reactance by only the ratio of $C_{r,p}$ and $C_{r,s}$.

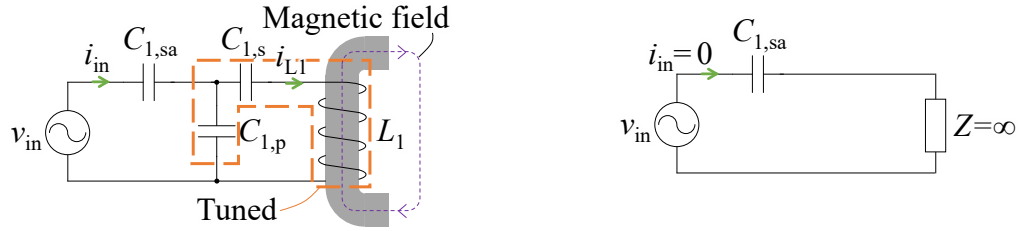
The proposed circuit has more degrees of freedom in its design because of the additional series compensation capacitors on both the transmitter and receiver sides. The benefit of the proposed reflexive tuning topology is that a higher power design can be achieved while maintaining uncoupled currents at the same level compared to the conventional circuit.

3.3 Theoretical analysis of the proposed circuit

Theoretical equations to design the proposed circuit are derived in this section. For simplicity, only the first transmitter coil is considered in this analysis.

3.3.1 Uncoupled condition

The transmitter side circuits to derive theoretical inverter current in the uncoupled condition is shown in Fig. 3.4. The transmitter side circuit in the uncoupled condition is



(a) Transmitter side circuit in the uncoupled condition
 (b) Redrawn circuit with the total impedance of L_1 , $C_{1,s}$, and $C_{1,p}$

Fig. 3.4: Circuit conversion process to derive theoretical inverter current in the uncoupled condition

shown in Fig. 3.4(a). Inverter current and transmitter current are represented as i_{in} and i_{L1} ,

respectively. The components $C_{1,p}$, $C_{1,s}$, and L_1 are tuned, and the equation is written as

$$j\omega L_1 + \frac{1}{j\omega C_{1,s}} + \frac{1}{j\omega C_{1,p}} = 0. \quad (3.1)$$

The total impedance of L_1 , $C_{1,s}$, and $C_{1,p}$ are represented as

$$Z = \frac{\frac{1}{j\omega C_{1,p}}(j\omega L_1 + \frac{1}{j\omega C_{1,s}})}{j\omega L_1 + \frac{1}{j\omega C_{1,s}} + \frac{1}{j\omega C_{1,p}}} = \infty \quad (3.2)$$

Therefore, the circuit can be represented with the total impedance Z as shown in Fig. 3.4(b), and the inverter current in the uncoupled condition is written as

$$i_{in}|_{k_{1,r}=0} = 0. \quad (3.3)$$

The transmitter side circuit in the uncoupled condition to derive the transmitter current is shown in Fig. 3.5. Using Norton's theorem, the voltage source in the uncoupled circuit

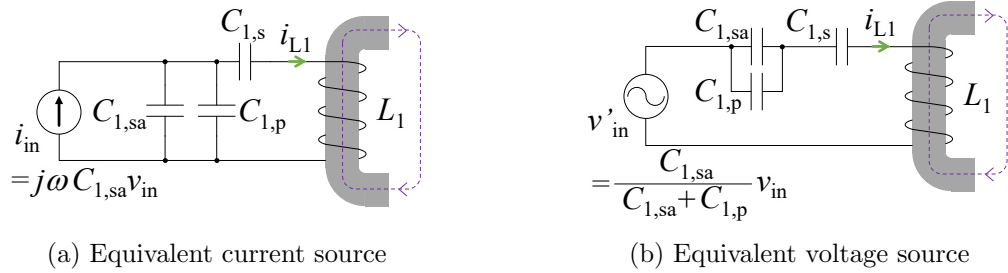


Fig. 3.5: Uncoupled transmitter side circuits to derive the equation of the transmitter current

shown in Fig. 3.4(a) is converted to the equivalent current source as shown in Fig. 3.5(a), and the equivalent current source i_{in} is represented as

$$i_{in} = j\omega C_{1,sa} v_{in}. \quad (3.4)$$

Using Thevenin's theorem, the current source is converted to the equivalent voltage

source, and the equivalent circuit Fig. 3.5(a) is converted to Fig. 3.5(b). The equivalent voltage source v'_{in} is represented as

$$v'_{in} = \frac{i'_{in}}{j\omega(C_{1,sa} + C_{1,p})} = \frac{C_{1,sa}}{C_{1,sa} + C_{1,p}} v_{in} \quad (3.5)$$

Therefore, the transmitter current in the uncoupled condition is

$$\begin{aligned} i_{L1}|_{k_{1,r}=0} &= \frac{v'_{in}}{j\omega L_1 - \frac{1}{\omega C_{1,s}} - \frac{1}{\omega(C_{1,sa} + C_{1,p})}} \\ &= \frac{-v_{in}}{j\omega k_{1,r}^2 L_1 \left(1 + \frac{C_{1,p}}{C_{1,sa}}\right) \left(1 + \frac{C_{r,p}}{C_{r,s}}\right) \left(1 + \frac{C_{r,p}}{C_{r,sa}}\right)} \\ &= \frac{-v_{in}}{j\omega k_{1,r}^2 L_1 c_1 c_2 c_3} \end{aligned}$$

where

$$c_1 = 1 + \frac{C_{1,p}}{C_{1,sa}}, \quad c_2 = 1 + \frac{C_{r,p}}{C_{r,s}}, \quad c_3 = 1 + \frac{C_{r,p}}{C_{r,sa}}. \quad (3.6)$$

3.3.2 Coupled condition

The equivalent circuit in the coupled condition is shown in Fig. 3.6.

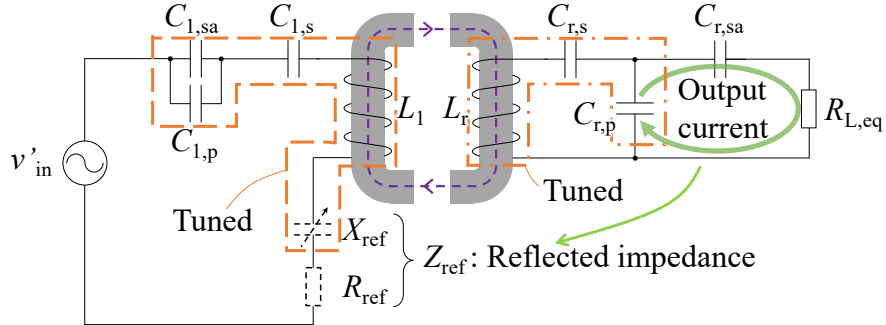


Fig. 3.6: Coupled condition

The loop current flowing $C_{r,p}$, $C_{r,sa}$, $R_{L,eq}$ creates reflected impedance Z_{ref} which is represented as $Z_{ref} = R_{ref} - jX_{ref}$ where R_{ref} is reflected resistance and X_{ref} is reflected reactance, respectively. The reflected reactance X_{ref} and the transmitter side components

$C_{1,sa}$, $C_{1,p}$, $C_{1,s}$, L_1 are tuned in the fully coupled condition, and the equation is represented as

$$\frac{1}{j\omega(C_{1,p} + C_{1,sa})} + \frac{1}{j\omega C_{1,s}} + j\omega L_1 - jX_{\text{ref}} = 0. \quad (3.7)$$

Therefore, the amplitudes of transmitter coils can be increased only when the reflected reactance X_{ref} is created in the coupled condition. The receiver side loop current flowing L_r , $C_{r,s}$, and $C_{r,p}$ are tuned, and the equation is represented as

$$\frac{1}{j\omega C_{r,s}} + \frac{1}{j\omega C_{r,p}} + j\omega L_r = 0. \quad (3.8)$$

3.3.3 Output power

An equivalent circuit in the coupled condition is defined to derive the theoretical equation of output power for the proposed circuit, as shown in Fig. 3.7. Circuit equations can

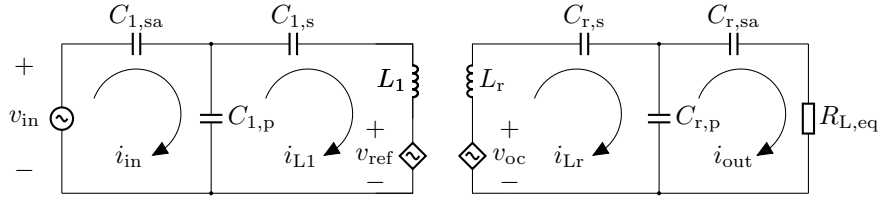


Fig. 3.7: Equivalent circuit in the coupled condition

be written in a matrix form as

$$\begin{bmatrix} \frac{1}{j\omega C_{1,sa}} + \frac{1}{j\omega C_{1,p}} & -\frac{1}{j\omega C_{1,p}} \\ -\frac{1}{j\omega C_{1,p}} & j\omega L_1' + \frac{1}{j\omega C_{1,p}} \end{bmatrix} \cdot \begin{bmatrix} i_{\text{in}} \\ i_{L1} \end{bmatrix} = \begin{bmatrix} v_{\text{in}} \\ -v_{\text{ref}} \end{bmatrix} \quad (3.9)$$

$$\begin{bmatrix} j\omega L_r' + \frac{1}{j\omega C_{r,p}} & -\frac{1}{j\omega C_{r,p}} \\ -\frac{1}{j\omega C_{r,p}} & \frac{1}{j\omega C_{r,p}} + \frac{1}{j\omega C_{r,sa}} + R_{L,eq} \end{bmatrix} \cdot \begin{bmatrix} i_{Lr} \\ i_{\text{out}} \end{bmatrix} = \begin{bmatrix} v_{\text{oc}} \\ 0 \end{bmatrix} \quad (3.10)$$

where ω is the angular switching frequency of the inverter, v_{in} is the equivalent input voltage, v_{ref} is the reflected voltage, v_{oc} is the induced voltage, $R_{L,eq}$ is the equivalent load resistance.

L'_1 , and L'_r are represented by

$$L'_1 = L_1 - \frac{1}{\omega^2 C_{1,s}}, \quad (3.11)$$

$$L'_r = L_r - \frac{1}{\omega^2 C_{r,s}}. \quad (3.12)$$

The reflected voltage v_{ref} and the induced voltage v_{oc} are depicted by the diamond mark since they are dependent voltage sources and represented by

$$v_{\text{ref}} = -j\omega M_{1,r} i_{Lr} \quad (3.13)$$

$$v_{\text{oc}} = j\omega M_{1,r} i_{L1}. \quad (3.14)$$

where

$$M_{1,r} = k_{1,r} \sqrt{L_1 L_r}. \quad (3.15)$$

At the fundamental harmonic frequency, the amplitude of the inverter voltage v_{in} and the rectifier voltage v_{out} are represented as

$$|v_{\text{in}}| = \frac{4V_{\text{dc}}}{\pi}, \quad (3.16)$$

$$|v_{\text{out}}| = \frac{4V_{\text{bat}}}{\pi}. \quad (3.17)$$

L_f and C_f are tuned as a bandpass filter for the inverter switching frequency f_{sw} to reduce the switching loss at the inverter in the uncoupled condition. L_f and C_f can be designed by

$$f_{\text{sw}} = \frac{1}{2\pi \sqrt{L_f C_f}}. \quad (3.18)$$

The reflected impedance Z_{ref} is represented by

$$Z_{\text{ref}} = \frac{v_{\text{ref}}}{i_{L1}} = -j\omega M_{1,r} \frac{i_{Lr}}{i_{L1}}. \quad (3.19)$$

At the receiver side, the resonant equation in the current loop i_{L_r} shown in Fig. 3.7 is represented by

$$\frac{1}{j\omega C_{r,p}} + j\omega L'_r = 0. \quad (3.20)$$

From (3.6) and (3.20), The compensation components at the receiver side $C_{r,s}$, $C_{r,p}$, $C_{r,sa}$ are represented by

$$C_{r,s} = \frac{c_2}{L_r \omega^2 (c_2 - 1)} \quad (3.21)$$

$$C_{r,p} = \frac{c_2}{L_r \omega^2} \quad (3.22)$$

$$C_{r,sa} = \frac{c_2}{L_r \omega^2 (c_3 - 1)} \quad (3.23)$$

where c_2 and c_3 are the ratios of $C_{r,p}$ and $C_{r,s}$, and $C_{r,p}$ and $C_{r,sa}$, respectively, which are already defined in (3.6).

From (3.9), (3.10), (3.14), (3.19), (3.21), (5.24), and (3.23), the reflected resistance R_{ref} and reflected reactance X_{ref} are represented by

$$R_{\text{ref}} = \frac{k_{1,r}^2 L_1 R_{L,\text{eq}} c_2^2}{L_r}, \quad (3.24)$$

$$X_{\text{ref}} = \omega k_{1,r}^2 L_1 c_2 c_3. \quad (3.25)$$

From (3.3), (3.6), and (3.7), $C_{1,s}$, $C_{1,p}$, and $C_{1,sa}$ are written as

$$C_{1,s} = \frac{1}{\omega^2 L_1 (1 - k_{\text{lim}}^2 c_1 c_2 c_3)}, \quad (3.26)$$

$$C_{1,p} = \frac{1}{\omega^2 k_{\text{lim}}^2 L_1 c_1 c_2 c_3}. \quad (3.27)$$

$$C_{1,sa} = \frac{1}{\omega^2 k_{\text{lim}}^2 L_1 c_1 (c_1 - 1) c_2 c_3}, \quad (3.28)$$

From the equations above, loop currents i_{in} , i_{L1} , i_{Lr} , and i_{out} can be written as

$$i_{\text{in}} = \frac{k_{1,r}^2 (\omega L_r c_3 + j R_{L,\text{eq}} c_2)}{\omega k_{\text{peak}}^2 L_1 c_1^2 c_2 c_3 \{k_{1,r}^2 R_{L,\text{eq}} c_2 + j\omega L_r (k_{\text{lim}}^2 - k_{1,r}^2) c_3\}} v_{\text{in}}, \quad (3.29)$$

$$i_{L1} = \frac{L_r}{L_1 c_1 c_2 \{k_{1,r}^2 R_{L,eq} c_2 + j\omega(k_{lim}^2 - k_{1,r}^2) L_r c_3\}} v_{in}, \quad (3.30)$$

$$i_{Lr} = \frac{k_{1,r}(\omega L_r c_3 + j R_{L,eq} c_2)}{\sqrt{L_1 L_r} c_1 \{k_{1,r}^2 R_{L,eq} c_2 + j\omega(k_{lim}^2 - k_{1,r}^2) L_r c_3\}} v_{in}, \quad (3.31)$$

$$i_{out} = \frac{\sqrt{L_r} k_{1,r}}{\sqrt{L_1} c_1 \{k_{1,r}^2 R_{L,eq} c_2 + j\omega(k_{lim}^2 - k_{1,r}^2) L_r c_3\}} v_{in}. \quad (3.32)$$

The loop current in the fully coupled condition ($k_{1,r} = k_{lim}$) can be written as

$$i_{in}|_{k_{1,r}=k_{lim}} = \frac{\omega L_r c_3 + j R_{L,eq} c_2}{\omega L_1 k_{lim}^2 c_1^2 c_2^2 c_3 R_{L,eq}} v_{in} \quad (3.33)$$

$$i_{L1}|_{k_{1,r}=k_{lim}} = \frac{L_r}{k_{lim}^2 L_1 R_{L,eq} c_1 c_2^2} v_{in} \quad (3.34)$$

$$i_{Lr}|_{k_{1,r}=k_{lim}} = \frac{\omega L_r c_3 + j R_{L,eq} c_2}{\omega k_{lim} \sqrt{L_1 L_r} R_{L,eq} c_1 c_2} v_{in}. \quad (3.35)$$

$$i_{out}|_{k_{1,r}=k_{lim}} = \frac{\sqrt{L_r}}{k_{lim} \sqrt{L_1} R_{L,eq} c_1 c_2} v_{in}. \quad (3.36)$$

The equivalent load resistance $R_{L,eq}$ can be represented as

$$R_{L,eq} = \frac{v_{out}}{i_{out}}. \quad (3.37)$$

From (3.32) and (3.37), the equivalent load resistance $R_{L,eq}$ can be rewritten as

$$R_{L,eq} = \frac{\omega \sqrt{L_1} L_r (k_{lim}^2 - k_{1,r}^2) c_1 c_3}{k_{1,r} \sqrt{L_r} \left(\frac{V_{dc}}{V_{bat}} \right)^2 - k_{1,r}^2 L_1 c_1^2 c_2^2}. \quad (3.38)$$

Finally, from (3.32) and (3.38), output power P_{out} can be calculated by

$$\begin{aligned} P_{out} &= i_{out} \cdot i_{out}^* \cdot \frac{R_{L,eq}}{2} \\ &= \frac{8 k_{1,r}^2 L_r R_{L,eq} V_{dc}^2}{\pi^2 L_1 c_1^2 \{k_{1,r}^4 R_{L,eq}^2 c_2^2 + \omega^2 (k_{lim}^2 - k_{1,r}^2)^2 L_r^2 c_3^2\}}. \end{aligned} \quad (3.39)$$

where i_{out}^* is the complex conjugate of i_{out} . The output power in the fully coupled condition can be written as

$$P_{\text{out}}|_{k_{1,r}=k_{\text{lim}}} = \frac{8L_r V_{\text{dc}}^2}{\pi^2 k_{\text{lim}}^2 L_1 R_{L,\text{eq}} c_1^2 c_2^2}. \quad (3.40)$$

The system efficiency can be estimated and designed by the equations of the loop currents. Additionally, the derived equations can be used for the conventional circuit by applying $c_1 = c_3 = 1$.

3.3.4 Soft switching analysis

This section investigates the zero-voltage-switching (ZVS) region when the inverter's transistors turn on. If the imaginary part of inverter current i_{in} is negative, the inverter's transistors achieve ZVS. Hence, the ZVS requirements can be written as

$$\text{Im}(i_{\text{in}}) < 0, \quad (3.41)$$

By combining (3.29), (3.38), and (3.41), the ZVS boundary is represented as

$$\frac{V_{\text{bat}}}{V_{\text{dc}}} < \frac{1}{k_{\text{lim}} c_1 c_2} \sqrt{\frac{L_r}{L_1}}. \quad (3.42)$$

The ZVS boundary equation is depicted on the surface of the voltage ratio $V_{\text{bat}}/V_{\text{dc}}$ and the multiplication of design parameters $k_{\text{lim}} c_1 c_2$ when the ratio of self-inductance L_r/L_1 is changed in three patterns, as shown in Fig. 3.8. The solid red line shows the ZVS boundary when $L_r/L_1 = 1$, and the area below the boundary is the ZVS region. As the ratio of self-inductance L_r/L_1 increases, the ZVS region is enlarged. The ZVS operation can be kept when the receiver coil moves since the ZVS condition is independent of the coupling coefficient $k_{1,r}$, as shown in (3.42).

3.3.5 Stability of the system

L'_r/L_r where $L'_r = L_r - \frac{1}{\omega^2 C_{r,\text{sb}}}$ is a value related to the resonance stability of the receiver circuit. If L'_r/L_r is small, a small percentage change in L_r will cause the receiver circuit to

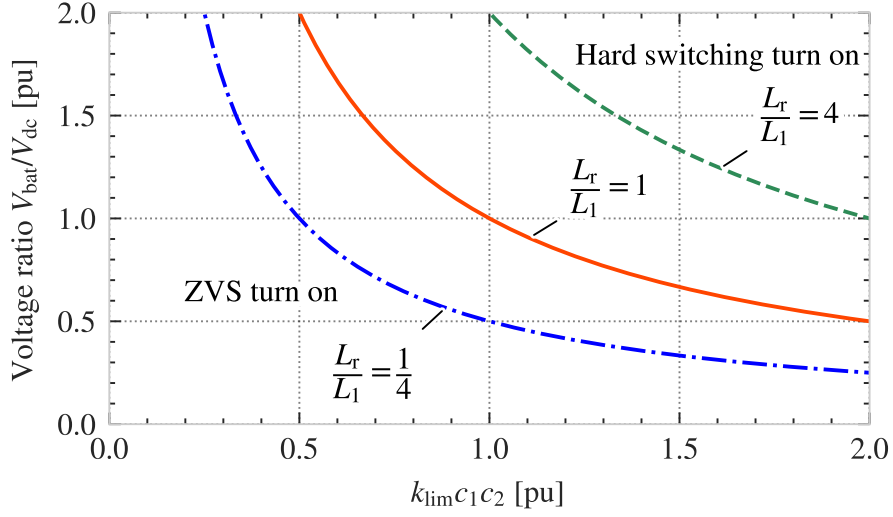


Fig. 3.8: ZVS region

lose resonance. L_r varies depending on the distance to the transmitter coils and surrounding metal objects. Since the conventional circuit has only c_2 as a design variable, it is necessary to increase c_2 to achieve a small uncoupled transmitter current. In the proposed circuit, c_1 and c_3 can be used to design the transmitter coil current small so that c_2 can be reduced, and the resonance stability of the receiver side circuit can be improved.

3.3.6 Comparison of the Pareto fronts

To compare the conventional and the proposed circuit designs, design points are plotted on the surface of coil efficiency versus output power P_{out} as shown in Fig. 3.9. P_{out} is calculated by (3.39). Efficiency is calculated by (3.29), (3.30), (3.31), and (3.32). As the fixed design requirements, the following values are used for both designs: $L_1 = L_2 = 18.42 \mu\text{H}$, $L_r = 43.85 \mu\text{H}$, $k_{1,r} = 0 \sim 0.120$, $k_{\text{peak}} = 0.124 \sim 0.130$, $Q_L = 400$, $Q_C = 800$. The low voltage (50 V) was used for input and output voltage to facilitate the experiment. In the proposed reflexive tuning circuit design plots, c_1 , c_2 , and c_3 are randomly selected from $0 < c_1 < 1$, $1 < c_2 < 10$, and $1 < c_3 < 10$. In the conventional reflexive tuning circuit design plots, c_1 , c_2 , and c_3 are randomly selected from $c_1 = 1$, $1 < c_2 < 10$, and $c_3 = 1$. The two lines show the Pareto fronts of the proposed and conventional circuits. Because

Table 3.1: Comparison between the proposed and conventional circuit typologies

	Conventional	Proposed
Uncoupled		$c_1 = \frac{C_{1,p}}{C_{1,sa}} + 1$
Coupled	$c_2 = \frac{C_{r,p}}{C_{r,s}} + 1$	$c_2 = \frac{C_{r,p}}{C_{r,s}} + 1$ $c_3 = \frac{C_{r,p}}{C_{r,sa}} + 1$
Uncoupled transmitter current	$i_{L1} = \frac{v_{in}}{\omega k_{peak}^2 L_1 c_2} \propto \frac{1}{c_2} \quad \text{Low } \checkmark$	$i_{L1} = \frac{v_{in}}{\omega k_{peak}^2 L_1 c_1 c_2 c_3} \propto \frac{1}{c_1 c_2 c_3} \quad \text{Low } \checkmark$
Output power	$P_{out} = \frac{L_r v_{in}^2}{2 k_{peak}^2 L_1 R_{L,eq} c_2^2} \propto \frac{1}{c_2^2} \quad \text{Low } \times$	$P_{out} = \frac{L_r v_{in}^2}{2 k_{peak}^2 L_1 R_{L,eq} c_1^2 c_2^2} \propto \frac{1}{c_1^2 c_2^2} \quad \text{High } \checkmark$
Resonant stability	$\frac{L'_r}{L_r} = 1 - \frac{1}{\omega^2 L_r C_{r,s}} \propto \frac{1}{c_2} \quad \text{Low } \times$	$\frac{L'_r}{L_r} = 1 - \frac{1}{\omega^2 L_r C_{r,s}} \propto \frac{1}{c_2} \quad \text{High } \checkmark$

the conventional circuit needs to design its function by only c_2 , the maximum output power is much lower than the proposed circuit. The graph shows that the proposed circuit has an advantage in the high output power area over approximately 1.6 kW in this design requirement case.

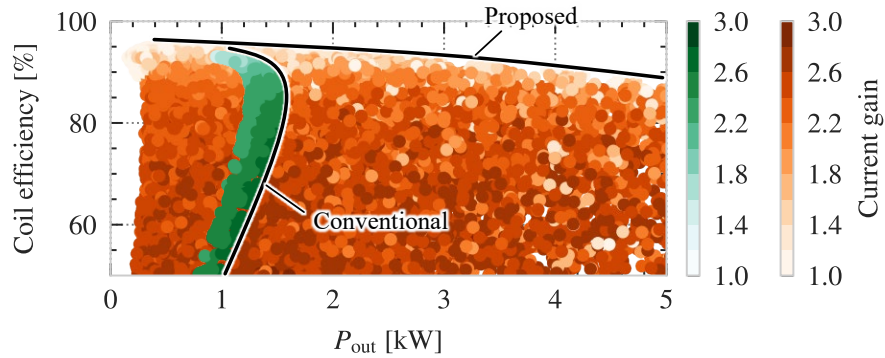


Fig. 3.9: Pareto fronts of the proposed and the conventional circuit on the surface of Efficiency versus output power P_{out}

3.3.7 Takeaways of the proposed circuit

The takeaways of the principle of the proposed circuit are shown in TABLE 3.1. In un-

coupled conditions, the transmitter current can be decreased compared to the conventional reflexive tuning circuit since the additional impedance is inserted between the input voltage and the transmitter coil. In the coupled conditions, the conventional reflexive tuning circuit needs to create the reflected reactance only using the receiver side capacitor $C_{r,p}$. Compared to the conventional circuit, the proposed circuit can create the reflected reactance using the receiver capacitors $C_{r,p}$ and $C_{r,sa}$. The relationship between the uncoupled transmitter current, output power, and the resonant stability for the conventional and proposed reflexive tuning circuit can be represented in theoretical equations, as shown on the lower side of TABLE 3.1. It is not easy for the conventional circuit to achieve high output power, low uncoupled transmitter current, and high resonant stability simultaneously since it needs to design the three characteristics using only c_1 . The proposed circuit can achieve high output power, low uncoupled transmitter current, and high resonant stability simultaneously since it has three independent design variables c_1 , c_2 , and c_3 .

3.4 Design and Sensitivity Analysis of the proposed circuit

To show the advantage of the proposed converter over the conventional reflexive tuning circuit, both designs are simulated under the same operating conditions. Through the sensitivity analysis, it is shown that the additional components in the proposed converter work well to address the effect of parasitic resistance and inductance.

3.4.1 Circuit design

The design requirements are shown in TABLE 3.2. The input voltage V_{dc} and output voltage V_{bat} are set at 50 V. A frequency of 85 kHz is selected as the transmission frequency f_{sw} for the prototype designed to follow the SAE standard [48]. The coupling factor between the transmitter coil and the receiver coil $k_{1,r}$ varies from 0 to 0.12, according to the position of the receiver coil due to longitudinal misalignment. The range of coupling factor $k_{1,r}$ was extracted from Maxwell-simulations. The quality factors of coils and capacitors Q_L and Q_C

Table 3.2: Design specifications for the proposed circuit

Parameter	Symbol	Value
Input voltage	V_{dc}	50 V
Output voltage	V_{bat}	50 V
Air gap	z_{gap}	250 mm
Switching frequency	f_{sw}	85 kHz
Coupling factor between L_1 and L_r	$k_{1,r}$	0.00 ~ 0.12
Coupling factor between L_1 and L_2	$k_{1,2}$	-0.04
Transmitter coil inductance	L_1 & L_2	18.42 μ H
Receiver coil inductance	L_r	43.85 μ H
Filter inductor	L_f	5.05 μ H
Filter capacitor	C_f	0.71 μ F
Output dc inductor	L_{dc}	10.33 μ H
Parasitic inductance of wires	$L_{para,wire}$	0.10 μ H
Parasitic inductance of capacitors	$L_{para,C}$	0.10 μ H
Quality factor of wireless coils and inductors	Q_L	400
Quality factor of capacitors	Q_C	800
Number of turns of the transmitter coils	$N_{L1}&N_{L2}$	3
Number of turns of the receiver coil	N_{Lr}	5

are defined as

$$Q_L = \frac{\omega L}{r_L} \quad \text{and} \quad Q_C = \frac{1}{\omega C r_C} \quad (3.43)$$

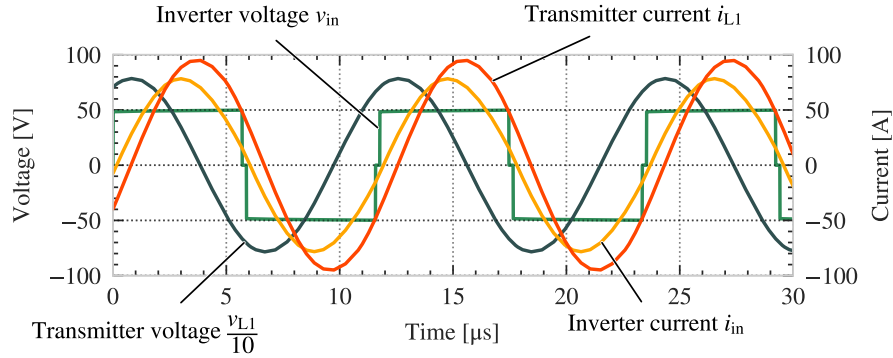
where r_L and r_C are the equivalent series resistance of L and C , respectively. The parasitic inductance of wires at the same line of $L_{n,sa}$ and L_f is defined as $L_{para,wire}$, and the parasitic inductance of each capacitor bank is defined as $L_{para,C}$.

The designed parameters of the proposed and the conventional circuit are shown in TABLE 3.3. Circuits were designed so that the amplitude of the uncoupled transmitter current $I_{L1,uncoupled}$ is 37 A in both cases. c_2 is fixed to 8.93 to compare the two circuits in the same design condition. c_1 and c_3 are set to 1 in the conventional circuit since the conventional circuit does not have $C_{1,sa}$ and $C_{r,sa}$.

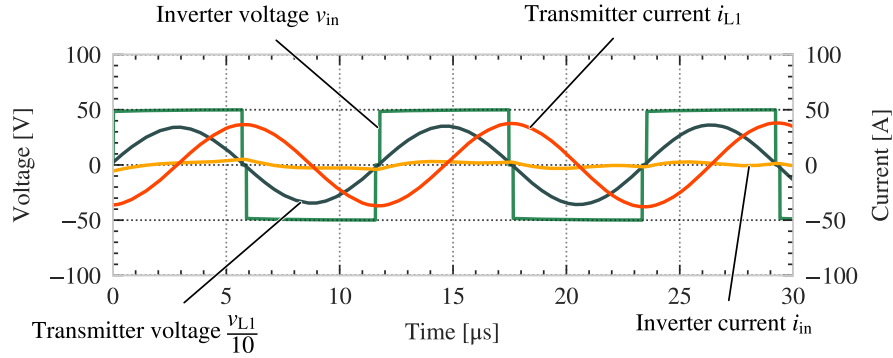
The LTspice simulation results of the proposed circuit are shown in Fig. 3.10. Figure 3.10(a) shows the wave forms in coupled condition ($k_{1,r} = k_{peak}$). The transmitter current becomes maximum, and the amplitude is 96 A. As the inverter current i_{in} is lagging the inverter voltage v_{in} , the inverter current i_{in} maintains the soft-switching condition. Output power at the coupled condition is 2,022 W. Figure 3.10(b) shows the wave forms in the

Table 3.3: Design conditions for the proposed and conventional circuit

Parameter	Proposed	Conventional
c_1	1.31	1.00
c_2	8.93	8.93
c_3	1.46	1.00
Series capacitor $C_{1,sa}$	$3.34 \mu\text{F}$	-
Series capacitor $C_{1,sb}$	239 nF	236 nF
Parallel capacitor $C_{1,p}$	$1.02 \mu\text{F}$	$0.99 \mu\text{F}$
Series capacitor $C_{r,sa}$	$1.54 \mu\text{F}$	-
Series capacitor $C_{r,sb}$	90 nF	90 nF
Parallel capacitor $C_{r,p}$	711 nF	711 nF



(a) Coupled condition

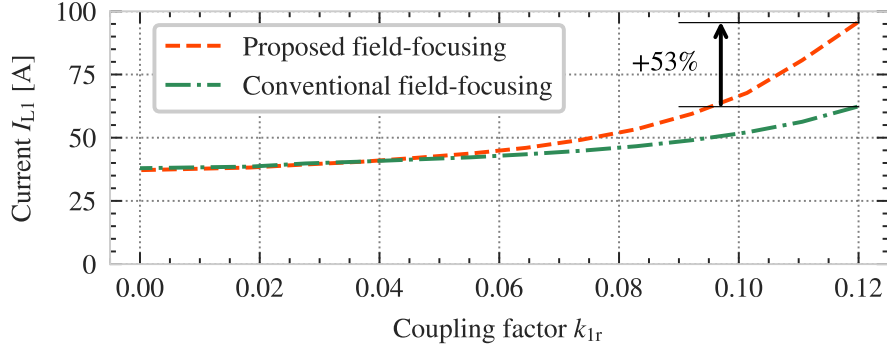


(b) Uncoupled condition

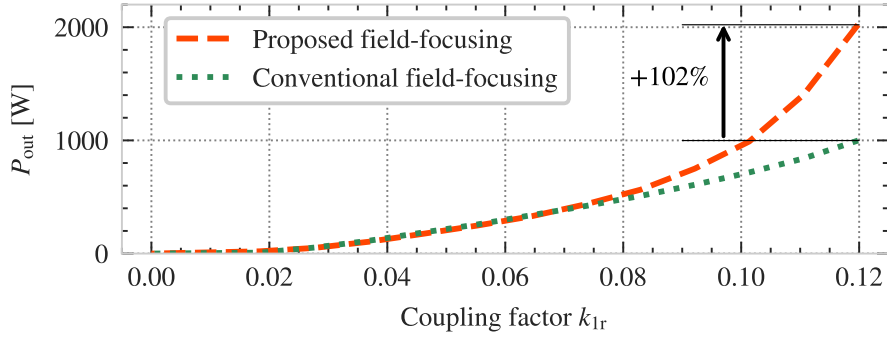
Fig. 3.10: LTspice-simulated waveforms

uncoupled condition ($k_{1,r} = 0$). The amplitude of the transmitter current i_{L1} is minimum and its value is 37 A. The inverter current i_{in} is close to zero since the impedance of the compensation circuit from the inverter side can be assumed as infinite in the uncoupled condition.

The sweep results of current amplitude I_{L1} and output power P_{out} with respect to coupling factor $k_{1,r}$ from 0 to 0.12 are shown in Fig. 3.11. The dashed line is the proposed



(a) Current amplitude I_{L1} with respect to coupling factor



(b) Output power P_{out} with respect to coupling factor

Fig. 3.11: LTspice-simulated current amplitude and output power

circuit and the dash-dotted line is the conventional circuit. The current amplitude of the transmitter coil with respect to coupling factor is shown in Fig. 3.11 (a). In the uncoupled condition ($k_{1,r} = 0$), the current amplitudes of both circuits are the same ($I_{L1,uncoupled} = 37$ A). In the coupled condition ($k_{1,r} = k_{peak} = 0.12$), the current amplitude of the proposed one is 53% higher than the conventional one. The sweep results of output power P_{out} with respect to coupling factor $k_{1,r}$ from 0 to 0.12 are shown in Fig. 3.11 (b). In the coupled condition ($k_{1,r} = k_{peak}$), the output power of the proposed solution is 102% higher than the conventional case.

3.4.2 Sensitivity analysis

In the actual experimental setup, parasitic resistance and inductance decrease the output power and current gain. Due to the unpredictable parasitic values, it is required to manipulate the output power and current gain after the hardware prototype design. This section shows that the proposed reflexive tuning circuit can increase the output power and current gain using the additional components.

The sensitivity analysis results are shown in Fig. 3.12. The analysis was conducted using

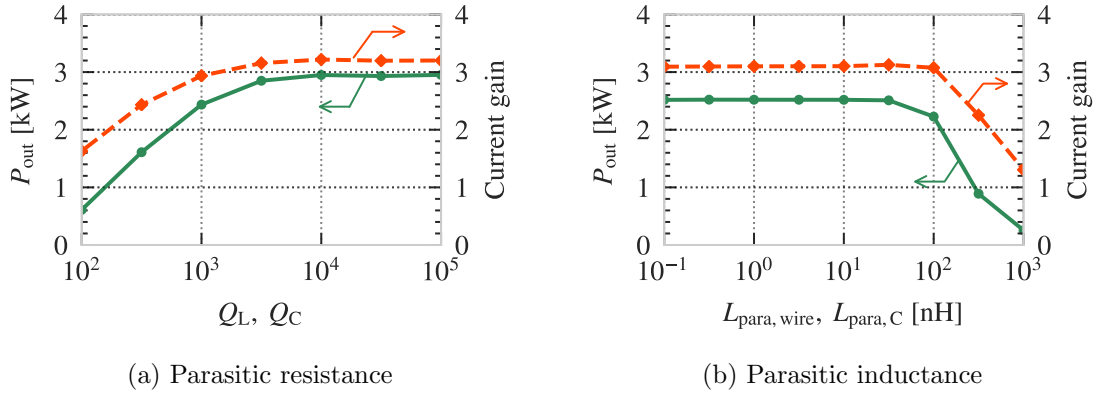


Fig. 3.12: LTspice-simulated sensitivity analysis results with respect to parasitic components

LTspice. The sensitivity of the output power and current gain with respect to the quality factors Q_L and Q_C are shown in Fig. 3.12 (a). To simplify the analysis, the same quality factors are used in each simulation points for Q_L and Q_C . In the same way, the sensitivity with respect to the parasitic inductance $L_{para,wire}$ and $L_{para,C}$ are shown in Fig. 3.12 (b). The results show that in the range of $Q_L, Q_C < 1,000$, or $L_{para,wire}, L_{para,C} > 100$ nH, both the output power and current gain are decreased significantly. Since both the range of the parasitic values are the common cases in practical systems, it is unavoidable for the circuit to be affected by the parasitic values.

To identify the compensation component to address the issue of parasitic components, sensitivity analysis with respect to all compensation components is conducted by sweeping the variation of each component from 80% to 120%, as shown in Fig. 3.13. The analysis

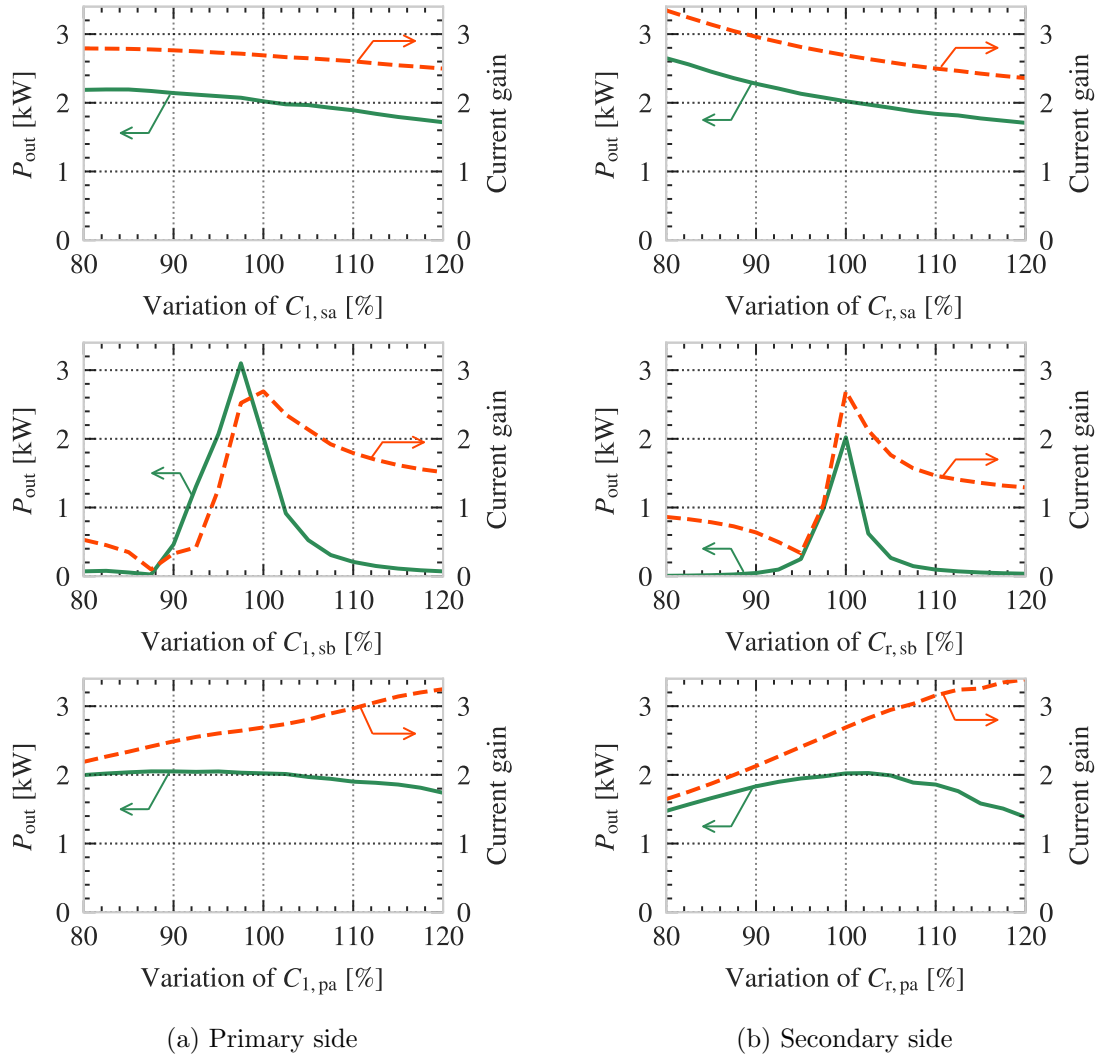


Fig. 3.13: LTspice-simulated sensitivity analysis results with respect to compensation components

results of the primary side and secondary side are shown in Fig. 3.13 (a) and (b), respectively. Only the components $C_{1,sa}$ and $C_{r,sa}$ can increase both the output power and current gain by decreasing the variation of the component values. The rest of the components $C_{1,sb}$, $C_{r,sb}$, $C_{1,pa}$, and $C_{r,pa}$ cannot increase the output power and current gain simultaneously. Therefore, the conventional circuit cannot address the issue of the parasitic components after its design by adjusting the compensation components since the conventional circuit does not have $C_{1,sa}$ and $C_{r,sa}$. Additionally, the component for the band pass filter C_f cannot be used to increase the output power and current gain instead of $C_{1,sa}$ since the input voltage

v_{in} for all the primary coil branches is changed when a primary coil is coupled and the current amplitude of all the other transmitter coils are increased and the reflexive tuning cannot be achieved. Eventually, it is difficult to manipulate the output power and current gain after the hardware prototype design using the conventional reflexive tuning circuit. On the other hand, the proposed circuit can increase the output power easily because of the additional compensation components $C_{1,sa}$ and $C_{r,sa}$ due to its ability to manipulate the circuit behaviour to higher output power and current gain.

3.5 Stray field simulation

As shown in the previous subsection, the output power of the conventional reflexive tuning circuit is lower than the proposed circuit. To compare and discuss the stray field of the proposed circuit at the same output power level, the constant current circuit topology is introduced in this subsection since the constant current circuit topology is one of the most common circuit topologies for DWPT application [13]. ANSYS Maxwell is used for magnetic field simulation. The SAE standard [48] for light-duty vehicles is considered to measure stray magnetic fields with the assumption that the width of the vehicle is 1.6 m [80]. The maximum values of the magnetic stray field at a distance of 800 mm in the lateral direction from the center of the secondary coil in the middle of 250 mm air gap between the primary and secondary coil is acquired as the stray field in this paper.

The Maxwell-simulation environment is shown in Fig. 3.14. The observation point of the stray field and the front of the vehicle are also shown in the figure.

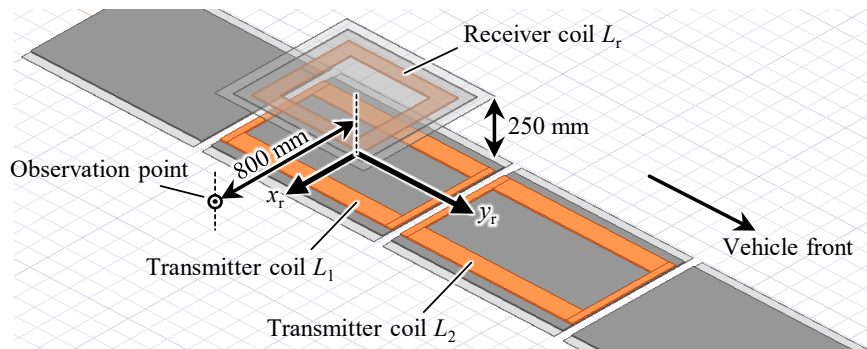


Fig. 3.14: Maxwell simulation setup

Table 3.4: Maxwell simulation conditions

(a) Aligned condition			(b) 100 mm-misalignment condition		
Variable	Proposed circuit	Constant current circuit	Variable	Proposed circuit	Constant current circuit
Transmitter current I_{L1}	96 A	96 A	Transmitter current I_{L1}	76 A	96 A
Transmitter current I_{L2}	37 A	96 A	Transmitter current I_{L2}	37 A	96 A
Receiver current I_r	87 A	23 A	Receiver current I_r	60 A	14 A
Coupling coefficient $k_{1,r}$	0.12	0.12	Coupling coefficient $k_{1,r}$	0.10	0.10
Phase of I_r from I_{L1}	159°	90°	Phase of I_r from I_{L1}	155°	90°
Stray magnetic field	3.8 μ T	10.7 μ T	Stray magnetic field	10.3 μ T	17.0 μ T
Output power	2.0 kW	2.0 kW	Output power	1.0 kW	1.0 kW
(c) Uncoupled condition					
Variable	Proposed circuit	Constant current circuit			
Transmitter current I_{L1}	37 A	96 A			
Transmitter current I_{L2}	37 A	96 A			
Receiver current I_r	0	0			
Coupling coefficient $k_{1,r}$	0	0			
Phase of I_r from I_{L1}	-	-			
Stray magnetic field	4.7 μ T	12.2 μ T			
Output power	0 kW	0 kW			

An aligned condition, a 100 mm-misalignment condition, and an uncoupled condition are simulated. In the coupled condition, the receiver coil L_r is set above the center of the transmitter coil L_1 . In the 100 mm misalignment condition, the receiver coil has a lateral misalignment of 100 mm to the direction of the side of the vehicle. In the uncoupled

condition, there is no receiver coil. To compare the stray magnetic fields with the constant current approach, the double-sided LCC circuit [81–83] has been simulated as well.

The simulation conditions and corresponding results are shown in TABLE 3.4 and Fig. 3.15, respectively. The simulation condition and the magnetic field in the aligned condition are shown in TABLE 3.4(a), Fig. 3.15(a), and Fig. 3.15(b). The observation point for the stray field is shown by circular mark in the figure. The phase angles of I_{L1} and I_{L2} are assumed to be the same. The stray field of the proposed reflexive tuning circuit ($3.8 \mu\text{T}$) is 64% less than that of the constant-current circuit ($10.7 \mu\text{T}$) since the field emission from L_2 is smaller and the phase of the receiver current I_r with respect to I_{L1} in the proposed circuit is close to 180° and the canceling effect of the currents are higher than the constant current circuit. The simulation condition and the magnetic field in the 100 mm-misalignment condition are shown in TABLE 3.4(b), Fig. 3.15(c), and Fig. 3.15(d). Similar to the aligned condition, the stray field of the proposed reflexive tuning circuit ($10.3 \mu\text{T}$) is 39% less than that of the constant current circuit ($17.0 \mu\text{T}$). The simulation condition and the magnetic field in the uncoupled condition are shown in TABLE 3.4(c), Fig. 3.15(e), and Fig. 3.15(f). The stray field of the proposed reflexive tuning circuit ($4.7 \mu\text{T}$) is 61% less than that of the constant current circuit ($12.2 \mu\text{T}$) since the proposed circuit can reduce the uncoupled transmitter current by 2.5 times compared to the constant current circuit.

3.6 Experimental verification

An experiment was conducted to validate the design of the proposed circuit. A prototype of the proposed circuit was constructed with the coil parameters and the compensation parameters in TABLE 3.2 and TABLE 3.3. The dimensions of the primary and the secondary coils are shown in Fig. 5.14. Figure 5.14(a) shows the dimension of the transmitter coils. The aluminum backplate used for shielding is placed in the bottom layer, the ferrite plate is placed in the middle layer, and the transmitter coil embedded in a coil former is placed on the top layer. The horizontal spacing between the transmitter coils is kept small (45 mm) to mitigate the decrease in the output power in the region between the coils due to lower coupling. Figure 5.14(b) shows the dimension of the receiver coil. The whole structure

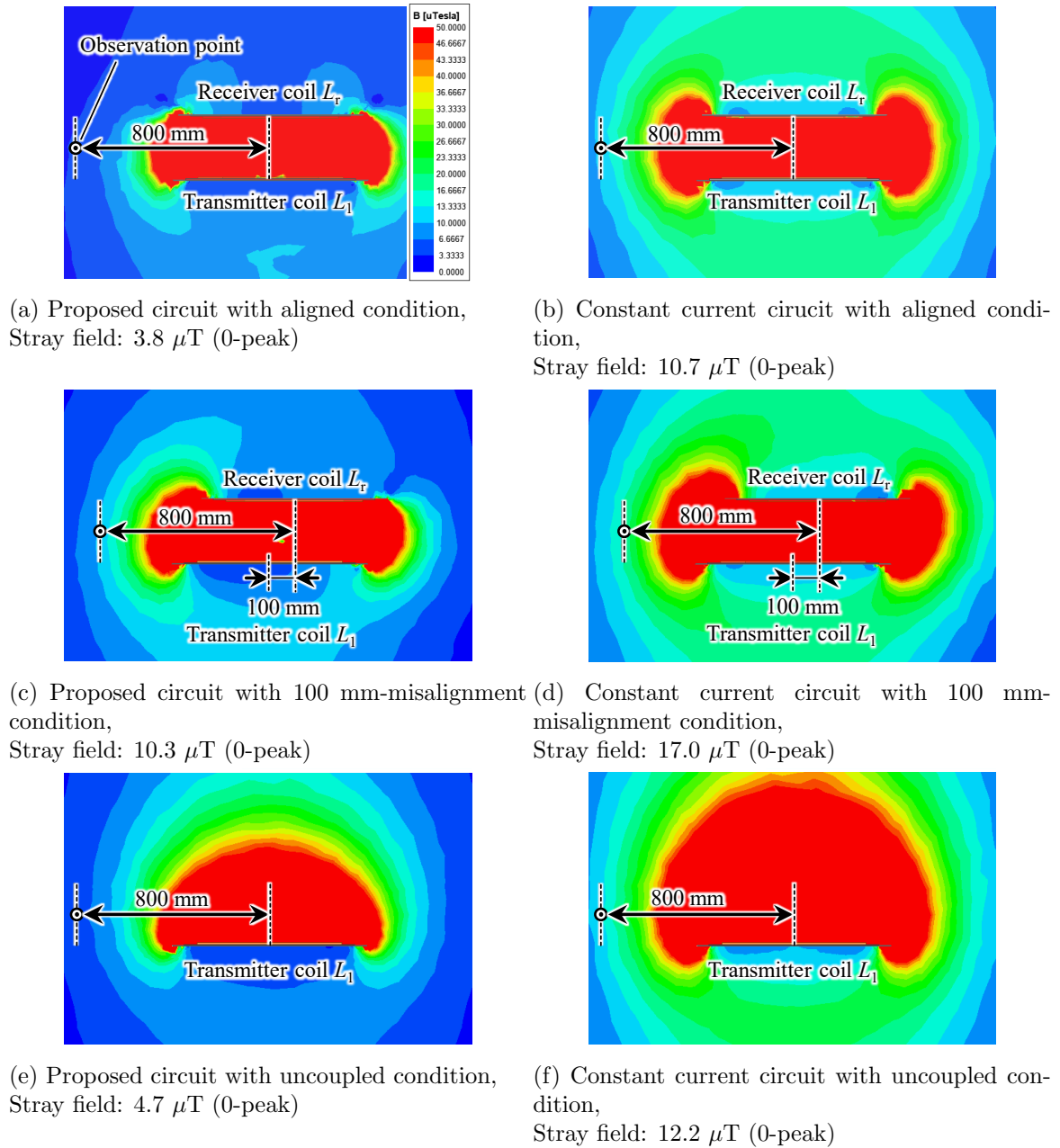


Fig. 3.15: Maxwell-simulated magnetic field emission. Proposed reflexive tuning circuit versus constant current circuit

is similar to the transmitter coil. The ferrite plate dimensions are larger than the winding to increase the coupling, and the aluminum plate dimensions are larger than the ferrite plate to decrease the stray field. Figure 5.14(c) shows the dimension of the thickness of the prototype system. The thickness of the ferrite plates is 5 mm and that of the aluminum

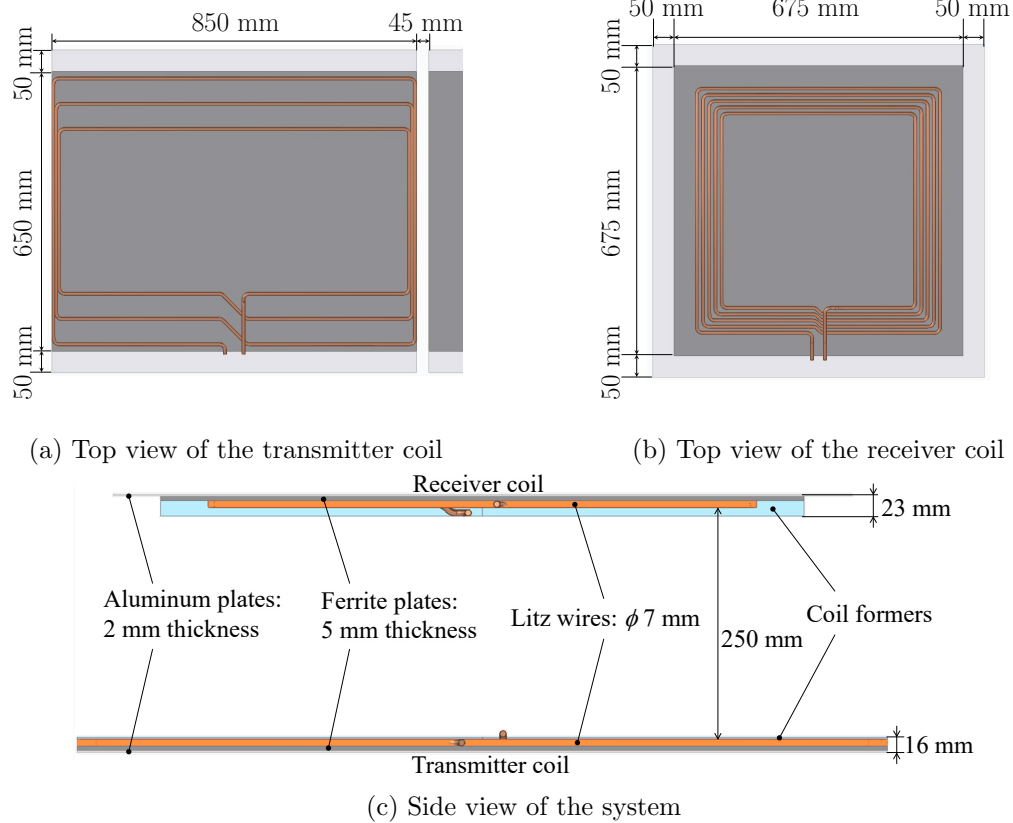


Fig. 3.16: Dimension of the prototype system

plates is 2 mm. Coil formers are made of high-density polyethylene (HDPE) sheets and the Litz wires are embedded into them.

The pictures of the experimental prototype of the proposed reflexive tuning dynamic power transfer system are shown in Fig. 3.17. The overview of the experimental setup is shown in Fig. 3.17(a). The prototype consists of two transmitter coils connected to compensation circuits, an inverter, a receiver coil, and a diode rectifier. To create a similar environment that replicates the intended application, adjacent coils are placed next to the transmitter coil L_1 and L_2 , respectively. This simulates the application of a DWPT system on the road. Magnetic stray field are measured at the observation point shown in Fig. 3.17(a) using a field analyzer (EHP-200A/AC). Figure 3.17(b) shows the side view of the experimental system. The output power and transmitter current are measured as the receiver coil is moved from the center of the transmitter coil L_1 to the center of the

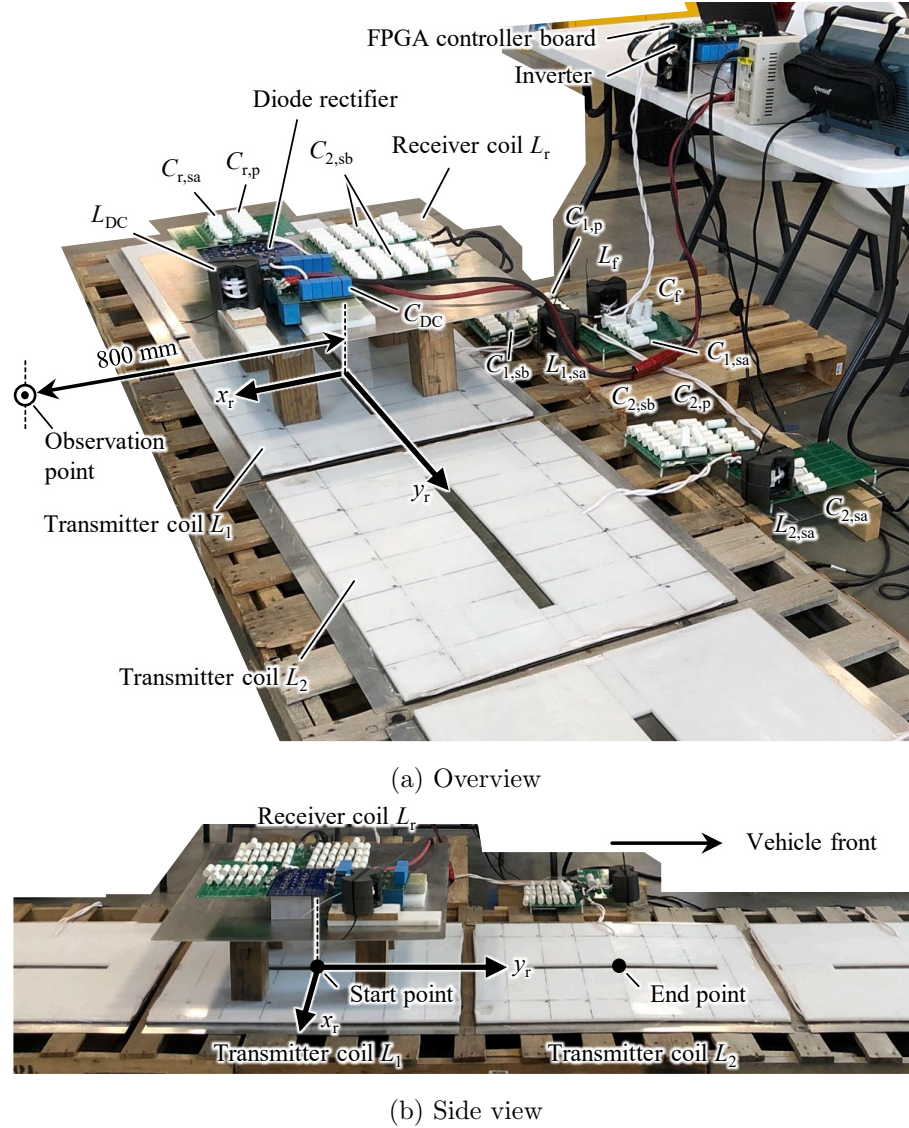


Fig. 3.17: Experimental prototype of the proposed reflexive tuning dynamic power transfer system

transmitter coil L_2 in the longitudinal direction.

The diagram of the test setup with power feedback at the dc link is shown in Fig. 3.18. The series compensation inductor $L_{1,sa}$ is added in series at $C_{1,sa}$ to cancel the effect of the parasitic inductance along the transmitter lines. In a practical system, these individual transmitter coils may be several meters away and each line to connect each transmitter coil and inverter has different lengths of wires. Then the inductance of the lines connecting

to the resonators can significantly detune and unbalance the system. The added series inductors are utilized to adjust and compensate the unbalance of inductance.

The power feedback via a dc wire allows circulating the transferred power within the system, instead of dissipating the power in a resistive load. While the transferred power is circulated, total losses are drawn from the external dc supply. Therefore, the dc current I_{loss} and the dc supply voltage V_{dc} can be measured to calculate the total power losses. The transferred power is calculated using the measured feedback current I_{fb} . All wireless coils and inductors were made from 2325-strand AWG 38 Litz-wire. Because of the small core loss and the large saturation flux density, MnZn ferrite core (PC95, TDK) was used for the magnetic material of the wireless coils and inductors. A general-purpose full-bridge inverter is used on the primary side to provide the ac excitation. It contains two silicon carbide (SiC) half-bridge MOSFET module (CAS325M12HM2) with a rating voltage of 1.2 kV. The same SiC MOSFET modules are used as the diode rectifier as well.

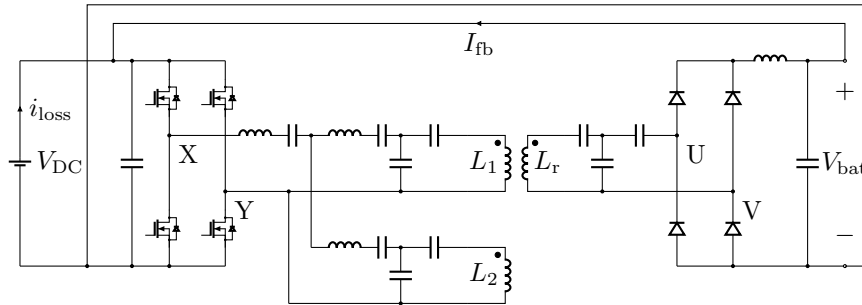


Fig. 3.18: Experimental setup diagram

The voltage of the inverter v_{in} and the current of the transmitter coil i_{L_1} are shown in Fig. 3.19. Figure 3.19(a) shows the waveforms when the receiver coil is at the center of the transmitter coil L_1 . The measured amplitude of the current is 92 A and the output power is 1,952 W. Figure 3.19(b) shows the waveforms in uncoupled conditions. The output power is 0 W, and the amplitude of the current is 37 A. Therefore, the amplitude of the transmitter current in the coupled case is 2.5 times that of the uncoupled case.

To verify the reflexive tuning capability of the system, the transmitter current and

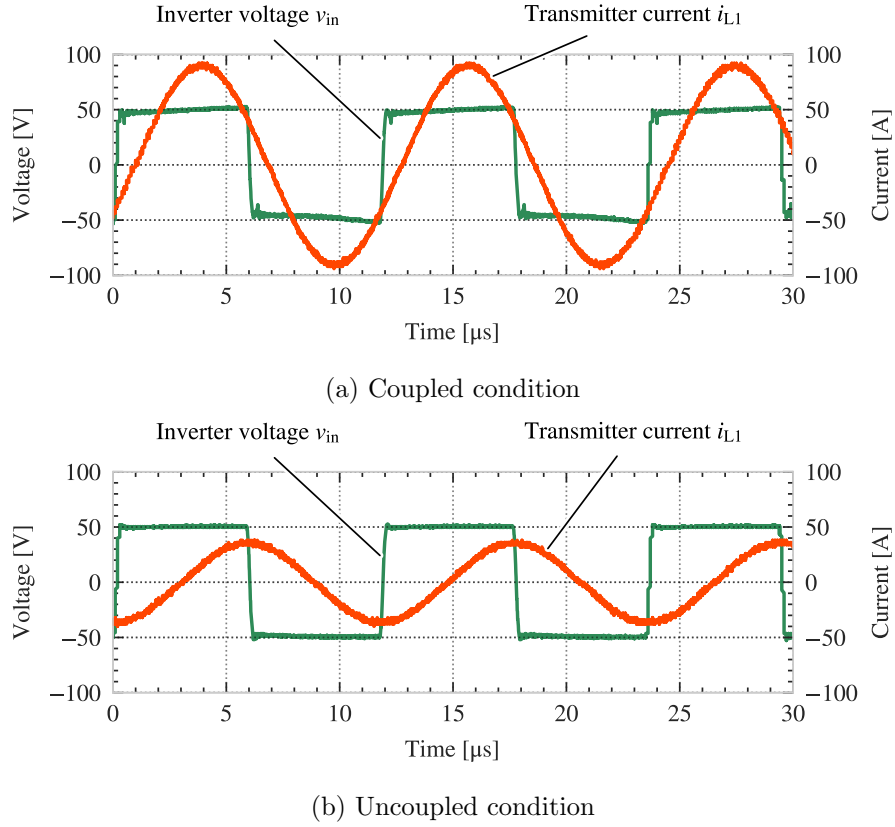


Fig. 3.19: Experimental waveforms of the proposed prototype

output power are measured as the receiver coil moves along the track. Fig. 3.20 shows the measured output power and dc-dc efficiency of the proposed circuit as the receiver coil moves with respect to the transmitter coils. Fig. 3.20 (a) shows the measured output power versus receiver position y_r . At $y_r = 0$ mm, the measured output power matches well with the simulation value, which is calculated by the LTspice simulation described in Section 3.4. However, the measured output power at $y_r = 895$ mm is 14% less than the measured value at $y_r = 0$ mm because of an unbalance in the length of wires and compensation circuit between the inverter and transmitter coils. Fig. 3.20(b) shows the measured dc-dc efficiency of the proposed circuit versus receiver position y_r . The measured efficiencies is 74.9% at $y_r = 0$ mm when output power is 1,952 W and matches well with the simulation values along with all ranges of the receiver position.

The measured amplitude of the transmitter current at different receiver positions is

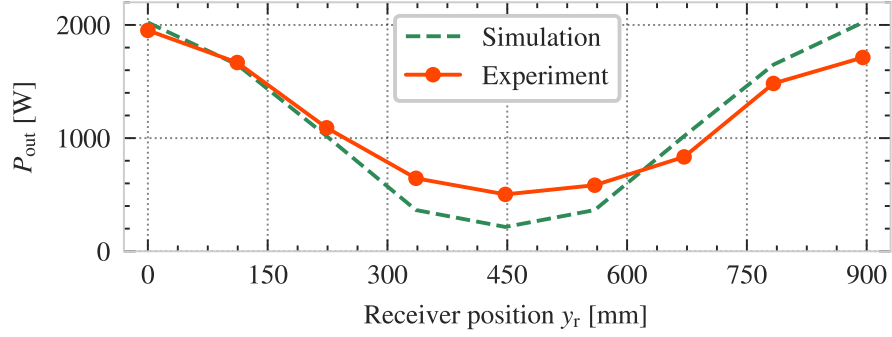
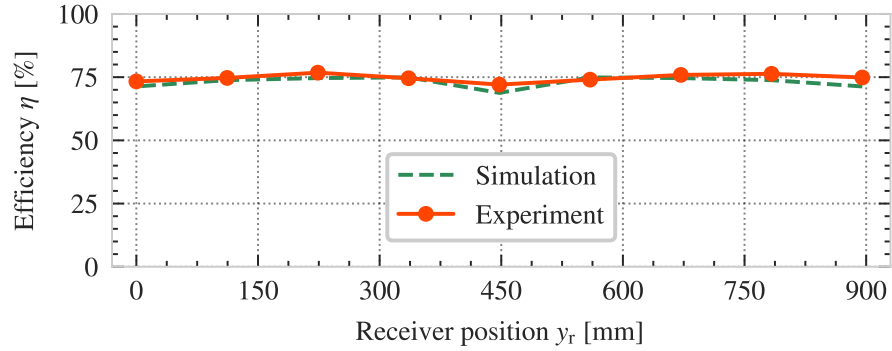
(a) System output power P_{out} (b) System efficiency η

Fig. 3.20: Measured output power and efficiency as the receiver coil moves from the center of L_1 to the center of L_2 .

shown in Fig. 3.21(a) and (b). As seen from Fig. 3.20 and Fig. 3.21, the experimental results match with the simulation results.

To verify the tolerance of the proposed circuit to misalignment in the lateral direction, transmitter current and output power have been measured with 100 mm misalignment in the lateral direction ($x_r = -100$ mm). Fig. 3.22 shows the measured transmitter coil current with 100 mm misalignment. Fig. 3.22(a) shows the current amplitude of the transmitter coil L_1 with respect to the receiver position at 100 mm misalignment. At $y_r = 0$ mm, the amplitude is 72 A. The current gain of transmitter coil L_1 is reduced by 22%. Fig. 3.22(b) shows the current amplitude of transmitter coil L_2 with respect to receiver position at 100 mm misalignment. In the same way, at $y_r = 0$ mm, the amplitude is 64 A. The current gain of transmitter coil L_1 is reduced by 28%.

The output power versus the receiver position at 100 mm misalignment are shown in

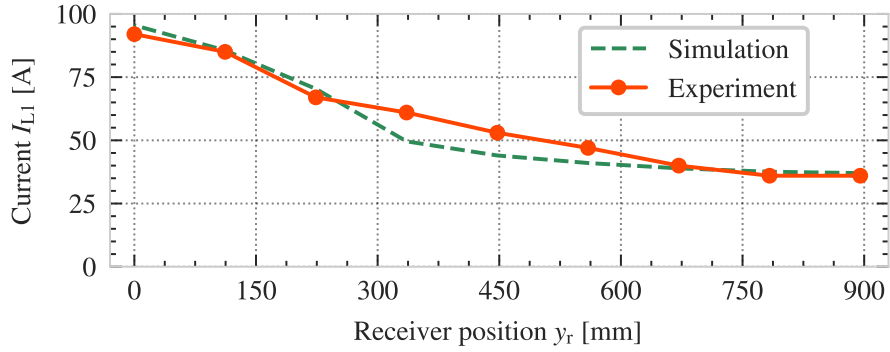
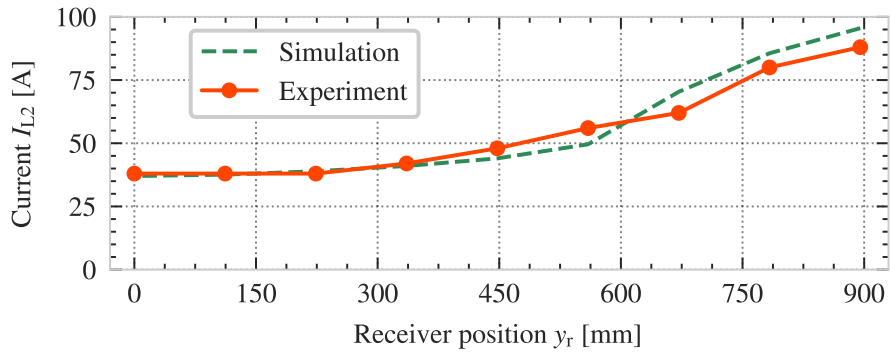
(a) Amplitude of the current I_{L1} (b) Amplitude of the current $I_{L_{vbn02}}$

Fig. 3.21: Measured amplitude of current as the receiver coil moves from the center of L_1 to the center of L_2 .

Fig. 3.23. At $y_r = 0$ mm, the output power is 1082 W. Compared to the aligned-case, the output power is decreased by 45%. To improve the tolerance to misalignment, larger ferrite plates are required for the transmitter and the receiver coils .

The measured magnetic field of the proposed circuit and the constant current circuit topology are shown in Fig. 3.24. In the measurement, the double-sided LCC compensation circuit in an uncoupled condition was used. The amplitude of the transmitter current is 92 A with the constant current circuit topology since the transmitter current is constant in both the coupled and uncoupled conditions. The measured maximum stray field of the constant current circuit is $13.3 \mu\text{T}$ (0-peak) at 85 kHz. On the other hand, the amplitude of the transmitter current created by the proposed circuit is 37 A in the uncoupled condition since the proposed circuit creates maximum current (= 92 A) in only the coupled condition.

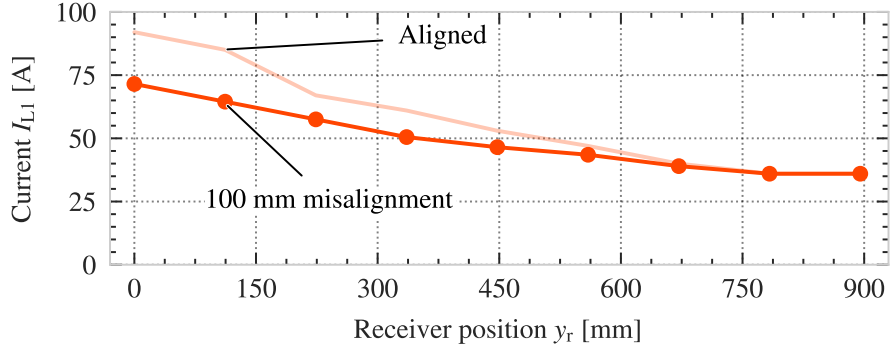
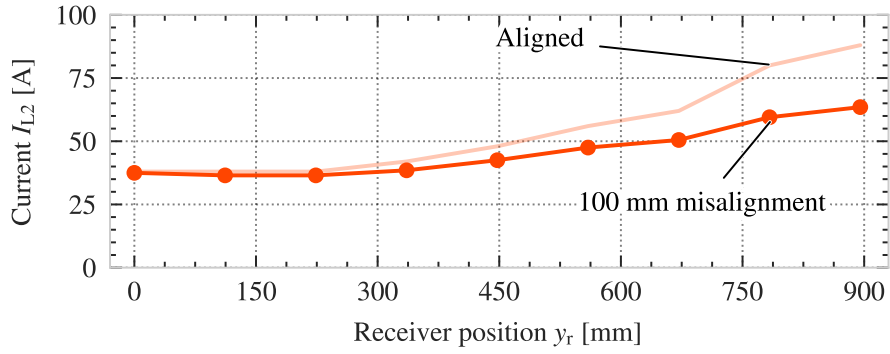
(a) Amplitude of current I_{L1} (b) Amplitude of current I_{L2}

Fig. 3.22: Variance of measured currents in the misalignment condition

The measured maximum stray field of the proposed circuit is $5.4 \mu\text{T}$ (0-peak) at 85 kHz.

The comparison of the measured and simulated results of the stray magnetic field in the uncoupled condition are shown in TABLE 3.5. The experimental and simulation results

Table 3.5: Comparison of the measured and simulation results of the stray magnetic field in the uncoupled condition

Description	Proposed circuit	Constant current circuit
Experiment	$5.4 \mu\text{T}$ (0-peak)	$13.3 \mu\text{T}$ (0-peak)
Simulation	$4.7 \mu\text{T}$ (0-peak)	$12.2 \mu\text{T}$ (0-peak)
Error	-13.0%	-8.3%

match well with a maximum error of 13.0%. From the results, the validity of the simulation results has been confirmed.

Using the LTspice simulator mentioned above, the power loss in each component can

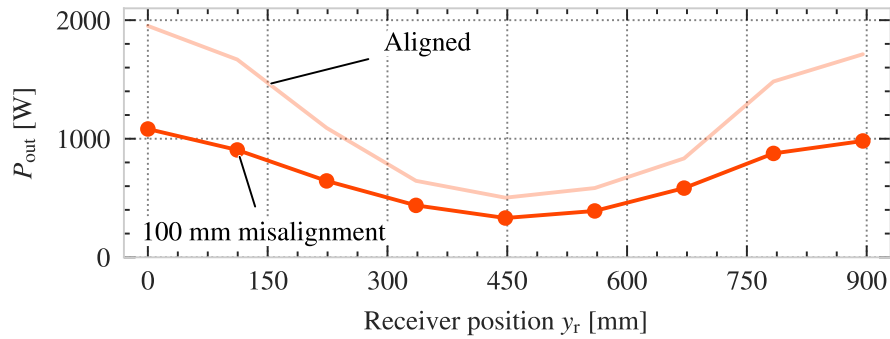


Fig. 3.23: Measured output power versus receiver position in the misalignment condition

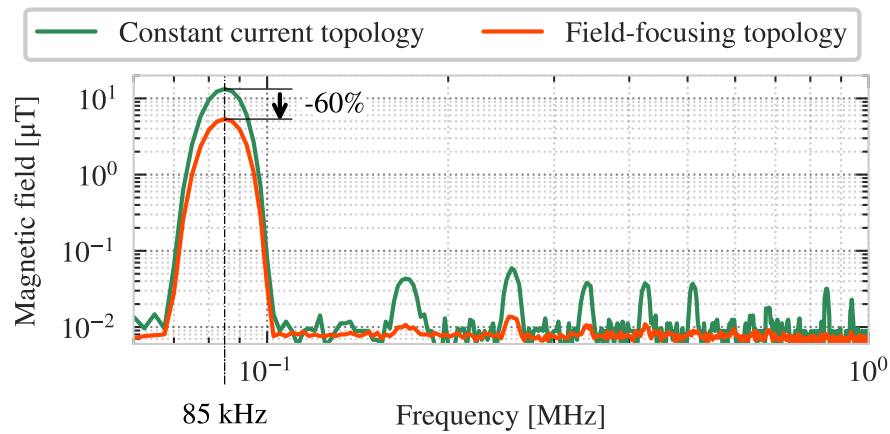


Fig. 3.24: Measured magnetic field at uncoupled condition

be estimated, as shown in Fig. 3.25. All parameters used in the simulation are the same as

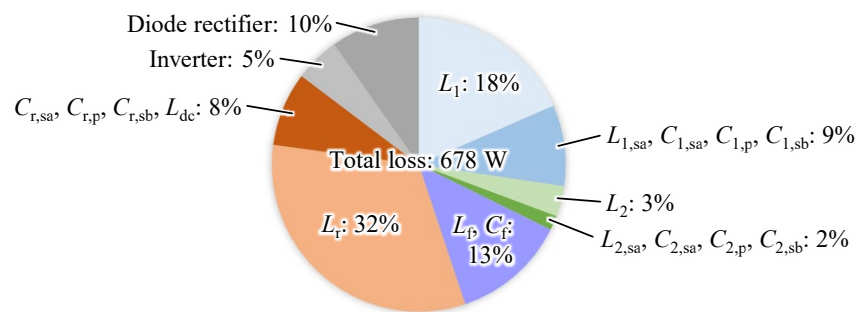


Fig. 3.25: LTspice simulated loss breakdown when output power is 2,022 W, total loss is 678 W, and total efficiency is 74.9%.

the values listed in TABLE 3.2. The transmitter coil L_1 and the receiver coil L_r consume

the highest power of all the components because the coil pads are not optimized for the proposed circuit. The system efficiency can be improved by using wider diameter Litz wires for the low voltage and high current system. Also, if the input voltage and output voltage are changed from 50 V to 400 V, which is the most common input and output dc voltage for vehicle applications, the system efficiency will improve as the low current, and high voltage system can decrease conduction losses. If the system is designed for a 50 kW, 400 V system with the same current gain of 2.5, the expected dc-dc efficiency is around 88% to 90% according to our simulation results.

3.7 Summary of the Chapter

This chapter proposed a reflexive tuning dynamic inductive power transfer (DIPT) system that utilizes a reflected reactance to allow a single inverter to drive multiple transmitter coils. The validity of the proposed circuit has been demonstrated through circuit simulation and experimental results. The proposed circuit topology can achieve a higher output power and higher transmitter coil current gain than the conventional circuit. The maximum output power of the proposed circuit is 102% higher than the conventional circuit in the demonstrated simulation. The sensitivity analysis results show that the additional compensation components in the proposed circuit can work well to address the effects of parasitic resistance and inductance.

A 2.0 kW prototype was constructed to validate the design of the proposed circuit. The experimental results show that the prototype matches well with the simulation results and that the circuit can amplify the current in the transmitter coil 2.5 times higher in the coupled condition than that in the uncoupled condition.

CHAPTER 4

ANN-based design optimization method

Conventional optimization methods for inductive power transfer (IPT) rely heavily on the finite element method (FEM) simulations to extract parameters such as inductances, coupling coefficients, and stray magnetic fields. These simulations are often time-consuming, and as a result, full optimization cannot be achieved. This chapter proposes a new design optimization method for IPT systems utilizing a combination of FEM simulations and a feedforward neural network. The proposed method can output a significantly larger number of design points than conventional methods in the same calculation time. Hence, users can select an optimized design point from higher-resolution plots. This paper presents the proposed design optimization method and compares its benefits and trade-offs to the conventional method. Additionally, a prototype designed by the proposed method is constructed, and experimental results are shown to verify the predicted values of inductances, coupling coefficients, and stray magnetic fields for the optimized solution against FEM simulation and the measured results.

4.1 Design Optimization Method for Inductive Power Transfer Systems

To design an IPT system, many parameters are considered, such as stray magnetic fields, variation of coupling due to misalignment, coil losses, core volume, and winding volume. For example, an IPT design must meet stray magnetic field limits at the edge of the vehicle [48, 84]. In terms of the magnetic coupling coefficient, the variation in the coupling coefficient due to misalignment must be taken into account. Depending on the coupling coefficient, a typical IPT system may adjust its input voltage, switching frequency, coil currents, or phase angle between the primary and secondary coils to regulate the output voltage [85–90]. Hence, if the IPT system has a large coupling coefficient variation, it needs to have a large margin for the wide control range. In most cases, this leads to high system

losses or high costs. Therefore, the difference in coupling coefficient due to misalignment is desired to be small.

4.1.1 Finite Element Method

Since stray magnetic field, coupling coefficient, and other aspects of IPT characteristic values are influenced by the geometry parameters of coils, their multi-objective optimization is required. For this reason, multi-objective optimization using a precise model [56, 91–93] has been discussed in previous works. This method performs the characteristic value mapping with a design parameter sweep using the loss model and FEM model to determine an optimized design point. In this method, the coupling coefficient and the stray magnetic fields are obtained by FEM simulation after determining the coil geometry. Due to the large air gap between the loosely coupled primary and secondary coils as well as the presence of ferrite to shape the fields, it is difficult to write exact expressions to represent the relationship between the geometric parameters of the IPT coil such as the various lengths, widths, and heights, and the magnetic parameters such as the inductances, coupling coefficients, and stray fields. As a result, conventional optimization methods for IPT coils rely heavily on FEM simulations to calculate these magnetic parameters. However, using FEM simulations to perform parametric sweeps is a time-consuming process to converge to an optimal solution, especially when the user need to run thousands of simulations to achieve a reasonable resolution.

4.1.2 Superposition Method

In order to reduce the calculation time for the stray magnetic field, an optimization method using superposition of stray magnetic fields was proposed [94]. In this method, the stray magnetic field is obtained for each turn of the coils, and expressed for any number of turns and currents using the superposition of magnetic fields. This method can significantly reduce the stray magnetic field calculation time. However, this method is not suitable for flexible design optimization of the coil if it includes magnetic core size and winding geometries because it requires a large inductance matrix and current-magnetic field coefficient

vector for each magnetic core geometry.

4.1.3 Nonlinear Fitting utilizing a Neural Network

An optimization method for inductors for a DC-DC converter utilizing a neural network was proposed [95]. The proposed method predicts the inductance and coupling coefficient of inductors from a 2-D FEM model of an inductor. As a result, this method can depict a pareto-front line by predicting and plotting a large amount of data in short time.

This method is an excellent approach for optimizing WPT systems since neural networks can fit nonlinear relationships between input and output variables. However, the conventional method requires a large amount of FEM data to accurately predict the stray magnetic field because the stray magnetic field of a WPT system varies with the primary and secondary currents and the number of primary and secondary windings. Therefore, this chapter proposes a new design optimization method for WPT systems utilizing a neural network.

4.2 Theory of the proposed ANN-based design method

The proposed optimization method is shown in Fig. 5.3. The proposed method learns the nonlinear relationship between geometry parameters (GP) and magnetic parameters (MP) obtained from FEM simulations using a feedforward neural network. Following this, many more geometric parameters are considered to interpolate between results to find the optimal design with a higher resolution.

Fig. 4.2 (a) and (b) show the coil models and its parameters that are considered for optimization. The square cross-section winding is used for both coils, and the length of one side of the cross-section is 6.6 mm. The thickness of the ferrite is 5 mm for both the primary and secondary side coils. Fig.4.2 (a) is the primary side coil model, which has five parameters to be optimized. Fig.4.2 (b) is the secondary side coil model. In this paper, the secondary side coil geometry is considered fixed as follows: The number of turns is 4, the length of the core is 340 mm, all pitches of winding are 13.2 mm, and the length of the

inner side of the winding is 200 mm. In the following, the proposed optimization process is shown step by step.

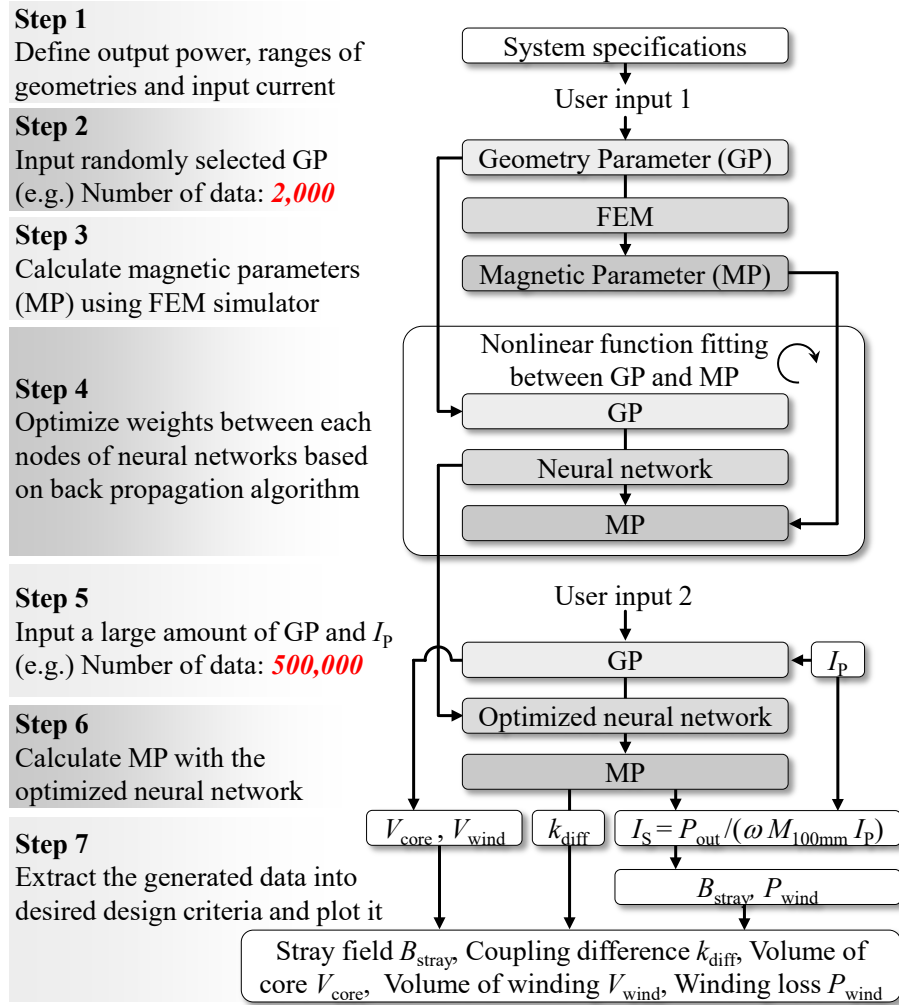


Fig. 4.1: The proposed design optimization method

In step 1, the output power, the ranges of the input current, the range of GP, the air gap, and the switching frequency were defined.

In step 2, randomly selected GP of primary coils were entered as user input 1. The five parameters of GP are assumed as follows:

$$GP : l, w_{in}, p_1, p_2, p_3 \quad (4.1)$$

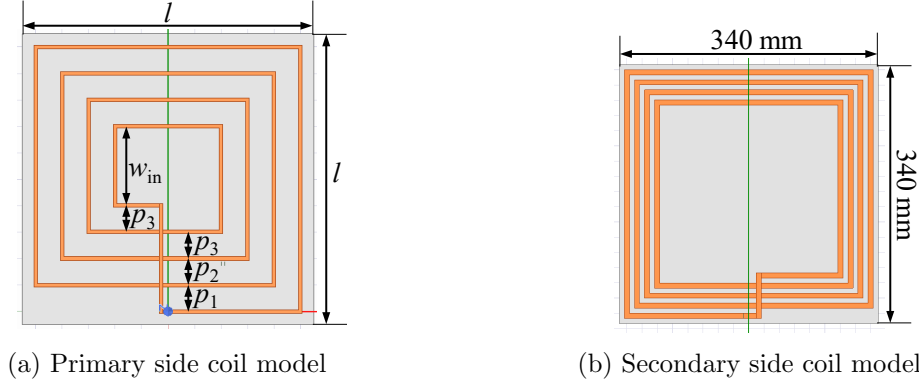


Fig. 4.2: Degree-of-freedom considered for the design optimization of the coils

In step 3, MP corresponding to the GP were calculated by FEM simulations. The 10 parameters of MP are assumed as follows:

$$\begin{aligned}
 \text{MP} : & L_{P,0\text{mm}}, L_{S,0\text{mm}}, k_{0\text{mm}}, L_{P,100\text{mm}}, L_{S,100\text{mm}}, \\
 & k_{100\text{mm}}, \mathbf{B}_{P,0\text{mm}}, \mathbf{B}_{S,0\text{mm}}, \mathbf{B}_{P,100\text{mm}}, \mathbf{B}_{S,100\text{mm}}.
 \end{aligned} \tag{4.2}$$

Here, $L_{P,0\text{mm}}$ and $L_{S,0\text{mm}}$ are self-inductance of primary side coil and self-inductance of secondary side coil when misalignment is 0 mm, respectively. In the same way, self-inductances, when misalignment is 100 mm in the lateral direction are defined as $L_{P,100\text{mm}}$ and $L_{S,100\text{mm}}$, respectively. Coupling coefficients when misalignment is 0 mm and 100 mm are defined as $k_{0\text{mm}}$ and $k_{100\text{mm}}$, respectively. The SAE standard [48] for light-duty vehicles is considered to design stray magnetic fields with the assumption that the width of the vehicle is 1.6 m. The maximum values of the magnetic stray field at a distance of 800 mm in the lateral direction from the center of secondary coil at the middle of 150 mm air gap between primary and secondary coil is acquired as the stray field. $\mathbf{B}_{P,0\text{mm}}$ and $\mathbf{B}_{P,100\text{mm}}$ are the complex values of magnetic field when primary coil current amplitude $I_P = 1$ A and secondary coil current amplitude $I_S = 0$ A when misalignment is 0 mm and 100 mm, respectively. In this paper, operational frequency is assumed as 85 kHz. $\mathbf{B}_{S,0\text{mm}}$ and $\mathbf{B}_{S,100\text{mm}}$ are the complex values of magnetic fields when $I_P = 0$ A and $I_S = 1$ A at misalignment of 0 mm and 100 mm, respectively. By acquiring complex values of magnetic field in this way, the magnitude of

stray magnetic field B_{stray} can be obtained for any combination of current (I_P , I_S) using the following equations:

$$B_{0\text{mm}} = \{[\text{Re}(\mathbf{B}_{P,0\text{mm}})I_P + \text{Re}(\mathbf{B}_{S,0\text{mm}})I_S]^2 + [\text{Im}(\mathbf{B}_{P,0\text{mm}})I_P + \text{Im}(\mathbf{B}_{S,0\text{mm}})I_S]^2\}^{1/2} \quad (4.3)$$

$$B_{100\text{mm}} = \{[\text{Re}(\mathbf{B}_{P,100\text{mm}})I_P + \text{Re}(\mathbf{B}_{S,100\text{mm}})I_S]^2 + [\text{Im}(\mathbf{B}_{P,100\text{mm}})I_P + \text{Im}(\mathbf{B}_{S,100\text{mm}})I_S]^2\}^{1/2} \quad (4.4)$$

$$B_{\text{stray}} = \max\{B_{0\text{mm}}, B_{100\text{mm}}\} \quad (4.5)$$

In step 4, the geometry parameters and the magnetic parameters are used for training a neural network that fits a nonlinear function between GP and MP. The classical back-propagation algorithm [96, 97] is used for the training. The constructed neural network has 5 nodes at the input layer and 30 nodes at the output layer. The number of hidden layers between the input and output layer is two, and each hidden layer has 100 nodes. Because of the better tendency to differentiate between similar input values, arc tangent was applied to all nodes in the hidden layers as an activation function. For the neural network topology with the configuration described above, the loss function is minimized by an iterative calculation that adjusts the bias and the weight between each node. Root mean square error (*RMSE*) was used as a loss function, and *RMSE* is defined as

$$RMSE = \sqrt{\sum_{i=1}^n (Y_i - \hat{Y}_i)^2}, \quad (4.6)$$

where n is the number of nodes at the output layer ($n = 30$), Y is normalized output parameters of FEM, and \hat{Y} is the normalized predicted output parameters.

In step 5, a large number of randomly selected geometry parameters were entered as the user input 2. The data for user input 2 can be several hundreds of times larger than that of user input 1 since the neural network can compute magnetic parameters several

hundreds of times more efficiently than FEM simulations. In this paper, 2,000 data points were used for user input 1, and 500,000 data points were used for user input 2.

In step 6, magnetic parameters for the geometry parameters from input 2 are entered.

In step 7, core volume and winding volume of primary side are calculated for each geometry parameter from input 2. Difference of coupling coefficient k_{diff} is calculated by the following equation:

$$k_{\text{diff}} = \frac{k_{0\text{mm}} - k_{100\text{mm}}}{k_{0\text{mm}}}. \quad (4.7)$$

In this paper, the series-series tuning circuit is assumed for the resonant operation of the IPT system. Hence, the resonant capacitors C_P and C_S are calculated by the following equations:

$$C_P = \frac{1}{\omega^2 L_{P,0\text{mm}}} \text{ and } C_S = \frac{1}{\omega^2 L_{S,0\text{mm}}}. \quad (4.8)$$

The output power at misalignment = 100 mm are defined as follows:

$$P_{\text{out}} = \omega \cdot k_{100\text{mm}} \sqrt{L_{P,100\text{mm}} \cdot L_{S,100\text{mm}}} \cdot I_P \cdot I_S. \quad (4.9)$$

Therefore, the RMS value of secondary coil current I_S at misalignment = 100 mm is calculated by the following equation:

$$I_S = \frac{P_{\text{out}}}{\omega M_{100\text{mm}} I_P}. \quad (4.10)$$

To calculate approximate winding coil loss, the following equation is assumed:

$$P_{\text{wind}} = \frac{\omega L_P I_P^2}{Q_{\text{coil},P}} + \frac{\omega L_S I_S^2}{Q_{\text{coil},S}}, \quad (4.11)$$

where $Q_{\text{coil},P} = Q_{\text{coil},S} = 400$ are assumed as the worst case.

By following the above procedure (Step 1 ~ Step 7), in this example, the proposed method can output a 250 times larger number of data plots (250 times higher plot resolution) than the conventional method requiring the same calculation time. Here, the time taken to train the neural network is ignored because the time is almost the same as the calculation

time of 15 data points by the FEM simulation.

4.3 Proposed design optimization method

The proposed optimization method shown in Fig. 5.3 utilizes a neural network to model a non-linear function between geometric parameters (GP) and magnetic parameters (MP). Each step is described step by step below.

In step 1, the input voltages V_{dc} , the output voltage V_{bat} , the output power $P_{out,x0,y0}$ when the secondary side coil is at the center of the primary coil, and the ranges of GP are defined. Fig. 4.2 shows the degrees of freedom considered for optimization of the primary and secondary coils, respectively. The seven GP are assumed as follows:

$$\text{GP} : l_{Px}, l_{Py}, w_P, a, p, l_S, w_S. \quad (4.12)$$

In step 2, randomly selected GP from the defined ranges of geometry are passed in as user input 1. In step 3, the FEM simulator calculates MP from the GP. The 26 parameters of the MP are assumed as follows:

$$\begin{aligned} \text{MP} : & L_{P,x0,yi}, L_{P,x1,y0}, L_{S,x0,yi}, L_{S,x1,y0}, k_{x0,yi}, \\ & k_{x1,y0}, \mathbf{B}_{P,x0,y0,0deg}, \mathbf{B}_{P,x0,y0,90deg}, \mathbf{B}_{S,x0,y0,0deg}, \\ & \mathbf{B}_{S,x0,y0,90deg}, \mathbf{B}_{P,x1,y0,0deg}, \mathbf{B}_{P,x1,y0,90deg}, \\ & \mathbf{B}_{S,x1,y0,0deg}, \mathbf{B}_{S,x1,y0,90deg}, \end{aligned} \quad (4.13)$$

where $L_{P,x0,yi}$, $L_{S,yi}$, and $k_{x0,yi}$ ($i = 0 \sim 4$) are self inductance of primary side coil, self inductance of secondary side coil, and coupling coefficient, when misalignment is 0 mm ($= x_0$), respectively. In the same way, self inductance and coupling coefficient when misalignment is 100 mm ($= x_1$) are defined as $L_{P,x1,y0}$, $L_{S,x1,y0}$, and $k_{x1,y0}$, respectively.

The SAE standard [48] is considered to design stray magnetic fields with the assumption that the width of the vehicles is 1.6 m. The maximum values of the magnetic stray field at a distance of 800 mm in the lateral direction from the center of secondary coil at the middle

of 200 mm air gap between primary and secondary coils are called the stray field in this paper. $\mathbf{B}_{P,x0,y0,0deg}$ and $\mathbf{B}_{P,x0,y0,90deg}$ are magnetic fields at 0 and 90 degree in one cycle of the operational frequency when primary coil current amplitude $I_P = 1$ A and secondary coil current amplitude $I_S = 0$ A with no misalignment, respectively. In this paper, operational frequency is assumed to be 85 kHz. $\mathbf{B}_{S,x0,y0,0deg}$ and $\mathbf{B}_{S,x0,y0,90deg}$ are magnetic fields at 0 and 90 degree when $I_P = 0$ A and $I_S = 1$ A with no misalignment, respectively. In the same way, $\mathbf{B}_{P,x1,y0,0deg}$, $\mathbf{B}_{P,x1,y0,90deg}$, $\mathbf{B}_{S,x1,y0,0deg}$, and $\mathbf{B}_{S,x1,y0,90deg}$ can be defined as magnetic fields when misalignment is 100 mm ($= x_1$). By splitting magnetic field in this way, the magnetic stray field B_{stray} can be obtained for any combination of current (I_P, I_S),

$$B_{x0,y0} = \{[\text{Re}(\mathbf{B}_{P,x0,y0})I_P + \text{Re}(\mathbf{B}_{S,x0,y0})I_S]^2 + [\text{Im}(\mathbf{B}_{P,x0,y0})I_P + \text{Im}(\mathbf{B}_{S,x0,y0})I_S]^2\}^{1/2} \quad (4.14)$$

$$B_{x1,y0} = \{[\text{Re}(\mathbf{B}_{P,x1,y0})I_P + \text{Re}(\mathbf{B}_{S,x1,y0})I_S]^2 + [\text{Im}(\mathbf{B}_{P,x1,y0})I_P + \text{Im}(\mathbf{B}_{S,x1,y0})I_S]^2\}^{1/2} \quad (4.15)$$

$$B_{stray} = \max\{B_{x0,y0}, B_{x1,y0}\}. \quad (4.16)$$

In step 4, a neural network learns the nonlinear relationship between GP and MP using the classical back-propagation algorithm [96,97]. The constructed neural network has 7 nodes on the input layer and 26 nodes on the output layer. Two hidden layers are used between the input and output layers, and each hidden layer has 100 nodes. Because of the better tendency to differentiate between similar input values, arc tangent was applied to all nodes in the hidden layers as an activation function. By minimizing a loss function, weights between each node and bias of each node are optimized. As a loss function, root mean square error (*RMSE*) is used, and *RMSE* is defined by

$$RMSE = \sqrt{\sum_{i=1}^n (Y_i - \hat{Y}_i)^2}, \quad (4.17)$$

where n is the number of nodes at the output layer ($n = 26$), Y is normalized output parameters of FEM, and \hat{Y} is the normalized predicted output parameters.

In step 5, a large number of randomly selected GP are passed in as the user input 2. The number of data points can be hundreds of times larger than that of user input 1 since the neural network can compute MP significantly faster than running additional FEM simulations. In this paper, 1,000 data points are used as the number of user input 1, and 500,000 data points are used as the number of user input 2, as an example. In step 6, the optimized neural network generates the predicted MP from GP. In step 7, the number of inverters N_{inv} , core volume V_{PriCore} and V_{SecCore} , and winding volume V_{PriWind} and V_{SecWind} are calculated from the generated MP. The number of inverters N_{inv} is calculated according to the assumption that each coil has an inverter. The difference of coupling coefficient k_{diff} between (x_0, y_0) and (x_1, y_0) is calculated to include the effect of misalignment for output power to the optimization process according to

$$k_{\text{diff}} = \frac{|k_{x_0, y_0} - k_{x_1, y_0}|}{\max\{|k_{x_0, y_0}|, |k_{x_1, y_0}|\}}. \quad (4.18)$$

In this paper, the double-sided LCCL compensation circuit [98] is assumed for resonant operation. The ratio of series capacitor C_{1s} , C_{2s} and parallel capacitor C_{1p} , C_{2p} , $n_1 (= 1 + \frac{C_{1p}}{C_{1s}})$ and $n_2 (= 1 + \frac{C_{2p}}{C_{2s}})$ are calculated as

$$n_1 = \frac{\pi\omega L_{P, x_0, y_0} I_P}{2\sqrt{2}V_{\text{dc}}}, \quad (4.19)$$

$$n_2 = \frac{\pi^2\omega P_{\text{out}, x_0, y_0} \sqrt{L_{P, x_0, y_0} L_{S, x_0, y_0}}}{8k_{x_0, y_0} n_1 V_{\text{dc}} V_{\text{bat}}}. \quad (4.20)$$

Using (4.19) and (4.20), current amplitude at the secondary coil I_S is calculated as

$$I_S = \frac{4V_{\text{bat}} n_2}{\pi\omega L_{S, x_0, y_0}}. \quad (4.21)$$

Table 4.1: Design specifications for the IPT system

Description	Symbol	Value
Output power	P_{out}	3,300 W
Input RMS current	I_{P}	20-100 A
Length of core	l	300-1300 mm
Length of winding	w_{in}	50-300 mm
Pitch of winding	p_1, p_2, p_3	13-46 mm
Air gap	z	150 mm
Switching frequency	f_s	85 kHz

Therefore, output power when the receiver position $y_S = y_1 \sim y_4$ is calculated as

$$P_{\text{out},x0,y_i} = \omega k_{x0,y_i} I_{\text{P}} I_{\text{S}} \sqrt{L_{\text{P},x0,y_i} L_{\text{S},x0,y_i}} \quad (i = 1, 2, 3), \quad (4.22)$$

$$P_{\text{out},x0,y_4} = 2\omega k_{x0,y_4} I_{\text{P}} I_{\text{S}} \sqrt{L_{\text{P},x0,y_4} L_{\text{S},x0,y_4}}. \quad (4.23)$$

The output power $P_{\text{out},x0,y_4}$ is doubled in the assumption of a system with an input and an output voltage source because the receiver coil is excited by the two primary coils when the receiver coil is at the edge of the primary coils [99]. Using (5.16) and (5.17), the average output power P_{ave} is calculated as

$$P_{\text{ave}} = (P_{\text{out},x0,y_0} + 2P_{\text{out},x0,y_1} + 2P_{\text{out},x0,y_2} + 2P_{\text{out},x0,y_3} + P_{\text{out},x0,y_4})/8.$$

To calculate the approximate coil loss, the following is assumed

$$P_{\text{loss}} = \frac{\omega L_{\text{P},x0,y_0} I_{\text{P}}^2}{Q_{\text{coil,P}}} + \frac{\omega L_{\text{S},x0,y_0} I_{\text{S}}^2}{Q_{\text{coil,S}}}, \quad (4.24)$$

where $Q_{\text{coil,P}} = Q_{\text{coil,S}} = 400$ are assumed as the worst case.

4.4 Optimization process

TABLE 4.1 shows the design specifications for the IPT system. 3.3 kW output is required at the 150 mm air gap and 85 kHz operational switching frequency.

Fig.4.3 shows the root mean square of training error and validation error versus the number of iterative calculations. The training error means the difference between the predicted data and the training data, which is used for fitting the neural network. The validation error means the difference between the predicted data and new data, which is used for certifying the accuracy of the trained neural network for new data. Because the validation error of the neural network is less than 4% when the number of iterative calculations is 100,000, the trained neural network can predict MP from new GP within 4% error.

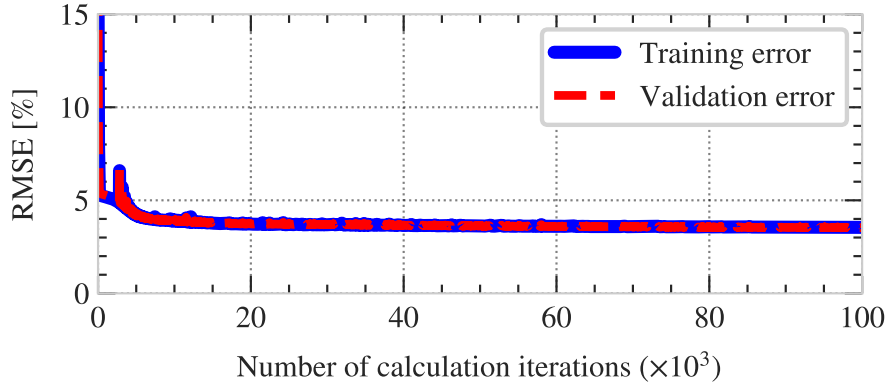
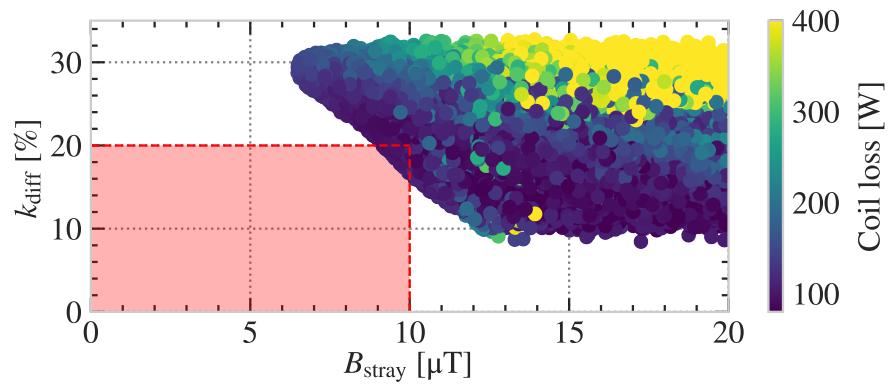


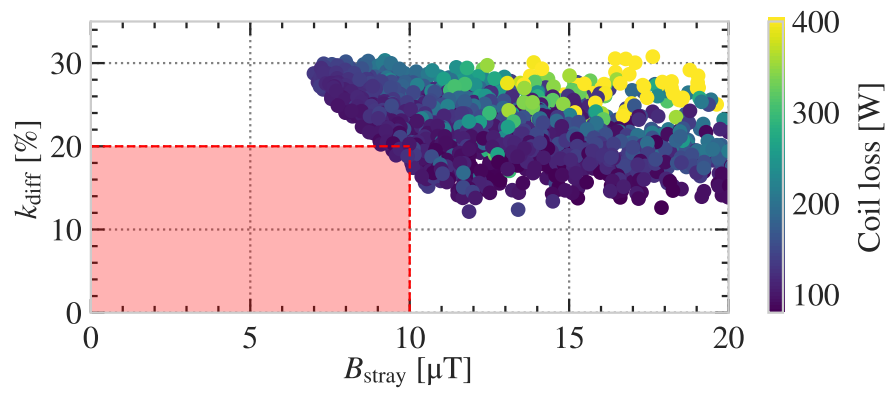
Fig. 4.3: Root mean square error vs. iterations

Fig.4.4 (a) and (b) show the scatter plots generated by the proposed method and the conventional method at $P_{\text{out}}=3.3$ kW, respectively. Fig. 4.4 (a) has 500,000 designs, because the neural network was used to interpolate between the initial 2,000 FEM data points. Likewise, Fig. 4.4 (b) has only 2,000 base designs that were used to generate Fig. 4.4 (a). The highlighted red area in both scatter plots indicates the area of interest to select an optimized design that has low B_{stray} and low k_{diff} . In this paper, $B_{\text{stray}} \leq 10 \mu\text{T}$ and $k_{\text{diff}} \leq 20\%$ are defined as an extraction condition.

Fig. 4.5 (a) and (b) shows the relationship between V_{core} , coil loss, and V_{wind} generated by the proposed method and the conventional method, respectively. Both plots were extracted from Fig. 4.4 (a) and (b), respectively. The final design point was chosen from the red highlighted area in Fig.4.5 (a) and (b), where the data satisfies the following con-

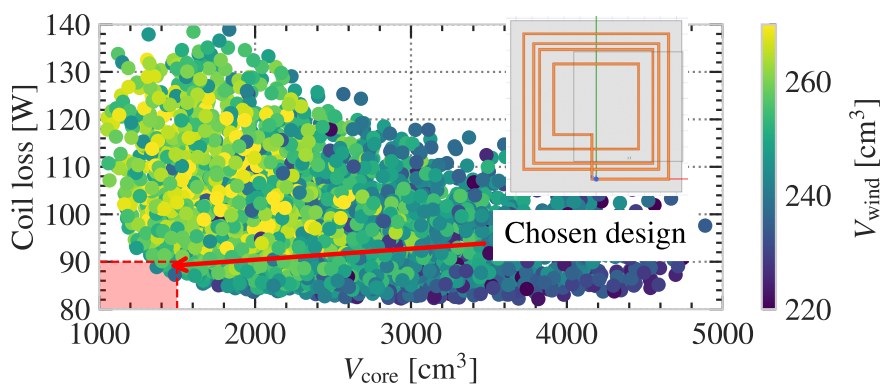


(a) Proposed method (Number of point: 500,000)

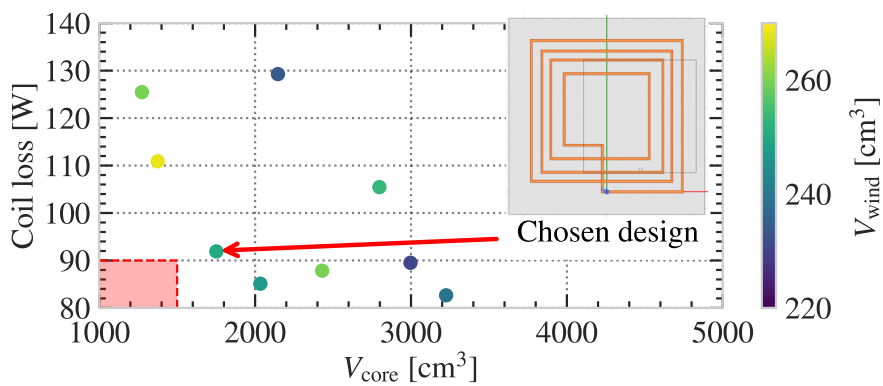


(b) Conventional method (Number of point: 2,000)

Fig. 4.4: Distribution of all data at $P_{\text{out}}=3.3$ kW. The calculation time for both method are the same.



(a) Proposed method (Number of point: 2,040)



(b) Conventional method (Number of point: 11)

Fig. 4.5: Extracted data from Fig.4.4 (a) and (b), respectively. All the data satisfy $B_{\text{stray}} \leq 10\mu\text{T}$ and $k_{\text{diff}} \leq 20\%$.

dition: $V_{\text{core}} \leq 1500 \text{ cm}^3$ and $P_{\text{loss}} \leq 90 \text{ W}$. The final design of the proposed method and the conventional method are shown by the red arrows in each figure, respectively. The comparison of appearance for the final design is shown also in Fig. 4.5. Because the resolution of the data plot generated by the proposed method (Fig.4.5 (a)) is significantly higher than that of the conventional method (Fig.4.5 (b)), the core volume and the coil loss of the proposed method can be designed to be smaller than those of the conventional method while maintaining the winding volume, the leakage magnetic field, and the variation of the coupling coefficient at the same level. Depending on the random values at input 1, the conventional method may result in a design with similar performance as the proposed method. However, compared to conventional methods, designs using the proposed method will take a similar amount of computation time, will never have lower performance, and will always achieve the desired resolution of the design space independent of the random seed at step 2 or additional intuition that the designer may lack for new conditions.

4.5 Experimental verification

Fig.4.6 shows the schematic diagram of the experimental setup. A DC power source and a DC power load are attached at the DC input and DC output port, and controlled at V_{dc} and V_{bat} , respectively. The design parameters of the IPT coils prototype are listed in TABLE 4.2. To make the designed primary and secondary RMS current I_{P} and I_{S} at the IPT coils, V_{dc} and V_{bat} are calculated by the following equations:

$$V_{\text{dc}} = \frac{\pi\omega M_{100\text{mm}} I_{\text{S}}}{2\sqrt{2}} \quad (4.25)$$

$$V_{\text{bat}} = \frac{\pi\omega M_{100\text{mm}} I_{\text{P}}}{2\sqrt{2}}. \quad (4.26)$$

To achieve accurate winding geometry, coil bobbins with the acrylic board were cut by a laser cutter. Litz wire is used for both primary and secondary coils, of which the diameter is 6.6 mm. Fig.4.7 shows a photograph of the whole experimental setup of the prototype. A magnetic field sensor (EHP-200A/AC) is set at a distance of 800 mm in the horizontal

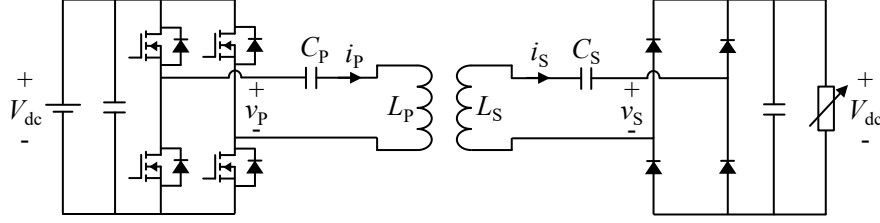


Fig. 4.6: Schematic diagram of the experimental setup

Table 4.2: Design parameters of the prototype

Description	Parameter	Value
Length of core	l	532 mm
Length of winding	w_{in}	237 mm
Pitch of winding	p_1	27 mm
Pitch of winding	p_2	23 mm
Pitch of winding	p_3	45 mm
Primary RMS current	I_P	42.3 A
Secondary RMS current	I_S	52.5 A
Input voltage	V_{dc}	87.0 V
Output voltage	V_{bat}	69.8 V
Resonant capacitor	C_P	210 μ F
Resonant capacitor	C_S	248 μ F

direction from the center of the secondary coil at the middle of the gap to measure the stray magnetic field.

Self-inductance and coupling coefficient were measured when misalignment is zero and misalignment is 100 mm. The prediction from the proposed method, FEM value, and the measured value are listed in TABLE 4.3. The results show that the prediction, measured value, and the FEM values of the self-inductance and the coupling coefficients are quite close.

Fig.4.8 (a) and (b) show voltage and current waveforms of the IPT coils when the experimental setup is operated at the misalignment = 100 mm. Fig.4.8 (a) shows the voltage and the current waveforms at the primary side coil. The measured primary RMS current is 43.8 A. Because the assumed waveform is not rectangular but sinusoidal when V_{dc} are calculated, the primary side current is slightly higher than the expected value (42.3 A). Fig.4.8 (b) shows the voltage and the current waveform at the secondary side coil. The

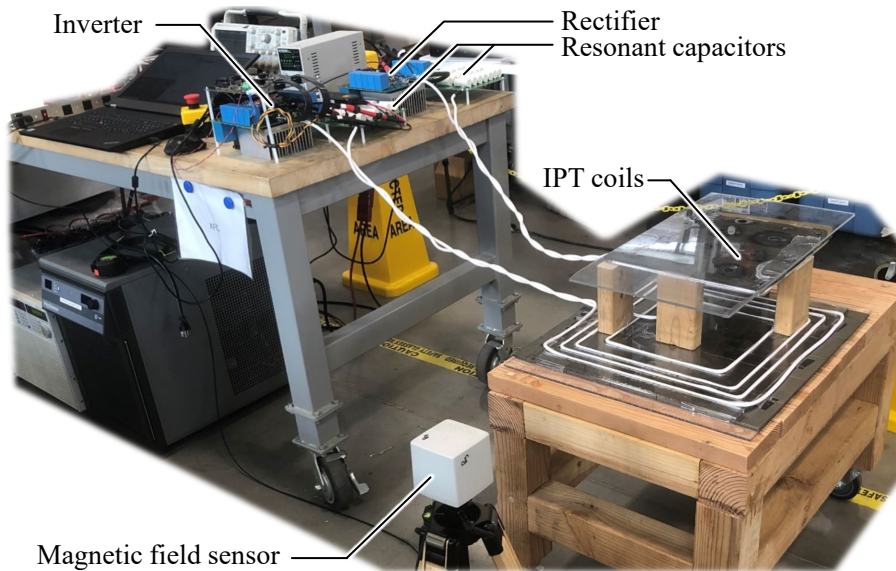


Fig. 4.7: Photograph of the whole experimental setup

Table 4.3: Measured magnetic parameters

Parameter	Prediction	FEM	Exp.
$L_{P,0mm}$ [μH]	16.28	16.62	16.55
$L_{P,100mm}$ [μH]	16.46	16.75	16.66
$L_{S,0mm}$ [μH]	13.67	13.80	14.13
$L_{S,100mm}$ [μH]	13.67	13.82	14.09
k_{0mm}	0.2317	0.2321	0.2224
k_{100mm}	0.1858	0.1868	0.1807
k_{diff} [%]	19.82	19.50	18.73
B_{stray} [μT]	9.9	10.1	11.3

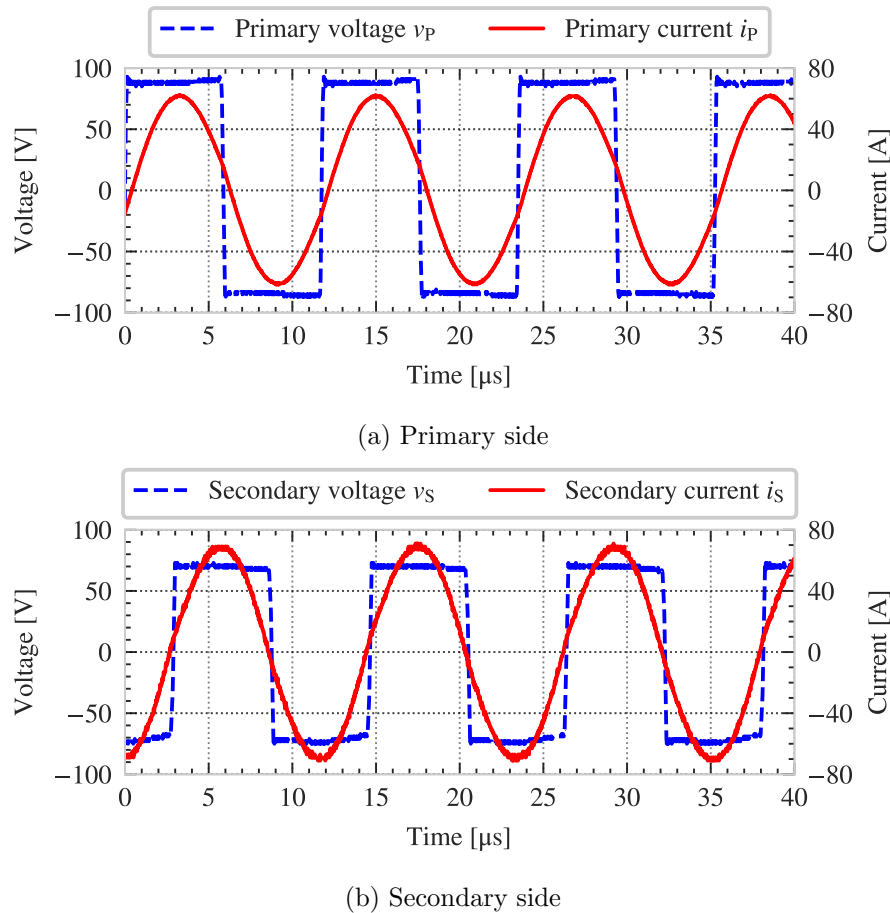


Fig. 4.8: Waveforms at the primary and the secondary side

measured secondary RMS current is 49.5 A. Since coil loss is not taken into account when V_{bat} is calculated, the secondary side current is slightly lower than the expected value (52.5 A).

Fig.4.9 shows the measured result of the stray magnetic field when the experimental setup is operated at the misalignment = 100 mm. The solid line is the measured stray field B_{stray} , and the dotted line is the limit of the ICNIRP 2020 General Public. In the whole range of the frequency, the stray field of the prototype is less than the limit. At the operational switching frequency, the stray magnetic field is 11.3 μT . The measured value is a little higher than the expected value (10.1 μT) because the primary current is higher than expected. The magnetic field sensor doesn't detect the value at a point but the average value of the pickup coil area inside the sensor, which could be another reason for the error.

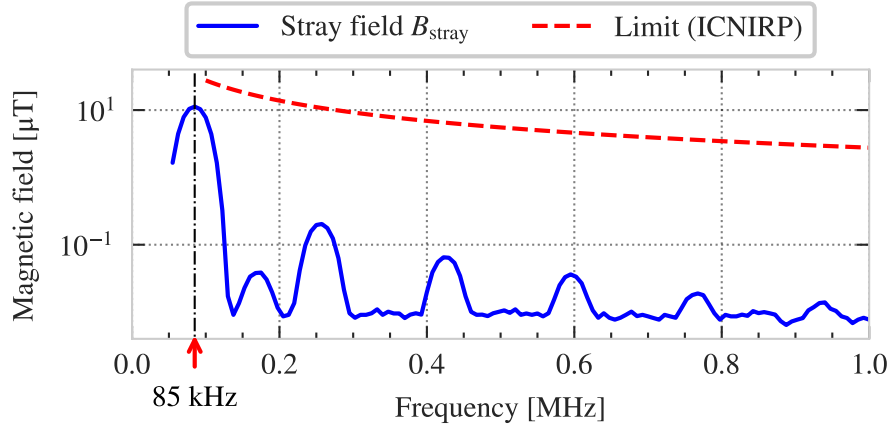


Fig. 4.9: Measured magnetic field

Table 4.4: Measured input and output power and the estimated loss distribution

Parameter	Design value	Measured and estimated value
P_{in} [W]	3,300	3,343
P_{out} [W]	3,300	3,169
P_{wind} [W]	90	62
P_{core} [W]	-	88
P_{cap} [W]	-	24

The measured input and output power and the estimated loss distribution of the coils and resonant capacitors are listed in TABLE 4.4. The measured input power P_{in} matches well with the designed value. Because winding loss P_{wind} , core loss P_{core} , and capacitor loss P_{cap} are not considered in the design value of the output power P_{out} , the measured output power is lower by 4%. The loss distribution of P_{wind} , P_{core} , and P_{cap} are estimated by the measured equivalent series resistances of the coils and the capacitors. Since $Q_{\text{coil,P}}=Q_{\text{coil,S}}=400$ is assumed as the worst case, the measured winding loss P_{wind} is lower than the design value.

To achieve the more accurate output power in the experiment for the design value, coil loss should not be calculated by the constant Q factor but by the FEM simulator. Therefore, there is a trade-off between the accuracy of output power and the time for the FEM simulation because the FEM simulation of the coil loss takes a longer time than that of magnetic parameters.

4.6 Summary of the Chapter

In this paper, a new design optimization method has been proposed and the validity has been demonstrated through FEM simulation and experimental results. The proposed method learns the nonlinear relationship between coil geometry parameters and magnetic parameters from FEM sample data using a neural network. The proposed method can evaluate a large number of geometric parameters without having to run additional FEM simulations. As a result, the proposed method can find hundreds of more designs that meet the designer's criteria, allowing the designer to select an optimized result. In the example presented, the primary side core of the proposed method is 20% smaller than that of the conventional method while maintaining the other criteria the same.

CHAPTER 5

ANN- and GA-based design optimization method

Multiple parameters with large nonlinear characteristics must be considered simultaneously to design the coil dimensions of static inductive power transfer (SIPT) systems as described in the previous chapter. The design of dynamic inductive power transfer (DIPT) systems is more challenging due to the large number of parameters needed to be considered. In the conventional artificial neural network (ANN)-based design approach, optimal coil dimensions are found using ANN that has learned the nonlinear characteristics between coil dimensions and magnetic characteristics using the finite element method (FEM). However, this approach requires a large amount of training data, and it is difficult to reach an optimum design if there are many design criteria. In order to overcome these challenges, this paper proposes a design optimization method using two approaches: improving the time efficiency of ANN training data collection by superposing the magnetic fields from the coils and improving the input value of ANN using a genetic algorithm. Design results predicted by the ANN are compared with FEM simulation, circuit simulations, and experimental results to verify the validity of the proposed algorithm. The FEM and circuit simulation results and the ANN prediction results match with errors of 10.2% or less for all design requirements. Experimental results are provided for a 3 kW DIPT system with four transmitter coils and an automated test rail. Comparison results between ANN predicted values and experimental values match with an error of less than 12.7%.

5.1 Introduction

In a DIPT system, transmitter coils are embedded in the road to supply electric power to EVs wirelessly. DIPT is expected to reduce the battery's weight and cost and improve the vehicle range and charging time [28, 100–103].

To perform design optimization of an inductive power transfer (IPT) system, engineers

need to consider many vital specifications, such as output power, stray magnetic fields, variation of coupling due to misalignment, coil losses, magnetic core volume, and copper winding volume [48, 84–90, 104]. In addition, DIPT requires further considerations beyond static inductive power transfer (SIPT) systems, such as the distribution of transmitted power on transmitter coils along the road and the average output power received by moving vehicles [62, 105–111].

To overcome the challenges in the design process for IPT systems, the Pareto front-based multi-objective optimization method has been discussed in previous works [56, 91–93]. The Pareto front is a performance boundary given by the set of designs in which an increase in one of the performances results in a decrease in the other. This method performs characteristic value mapping with a design parameter sweep using the loss model and FEM model to determine an optimized design point. In this method, the coupling coefficient and the stray magnetic fields are obtained by FEM simulation after determining the coil geometry. Due to the large air gap between the loosely coupled primary and secondary coils, as well as the presence of ferrite to shape the fields, it is difficult to define an exact mathematical model to represent the relationship between the geometric parameters of the coils for the IPT systems such as the various lengths, widths, and heights, and the magnetic parameters such as the inductances, coupling coefficients, and stray fields. As a result, the multi-objective design optimization methods for IPT systems rely heavily on FEM simulations to calculate these magnetic parameters. Using FEM simulations to perform parametric sweeps is time-consuming, especially when the user needs to run thousands of simulations to achieve the desired resolution.

In order to reduce the calculation time for the stray magnetic fields, optimization methods using the superposition of stray magnetic fields have also been proposed [94, 112]. In these methods, the stray magnetic field is obtained with each turn of the coils and represented as any number of turns and currents using the superposition of magnetic fields. These methods can significantly reduce the stray magnetic field calculation time. However, these methods are unsuitable for flexible design optimizations of IPT systems if they include

magnetic core size and winding geometries because they require a large inductance matrix and a current-magnetic field coefficient vector for each magnetic core geometry.

As an alternative to the optimization method above, artificial neural network (ANN)-based approaches have been proposed [95, 113–115]. The ANNs generate the Pareto fronts and select the optimal designs from given specifications and goals. In the literature [95], the ANNs predict the inductance and coupling coefficient of inductors from a 2-D FEM model of an inductor. The trained ANN learns the nonlinear characteristics of inductors and can depict a Pareto-front line by quickly predicting and plotting a large amount of data. This method is excellent for optimizing IPT systems since neural networks can represent nonlinear relationships between input and output variables. However, there are two challenges in systems with many input and output variables, such as DIPT, as shown in Fig. 5.1.

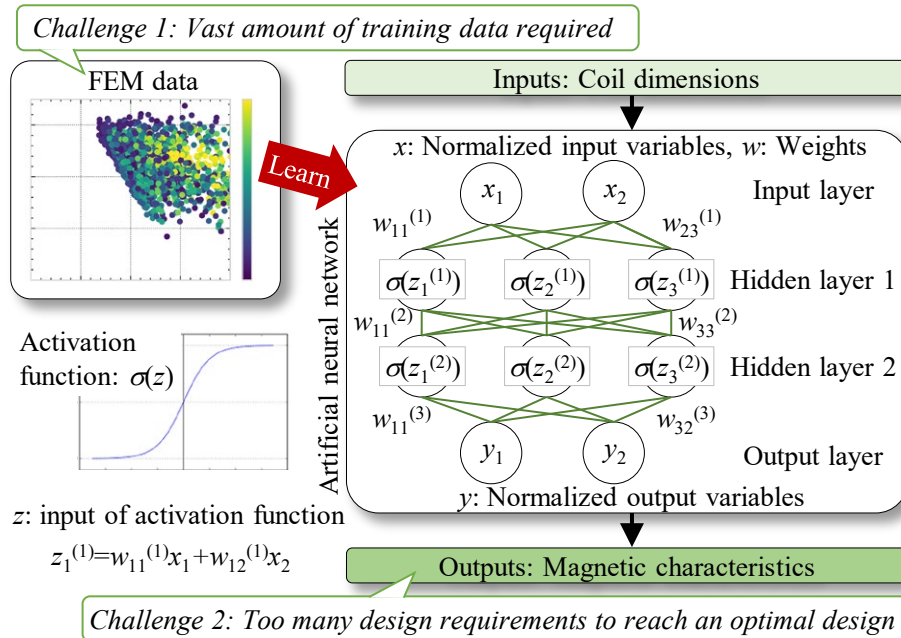


Fig. 5.1: Challenges with the conventional ANN-based design optimization approach

The first challenge is that a vast amount of training data is required. In the conventional approach, ANN learns the nonlinear relationship between coil dimensions and magnetic characteristics from FEM data. A vast amount of FEM data is required to learn

relationships if there are many input variables.

The second challenge is too many design criteria to reach the optimal design. Even if an ANN can learn nonlinear relationships, too many design requirements will take too much time to find an optimal design point that satisfies all design criteria.

To overcome the two challenges, this paper proposes a new fast design optimization method utilizing a combination of ANNs and genetic algorithms (GAs) for DIPT systems. The motivation of this paper is to find the Pareto front and perform multi-objective optimization in a short time. Section 5.2 presents an overview of the proposed algorithm in which superposition can help ANNs learn stray magnetic field data quickly, and GAs in the feedback step select input variables effectively. The proposed method demonstrates design optimization in Section 5.3. In Section 5.4, simulations verify the validity of the optimized design. In Section 5.5, the validity of the optimized design is verified experimentally.

5.2 The proposed design optimization process

In this section, a method to efficiently collect ANN training data by superposition of the magnetic fields of the transmitter and receiver coils in order to overcome the challenge 1 mentioned in the previous section is proposed. Furthermore, a method to improve input value by a GA to overcome the challenge 2 is proposed.

5.2.1 Assumption of the optimization problem

The coil model to be optimized is shown in Fig. 5.2. There are ten design variables, including the width of coil winding, the coil length, the distance between two transmitter coils, and the number of turns, listed in Table 5.1.

As the receiver coil moves from above the center of the transmitter coil to the edge according to the vehicle traveling direction, the coupling coefficient between the transmitter coil and receiver coil changes significantly from maximum to minimum. Since this coupling coefficient profile significantly affects the average output power, it is necessary to accurately simulate the coupling coefficient profile. In this paper, the coupling coefficient profiles are calculated in an FEM model with five receiver positions from y_0 to y_4 depicted in Fig. 5.2(a).

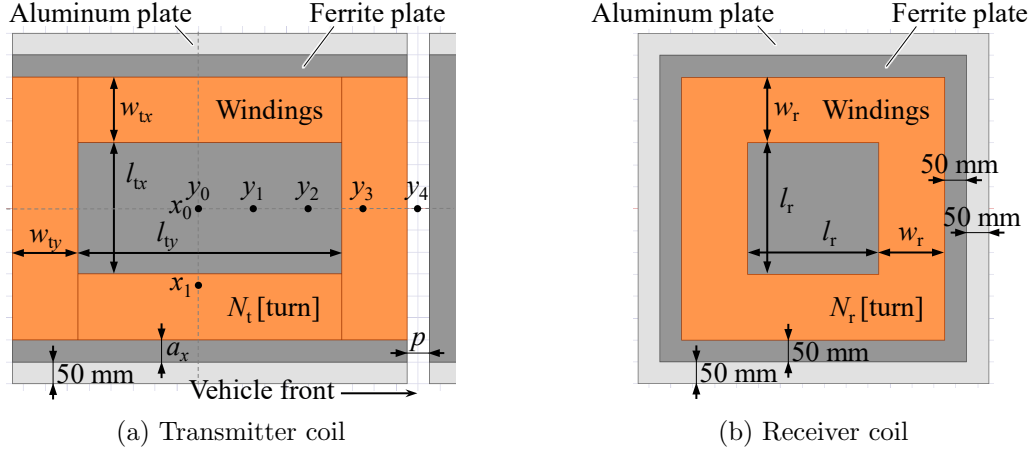


Fig. 5.2: The coil model and its design variables to be optimized

Table 5.1: Ranges of ten random input variables for the coil dimensions

Description	Parameter	Value	Unit
X-direction length of the transmitter coil	l_{tx}	50~650	mm
Y-direction length of the transmitter coil	l_{ty}	50~2050	mm
X-direction width of the transmitter coil winding	w_{tx}	25~325	mm
Y-direction width of the transmitter coil winding	w_{ty}	25~325	mm
Length of the edge of the transmitter coil	a_t	0~200	mm
Distance between adjacent transmitter coils	p	0~200	mm
Length of the receiver coil	l_r	50~450	mm
Width of the receiver coil winding	w_r	25~225	mm
Turn number of the transmitter coil	N_t	2~10	turns
Turn number of the receiver coil	N_r	2~10	turns

Since the transmitter coil is symmetrical about the center points x_0 and y_0 , symmetry was used to calculate the coupling coefficient profile of the entire transmitter coil with respect to the vehicle's traveling direction. Additionally, it is assumed that all of the multiple transmitter coils have the same magnetic profiles and that adjacent transmitter coils do not affect the magnetic characteristics of each other. The coupling coefficients between each transmitter coil are ignored in this paper to simplify the analysis.

The conventional ANN-based design optimization flow is shown in Fig. 5.3. In step 1, ten random values, one for each design variable, are input into the FEM simulator. In step 2, the FEM simulator calculates magnetic characteristics from the input design variables. In step 3, ANN learns the nonlinear relationship between coil dimensions and magnetic

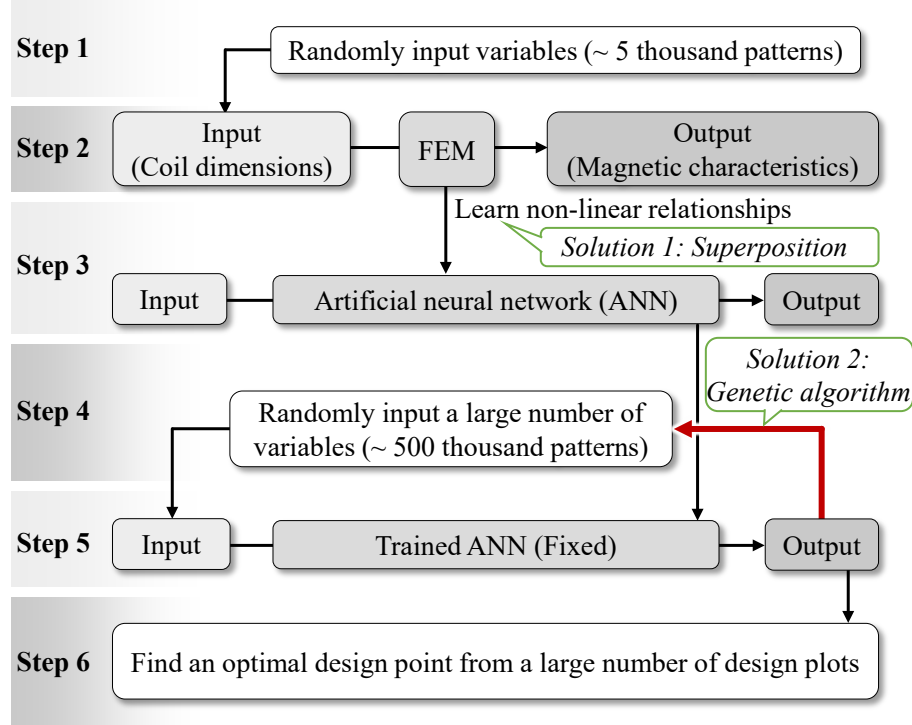


Fig. 5.3: The conventional design flow and proposed solutions

characteristics. In step 4, the design variables are input into the trained ANN that is fixed. In step 5, a large number of design points are output from the trained ANN. In step 6, the optimal design point that satisfies all design criteria is found from a large number of design points.

The design criteria selected in this paper are listed in Table 5.2. Although many more design criteria exist for an actual DIPT system, 12 parameters that mainly affect system characteristics are selected. The coil interval l_{interval} is represented as

$$l_{\text{interval}} = l_{\text{ty}} + 2w_{\text{ty}} + p. \quad (5.1)$$

If the coil interval is increased, the number of inverters and compensation circuits on the transmitter side can be reduced, hence the system cost can be reduced. However, longer coil tends to cause higher loss and higher stray fields.

Table 5.2: Design criteria of extraction process

No.	Description	Symbol	Design criteria
1	Coil interval	l_{interval}	$> 850 \text{ mm}$
2	Coil loss	P_{loss}	$< 150 \text{ W}$
3	Stray field	B_{stray}	$< 20 \mu\text{T}(\text{rms})$
4	Difference of coupling coefficient	k_{diff}	$< 50 \%$
5	Volume of transmitter core	-	$< 3500 \text{ cm}^3/\text{m}$
6	Average output power	P_{ave}	$> 2.5 \text{ kW/m}$
7	Volume of receiver core	-	$< 2500 \text{ cm}^3$
8	Ripple of output power	P_{ripple}	$< 40 \%$
9	Voltage of transmitter coil	V_{t}	$< 800 \text{ V}(\text{rms})$
10	Voltage of receiver coil	V_{r}	$< 800 \text{ V}(\text{rms})$
11	Current of transmitter coil	I_{t}	$< 60 \text{ A}(\text{rms})$
12	Current of receiver coil	I_{r}	$< 40 \text{ A}(\text{rms})$

The difference of coupling coefficient k_{diff} is defined as

$$k_{\text{diff}} = \frac{|k_{x_0,y_0} - k_{x_1,y_0}|}{\max\{|k_{x_0,y_0}|, |k_{x_1,y_0}|\}}. \quad (5.2)$$

where k_{x_0,y_0} and k_{x_1,y_0} are the coupling coefficients at (x_0, y_0) and (x_1, y_0) , respectively. A small k_{diff} improves the output power reduction in misalignment conditions in the lateral direction but requires larger transmitter coils.

The power ripple P_{ripple} is the difference between the maximum power and the minimum power when the receiver coil passes over the transmitter coils and is expressed by

$$P_{\text{ripple}} = \left(1 - \frac{P_{\text{dip}}}{P_{\text{peak}}}\right) \times 100 \text{ [\%]} \quad (5.3)$$

where P_{dip} is the lowest output power and P_{peak} is the peak output power. Reducing the power ripple can be expected to reduce the size of filters and compensation circuits on the receiver side. However, a small P_{ripple} tends to increase the size of the transmitter coil and decrease the length of the transmitter coil interval.

Reducing the transmitter and receiver coil's current and voltage is expected to reduce the costs of the Litz wire and the compensation circuits. However, low currents and voltages make it difficult to transmit high power.

5.2.2 Solution 1: Reduction of ANN training data collection time by superposition of magnetic fields

In solution 1, the ANN learns the stray magnetic field data with only the transmitter coil and with only the receiver coil separately. The turn numbers of the transmitter and receiver coils are a single turn, respectively. The currents that flow in the transmitter and receiver coils are unit currents. The trained ANN predicts the nonlinear characteristics of the stray magnetic field at an arbitrary current and an arbitrary number of turns using the superposition of magnetic fields. An FEM simulation model used to calculate stray magnetic fields is shown in Fig. 5.4. The SAE standard [48] is considered to design stray

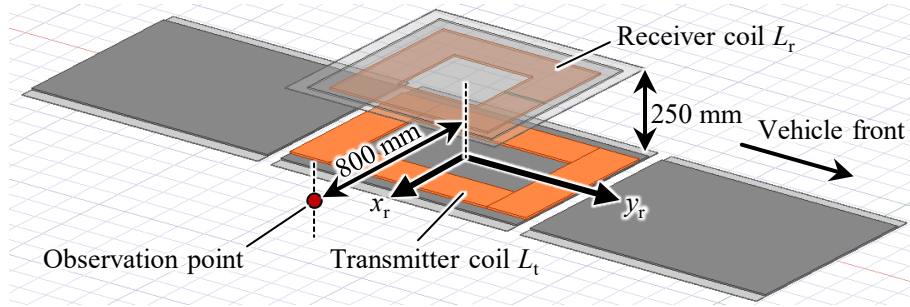


Fig. 5.4: 3-D FEM simulation model

magnetic fields with the assumption that the width of the vehicles is 1.6 m. A position 800 mm away from the center of the receiver coil in the horizontal direction is defined as the measurement point of the stray magnetic field. The height of the measurement point is half the vertical gap between the receiver and transmitter coils.

The calculation methods for stray magnetic fields are compared in Fig. 5.5. The conventional stray magnetic field calculation method is shown in Fig. 5.5(a). The conventional method calculates the total value of the stray magnetic field when an arbitrary current flows through an arbitrary number of turns of the transmitter and receiver coil. The proposed stray magnetic field calculation method is shown in Fig. 5.5(b). The stray magnetic field from the one-turn receiver coil when a unit current flows and the stray magnetic field from the one-turn transmitter coil when a unit current flows are calculated separately. The super-

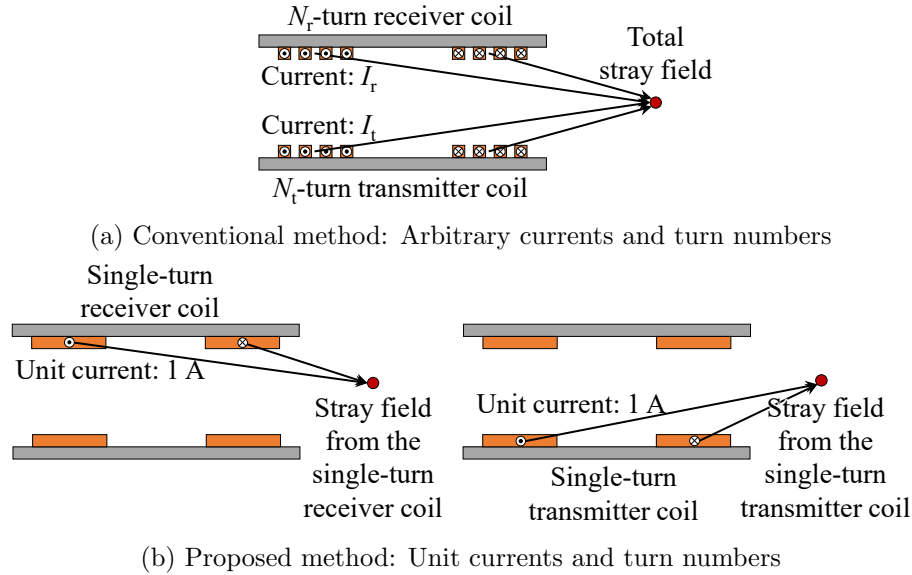


Fig. 5.5: Solution 1: Calculation method for stray fields

position of the magnetic fields can be used to calculate the total value of the stray magnetic fields for any number of turns and currents. Therefore, the ANN can predict the stray magnetic field at an arbitrary current and number of turns by learning the stray magnetic fields from the one-turn transmitter and receiver coils. Rather than calculating the stray magnetic field for any combination of turns and current by FEM, it is more time-efficient to train the ANN by using superposition after calculating the stray field of only the unit current and unit winding by FEM. Additionally, since stray magnetic fields are calculated with superposition, the currents can be calculated given whatever circuit topology is used and simultaneously can be optimized in the circuit to meet stray magnetic field limits as well as maximize efficiency. Typically, these two processes are done separately [91]. If it is assumed that three points of training data are required for one input variable, the proposed method can reduce the time required for data collection to about 1/40. A mid-range desktop personal computer (Intel Core i7- 9700K with 32 GB RAM) completes one FEM simulation in a minute. Therefore, the proposed method reduced the time required for data collection from about 40 months to about one month.

5.2.3 Solution 2: Genetic algorithm to improve the random input

Solution 2 uses a genetic algorithm (GA) to improve the random input variables to the ANN. The comparison between the conventional ANN-based method and the proposed ANN- and GA-based method is shown in Fig. 5.6. The conventional ANN-based method to

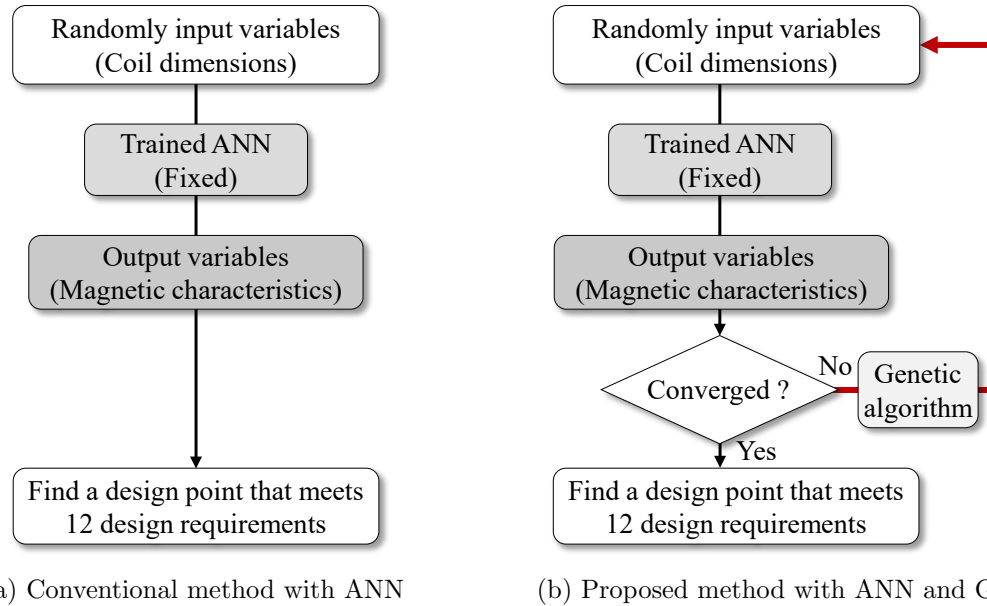


Fig. 5.6: Solution 2: Comparison between the conventional ANN-based method and the proposed ANN and GA-based method

output design points is shown in Fig. 5.6(a). The ten design variables are randomly input to the fixed trained ANN, and the magnetic characteristics are output from the ANN. Design points satisfying 12 design criteria are found from a large number of design points. This conventional method is challenging because many unnecessary design points are output from the random input values. The proposed method with the combination of ANN and GA is shown in Fig. 5.6(b). The GA improves the random input values to the ANN. By finding the input value area that can output appropriate design points, ANN can more effectively output design points that satisfy 12 design criteria.

5.3 Design optimization

In this section, a proposed algorithm combining ANN and GA is constructed, and an optimal design point is extracted by the algorithm.

5.3.1 Construction of ANN

The input variables are assumed as follows:

$$l_{tx}, l_{ty}, w_{tx}, w_{ty}, a_t, p, l_r, w_r, N_t, N_r. \quad (5.4)$$

The three-dimensional components of the magnetic fields due to the unit current from the transmitter coil and the three-dimensional components of the magnetic fields due to the unit current from the receiver coil are calculated separately by FEM. The magnetic fields are calculated in both cases with and without misalignment. In order to calculate the power transmission distribution of the coil, five measurement points are set along the vehicle traveling direction, and the magnetic parameters are calculated.

As the output of ANN, 90 magnetic parameters are assumed as follows:

$$\begin{aligned} \text{Output : } & L_{t,xi,yj}, L_{r,xi,yj}, k_{xi,yj}, \\ & \text{Re}(\mathbf{B}_{t,xi,yj}), \text{Im}(\mathbf{B}_{t,xi,yj}), \text{Re}(\mathbf{B}_{r,xi,yj}), \text{Im}(\mathbf{B}_{r,xi,yj}) \end{aligned} \quad (5.5)$$

where $L_{t,xi,yj}$ and $L_{r,xi,yj}$ are the self-inductance of the transmitter and receiver coils, and $k_{xi,yj}$ is the coupling coefficient between the transmitter and receiver coils. $[x_i, y_j]$ is represented by

$$[x_i, y_j] = [x_0, y_0], [x_0, y_1], [x_0, y_2], [x_0, y_3], [x_0, y_4], [x_1, y_0]. \quad (5.6)$$

$\text{Re}(\mathbf{B}_{t,xi,yj})$, $\text{Im}(\mathbf{B}_{t,xi,yj})$, $\text{Re}(\mathbf{B}_{r,xi,yj})$, and $\text{Im}(\mathbf{B}_{r,xi,yj})$ are three dimensional vector values and represented as follows:

$$\text{Re}(\mathbf{B}_{t,xi,yj}) = [\text{Re}(B_{x,t,xi,yj}), \text{Re}(B_{y,t,xi,yj}), \text{Re}(B_{z,t,xi,yj})] \quad (5.7)$$

$$\text{Im}(\mathbf{B}_{t,xi,yj}) = [\text{Im}(B_{x,t,xi,yj}), \text{Im}(B_{y,t,xi,yj}), \text{Im}(B_{z,t,xi,yj})] \quad (5.8)$$

$$\text{Re}(\mathbf{B}_{r,xi,yj}) = [\text{Re}(B_{x,r,xi,yj}), \text{Re}(B_{y,r,xi,yj}), \text{Re}(B_{z,r,xi,yj})] \quad (5.9)$$

$$\text{Im}(\mathbf{B}_{r,xi,yj}) = [\text{Im}(B_{x,r,xi,yj}), \text{Im}(B_{y,r,xi,yj}), \text{Im}(B_{z,r,xi,yj})] \quad (5.10)$$

$\text{Re}(\mathbf{B}_{t,xi,yi})$ and $\text{Im}(\mathbf{B}_{t,xi,yi})$ are the real and imaginary part of magnetic fields when the transmitter current I_t is 1 A(rms) and the receiver current I_r is 0 A(rms) in the receiver position $[x_i, y_i]$. $\text{Re}(\mathbf{B}_{r,x0,y0})$ and $\text{Im}(\mathbf{B}_{r,x0,y0})$ are the real and imaginary part of the magnetic field when I_t is 0 A(rms) and I_r is 1 A(rms) in the receiver position $[x_i, y_i]$. By splitting the magnetic field in this way, the magnetic field $B_{xi,yi}$ when the receiver position is $[x_i, y_i]$ can be obtained for any combination of current (I_t, I_r) as follows:

$$B_{xi,yi} = \{[\text{Re}(\mathbf{B}_{t,xi,yi})N_t I_t + \text{Re}(\mathbf{B}_{r,xi,yi})N_r I_r]^2 + [\text{Im}(\mathbf{B}_{t,xi,yi})N_t I_t + \text{Im}(\mathbf{B}_{r,xi,yi})N_r I_r]^2\}^{1/2} \quad (5.11)$$

where N_t and N_r are the number of turns in transmitter and receiver coils. When the magnetic field is split into real and imaginary components, and the x, y, and z components are also split, the magnetic fields for each component are proportional to the number of turns (N_t, N_r) and the currents (I_t, I_r) [94, 112, 116, 117]. Splitting stray fields is required to calculate the total stray fields since the phase angle between the transmitter and receiver currents is different by 90 degrees. The reflected magnetic fields from coil winding and aluminum plates must also be considered as stray fields with varying phase angles. The maximum value of the magnetic fields $B_{xi,yi}$ is defined as

$$B_{\text{stray}} = \max\{B_{xi,yi}\}. \quad (5.12)$$

It is assumed that the simulations run with even current distribution and that the Litz wire will approximately emulate this. Any mismatches between the ideal current distribution and an actual bundle of Litz wire are expected to be insignificant at the points where the stray fields are measured since they are far away from the Litz wires. Additionally, it is typical to design wireless charging systems to operate the magnetic cores in the linear region

and at reasonably low magnetic fields so that the losses are low.

It is necessary to obtain the magnetic characteristics when the receiver coil is placed at six different positions, with a unit current flowing only in the transmitter coil and a unit current flowing only in the receiver coil. Therefore, a total of 12 patterns of FEM simulation must be performed for one coil geometry.

The constructed ANN has eight nodes on the input layer and 90 nodes on the output layer. Since the ANN predicts the magnetic characteristics when the turn number of windings N_t and N_r are single winding, the input variables to the ANN are 8 out of 10 variables. Two hidden layers are used between the input and output layers, and each hidden layer has 100 nodes. By minimizing the loss function, weights between each node and the bias of each node are optimized. As the loss function, root mean square error (*RMSE*) is used, and the *RMSE* is defined by

$$RMSE = \sqrt{\sum_{i=1}^n (Y_i - \hat{Y}_i)^2}, \quad (5.13)$$

where n is the number of nodes on the output layer ($n = 90$), Y is the normalized output parameters of FEM, and \hat{Y} is the normalized predicted output parameters.

Nodes on each hidden layer have activation function σ . The type of activation function can be chosen according to the nonlinear model the user wants to fit. On the hidden layer one, the activation function at node one is represented as

$$\sigma(z_1^{(1)}) = \sigma(w_{11}^{(1)}x_1 + w_{21}^{(1)}x_2 + \dots + w_{m1}^{(1)}x_m) \quad (5.14)$$

where m is the number of input variables ($m = 8$), the activation function can be chosen from any nonlinear function such as the sigmoid function, hyperbolic tangent function, and arc tangent function. A comparison of activation functions is shown in Fig. 5.7. The sigmoid function maps the input values in the range (0, 1) as shown in Fig. 5.7(a). Therefore, it is mostly used for multi-class classification. The hyperbolic tangent function and arc tangent function provides an output that is zero-centered. Hence, large negative values

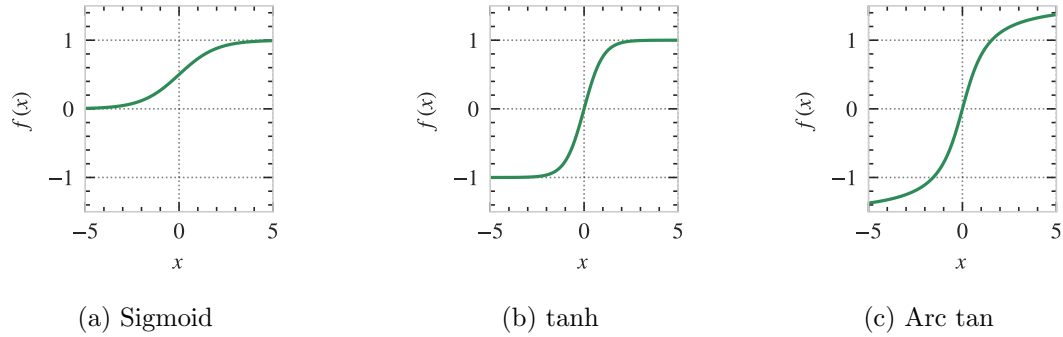


Fig. 5.7: Activation functions

are mapped to negative outputs [118] as shown in Fig. 5.7(b). The arc tangent function is slightly flatter than the hyperbolic tangent function, as shown in Fig. 5.7(c). Hence, it has a better tendency to differentiate between similar inputs [119]. This paper uses the arc tangent function as the activation function since the relationship between coil dimension and magnetic characteristics in DIPT systems tends to be moderate.

By minimizing the error between the output of the ANN and FEM data from the same input value in iteration calculation, weights between each node are optimized using the back-propagation algorithm [96,97]. The ANN can represent the nonlinear relationship because the hidden layers have nonlinear activation functions. If a linear function is used for the activation function, the fitting result is essentially the same as the linear regression.

In this paper, the double-sided LCC compensation network [81–83,98] is assumed for the IPT system. The circuit topology is shown in Fig. 5.8. The circuit makes the transmitter

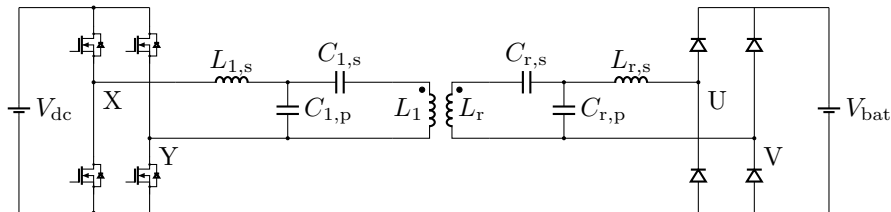


Fig. 5.8: IPT system with the double-sided LCC compensation network

coil current constant regardless of the coupling coefficient between the transmitter and receiver coils. For this reason, the LCC compensation network is appropriate for DIPT

systems since the coupling coefficient changes in a wide range. In addition, the compensation network is suitable for battery charging applications such as EV charging since the load on the receiver side is charged with a constant current.

The rms receiver current I_r is represented as

$$I_r = \frac{P_{\text{out},x0,y0}}{\omega I_t k_{x0,y0} \sqrt{L_{t,x0,y0} L_{r,x0,y0}}} \quad (5.15)$$

where I_t is the rms current of the transmitter coil, $P_{\text{out},x0,y0}$ is output power when the receiver coil is above the center of the transmitter coil, and ω is the angular switching frequency of the system. Therefore, output power when the receiver position is at y_r ($= y_1, \dots, y_4$) is calculated as

$$P_{\text{out},x0,yi} = \omega k_{x0,yi} I_t I_r \sqrt{L_{t,x0,yi} L_{r,x0,yi}} \quad (i = 1, 2, 3), \quad (5.16)$$

$$P_{\text{out},x0,y4} = 2\omega k_{x0,y4} I_t I_r \sqrt{L_{t,x0,y4} L_{r,x0,y4}}. \quad (5.17)$$

The output power $P_{\text{out},x0,y4}$ is doubled because the receiver coil is induced by the two primary coils when the receiver coil is at the edge of the primary coil [99]. Using (5.16) and (5.17), the average output power P_{ave} is calculated as

$$P_{\text{ave}} = (P_{\text{out},x0,y0} + 2P_{\text{out},x0,y1} + 2P_{\text{out},x0,y2} + 2P_{\text{out},x0,y3} + P_{\text{out},x0,y4})/8. \quad (5.18)$$

The approximated coil loss is calculated by

$$P_{\text{loss}} = \frac{\omega L_{t,x0,y0} I_t^2}{Q_{\text{coil},t}} + \frac{\omega L_{r,x0,y0} I_r^2}{Q_{\text{coil},r}} \quad (5.19)$$

where $Q_{\text{coil},t} = Q_{\text{coil},r} = 400$ is assumed as a general case of the coil quality factors. Once the input voltage V_{dc} , the output voltage V_{bat} , and the transmitter current I_t are determined,

the values of the compensation circuits are uniquely determined as

$$L_{1,s} = \frac{2\sqrt{2}V_{dc}}{\pi\omega I_t}, \quad (5.20)$$

$$C_{1,p} = \frac{\pi I_t}{2\sqrt{2}\omega V_{dc}}, \quad (5.21)$$

$$C_{1,s} = \frac{\pi I_t}{\omega(\pi\omega I_t L_{t,x0,y0} - 2\sqrt{2}V_{dc})}, \quad (5.22)$$

$$C_{r,s} = \frac{\pi P_{out,x0,y0}}{\omega^2(\pi L_{r,x0,y0} P_{out,x0,y0} - 2\sqrt{2}I_t V_{bat} M_{x0,y0})}, \quad (5.23)$$

$$C_{r,p} = \frac{\pi P_{out,x0,y0}}{2\sqrt{2}\omega^2 I_t V_{bat} M_{x0,y0}}, \quad (5.24)$$

$$L_{r,s} = \frac{2\sqrt{2}I_t V_{bat} M_{x0,y0}}{\pi P_{out,x0,y0}}, \quad (5.25)$$

where the mutual inductance $M_{x0,y0}$ is represented as

$$M_{x0,y0} = k_{x0,y0} \sqrt{L_{t,x0,y0} L_{r,x0,y0}}. \quad (5.26)$$

Additionally, the transmitter voltage V_t and the receiver voltage V_r are represented as

$$V_t = \sqrt{\omega^2 I_t^2 L_{t,x0,y0}^2 + \frac{P_{out,x0,y0}^2}{I_t^2}}, \quad (5.27)$$

$$V_r = \sqrt{\omega^2 M_{x0,y0}^2 I_t^2 + \frac{P_{out,x0,y0}^2 L_{r,x0,y0}^2}{I_t^2 M_{x0,y0}^2}}. \quad (5.28)$$

5.3.2 Fitting of ANN

The design specifications for the DIPT system are shown in TABLE 5.3. Input and output voltages and output power at the center of the primary side coil are defined as $V_{dc} = 100$ V, $V_{bat} = 100$ V, and $P_{out,x0,y0} = 3.3$ kW. Although the proposed algorithm can design systems with different V_{dc} and V_{bat} , the same voltages are used since an experimental system that recirculates power is planned. The low input and output voltage are used to

Table 5.3: Design specifications for the DIPT system

Description	Symbol	Value	Unit
Input dc voltage	V_{dc}	100	V
Output dc voltage	V_{bat}	100	V
Output power at the center	$P_{out,x0,y0}$	3.3	kW
Switching frequency	f_s	85	kHz
Air gap	g	250	mm
Transmitter current	I_t	20~100	A(rms)

simplify the prototype system's safety setup since the prototype's purpose is to compare the experimental results and ANN predictions. The transmitter current I_t is also swept in the range of 20 to 100 A(rms) to find the best driving point. The ANN is trained using the 4600 FEM data points for the training data. 100 FEM data points are used for the validation data. The ranges of the random geometric input values are defined in TABLE 5.1.

The graph of the root mean square of training error and validation error versus the number of iterative calculations when the number of the training data is 200 is shown as an example in Fig. 5.9. The training error means the difference between the predicted data

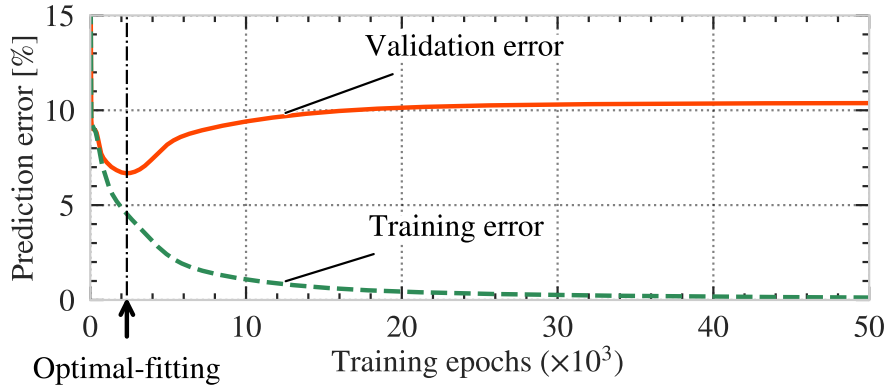


Fig. 5.9: Prediction error with respect to the number of iterative calculations

and training data used to fit the ANN. The validation error means the difference between the predicted data and new data, which is used to verify the accuracy of the trained neural network for new data. In Fig. 5.9, the verification error in the graph turns to increase after the dashed line, but the training error continues to decrease. This means that ANN

overfitting occurs in the region where the number of iterative calculations is greater than the dashed line [95]. In other words, the ANN only fits the training data accurately and cannot output accurate data when new data comes. In order to prevent overfitting, the iterative calculations are stopped at the point where the validation data is minimum, and the prediction error is defined as the accuracy of the ANN using this number of data.

The graph of the number of data versus prediction error is shown in Fig. 5.10. When

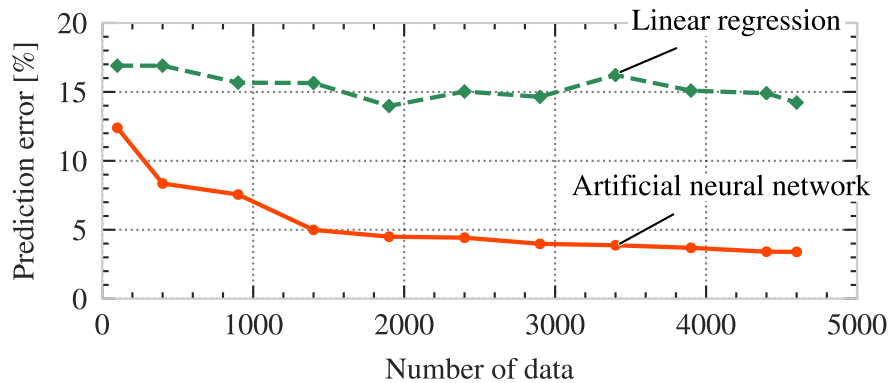


Fig. 5.10: Prediction error with respect to the number of training data

the number of data is 4700, the validation error of the ANN is less than 4%. This means that the trained ANN can predict magnetic characteristics from new coil dimensions within a 4% error.

5.3.3 Construction of GA

The algorithm flow of the constructed genetic algorithm is shown in Fig. 5.11. At each generation of the GA, the trained ANN is used to calculate each potential design solution's magnetic characteristics quickly. A random geometric design represented as a vector of 10 parameters is selected from the ranges defined in Table 5.1 and called an initial population. The size of the population is 5000. Magnetic characteristics are output through the fixed ANN from the initial population.

Design outputs are extracted to find an optimal solution based on the design criteria listed in Table 5.2. The design solutions that satisfy design criteria 1 and 2 are defined as

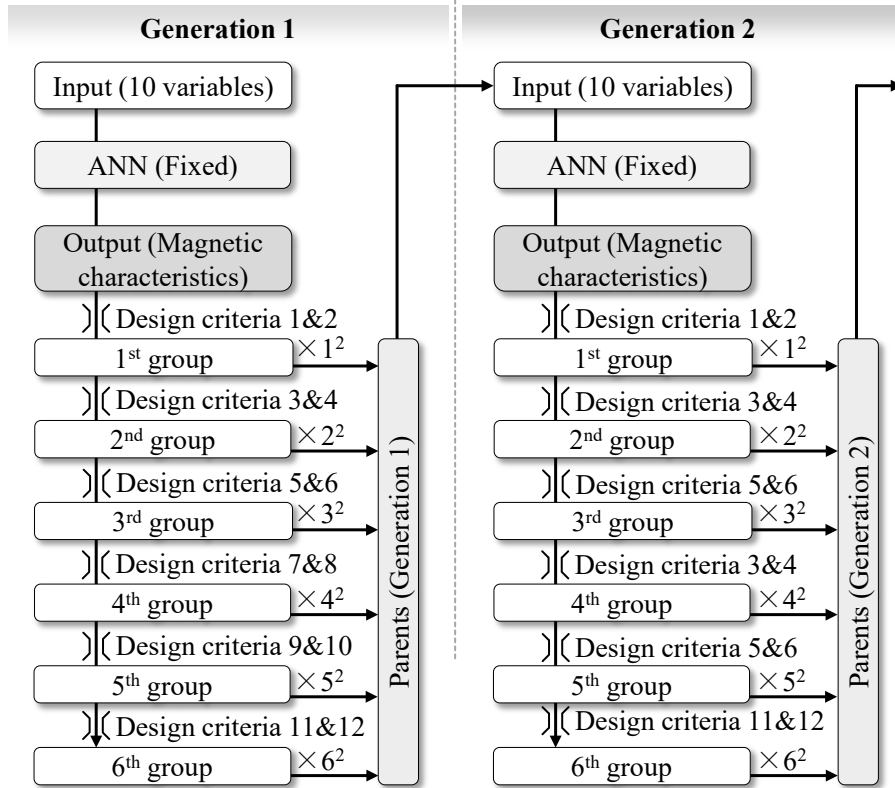


Fig. 5.11: Proposed flow of the genetic algorithm

the 1st group. The design solutions that satisfy the design criteria 3 and 4 out of the 1st group are defined as the 2nd group. In the same way, the 3rd group, 4th group, 5th group, and 6th group are defined. Hence, the 6th group satisfies all the design criteria from 1 to 12. The 5000 pairs of design points are selected from the 1st group to the 6th group, and the members of the selected subset are called parents. At the time, the incentives are applied for the probability of being selected as a parent from each group as follows: the members in the s -th group have s^2 times more probability.

The new set of geometry parameters is created through crossover and mutation from the selected parents [120, 121], and the members of the created subset are called children. The ratio of two parents-parameters out of ten variables is randomly determined using the 1-point crossover method [122]. As mutation elements, three out of ten variables of the coil geometry after the combination of parents parameters are randomly selected and changed randomly in the $\pm 30\%$. The created children become the input variables to the fixed ANN

in the next generation. The process is iterated until the number of design points in the 6th group converges. The number of design points extracted after 33 generations is 579 plots in this paper.

5.3.4 The extraction process of an optimized design point

The comparison of the obtained Pareto fronts by the conventional and proposed methods is shown in Fig. 5.12 and Fig. 5.13. Both scatter plots are output using the fixed ANN

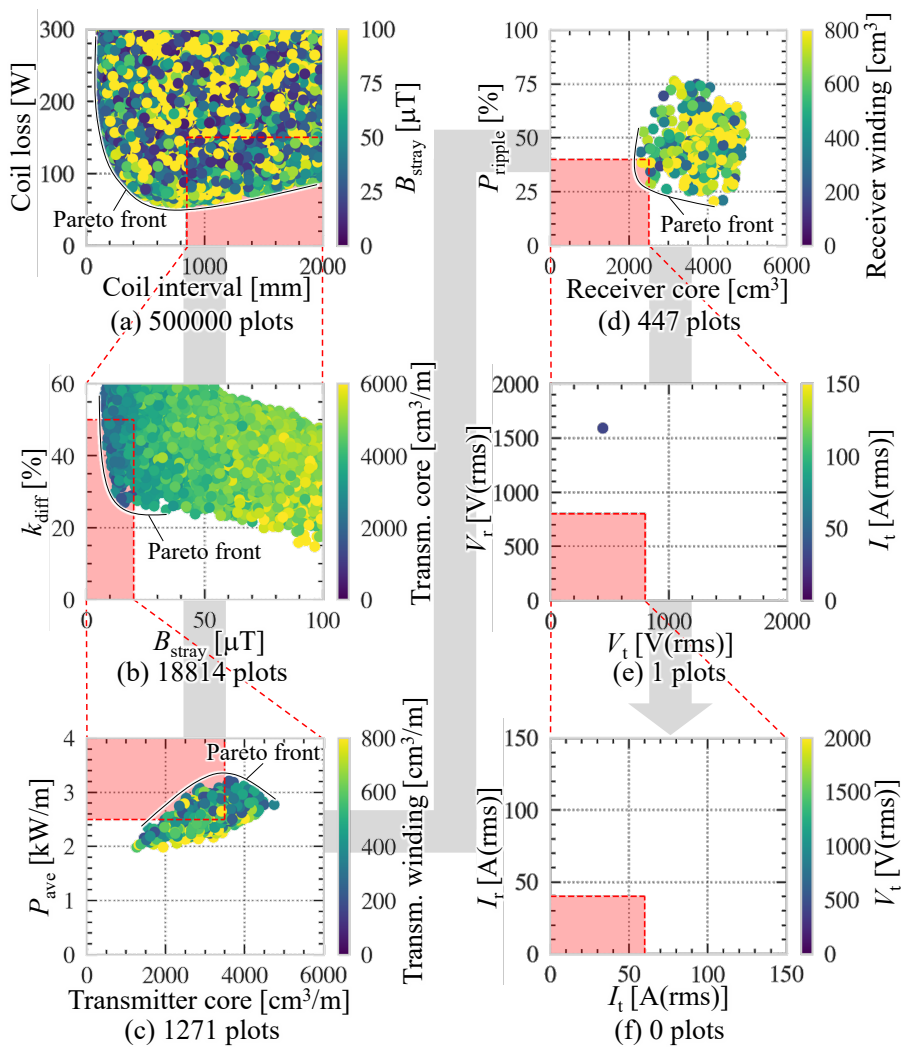


Fig. 5.12: Conventional: design extraction process without GA

trained on the data obtained using the method of superposition in Solution 1. Both algo-

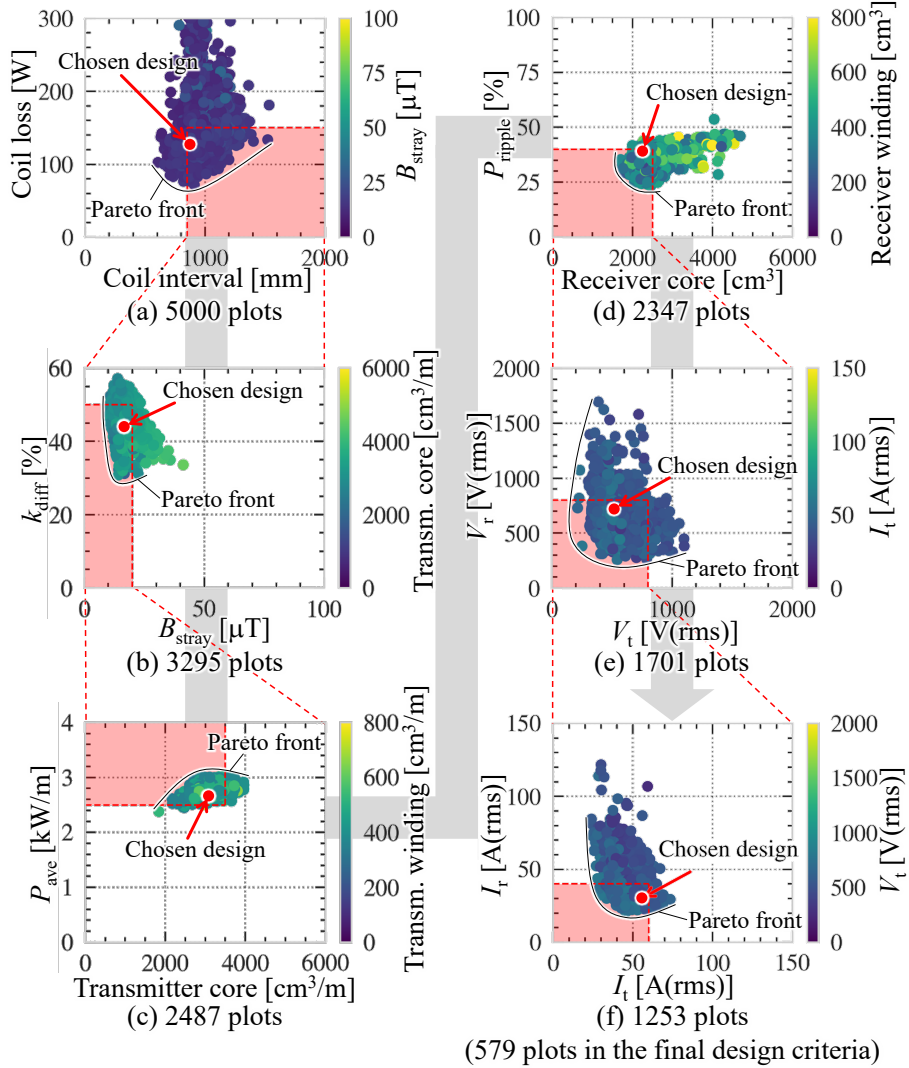


Fig. 5.13: Proposed: design extraction process with GA

algorithms finished plotting in about ten minutes using a mid-range desktop personal computer (Intel Core i7- 9700K with 32 GB RAM). The design results of the conventional method are shown in Fig. 5.12. In the conventional method, 500000 random design values are input. There was no design point in the final design criteria. Hence, the optimum design point could not be found since the Pareto front could not be obtained in the last two planes, as shown in Fig. 5.12(e) and (f). The result of the proposed method after 33 generations is shown in Fig. 5.13. The proposed method outputs 579 points of data for the final design criteria and finds Pareto fronts for all planes to choose an optimal design point since GA

improves the input parameter space instead of the purely random input. Hence, the proposed method using ANN and GA was able to find the optimum design point that could not be found by the conventional method. The design point that the red arrows indicate in Fig. 5.13 is chosen as the optimized design point. A design point with good performance in all aspects was manually selected based on all the Pareto fronts of Fig. 5.13 in an iterative process when the indicated design point was chosen. For this reason, the selected design point in the Pareto planes is located close to but not precisely on the Pareto fronts. For systematically identifying an optimal design, calculating the distance between the design points and each Pareto front on a standardized surface and balancing the distance on each plane could be one of the approaches. The simulation and experimental results of the design are shown in the following sections.

5.4 Verification in FEM and circuit simulation

In this section, the errors between the predicted value and the calculated value are evaluated using FEM and a circuit simulator in order to verify the accuracy of the ANN prediction values. The overview of the optimized coils is shown in Fig. 5.14. Input values

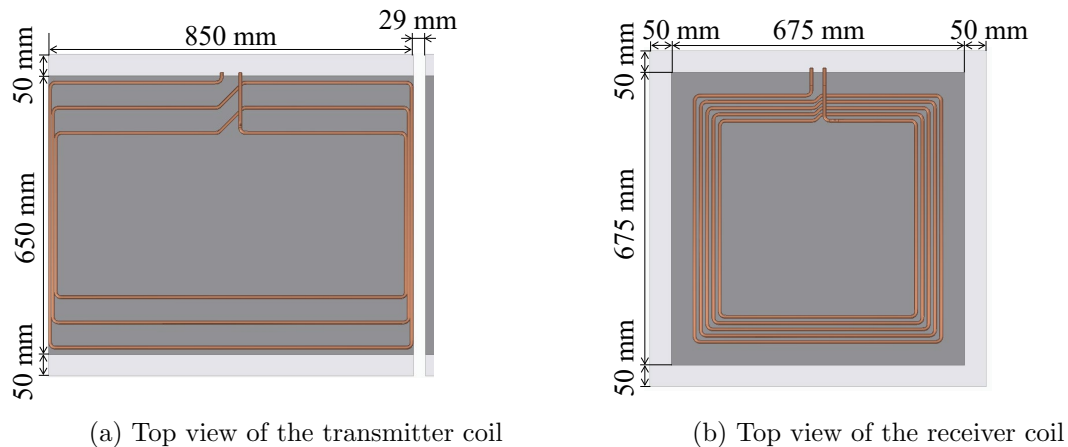


Fig. 5.14: Dimension of the DIPT system designed by the proposed method

after the design optimization are shown in Table 5.4. The turn number of the transmitter and receiver coils are 3 and 5. The distance between adjacent coils is 29.2 mm, the coil

Table 5.4: Geometry parameters of the optimized coils

Parameter	Value	Unit
l_{tx}	376.5	mm
l_{ty}	810.4	mm
w_{tx}	124.0	mm
w_{ty}	19.8	mm
a_t	12.8	mm
p	29.2	mm
l_r	445.8	mm
w_r	64.5	mm
N_t	3	turns
N_r	5	turns

interval is 879.2 mm, the receiver coil volume is 2277.2 cm³, and the core volume of the transmitter coils per meter is 3142.1 cm³/m.

The graph of the coupling coefficient between the transmitter coils and the receiver coil with respect to the receiver position is shown in Fig. 5.15. The dashed lines are the

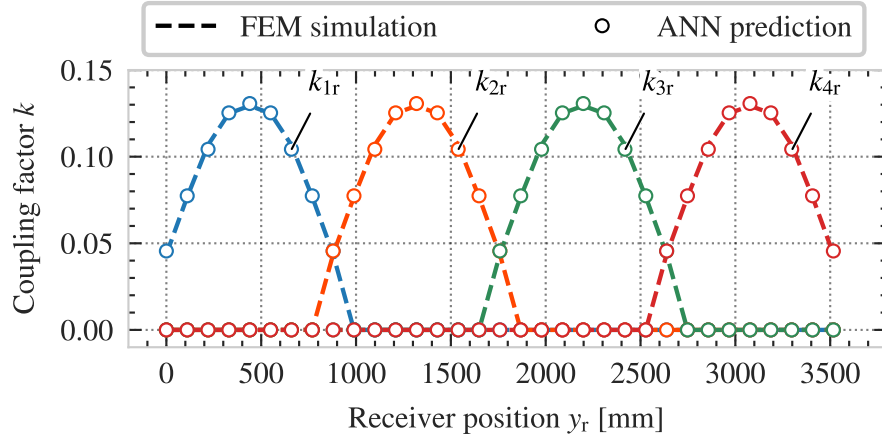


Fig. 5.15: Comparison between the ANN prediction and FEM results

FEM simulation result, and the markers are the predicted values of the ANN. The predicted values of ANN are generated using the symmetry and repeatability of the transmitter coil using the ANN predictions of magnetic coupling coefficients from y_0 to y_4 . The ANN can predict the FEM result of the coupling coefficient with a 1% error or less error in the entire

region where the transmitter coil moves. The comparison between the ANN predictions and FEM, including other magnetic characteristics, is shown in Table 5.5. Self-inductance,

Table 5.5: Comparison between the ANN prediction and FEM results

Description	Symbol	Prediction	FEM	Error [%]
Self-inductance of the transmitter coil	L_t	17.31 μH	17.23 μH	0.5
Self-inductance of the receiver coil	L_r	43.68 μH	43.15 μH	1.2
Peak coupling coefficient between transmitter and receiver	$k_{t,r}$	0.1307	0.1294	1.0
Difference of coupling coefficient	k_{diff}	44.4%	47.3%	6.1
Stray field	B_{stray}	17.4 $\mu\text{T}(\text{rms})$	18.7 $\mu\text{T}(\text{rms})$	7.0

the coupling coefficient, and the stray magnetic field are all predicted with an error of 7% or less.

A comparison between ANN predictions and circuit simulation results is shown in Table 5.6. Matlab Simulink and PLECS are used for the circuit simulation. The output

Table 5.6: Comparison between ANN prediction versus circuit simulation results

Description	Symbol	ANN prediction	Circuit simulation	Error [%]
Input power	P_{in}	3300.0 W	3396.9 W	2.9
Output power	P_{out}	3300.0 W	2994.4 W	10.2
Ripple of output power	P_{ripple}	40.0%	39.9%	0.3
Average output power	P_{ave}	2652.8 W	2563.5 W	3.5
Coil loss	-	128.0 W	129.7 W	1.3
Transmitter coil voltage	V_t	526.4 V(rms)	523.7 V(rms)	0.5
Receiver coil voltage	V_r	717.1 V(rms)	767.3 V(rms)	6.5
Transmitter coil current	I_t	56.6 A(rms)	55.3 A(rms)	2.4
Receiver coil current	I_r	30.4 A(rms)	31.8 A(rms)	4.5

power is fixed at 3300 W in the ANN algorithm. Since the constructed ANN algorithm considers only the coil loss and not the total loss, the output power is the same as the input power. It was confirmed that coil loss, voltage, and current could be predicted with an error of 10% or less.

The simulation result of the output power with respect to the receiver coil position is

shown in Fig. 5.16. The ANN can predict the circuit simulator results of output power with

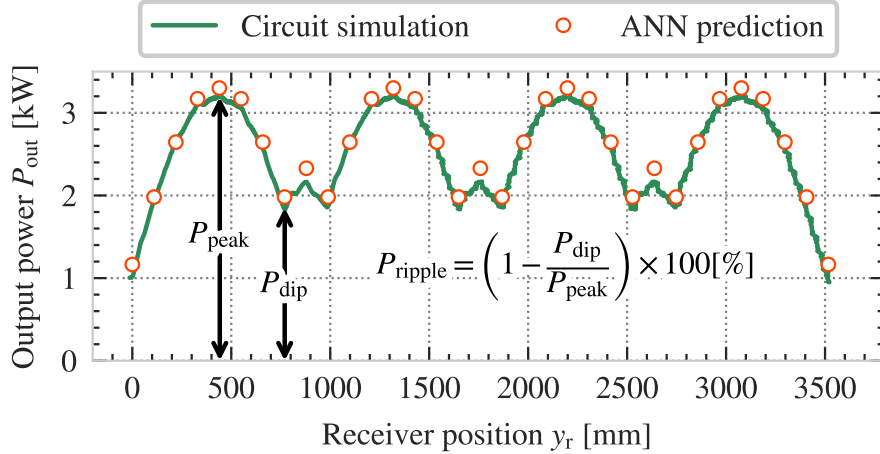


Fig. 5.16: Comparison between the ANN prediction and the circuit simulation result

reasonable accuracy over the entire moving range of the receiver coil position. The error of the power ripple is 0.3%, and the error of the average power is 3.5%.

5.5 Experimental results

In this section, the accuracy of the prediction values of the ANN is evaluated using an experimental prototype system.

5.5.1 Prototype system

The prototype coils are shown in Fig. 5.17. The transmitter and receiver coils are shown in Fig. 5.17 (a) and (b), respectively. High-density polyethylene (HDPE) sheets were used for the coil formers to make the designed coils precisely. A side view of the prototype coils is shown in Fig. 5.17(c). The ferrite cores, Litz-wires, and coil formers are stacked in this order on a 2 mm aluminum plate. MnZn ferrite core (PC95, TDK) with 5 mm thickness is used for wireless coils. All wireless coils and inductors were made from 2325-strand AWG 38 Litz-wire. A general-purpose full-bridge inverter is used on the primary side to provide the ac excitation. It contains two silicon carbide (SiC) half-

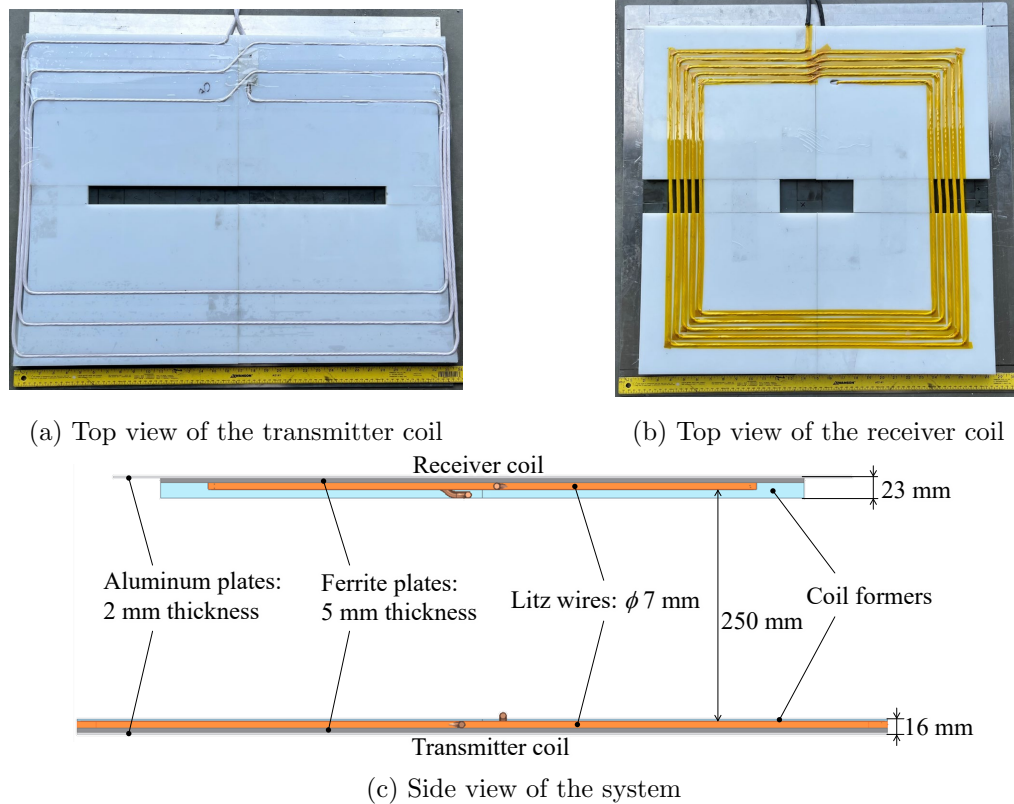


Fig. 5.17: Overview of the constructed coils

bridge MOSFET modules (CAS325M12HM2) with a rating voltage of 1.2 kV. The same SiC MOSFET modules are used for the diode rectifier.

A rail system is constructed to measure the average power and power ripple when the receiving coil moves at a constant speed. The constructed rail system is shown in Fig. 5.18. The receiver coil is mounted on the cart and can be moved at a constant speed by belts mounted on the rails and the electric motor. The cart can move at a maximum speed of 10 km/h and has a maximum payload of 200 kg. In order to accurately measure the stray magnetic field, glass fiber was used for the frame material of the base of the rail.

5.5.2 Measurement methods

A DWPT system that has an individual inverter for each transmitter coil is assumed in this paper. Therefore, efficiency and stray field measurements have been conducted with a single inverter and a single transmitter coil. The circuit configuration used in the

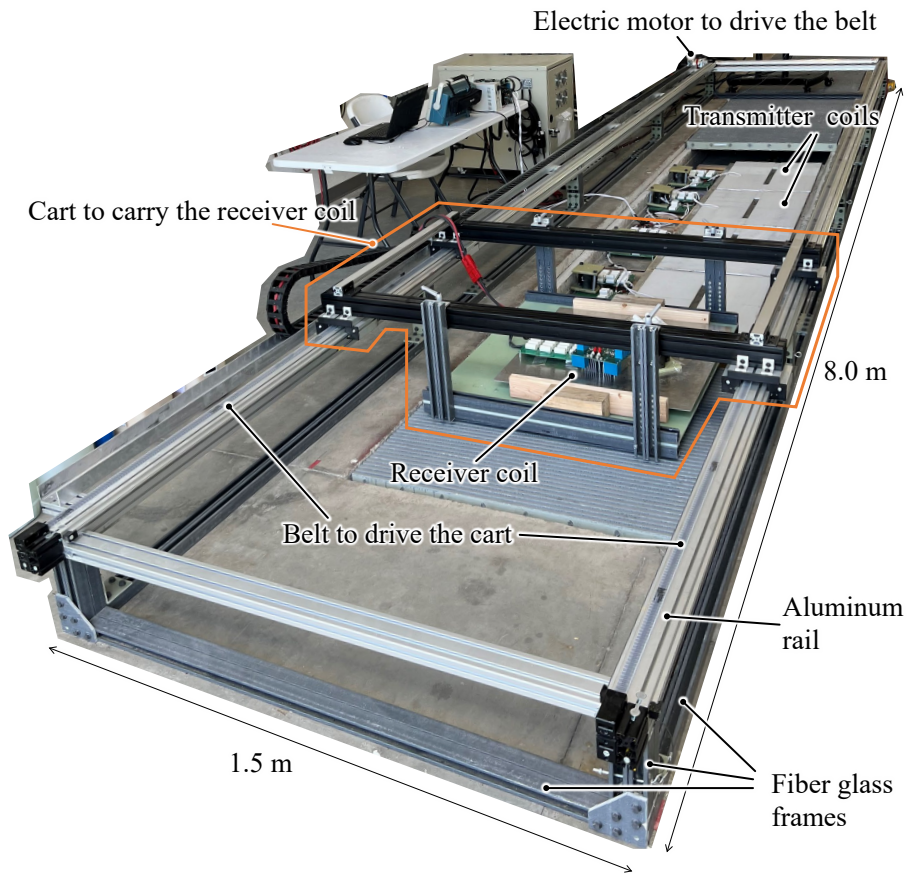


Fig. 5.18: Automated rail system

experiment is shown in Fig. 5.19. The power feedback via a dc wire allows the circulating

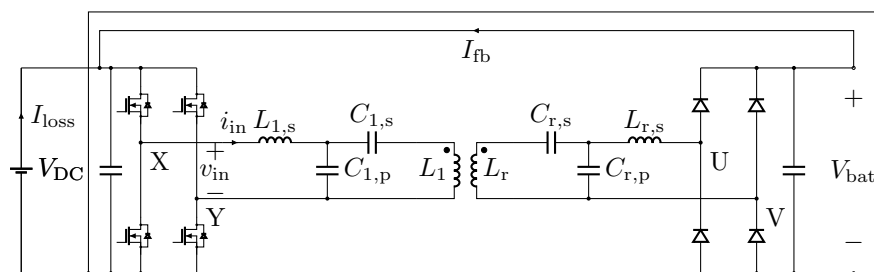


Fig. 5.19: Schematic diagram for efficiency and stray field measurements

of the transferred power within the system instead of dissipating the power in a resistive load. While the transferred power is circulated, total losses are drawn from the external

dc supply. Therefore, the dc current I_{loss} and the dc supply voltage V_{dc} can be measured to calculate the total power losses. The transferred power is calculated using the measured feedback current I_{fb} . The values for the compensation components are listed in Table 5.7.

Table 5.7: Values of the compensation components

Description	Symbol	Values	Unit
Series inductor	$L_{1,s}$	2.98	μH
Parallel capacitor	$C_{1,p}$	1.18	μF
Series capacitor	$C_{1,s}$	246	nF
Series capacitor	$C_{r,s}$	93	nF
Parallel capacitor	$C_{r,p}$	644	nF
Series inductor	$L_{r,s}$	5.4	μH

The measurement method of the strength of the stray magnetic fields is shown in Fig. 5.20. The magnetic field is measured at 800 mm away from the center of the receiver

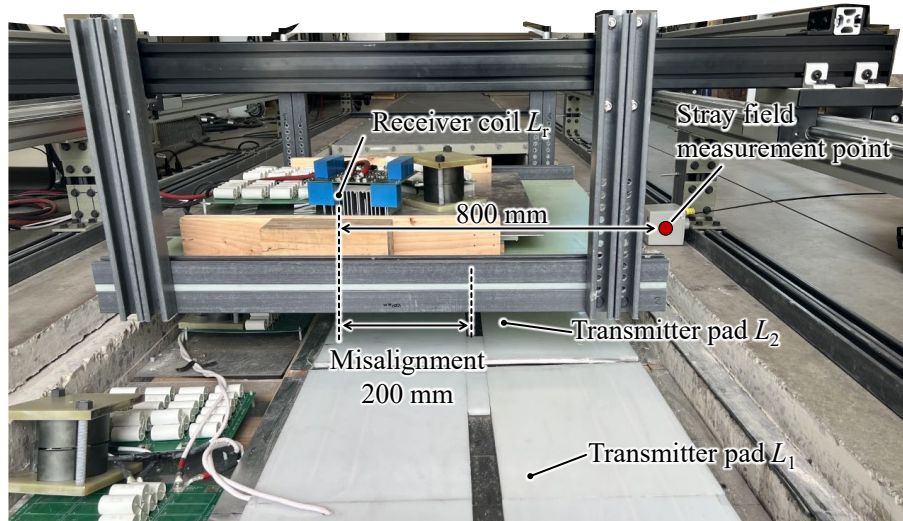


Fig. 5.20: Measurement method of stray fields

coil when there is a lateral misalignment of 200 mm between the receiver and the transmitter coil. The measurement height is the middle point between the transmitter and receiver coil.

The schematic diagram for power ripple and average output power is shown in Fig. 5.21. In order to simplify the measurement of average output power and power ripple, a parallel

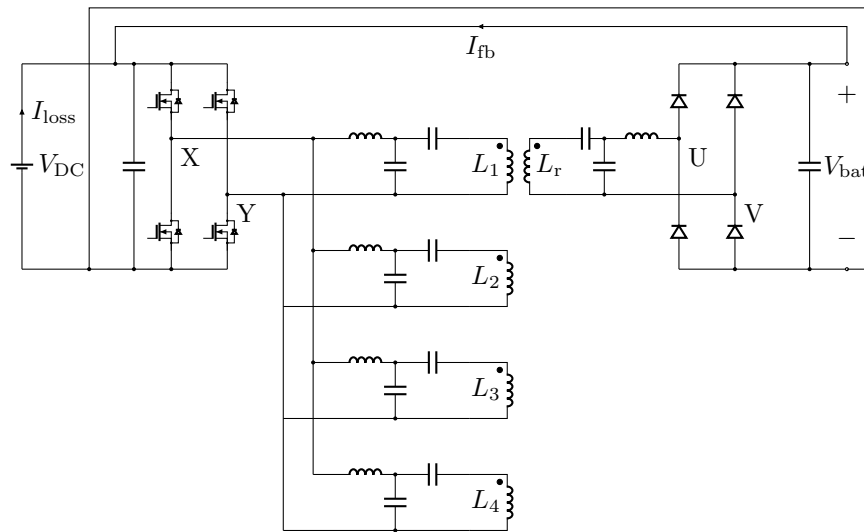


Fig. 5.21: Schematic diagram for power ripple and average output power measurements

connection of the four transmitter coils to one inverter is used instead of attaching an individual inverter for each transmitter coil.

The top view of the constructed experimental system is shown in Fig. 5.22. The receiver coil is moved from coil 1 to 4 at a speed of 6 km/h.

5.5.3 Experimental results

The voltage and current waveforms of the prototype system when the output power is 3 kW with a single transmitter coil are shown in Fig. 5.23.

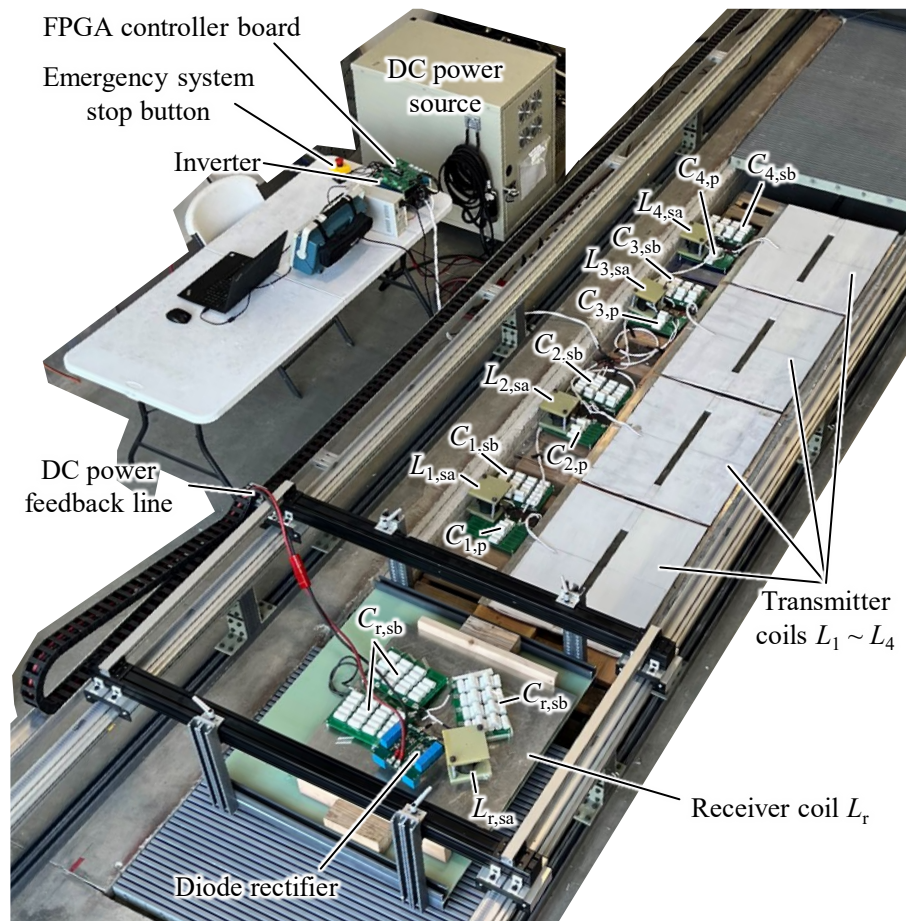
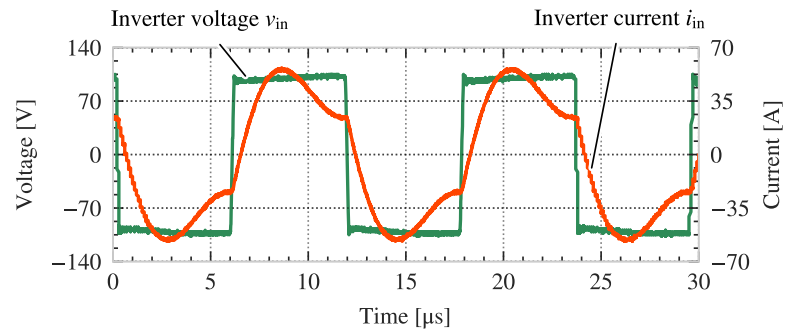
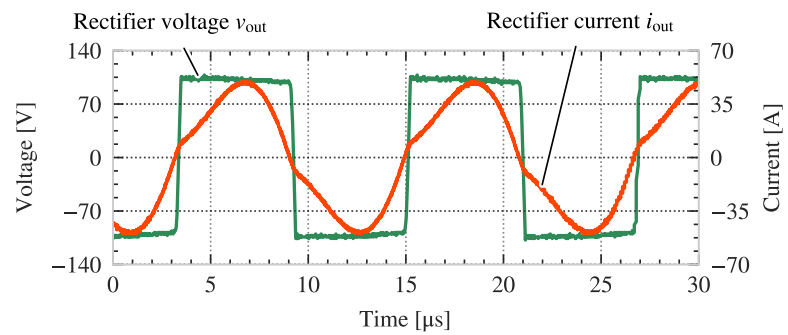


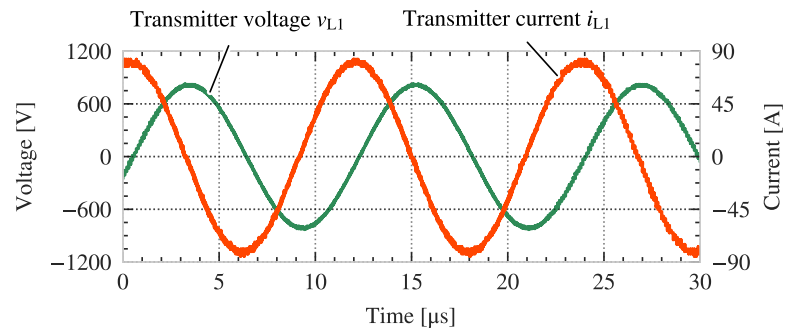
Fig. 5.22: Top view of the experimental system



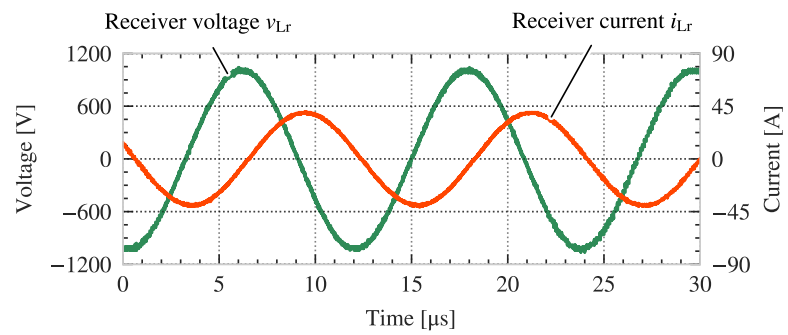
(a) Inverter



(b) Rectifier



(c) Transmitter



(d) Receiver

Fig. 5.23: Voltage and current waveforms at $P_{out} = 3$ kW

The inverter's voltage and current waveforms are shown in Fig. 5.23(a). The load is inductive since the inverter current is positive when the inverter voltage changes from positive to negative. The diode rectifier's voltage and current waveforms are shown in Fig. 5.23(b). The diode is switched according to the positive and negative current, and the rectifier voltage is inverted. The voltage and current waveforms of the transmitter and receiver coil are shown in Fig. 5.23(c) and (d), respectively. The measured transmitter and receiver current have been 56.6 A(rms) and 28.9 A(rms) and matched with an accuracy of 5.4% or less.

The measurement result of the stray magnetic fields is shown in Fig. 5.24. The solid line

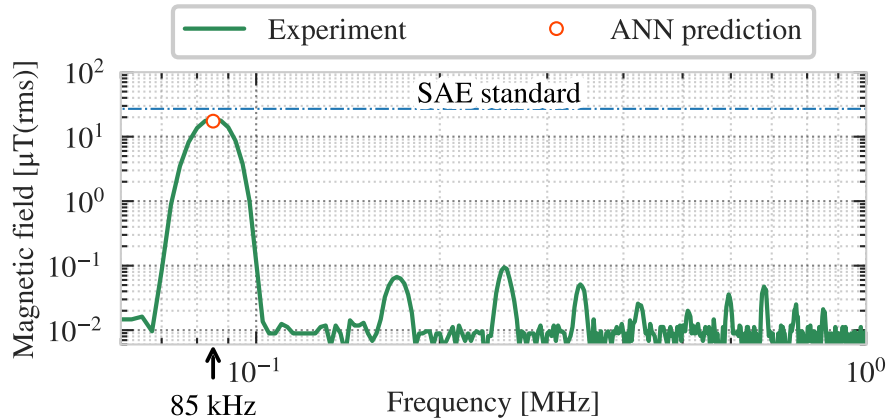


Fig. 5.24: Measured stray magnetic field

is the experimental value, and the marker is the predicted value of ANN. The stray magnetic field reached a maximum value of $19.0 \mu\text{T(rms)}$ at 85 kHz. The ANN predicted value of $17.4 \mu\text{T(rms)}$ matched the experimental value with an error of 8.4%. In all frequency bands, the stray magnetic field was below the SAE standard value of $27 \mu\text{T(rms)}$.

Power ripple measurement results are shown in Fig. 5.25. The solid line is the experimental value, and the markers are the predicted values of ANN. The measured power ripple was 35.5%. The error was 12.7% compared to the ANN prediction value of 40.0%. There are two reasons why the experimental value is smaller than the ANN predicted value. First, the peak value becomes smaller in the experimental value than the predicted value since the

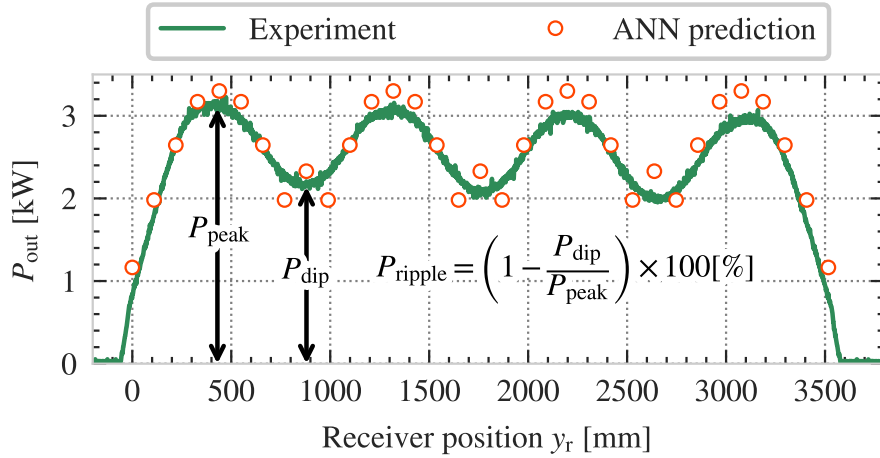


Fig. 5.25: Measured output power with respect to the receiver position (Moving speed: 6 km/h)

ANN predicted value does not consider the circuit loss in the output power value. Second, the experimental value has a smoother power distribution since the coupling coefficient between the adjacent transmitter coils is not considered in the ANN prediction. In order to predict the power ripple with higher accuracy, it is necessary to consider the circuit loss and the coupling coefficient between the transmitter coils.

A list of comparisons between ANN prediction and experimental values is shown in Table. 5.8. All items except coil loss are within 12.7% error. The reason why the power ripple error is relatively large is as described above. The coil loss error is large because the coil quality factor Q is different. In the ANN prediction value, 400 was used as a constant for the coil quality factor. However, in the experimental values, the quality factors of the transmitter coils and receiver coil were 242.7 and 319.6, respectively. For this reason, the experimental value is much larger than the predicted value of ANN. The prediction error of the coil loss causes a 1.7% error in the dc-dc efficiency of the system. If the 1-2% error of the dc-dc efficiency is acceptable, the proposed method can be utilized with accurately predicted power transfer capability, coupling coefficient, stray field, maximum current, and voltage value. Suppose a higher prediction accuracy of dc-dc efficiency is required. In that case, the proposed method can iterate the optimization using calculated coil quality

Table 5.8: Comparison between ANN prediction versus experimental results

Description	Symbol	ANN prediction	Experiment	Error [%]
Self-inductance of the transmitter coil	L_t	17.31 μH	17.23 μH	0.5
Self-inductance of the receiver coil	L_r	43.68 μH	43.15 μH	1.2
Coupling coefficient	$k_{t,r}$	0.1307	0.1294	1.0
Difference of coupling coefficient	k_{diff}	44.4	47.3	6.1
Input power	P_{in}	3300.0 W	3470.0 W	4.9
Output power	P_{out}	3300.0 W	3039.3 W	8.6
Ripple of output power	P_{ripple}	40.0%	35.3%	12.7
Average output power	P_{ave}	2652.8 W	2572.7 W	3.1
Coil loss	-	128.0 W	182.6 W	29.9
Transmitter coil current	I_t	56.6 A(rms)	56.6 A(rms)	0.1
Receiver coil current	I_r	30.4 A(rms)	28.9 A(rms)	5.4
Transmitter coil voltage	V_t	526 V(rms)	573.2 V(rms)	8.2
Receiver coil voltage	V_r	717.1 V(rms)	693.4 V(rms)	3.5
Stray field	B_{stray}	17.4 μT (rms)	19.0 μT (rms)	8.4

factors from the previous iteration since the accurate coil quality factors can be calculated by acquiring the magnetic field on the Litz wire and ferrite core surface [117, 123]. The error of the coil loss is improved from 29.9% to 3.8% if the accurate coil quality factors are used for transmitter and receiver coils.

5.6 Conclusion

This chapter proposes an optimal design method combining ANN and GA for the design optimization of DIPT systems. The proposed algorithm uses the superposition of calculated stray magnetic fields to collect training data for ANN. As a result, the data collection time has been decreased from about 40 months to one month. In addition, the proposed algorithm uses a GA-based input value improvement method so that the trained ANN can efficiently output design points that satisfy many design criteria simultaneously. The conventional approach could not find any optimal design; however, the proposed method found 579 points. Design results predicted by the ANN have been compared with FEM simulation, circuit simulation, and experimental results to verify the validity of the proposed algorithm. The FEM and circuit simulation results and the ANN prediction results match with errors

of 10.2% or less for all design criteria. As for the comparison between ANN prediction and experimental values, the values except for the coil loss match each other with an error of less than 12.7%. If a higher prediction accuracy of coil loss is required, the proposed method can be modified to include calculating and optimizing the coil quality factors.

CHAPTER 6

High-power reflexive tuning DIPT system optimization

This chapter demonstrates the integration of the proposed reflexive tuning circuit and ANN- and GA-based design optimization method for 50 kW DIPT system design. Design optimization and simulation are conducted for the proposed and conventional circuits to verify the limitation of both circuits. The simulation results show that the maximum output power of the proposed circuit is higher than the conventional circuit by 44%. A 50 kW prototype is designed and demonstrated on both automated rail and vehicle systems.

6.1 Design of a 50 kW reflexive tuning system

The proposed circuit is designed and simulated on a circuit simulator to verify the validity of the design results.

6.1.1 ANN- and GA-based design optimization

The developed ANN- and GA-based design optimization in the previous chapter are applied to the 50 kW reflexive tuning circuit design. Coil geometry and circuit design parameters (c_1 , c_2 , c_3) are included in the optimization program. The design output result of the proposed method after 90 generations of GA is shown in Fig. 6.1. The algorithm finds Pareto fronts for all planes to choose an optimal design point. The design point that the red arrows indicate in Fig. 6.1 is chosen as the optimized design point. A design point with good performance in all aspects was manually selected based on all the Pareto fronts of Fig. 6.1 in an iterative process when the indicated design point was chosen.

6.1.2 Design comparison of the proposed and conventional reflexive tuning circuits

The conventional reflexive tuning circuit is also designed to compare the performance of

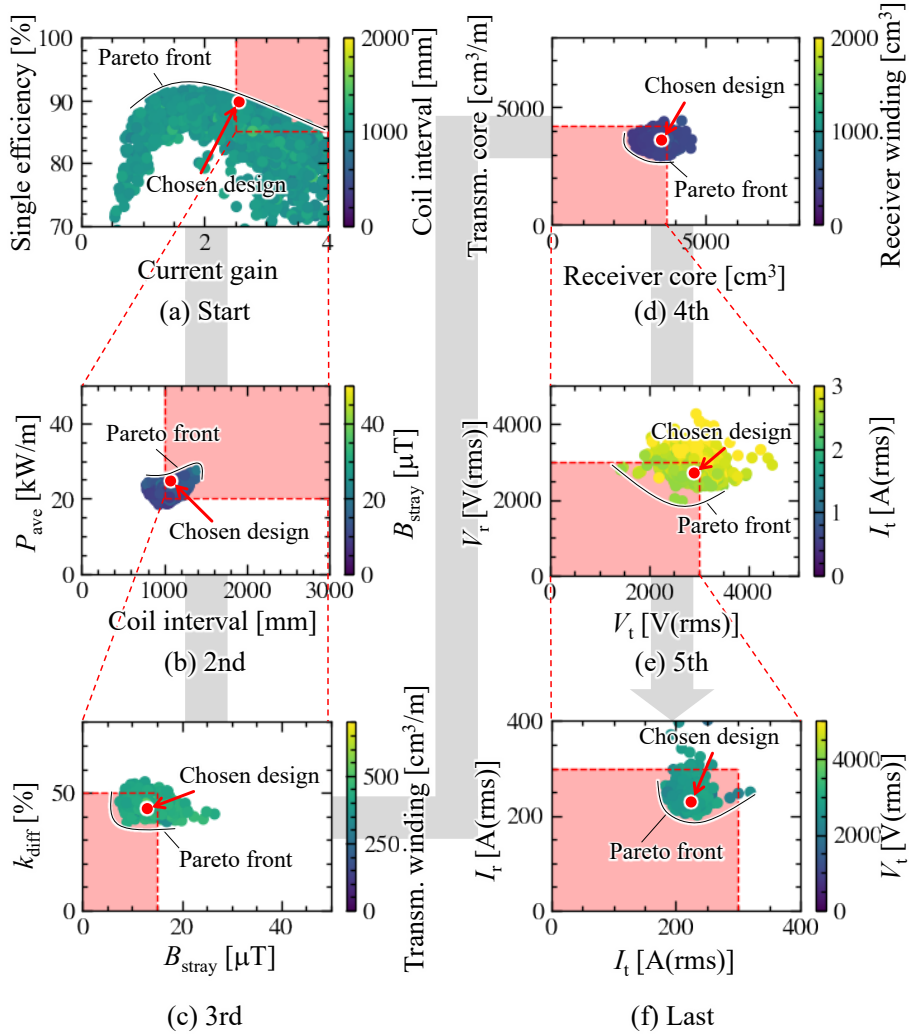


Fig. 6.1: Design output result after 90 generations of GA

the proposed reflexive tuning circuit. The shared design parameters between the proposed and conventional circuits are shown in TABLE 6.1. The input voltage V_{dc} and output voltage V_{bat} are set at 400 V. The common inverter's switching frequency is 85 kHz to follow the SAE standard [48]. The coupling coefficient between the transmitter and receiver coils $k_{1,r}$ varies from 0 to 0.22, according to the position of the receiver coil, due to longitudinal misalignment. The range of coupling factor $k_{1,r}$ was extracted from Maxwell simulations.

Table 6.1: Shared design parameters between the proposed and conventional circuits

Description	Symbol	Value	Unit
Input voltage	V_{dc}	400	V
Output voltage	V_{bat}	400	V
Air gap	z_{gap}	223	mm
Switching frequency	f_{sw}	85	kHz
Coupling coefficient between L_1 & L_r	$k_{1,r}$	0.00~0.22	-
Transmitter coil inductance	L_1	24.38	μH
Receiver coil inductance	L_r	21.94	μH
Filter inductor	L_f	5.31	μH
Filter capacitor	C_f	0.66	μF
Output dc inductor	L_{dc}	15.00	μH
Quality factor of wireless coils and inductors	Q_L	400	-
Quality factor of capacitors	Q_C	800	-
Turn number of turns of the transmitter coils	N_{L1}	4	turn
Number of turns of the receiver coil	N_{Lr}	4	turn

The quality factors of coils and capacitors Q_L and Q_C are defined as

$$Q_L = \frac{\omega L}{r_L} \quad \text{and} \quad Q_C = \frac{1}{\omega C r_C} \quad (6.1)$$

where r_L and r_C are the equivalent series resistance of L and C , respectively.

The designed parameters of the proposed and the conventional circuit are shown in TABLE 6.2. Circuits were designed so that the amplitude of the uncoupled transmitter

Table 6.2: Separately design parameters for the proposed and conventional circuits

Description	Symbol	Proposed	Conventional	Unit
Ratio	c_1	1.19	1.00	-
Ratio	c_2	3.10	3.50	-
Ratio	c_3	1.36	1.00	-
Series capacitor	$C_{1,sa}$	2.33	-	μF
Series capacitor	$C_{1,s}$	212 nF	210	nF
Parallel capacitor	$C_{1,p}$	446 nF	456	μF
Series capacitor	$C_{r,sa}$	1.38	-	μF
Series capacitor	$C_{r,s}$	235 nF	223	nF
Parallel capacitor	$C_{r,p}$	494 nF	557	nF
Limit of $k_{1,r}$	k_{lim}	0.25	0.30	-

current $i_{L1}|_{k_{1,r}=0}$ is 121 A in both cases. c_1 and c_3 are set to 1 in the conventional circuit since the conventional circuit does not have $C_{1,sa}$ and $C_{r,sa}$.

6.1.3 Circuit simulation of transmitter current and output power

A FEM simulation model to simulate the proposed tuning topology is shown in Fig. 6.2. Self-inductances L_1 , L_r and coupling coefficient $k_{1,r}$ are calculated to use the values in circuit

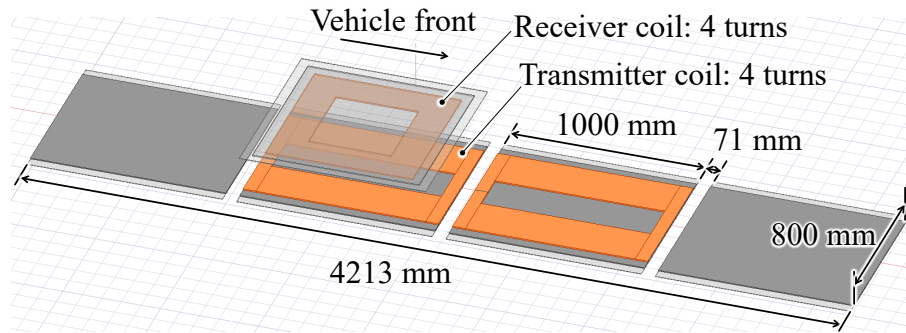


Fig. 6.2: Maxwell simulation model

simulations. The transmitter and receiver coil have four turn windings, and the length and width of the transmitter coil are 1000 mm and 800 mm, respectively.

The circuit diagram used in the LTspice simulation is shown in Fig. 6.3. The designed

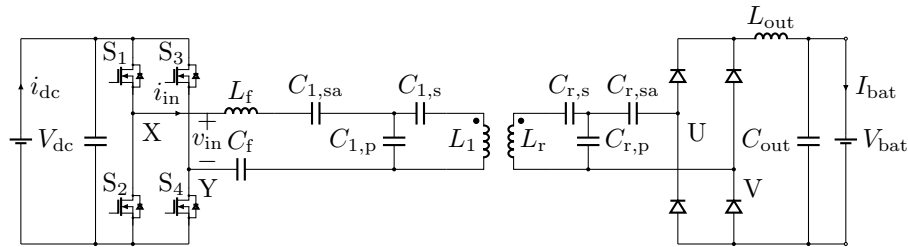
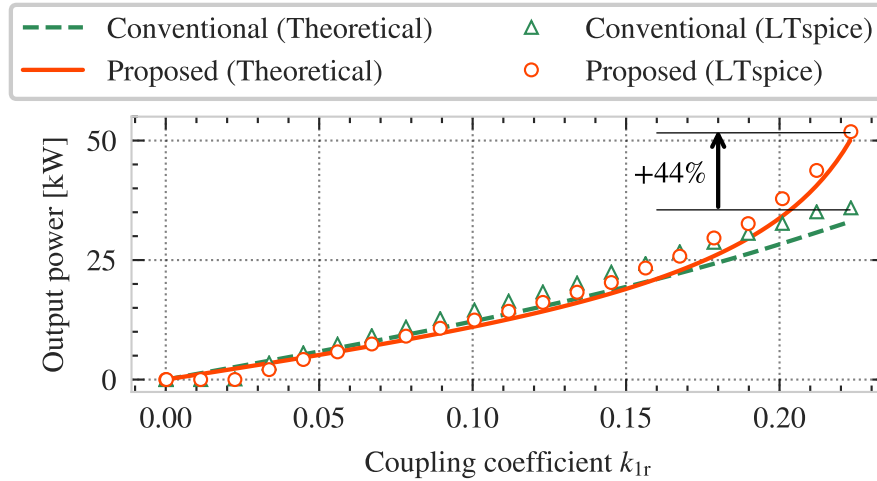


Fig. 6.3: LTspice simulation model of the proposed circuit

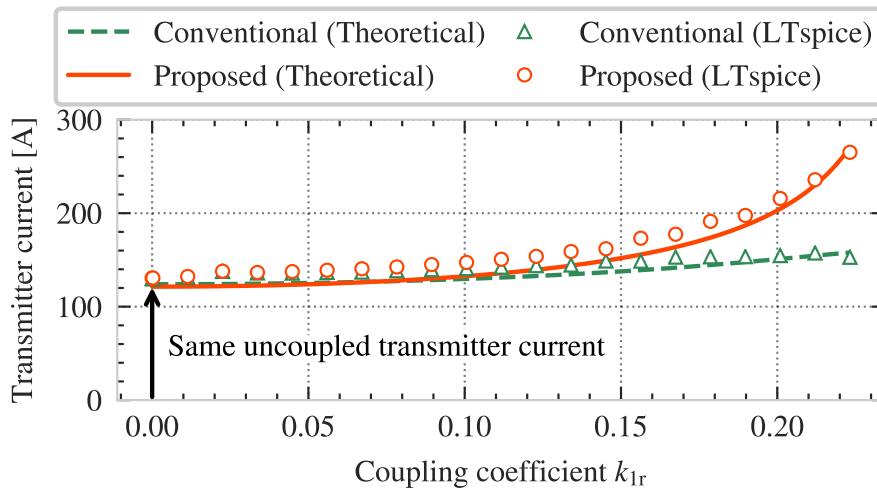
parameters in TABLE 6.1 and TABLE 6.2 are used in the circuit simulation.

The sweep results of output power and the amplitude of the transmitter current I_{L1} (zero-to-peak) with respect to coupling coefficient $k_{1,r}$ from 0.00 to 0.22 are shown in Fig. 6.4.

The triangle and circle markers represent the simulated value of the conventional and pro-



(a) LTSpice-simulated results: Comparison of output power P_{out} between the proposed and the conventional reflexive field focusing circuit



(b) LTSpice-simulated results: Comparison of current amplitude I_{L1} between the proposed and the conventional reflexive field focusing circuit

Fig. 6.4: LTSpice-simulated waveforms

posed circuits, and the dotted and solid lines represent the theoretical values of the conventional and proposed circuits derived in the previous section, respectively. The simulation results of the output power P_{out} with respect to the coupling coefficient $k_{1,r}$ are shown in Fig. 6.4(a). In the peak-coupled condition ($k_{1,r} = 0.22$), the output power of the proposed

circuit is 44% higher than the conventional circuit. The simulation results of the transmitter current with respect to the coupling coefficient are shown in Fig. 6.4(b). The proposed circuit's transmitter current in the peak-coupled condition ($k_{1,r} = 0.22$) is higher than that of the conventional circuit because of the higher peak output power. However, the proposed circuit can maintain the uncoupled transmitter current at the same level as the conventional circuit.

6.1.4 Circuit simulation for soft-switching analysis

The LTspice simulation with different pairs of input and output voltage is conducted to verify the soft-switching analysis presented in the previous section. The simulation results of the soft-switching analysis are shown in Fig. 6.5. All the parameters used in the simulation

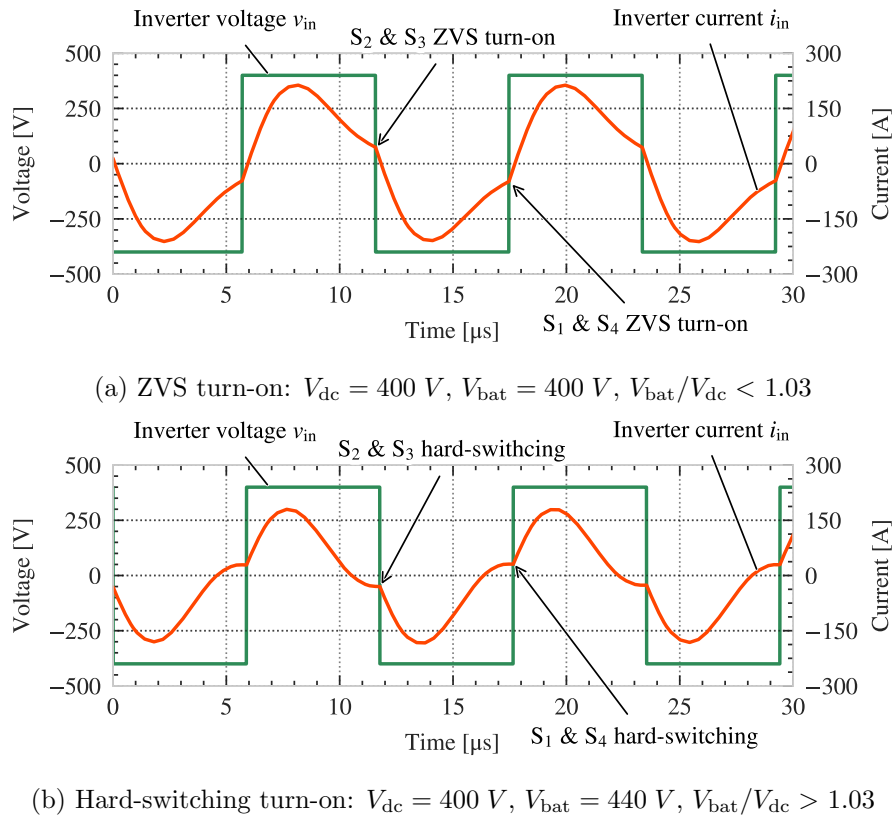


Fig. 6.5: LTspice-simulated waveforms

except for the input and output voltages are the same as TABLE 6.1 and TABLE 6.2. Since the right side of the inequality (3.42) is 1.03, the voltage ratio $V_{\text{bat}}/V_{\text{dc}}$ needs to be smaller than the value. The waveforms of the inverter voltage and current when both the input voltage V_{dc} and the output voltage V_{bat} are 400 V are shown in Fig. 6.5(a). Since $\sqrt{L_r/L_1}/(k_{\text{lim}}c_1c_2) = 1.03$ and $V_{\text{bat}}/V_{\text{dc}} = 1.00$, the ZVS requirement (3.42) is satisfied. The waveforms in the simulation result show that the ZVS turn-on is achieved since the inverter current is positive when the inverter voltage changes from positive to negative. The waveforms of the inverter voltage and current when the input voltage V_{dc} is 400 V and the output voltage V_{bat} is 440 V are shown in Fig. 6.5(b). Since $1/(k_{\text{lim}}c_1c_2)\sqrt{L_r/L_1} = 1.03$ and $V_{\text{bat}}/V_{\text{dc}} = 1.10$, the ZVS requirement (3.42) is not satisfied. The waveforms in the simulation result show that the ZVS turn-on failed since the inverter current is negative when the inverter voltage changes from positive to negative.

6.1.5 Output power sensitivity for the input and output voltages

The output power sensitivity of the designed system for the input and output voltages is analyzed using the theoretical equations (3.38) and (3.39). The analysis result is shown in Fig. 6.6. The designed system outputs 50 kW at $V_{\text{dc}}=V_{\text{bat}}=400$ V, which is the center

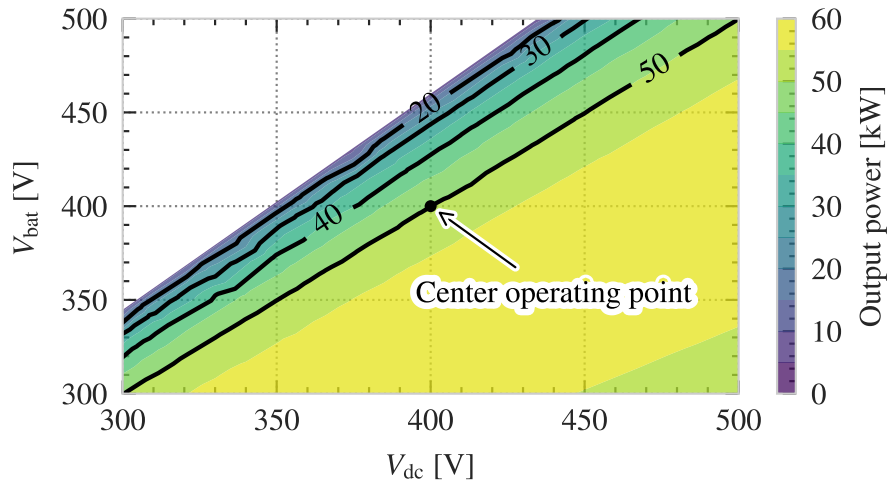


Fig. 6.6: Output power sensitivity for the input and output voltages

operating point. The operation in light load conditions can be achieved by decreasing the input voltage V_{dc} or increasing the output voltage V_{bat} . The decrease of the input voltage V_{dc} can be realized by decreasing the switching phase of the common inverter. The increasing output voltage V_{bat} can be realized if a dc-dc converter is connected at the output port of the system.

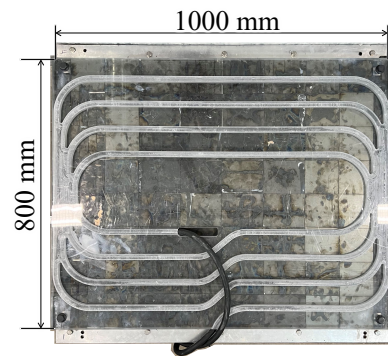
6.2 Coil prototype

A 50 kW system is constructed based on the presented design to verify the validity of the proposed circuit.

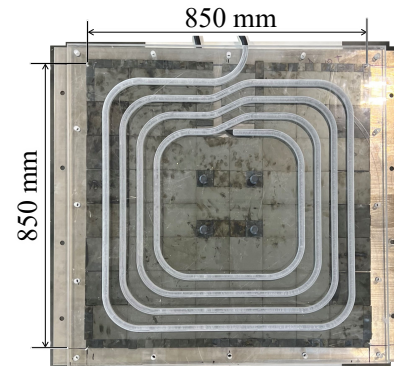
The dimensions of the transmitter and receiver coils are shown in Fig. 6.7. The coils are constructed with an 8000-strand Litz wire with a strand diameter of 0.1 mm. The selected Litz wire strand diameter of 0.1 mm is small enough compared to the skin depth (0.22 mm at 85 kHz). The outer diameter of the wire, including the insulation, is 16.4 mm. The air gap between the transmitter and receiver coils is 223 mm. MnZn ferrite core (PC95, TDK) with 5 mm thickness is used for wireless coils. Figure 6.7(a) shows the dimension of the transmitter coils. The aluminum backplate used for shielding is placed in the bottom layer, the ferrite plate is placed in the middle layer, and the transmitter coil embedded in a coil former is placed on the top layer. Figure 6.7(b) shows the dimension of the receiver coil. The whole structure is similar to the transmitter coil. Figure 6.7(c) shows the dimension of the thickness of the prototype system. Coil formers are made of transparent acrylic sheets, and the Litz wires are embedded. Figure 6.7(d) shows the layout of the transmitter coils. Each transmitter coil has a gap of 71 mm. Hence, the total length of the four transmitter coils is 4213 mm.

6.3 50 kW test on the automated rail

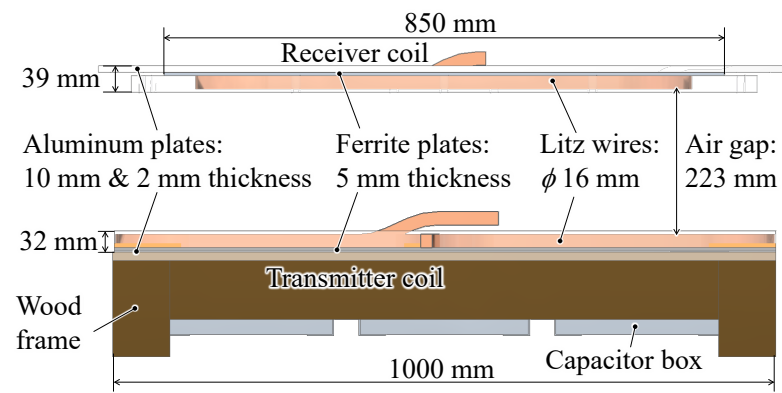
The constructed 50 kW rail test setup is shown in Fig. 6.8. An automated test rail is constructed to move the receiver coil above the transmitter coils. The receiver coil is set on the cart, and an electric motor drives the cart at a constant speed. The maximum speed of the test rail is 15 km/h, and the full weight of the load is 200 kg.



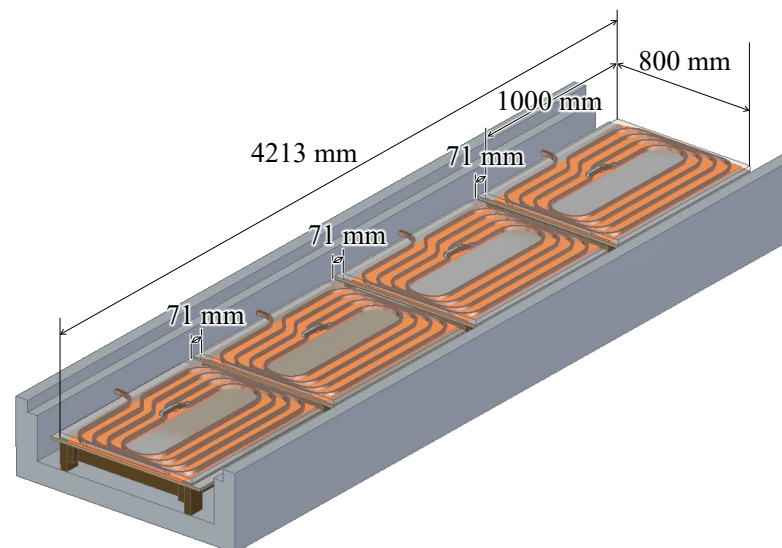
(a) Top view of the transmitter coil



(b) Top view of the receiver coil



(c) Side view of the coils



(d) Layout of the transmitter coils

Fig. 6.7: Detail of the prototype coils

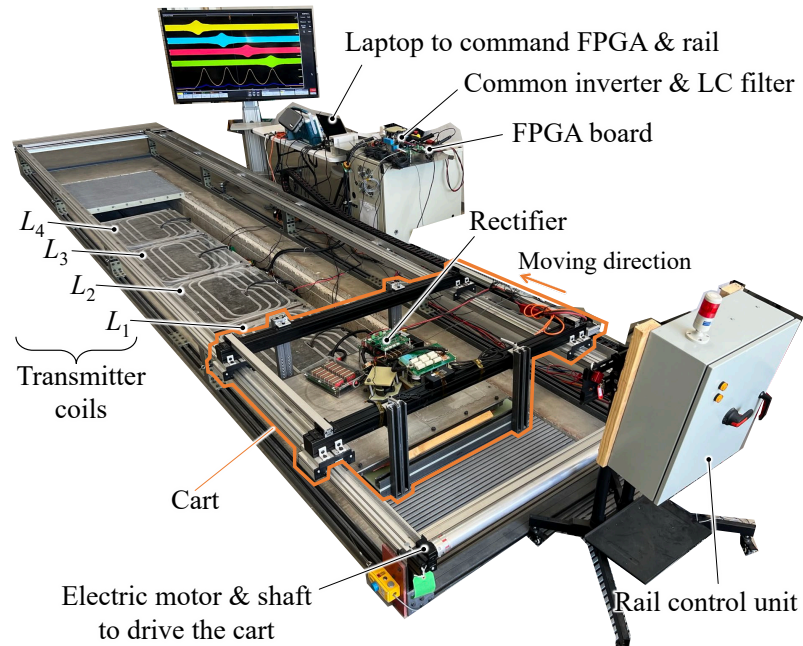


Fig. 6.8: Overview of the experimental setup

The circuit diagram of the experimental setup with energy feedback for power loss and efficiency measurements is shown in Fig. 6.9. Both the input and output voltages

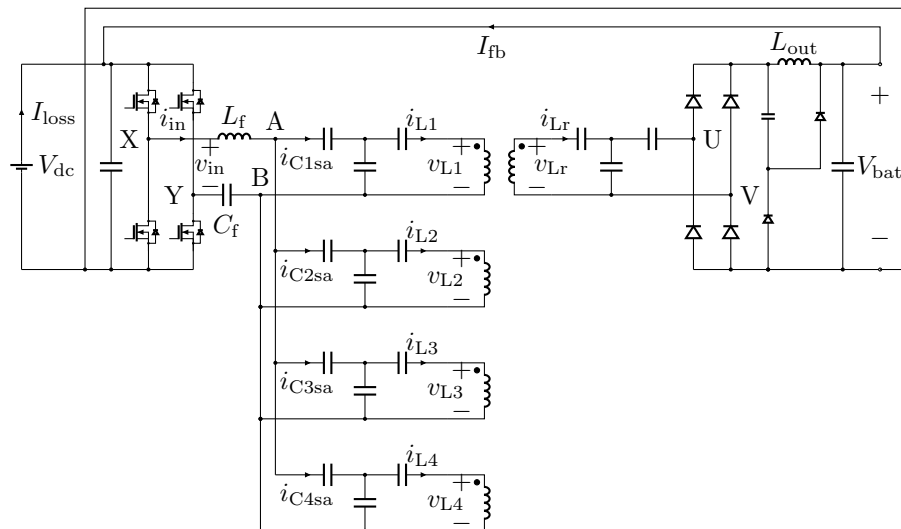


Fig. 6.9: Circuit diagram of the experiment in the rail setup

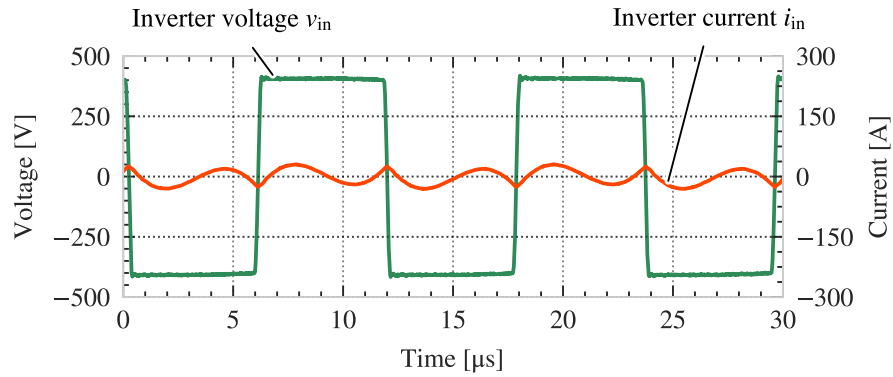
are fixed at 400 V. The equivalent load resistance R_{load} is defined by the equation (3.37), which changes according to the coupling coefficient $k_{1,r}$. In the peak-coupled condition ($k_{1,r} = 0.22$), the equivalent load resistances of the experimental system is 1.74 Ω . The power feedback via a dc wire allows the circulating of the transferred power within the system instead of dissipating the energy in a resistive load. While the transferred power is circulated, total losses are drawn from the external dc supply. Hence, the dc current I_{loss} and the dc supply voltage V_{dc} can be measured to calculate the total power losses. The transferred power can be calculated from the measured feedback current I_{fb} . Considering the high switching frequency of 85 kHz, silicon carbide (SiC) half-bridge MOSFETs module (CAS325M12HM2) with a rating voltage of 1.2 kV are used for the low ZVS losses. A passive lossless snubber is implemented in the output dc inductor L_{out} [124] to mitigate the voltage spike created in the current-type rectifier. The same SiC MOSFET modules are used as the diode rectifier and snubber diodes. The values for each component are listed in Table 6.3. Waveforms of the inverter voltage v_{in} and the inverter current i_{in} in the uncoupled and coupled conditions are shown in Fig. 6.10. In the uncoupled condition, the inverter current amplitude of the switching frequency is close to zero, and there is only the harmonic component, as shown in 6.10(a). In the coupled condition, the inverter current i_{in} increases with sinusoidal waveform, maintaining the lagged current against the inverter voltage v_{in} for ZVS requirement, as shown in 6.10(b). The measured amplitude of the inverter current i_{in} is 238 A, and the output power is 50 kW in the coupled condition.

The current waveforms of the series capacitors $C_{1,\text{sa}}$, $C_{2,\text{sa}}$, $C_{3,\text{sa}}$, and $C_{4,\text{sa}}$ when the third transmitter coil L_3 is coupled are shown in Fig. 6.11. The current amplitudes of all the series capacitors in the uncoupled transmitters are close to zero. The measured amplitude of the series capacitor current $i_{C_{3\text{sa}}}$ is 215 A.

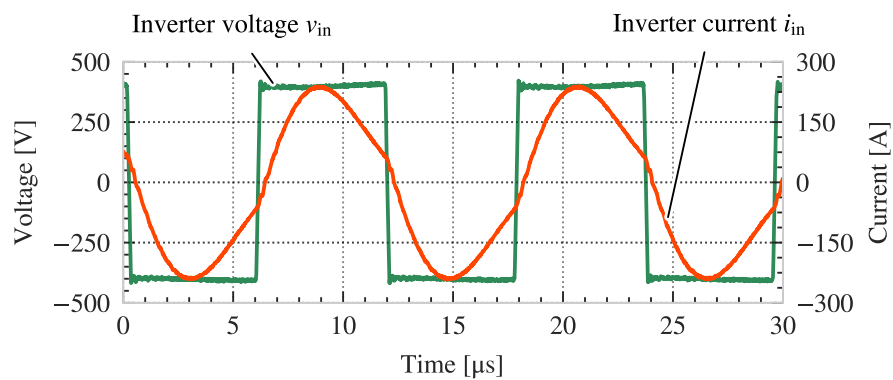
The current waveforms of transmitter coils L_1 , L_2 , L_3 , and L_4 when the third transmitter coil L_3 is coupled with the receiver coil L_r are shown in Fig. 6.12. The current amplitudes of all the uncoupled transmitters are 120 A. Only the coupled transmitter coil current i_{L_3} is amplified to 270 A. The voltage of the transmitter coil v_{L_3} is amplified from

Table 6.3: System parameters of the experimental setup

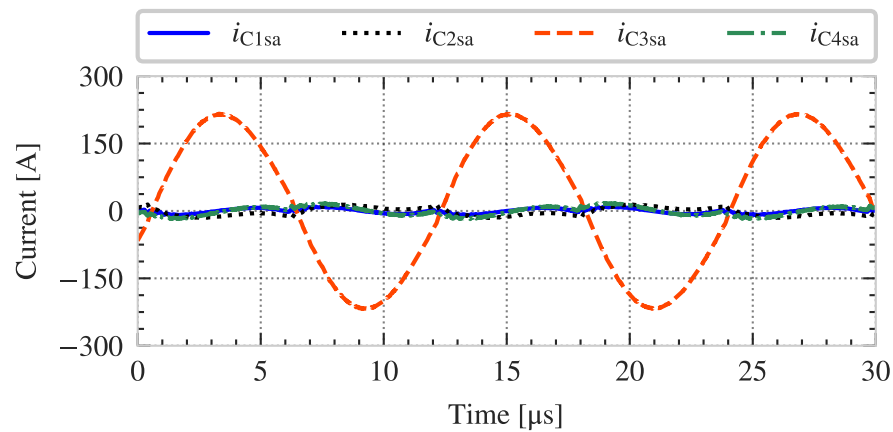
Description	Symbol	Value	Unit
Input voltage	V_{dc}	400	V
Output voltage	V_{bat}	400	V
Air gap	z_{gap}	223	mm
Switching frequency	f_{sw}	85	kHz
Coupling coefficient between L_1 & L_r	$k_{1,r}$	0.00~0.22	-
Transmitter coil inductance	L_1	24.62	μ H
Receiver coil inductance	L_r	23.19	μ H
Filter inductor	L_f	5.31	μ H
Filter capacitor	C_f	0.66	μ F
Output dc inductor	L_{dc}	15.00	μ H
Transmitter coil's turn number	N_{L1}	4	turn
Receiver coil's turn number	N_{Lr}	4	turn
Series capacitor	$C_{1,sa}$	2.12	μ F
Series capacitor	$C_{1,s}$	220	nF
Parallel capacitor	$C_{1,p}$	450	nF
Series capacitor	$C_{r,sa}$	660	nF
Series capacitor	$C_{r,s}$	238	nF
Parallel capacitor	$C_{r,p}$	484	nF
Ratio of capacitors $1 + C_{1,p}/C_{1,sa}$	c_1	1.21	-
Ratio of capacitors $1 + C_{r,p}/C_{r,s}$	c_2	3.04	-
Ratio of capacitors $1 + C_{r,p}/C_{r,sa}$	c_3	1.73	-
Limit of $k_{1,r}$	k_{lim}	0.23	-
Equivalent load resistance	$R_{L,eq}$	1.74	Ω



(a) Uncoupled condition



(b) Coupled condition at 50 kW output power

Fig. 6.10: Experimental waveforms of the inverter voltage v_{in} and inverter current i_{in} Fig. 6.11: Series capacitor currents i_{C1sa} , i_{C2sa} , i_{C3sa} , and i_{C4sa} when the transmitter coil L_3 is active at 50 kW output power

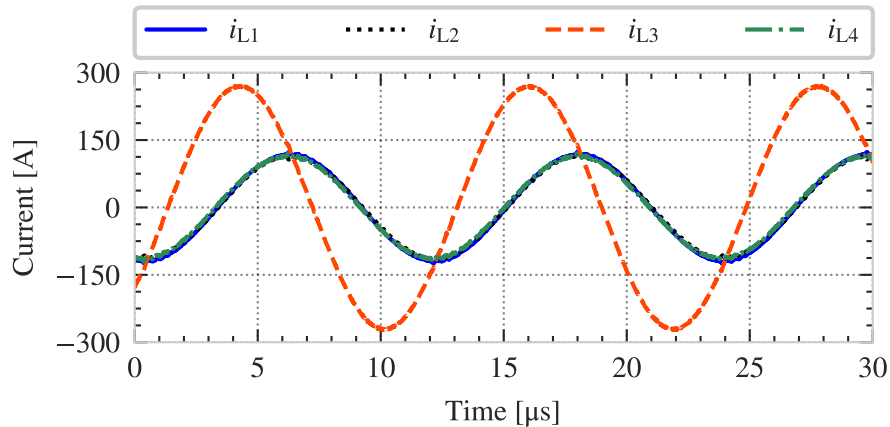


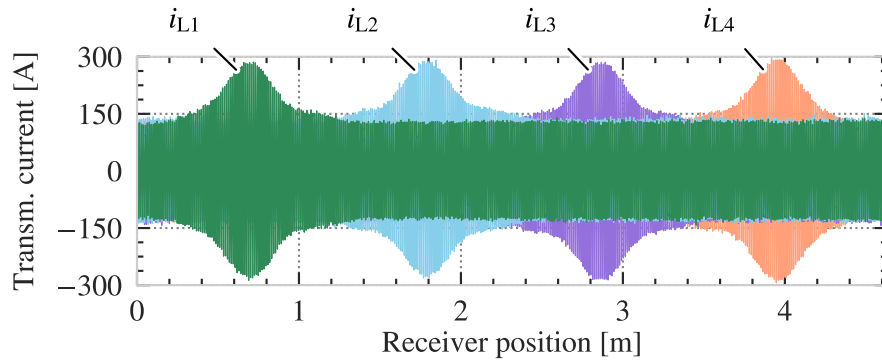
Fig. 6.12: Transmitter coil currents i_{L1} , i_{L2} , i_{L3} , and i_{L4} when the transmitter coil L_3 is active at 50 kW output power

1500 V in the uncoupled condition to 2590 V in the coupled condition. In the coupled condition, sinusoidal voltage and current are induced in the receiver coil. The amplitude of the receiver coil voltage is 3670 V, and the current is 363 A at 50 kW output power.

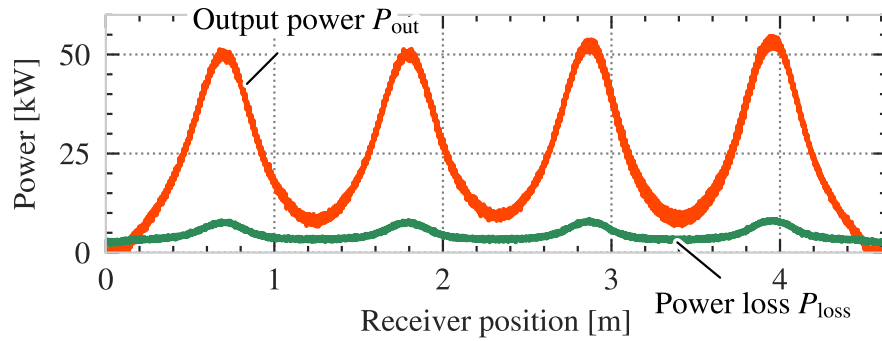
The stray magnetic fields from the uncoupled transmitter coils are measured at 800 mm away from the center of the uncoupled transmitter coil, and the measurement height is 110 mm from the top surface of the transmitter coil. The measured stray fields are compared to the SAE static wireless charging standard value [48]. The standards for where or how to measure stray fields for DIPT applications are still in development. In the recently published technical information report for J2954/2 for heavy-duty electric vehicles, an appendix is included for DIPT applications that suggests fields in dynamic systems will be measured at the edge of the lane rather than the edge of the vehicle when vehicles are traveling at speeds above 10 km/h [125]. At lower speeds, the requirement reverts to that of static wireless charging systems and could be achieved in DIPT systems with the proposed solution by disabling or reducing the currents when vehicles are operated at low speeds. Thus, measuring 800mm from the side of a dynamic charging system is expected to be acceptable for roadway applications. In the uncoupled condition, the measured stray field is 23.9 $\mu\text{T(rms)}$, below the SAE stationary charging standard value of 27 $\mu\text{T(rms)}$.

The receiver coil is moved above the transmitter coils from edge to edge of the system at

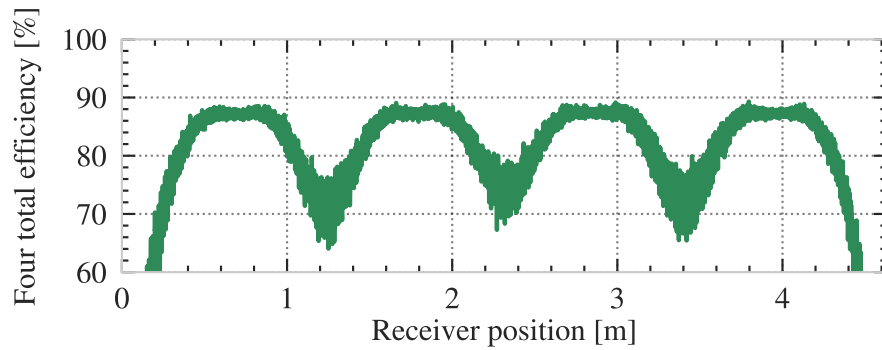
a constant speed of 10 km/h. The distributions of transmitter currents, output power, power loss, and efficiency are measured, as shown in Fig. 6.13. The measured transmitter currents



(a) Transmitter current I_{L1}



(b) System output power P_{out}



(c) System dc-dc efficiency

Fig. 6.13: Distribution of transmitter currents, output power, and efficiency at 10 km/h

with respect to the receiver coil position are shown in Fig. 6.13(a). The amplitudes of the transmitter coils naturally increase only when the receiver coil passes above each transmitter

coil. The measured output power and power loss with respect to the receiver coil position are shown in Fig. 6.13(b). The output power distribution has peaks of 50 kW above the centers of each transmitter coil. The average output power is 25.1 kW. The minimum output power in the middle of transmitter coils is 10 kW at the least coupled condition. To purely verify the proposed circuit's validity, the circular coil topology is chosen in this prototype. However, suppose the coil topologies that can mitigate the coupling coefficient distribution, such as DDQ coil topology [37] are utilized. In that case, the power dip at the edges of each transmitter coil can be improved. Otherwise, the dip at the edge of the transmitter coils would not affect the average output power if the transmitter coils are designed to have longer length than the receiver coil. The efficiency distribution calculated from the measured output power and power loss is shown in Fig. 6.13(c). The dc-dc efficiency is 87.9% at 51.7 kW when the receiver coil is centered above the third transmitter coil L_3 .

Output power distribution with 100 mm and 200 mm misalignment in the lateral direction is shown in Fig. 6.14. The peak power in the 100 mm misalignment condition

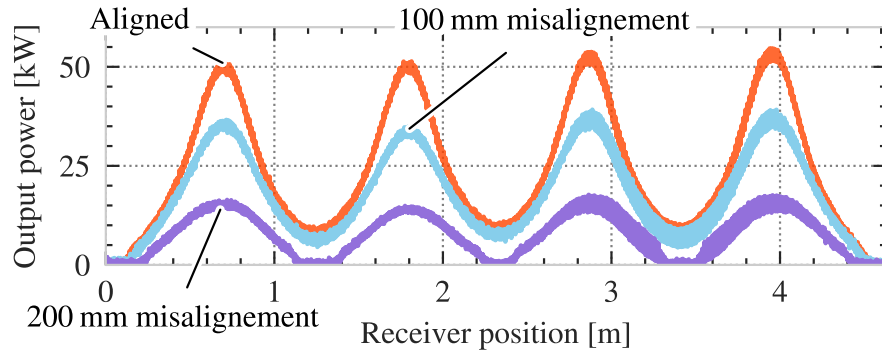


Fig. 6.14: Comparison between the aligned and misaligned conditions

is decreased by 30% compared to the aligned condition. The peak power in the 200 mm misalignment condition is decreased by 70% compared to the aligned state.

The power loss of each component in the aligned condition can be estimated, as shown in Fig. 6.15. In the estimation, the quality factors of coils and capacitors defined by (6.1) are assumed as $Q_L = 400$, $Q_C = 500$, respectively. The first transmitter L_1 is activated,

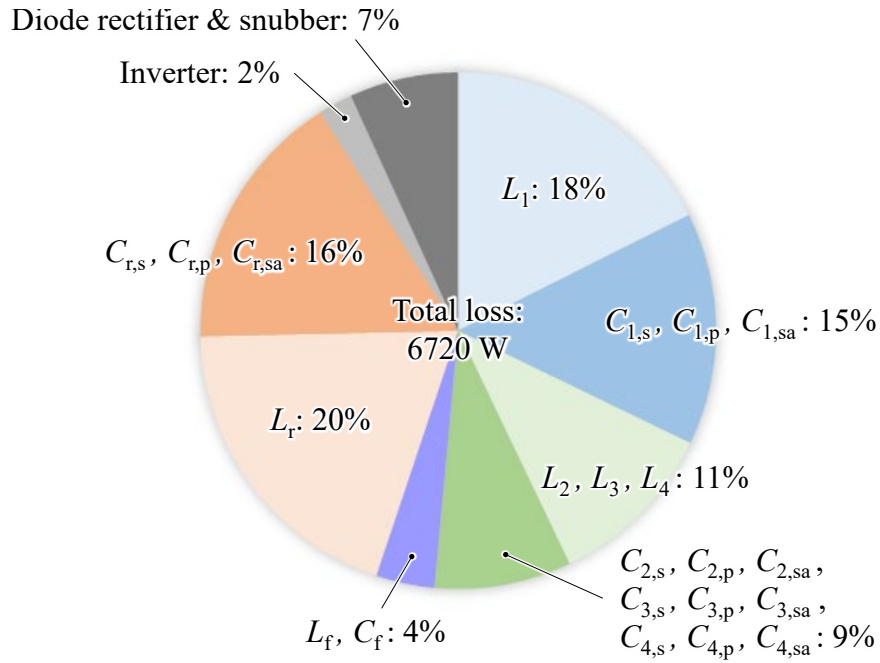


Fig. 6.15: Estimated loss breakdown when the output power is 50 kW

and output power is 50 kW. The estimated total power loss is 6720 W, and the estimated total dc-dc efficiency with the four transmitter configurations is 88.2%, which is close to the measured dc-dc efficiency of 87.9%. The main loss factors are the coupled transmitter coil L_1 and the receiver coil L_r . The loss of the uncoupled transmitter coils and their compensation components are retained at a low level since the uncoupled transmitters have 2.25 times lower currents than the coupled transmitter.

The comparison between the theoretical and experimental total dc-dc efficiencies is listed in TABLE 6.4. The experimental efficiency with the single and the four transmitter

Table 6.4: Comparison of the theoretical and experimental total dc-dc efficiencies

Configuration	Theoretical efficiency	Experimental efficiency
Single transmitter coil	90.2%	90.0%
Four transmitter coils	88.2%	87.9%

coils are 90.0% and 87.9%, respectively. The experimental total dc-dc efficiency with the four

transmitter configurations is directly measured from the experimental setup, and the value matches the theoretical model's efficiency within 0.3% error. The experimental efficiency with the single transmitter configuration is calculated using the measured loss of the four transmitter configurations and the theoretical loss difference between the single and four transmitter coils configurations.

Utilizing the theoretical loss model, the relationships of power loss for the number of parallel connected transmitters with 50 kW design are compared between the double-sided LCC circuit [98], conventional reflexive tuning circuit, and the proposed reflexive tuning circuit, as shown in Fig. 6.16. Here, the double-sided LCC circuit is assumed without reflexive tuning, where multiple LCC tanks are driven in parallel from a single inverter. All the circuit topology has a common inverter at the center, and the transmitter coils and

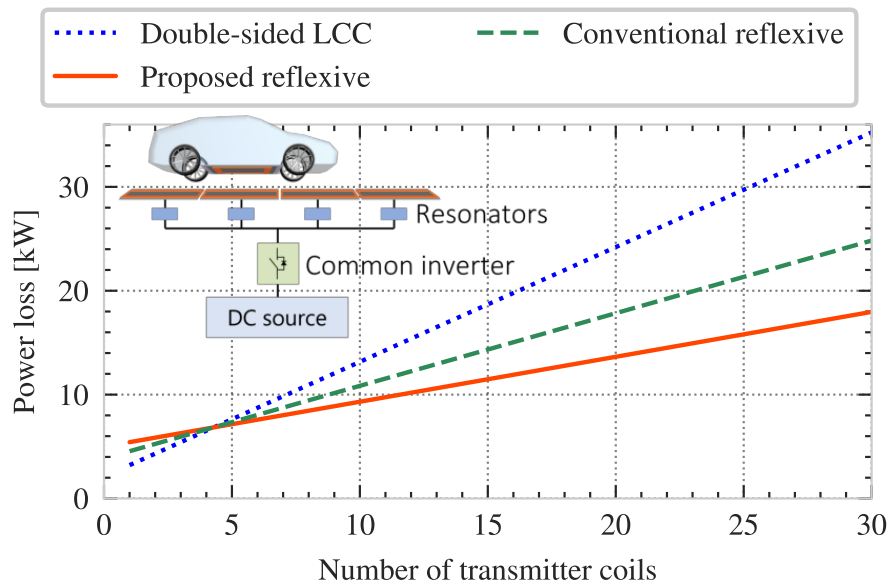


Fig. 6.16: Theoretical power loss versus number of transmitters with 50 kW design

the resonators are connected in parallel without any relays or four-quadrant switches. The system output power is 50 kW. The dotted line shows the power loss of the double-sided LCC circuit. The power loss of the double-sided LCC circuit increases significantly as the number of paralleled transmitters grows since the transmitter coil currents are constant

in all the transmitter coils. The dashed line shows the power loss of the conventional reflexive tuning circuit. The power loss with many parallel transmitter configurations can be decreased since the transmitter current decreases in the uncoupled transmitters. The solid line represents the power loss of the proposed reflexive tuning circuit. The power loss of the proposed circuit under four parallel configurations is higher than the double-sided LCC and conventional reflexive tuning circuit due to the additional components. However, the power loss of the proposed circuit over four parallel configurations is lower than the double-sided LCC and conventional reflexive tuning circuits since the uncoupled transmitter currents of the proposed circuit are much lower than the double-sided LCC and conventional reflexive tuning circuit. Therefore, the proposed circuit can achieve lower loss than the double-sided LCC and conventional reflexive tuning circuit if the transmitters are connected over four in parallel.

6.4 60 km/h Vehicle Test

The constructed rail setup cannot move the cart over the speed of 15 km/h. To evaluate the output power response over 15 km/h, and the validity of the proposed circuit in an actual application, the proposed circuit is implemented in a vehicle system. The schematic diagram of the vehicle test setup is shown in Fig. 6.17. An auxiliary battery is implemented on an electric vehicle as the output-side battery. The input voltage is reduced from 400 V to 250 V to reduce the peak output power from 50 kW to 20 kW. The output voltage is set at 350 V since the battery's voltage range is 300 to 400 V, which is a practical range for electric vehicles. Due to the utility restriction in the depth of the trench, the air gap between the transmitter coils and the receiver coil is changed from 223 mm to 170 mm. The series compensation capacitor $C_{r,s}$ is changed from 238 nF to 357 nF to adjust the difference of the peak coupling coefficient between the transmitter coils and the receiver coil.

The overview of the constructed vehicle system is shown in Fig. 6.18. The transmitter coils are implemented in a trench and covered with fiberglass lids so the vehicle can run above them. The common inverter and the LC filter are implemented in the shed. Only

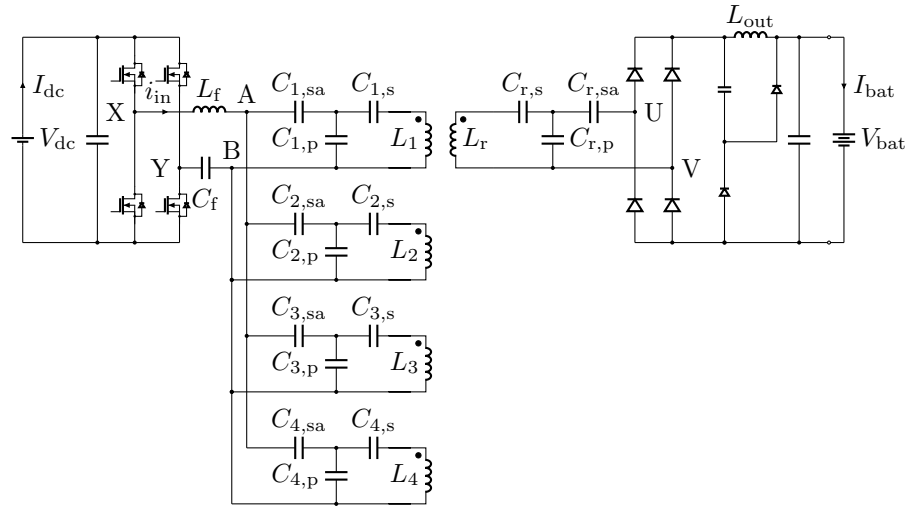


Fig. 6.17: Schematic diagram of the vehicle test setup

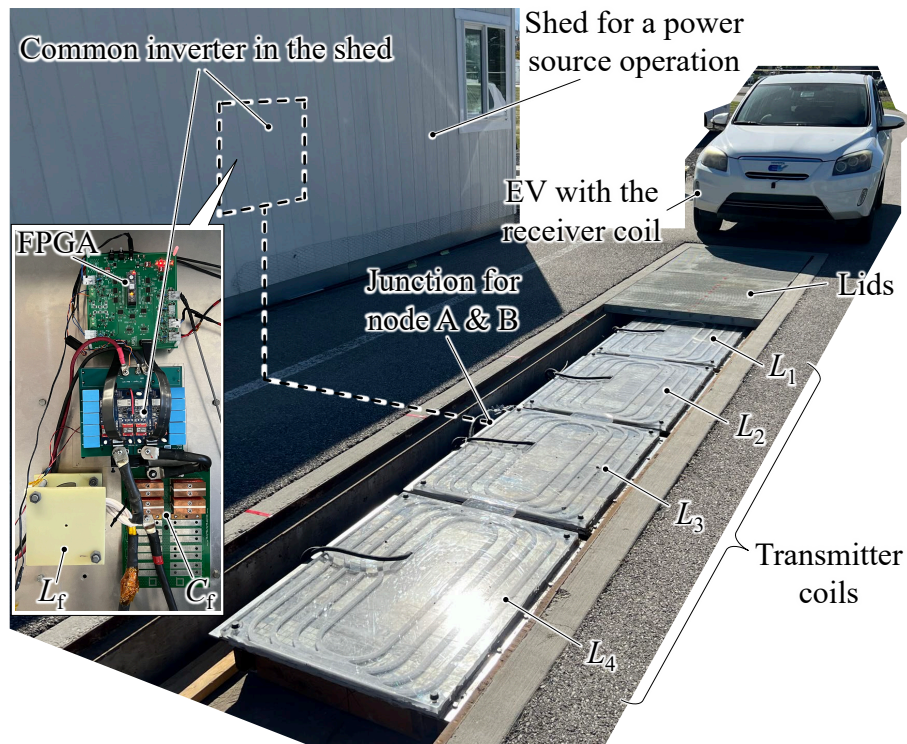


Fig. 6.18: Overview of the vehicle test setup

the two wires from the LC filter are wired through a hole between the shed and the outside trench. Junctions for nodes A and B are implemented in the outside trench, and each transmitter and compensation capacitor is connected to the nodes. In contrast to the

conventional individual inverter type, the common inverter type can reduce the number of wires between the inverter and transmitter coils.

The details of the vehicle system are shown in Fig. 6.19. Underneath the vehicle, the

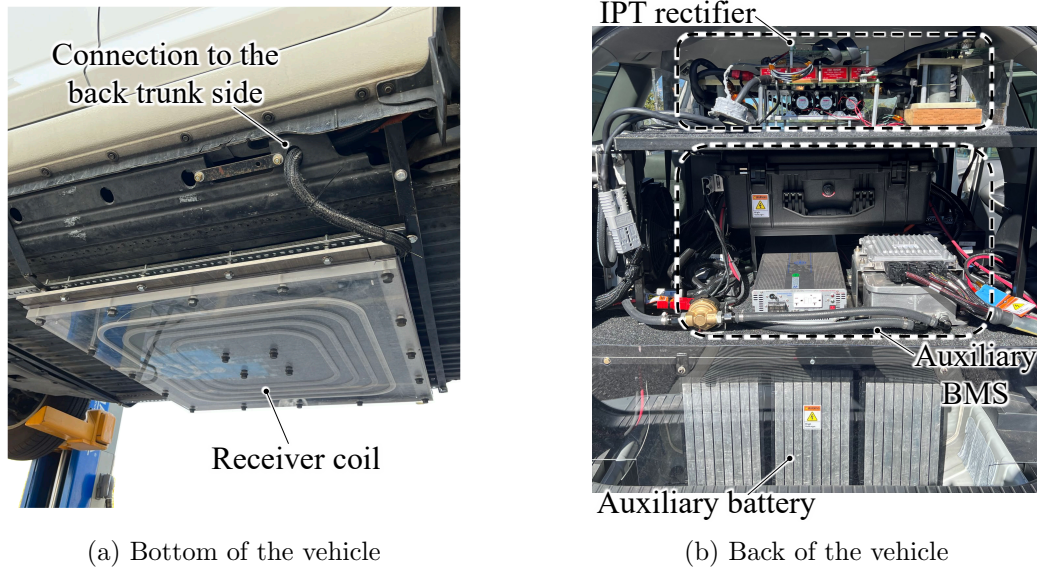


Fig. 6.19: Photos of the vehicle system

receiver coil is shown in Fig. 6.19(a). The receiver coil is attached to the bottom of the vehicle and is connected to the IPT rectifier. The vehicle's trunk is shown in Fig. 6.19(b). The dc output of the rectifier is connected to the auxiliary battery via the auxiliary battery management system box.

The transmitter current distributions when the vehicle runs at 10 km/h are shown in Fig. 6.20(a). The measured uncoupled and coupled transmitter current is 75 A and 165 A, respectively.

The output response is compared between 10 km/h and 60 km/h. 60 km/h is the maximum speed limit of the test track. The test result is shown in Fig. 6.20(b). The difference in the third output power wave timing is caused by the difficulty in keeping the vehicle speed constant while driving. However, there is no noticeable difference in the shape of each output power waveform at 10 km/h and 60 km/h. Hence, the time delay of output power due to high vehicle speed is negligible, at least up to 60 km/h. The output power

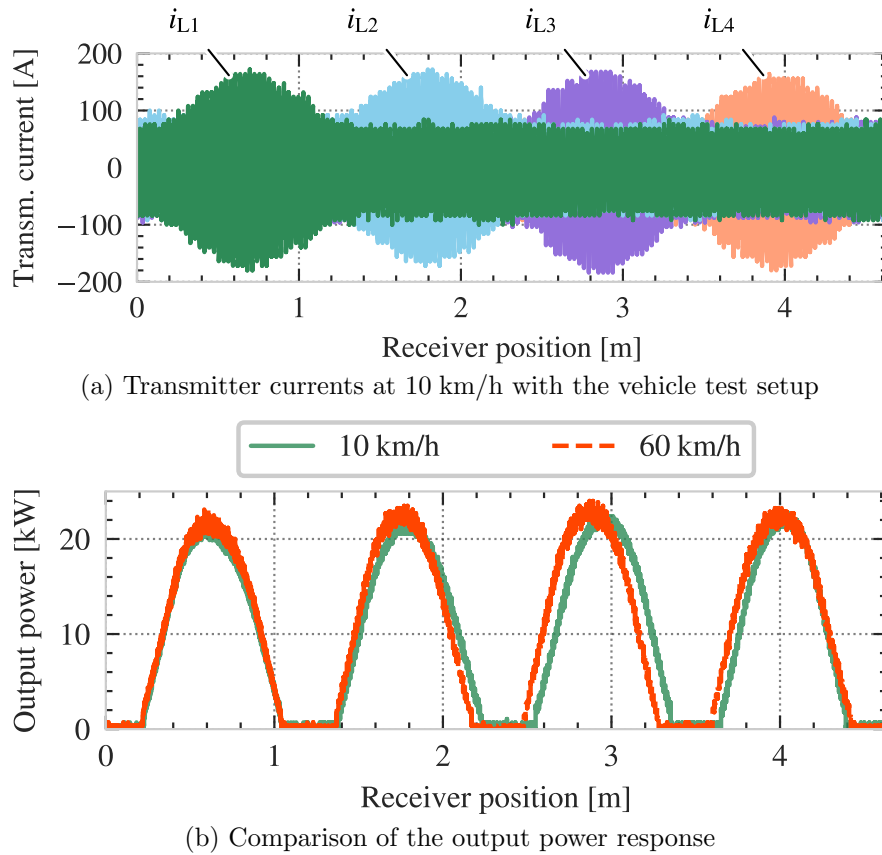


Fig. 6.20: Distribution of transmitter currents and output power with the vehicle test setup

distribution at the edge of the transmitter coils differs from that in the rail test since the air gap change alters the coupling coefficient distribution. The peak output power is 22 kW, and dc-dc efficiency is 85.3%. The dc-dc efficiency is decreased because the series capacitor $C_{r,s}$ is detuned to address the air gap change.

6.5 Summary of the Chapter

This chapter demonstrated a 50 kW reflexive tuning circuit designed by the proposed ANN- and GA-based design optimization method. The conventional DIPT system has individual inverters for each transmitter coil; hence the cost of the inverters accounts for the main factor of the system cost. Inserting mechanical relays or four-quadrant semiconductor switches between a common inverter and transmitter branches can reduce the number of inverters. However, the approach compromises the system's reliability and lifetime of the

system and results in increased maintenance costs. Moreover, the cost-effectiveness of the method is limited due to the impact of the mechanical relays or four-quadrant semiconductor switches on the power lines. In resonant circuits, start-up and shutdown transients circuits cause additional output power fluctuations at the vehicle side. Furthermore, the activation and deactivation of mechanical relays or four-quadrant semiconductor switches require extra receiver-position sensors for each transmitter coil. The reflexive tuning approach can change the amplitude of the current in the transmitter coil automatically, utilizing the reflected reactance without any mechanical relays or four-quadrant semiconductor switches. Hence, this approach can reduce the number of inverters and receiver-position sensors. Theoretical analysis, simulation, and experimental validation were conducted. The simulation result shows that the proposed circuit can increase the output power by 44% compared to the conventional reflexive tuning circuit while maintaining the uncoupled transmitter currents at the same level. A 50 kW proposed reflexive tuning circuit was constructed, and the measured dc-dc efficiency with a single and four transmitter coils are 90.0% and 87.9%, respectively. A vehicle test setup was constructed to evaluate the time response of the output power at the speed of 60 km/h. The measured results show that the time response delay is negligible, at least up to 60 km/h.

CHAPTER 7

Conclusion & Outlook

7.1 Results & Conclusions

This dissertation has proposed and demonstrated a new reflexive tuning circuit that can achieve higher output power than the conventional reflexive tuning circuit. Also, a new ANN- and GA-based design optimization method has been proposed and demonstrated in this dissertation since a DIPT system has many design variables and requirements, making the design further difficult for the proposed reflexive tuning DIPT system. Using the newly developed ANN- and GA-based optimization method, a 50 kW proposed DIPT system has been designed and demonstrated on an automated rail and vehicle system. The main contributions of this dissertation can be summarized in four parts.

7.1.1 Contribution 1

In **Chapter 3**, a new high-power reflexive tuning circuit topology has been proposed. Using the additional series capacitors on the transmitter and receiver side, the proposed circuit can achieve higher output power while maintaining the uncoupled transmitter current and the resonance stability at the same level compared to the conventional circuit. The validity of the proposed circuit has been demonstrated through circuit simulation and experimental results. The maximum output power of the proposed circuit is 102% higher than the conventional circuit in the demonstrated simulation. The constructed 2.0 kW experimental results show that the prototype matches well with the simulation results and that the circuit can amplify the current in the transmitter coil 2.5 times higher in the coupled condition than that in the uncoupled condition. The work presented in this chapter was published in a peer-reviewed international conference paper [126]. Also, the proposed reflexive tuning network is under a patent process.

7.1.2 Contribution 2

In **Chapter 4**, the ANN-based design optimization method for stationary IPT systems has been proposed. The proposed algorithm uses the superposition of calculated stray magnetic fields to collect ANN training data. As a result, the data collection time has been decreased from about 40 months to one month. The proposed method can find hundreds of more designs that meet the designer's criteria, allowing the designer to select an optimized result based on the plotted Pareto fronts. In the example presented, the primary side core of the proposed method is 20% smaller than that of the conventional method while maintaining the other criteria the same. Some of the work in this chapter was presented in two peer-reviewed international conference papers [104, 111].

7.1.3 Contribution 3

In **Chapter 5**, a design optimization method for the DIPT systems combining ANN and GA has been proposed. The proposed algorithm uses a GA-based input value improvement method so that the trained ANN can efficiently output design points that satisfy many design criteria simultaneously. The conventional approach could not find any optimal design; however, the proposed method found 579 points. Design results predicted by the ANN have been compared with FEM simulation, circuit simulation, and experimental results to verify the validity of the proposed algorithm. The FEM and circuit simulation results and the ANN prediction results match with errors of 10.2% or less for all design criteria. As for the comparison between ANN prediction and experimental values, the values except for the coil loss match each other with an error of less than 12.7%. If a higher prediction accuracy of coil loss is required, the proposed method can be modified to include calculating and optimizing the coil quality factors. The work presented in this chapter was published in a peer-reviewed IEEE journal [127].

7.1.4 Contribution 4

In **Chapter 6**, integration of the proposed reflexive tuning and the ANN- and GA-based design optimization method has been demonstrated through a 50 kW DIPT system.

With the 50 kW design, the simulation result shows that the proposed circuit can increase the output power by 44% compared to the conventional circuit while maintaining the uncoupled transmitter currents at the same level. A 50 kW four transmitter coils configuration with a rail system was constructed, and the measured dc-dc efficiency is 87.9%. Losses in the inactive transmitter coils and compensation capacitors can be reduced by 80.0% compared to the case where the transmitter coil current is constant. A vehicle test setup was constructed to evaluate the time response of the output power at the speed of 60 km/h. The measured results show that the time response delay is negligible in the speed range. The work presented in this chapter is under a peer-reviewed IEEE journal review process [128].

7.2 Future Research Areas

There are three major directions for future research: a combination of passive and active control, high frequency, and calculation methods for ANN training data.

First, a combination of passive and active control for the reflexive tuning circuit may improve the system's characteristics. The proposed reflexive tuning circuit uses passive control to switch active transmitter coils. The combination of the passive and active control using receiver side switches may enhance more advantages of the reflexive tuning DIPT systems.

Second, a higher switching frequency beyond 85 kHz could be one of the research directions in IPT technology. By increasing frequency, power density could be dramatically increased, which could result in reducing road work costs. Further investigations on the effect of the high-frequency stray field on human bodies and electrical components are required.

Third, the technique to speed up the calculation time for ANN training is a key factor for ANN-based design algorithms. In the existing technologies, calculating vast training data related to coil quality factors and parasitic components of an electric system in a practical time is a challenging topic. This issue will get more critical in complicated systems design.

In summary, reflexive tuning technology and its design optimization method have been developed. It has been shown the technology is a valid alternative to conventional DIPT

technology.

7.3 Published papers

7.3.1 Conference papers

- [104] “High-Resolution Design Optimization for IPT Including Stray Field and Coupling Coefficient,” S. Inoue, R. Nimri, A. Kamineni, R. Zane, 2021 IEEE Applied Power Electronics Conference and Exposition (APEC), 1573-1579, DOI: 10.1109/APEC42165.2021.9487332
- [111] “A New Design Optimization Method for Dynamic Inductive Power Transfer Systems utilizing a Neural Network,” S. Inoue, R. Nimri, A. Kamineni, R. Zane, 2021 IEEE Energy Conversion Congress and Exposition (ECCE), 1496-1501, DOI: 10.1109/ECCE47101.2021.9595560
- [126] “High-Power Field-Focusing Circuit for Dynamic Wireless Power Transfer Systems,” S. Inoue, C.R. Teeneti, D. Goodrich, J. Larsen, A. Kamineni, R. Zane, 2022 Wireless Power Week (WPW), 699-704, DOI: 10.1109/WPW54272.2022.9901335

7.3.2 Journals

- [127] “Fast Design Optimization Method Utilizing a Combination of Artificial Neural Networks and Genetic Algorithms for Dynamic Inductive Power Transfer Systems,” S. Inoue, D. Goodrich, S. Saha, R. Nimri, A. Kamineni, N.S. Flann, R.A. Zane, IEEE Open Journal of Power Electronics, DOI: 10.1109/OJPEL.2022.3224422
- [128] “50 kW Reflexive Tuning Networks for Dynamic Inductive Power Transfer Systems,” S. Inoue, S. Kiguthi, J. Newman, T. Goodale, C. R. Teeneti, B. Hesterman,

A. Kamineni, and R. A. Zane, IEEE Transaction on Power Electronics, 2022, [Under review process].

7.3.3 Patent

- HIGH-POWER REFLEXIVE FIELD CONTAINMENT CIRCUIT TOPOLOGY FOR DYNAMIC WIRELESS POWER TRANSFER SYSTEMS, [Under review process]

REFERENCES

- [1] P. Lazzeroni, V. Cirimele, and A. Canova, “Economic and environmental sustainability of dynamic wireless power transfer for electric vehicles supporting reduction of local air pollutant emissions,” *Renewable and Sustainable Energy Reviews*, vol. 138, p. 110537, 2021.
- [2] A. P. Hu, “Selected resonant converters for ipt power supplies,” Ph.D. dissertation, ResearchSpace@ Auckland, 2001.
- [3] H. Feng, R. Tavakoli, O. C. Onar, and Z. Pantic, “Advances in high-power wireless charging systems: Overview and design considerations,” *IEEE Transactions on Transportation Electrification*, vol. 6, no. 3, pp. 886–919, 2020.
- [4] D. Hall, N. Pavlenko, and N. Lutsey, “Beyond road vehicles: survey of zero-emission technology options across the transport sector,” *International Council on Clean Transportation Working Paper*, vol. 11, 2018.
- [5] NREL, “Medium-and Heavy-Duty Electric Vehicle Charging,” <https://www.nrel.gov/transportation/medium-heavy-duty-vehicle-charging.html>, 2021, [Online; accessed 1-Aug-2021].
- [6] W. Tianyu, “EV battery-swapping finds new life in China,” <https://news.cgtn.com/news/2020-08-16/EV-battery-swapping-finds-new-life-in-China-SWZQhFZoEE/index.html>, 2020, [Online; accessed 1-Aug-2021].
- [7] Electreon, “,” <https://www.electreon.com/>, 2021, [Online; accessed 1-Aug-2021].
- [8] M. H. Rashid, *Power electronics handbook*. Butterworth-Heinemann, 2017.
- [9] N. Shinohara, Y. Kubo, and H. Tonomura, “Mid-distance wireless power transmission for electric truck via microwaves,” in *2013 International Symposium on Electromagnetic Theory*. IEEE, 2013, pp. 841–843.
- [10] R. W. Erickson and D. Maksimovic, *Fundamentals of power electronics*. Springer Science & Business Media, 2007.
- [11] S. Choi, J. Huh, W. Lee, S. Lee, and C. T. Rim, “New cross-segmented power supply rails for roadway-powered electric vehicles,” *IEEE transactions on Power Electronics*, vol. 28, no. 12, pp. 5832–5841, 2013.
- [12] V. Cirimele, M. Diana, F. Freschi, and M. Mitolo, “Inductive power transfer for automotive applications: State-of-the-art and future trends,” *IEEE Transactions on Industry Applications*, vol. 54, no. 5, pp. 4069–4079, 2018.
- [13] R. Tavakoli and Z. Pantic, “Analysis, design, and demonstration of a 25-kw dynamic wireless charging system for roadway electric vehicles,” *IEEE Journal of Emerging and Selected Topics in Power Electronics*, vol. 6, no. 3, pp. 1378–1393, 2017.

- [14] G. R. Nagendra, J. T. Boys, G. A. Covic, B. S. Riar, and A. Sondhi, "Design of a double coupled ipt ev highway," in *IECON 2013-39th Annual Conference of the IEEE Industrial Electronics Society*. IEEE, 2013, pp. 4606–4611.
- [15] S. Zhou and C. C. Mi, "Multi-paralleled lcc reactive power compensation networks and their tuning method for electric vehicle dynamic wireless charging," *IEEE Transactions on Industrial Electronics*, vol. 63, no. 10, pp. 6546–6556, 2015.
- [16] S. Y. Jeong, J. H. Park, G. P. Hong, and C. T. Rim, "Autotuning control system by variation of self-inductance for dynamic wireless ev charging with small air gap," *IEEE Transactions on Power Electronics*, vol. 34, no. 6, pp. 5165–5174, 2018.
- [17] K. Lee, Z. Pantic, and S. M. Lukic, "Reflexive field containment in dynamic inductive power transfer systems," *IEEE Transactions on power Electronics*, vol. 29, no. 9, pp. 4592–4602, 2013.
- [18] G. Iyer, C. Ledna, L. Clarke, H. McJeon, J. Edmonds, and M. Wise, "Gcam-usa analysis of us electric power sector transitions," *Richland, Washington: Pacific Northwest National Laboratory*, 2017.
- [19] E. L. Hodson, M. Brown, S. Cohen, S. Showalter, M. Wise, F. Wood, J. Caron, F. Feijoo, G. Iyer, and K. Cleary, "Us energy sector impacts of technology innovation, fuel price, and electric sector co2 policy: Results from the emf 32 model intercomparison study," *Energy Economics*, vol. 73, pp. 352–370, 2018.
- [20] P. Jadun, C. McMillan, D. Steinberg, M. Muratori, L. Vimmerstedt, and T. Mai, "Electrification futures study: end-use electric technology cost and performance projections through 2050," National Renewable Energy Lab.(NREL), Golden, CO (United States), Tech. Rep., 2017.
- [21] U. UNFCCC, "Kyoto protocol to the united nations framework convention on climate change," in *Proceedings of the 3rd Conference of the Parties, FCCC/CP/1997/L.7/Add. 1*. United Nations Framework Convention on Climate Change, 1997.
- [22] L. W. Bedsworth and M. R. Taylor, "Learning from california's zero-emission vehicle program," *California Economic Policy*, vol. 3, no. 4, 2007.
- [23] J. G. Olivier, K. Schure, J. Peters *et al.*, "Trends in global co2 and total greenhouse gas emissions," *PBL Netherlands Environmental Assessment Agency*, vol. 5, 2017.
- [24] U. S. E. P. Agency, "Inventory of u.s. greenhouse gas emissions and sinks: 1990-2019," *Annual report*, 2019.
- [25] M. F. Ruth, P. Jadun, N. Gilroy, E. Connelly, R. Boardman, A. Simon, A. Elgowainy, and J. Zuboy, "The technical and economic potential of the h2@ scale hydrogen concept within the united states," National Renewable Energy Lab.(NREL), Golden, CO (United States), Tech. Rep., 2020.

- [26] C. J. Michelbacher, S. Ahmed, I. Bloom, A. Burnham, B. Carlson, F. Dias, E. J. Dufek, A. N. Jansen, M. Keyser, D. Howell *et al.*, “Enabling fast charging: A technology gap assessment,” Idaho National Lab.(INL), Idaho Falls, ID (United States), Tech. Rep., 2017.
- [27] M. Ban, J. Yu, Z. Li, D. Guo, and J. Ge, “Battery swapping: An aggressive approach to transportation electrification,” *IEEE Electrification Magazine*, vol. 7, no. 3, pp. 44–54, 2019.
- [28] B. J. Limb, Z. D. Asher, T. H. Bradley, E. Sproul, D. A. Trinko, B. Crabb, R. Zane, and J. C. Quinn, “Economic viability and environmental impact of in-motion wireless power transfer,” *IEEE Transactions on Transportation Electrification*, vol. 5, no. 1, pp. 135–146, 2018.
- [29] Z. Bi, T. Kan, C. C. Mi, Y. Zhang, Z. Zhao, and G. A. Keoleian, “A review of wireless power transfer for electric vehicles: Prospects to enhance sustainable mobility,” *Applied Energy*, vol. 179, pp. 413–425, 2016.
- [30] M. Budhia *et al.*, “Design and optimization of circular magnetic structures for lumped inductive power transfer systems,” *IEEE Transactions on Power Electronics*, vol. 26, no. 11, pp. 3096–3108, 2011.
- [31] G. A. Covic and J. T. Boys, “Inductive power transfer,” *Proceedings of the IEEE*, vol. 101, no. 6, pp. 1276–1289, 2013.
- [32] P. A. J. Lawton, F. J. Lin, and G. A. Covic, “Magnetic design considerations for high-power wireless charging systems,” *IEEE Transactions on Power Electronics*, 2022.
- [33] K. W. Klontz, D. M. Divan, D. W. Novotny, and R. D. Lorenz, “Contactless power delivery system for mining applications,” *IEEE Transactions on Industry Applications*, vol. 31, no. 1, pp. 27–35, 1995.
- [34] W. Lee, J. Huh, S. Choi, X. Thai, J. H. Kim, E. Al-Ammar, M. El-Kady, and C. T. Rim, “Finite-width magnetic mirror models of mono and dual coils for wireless electric vehicles,” *IEEE Transactions on Power Electronics*, vol. 28, no. 3, pp. 1413–1428, 2012.
- [35] S. Lee, B. Choi, and C. T. Rim, “Dynamics characterization of the inductive power transfer system for online electric vehicles by laplace phasor transform,” *IEEE Transactions on Power Electronics*, vol. 28, no. 12, pp. 5902–5909, 2013.
- [36] S. Y. Choi, J. Huh, W. Y. Lee, and C. T. Rim, “Asymmetric coil sets for wireless stationary ev chargers with large lateral tolerance by dominant field analysis,” *IEEE Transactions on Power Electronics*, vol. 29, no. 12, pp. 6406–6420, 2014.
- [37] M. Budhia, J. T. Boys, G. A. Covic, and C.-Y. Huang, “Development of a single-sided flux magnetic coupler for electric vehicle ipt charging systems,” *IEEE Transactions on Industrial Electronics*, vol. 60, no. 1, pp. 318–328, 2011.

- [38] G. A. Covic, J. T. Boys, M. L. Kissin, and H. G. Lu, "A three-phase inductive power transfer system for roadway-powered vehicles," *IEEE Transactions on Industrial Electronics*, vol. 54, no. 6, pp. 3370–3378, 2007.
- [39] C.-S. Wang, G. A. Covic, and O. H. Stielau, "Power transfer capability and bifurcation phenomena of loosely coupled inductive power transfer systems," *IEEE transactions on industrial electronics*, vol. 51, no. 1, pp. 148–157, 2004.
- [40] A. L. Stein, P. A. Kyaw, and C. R. Sullivan, "Wireless power transfer utilizing a high- q self-resonant structure," *IEEE Transactions on Power Electronics*, vol. 34, no. 7, pp. 6722–6735, 2018.
- [41] B. Regensburger, S. Sinha, A. Kumar, S. Maji, and K. K. Afridi, "High-performance multi-mhz capacitive wireless power transfer system for ev charging utilizing interleaved-foil coupled inductors," *IEEE Journal of Emerging and Selected Topics in Power Electronics*, 2020.
- [42] S. Sinha, A. Kumar, B. Regensburger, and K. K. Afridi, "A new design approach to mitigating the effect of parasitics in capacitive wireless power transfer systems for electric vehicle charging," *IEEE Transactions on Transportation Electrification*, vol. 5, no. 4, pp. 1040–1059, 2019.
- [43] A. Kumar, S. Sinha, A. Sepahvand, and K. K. Afridi, "Improved design optimization for high-efficiency matching networks," *IEEE Transactions on Power Electronics*, vol. 33, no. 1, pp. 37–50, 2017.
- [44] F. Lu, H. Zhang, and C. Mi, "A two-plate capacitive wireless power transfer system for electric vehicle charging applications," *IEEE Transactions on Power Electronics*, vol. 33, no. 2, pp. 964–969, 2017.
- [45] S. Li, Z. Liu, H. Zhao, L. Zhu, C. Shuai, and Z. Chen, "Wireless power transfer by electric field resonance and its application in dynamic charging," *IEEE Transactions on Industrial Electronics*, vol. 63, no. 10, pp. 6602–6612, 2016.
- [46] X. Li, B. Duan, L. Song, Y. Yang, Y. Zhang, and D. Wang, "A new concept of space solar power satellite," *Acta Astronautica*, vol. 136, pp. 182–189, 2017.
- [47] B. Hu, H. Li, T. Li, H. Wang, Y. Zhou, X. Zhao, X. Hu, X. Du, Y. Zhao, X. Li *et al.*, "A long-distance high-power microwave wireless power transmission system based on asymmetrical resonant magnetron and cyclotron-wave rectifier," *Energy Reports*, vol. 7, pp. 1154–1161, 2021.
- [48] J. Schneider, "Wireless power transfer for light-duty plug-in/electric vehicles and alignment methodology," *SAE International J2954 Taskforce*, 2016.
- [49] Magment, "," <https://www.magment.co/>, 2022, [Online; accessed 30-Nov-2022].
- [50] S. Y. Choi, B. W. Gu, S. W. Lee, W. Y. Lee, J. Huh, and C. T. Rim, "Generalized active emf cancel methods for wireless electric vehicles," *IEEE Transactions on Power Electronics*, vol. 29, no. 11, pp. 5770–5783, 2013.

- [51] J. Lu, G. Zhu, and C. C. Mi, "Foreign object detection in wireless power transfer systems," *IEEE Transactions on Industry Applications*, vol. 58, no. 1, pp. 1340–1354, 2021.
- [52] Y. Zhang, Z. Yan, J. Zhu, S. Li, and C. Mi, "A review of foreign object detection (fod) for inductive power transfer systems," *eTransportation*, vol. 1, p. 100002, 2019.
- [53] D. Bortis, L. Fässler, A. Looser, and J. W. Kolar, "Analysis of rotary transformer concepts for high-speed applications," in *2013 Twenty-Eighth Annual IEEE Applied Power Electronics Conference and Exposition (APEC)*. IEEE, 2013, pp. 3262–3269.
- [54] S. Bandyopadhyay, P. Venugopal, J. Dong, and P. Bauer, "Comparison of magnetic couplers for ipt-based ev charging using multi-objective optimization," *IEEE Transactions on Vehicular Technology*, vol. 68, no. 6, pp. 5416–5429, 2019.
- [55] R. Bosshard, J. Mühlethaler, J. W. Kolar, and I. Stevanović, "Optimized magnetic design for inductive power transfer coils," in *2013 Twenty-Eighth Annual IEEE Applied Power Electronics Conference and Exposition (APEC)*. IEEE, 2013, pp. 1812–1819.
- [56] R. Bosshard *et al.*, "Comprehensive evaluation of rectangular and double-d coil geometry for 50 kw/85 khz ipt system," *IEEE Journal of Emerging and Selected Topics in Power Electronics*, vol. 4, no. 4, pp. 1406–1415, 2016.
- [57] A. Zaheer, G. A. Covic, and D. Kacprzak, "A bipolar pad in a 10-khz 300-w distributed ipt system for agv applications," *IEEE Transactions on Industrial Electronics*, vol. 61, no. 7, pp. 3288–3301, 2013.
- [58] G. A. Covic, M. L. Kissin, D. Kacprzak, N. Clausen, and H. Hao, "A bipolar primary pad topology for ev stationary charging and highway power by inductive coupling," in *2011 IEEE energy conversion congress and exposition*. IEEE, 2011, pp. 1832–1838.
- [59] A. Zaheer, D. Kacprzak, and G. A. Covic, "A bipolar receiver pad in a lumped ipt system for electric vehicle charging applications," in *2012 IEEE Energy Conversion Congress and Exposition (ECCE)*. IEEE, 2012, pp. 283–290.
- [60] S. Kim, G. A. Covic, and J. T. Boys, "Tripolar pad for inductive power transfer systems for ev charging," *IEEE Transactions on Power Electronics*, vol. 32, no. 7, pp. 5045–5057, 2016.
- [61] L. Chen, G. R. Nagendra, J. T. Boys, and G. A. Covic, "Double-coupled systems for ipt roadway applications," *IEEE Journal of Emerging and Selected Topics in Power Electronics*, vol. 3, no. 1, pp. 37–49, 2014.
- [62] D. Patil, M. K. Mcdonough, J. M. Miller, B. Fahimi, and P. T. Balsara, "Wireless power transfer for vehicular applications: Overview and challenges," *IEEE Transactions on Transportation Electrification*, vol. 4, no. 1, pp. 3–37, 2017.
- [63] C.-S. Wang, O. H. Stielau, and G. A. Covic, "Design considerations for a contactless electric vehicle battery charger," *IEEE Transactions on industrial electronics*, vol. 52, no. 5, pp. 1308–1314, 2005.

- [64] A. Dayerizadeh, H. Feng, and S. M. Lukic, "Dynamic wireless charging: Reflexive field containment using saturable inductors," *IEEE Transactions on Industry Applications*, vol. 56, no. 2, pp. 1784–1792, 2020.
- [65] J. Huh, S. W. Lee, W. Y. Lee, G. H. Cho, and C. T. Rim, "Narrow-width inductive power transfer system for online electrical vehicles," *IEEE Transactions on Power Electronics*, vol. 26, no. 12, pp. 3666–3679, 2011.
- [66] S. Y. Choi, S. Y. Jeong, B. W. Gu, G. C. Lim, and C. T. Rim, "Ultraslim s-type power supply rails for roadway-powered electric vehicles," *IEEE Transactions on Power Electronics*, vol. 30, no. 11, pp. 6456–6468, 2015.
- [67] G. Elliott, J. Boys, and G. Covic, "A design methodology for flat pick-up icpt systems," in *2006 1ST IEEE conference on industrial electronics and applications*. IEEE, 2006, pp. 1–7.
- [68] B.-M. Song, R. Kratz, and S. Gurol, "Contactless inductive power pickup system for maglev applications," in *Conference Record of the 2002 IEEE Industry Applications Conference. 37th IAS Annual Meeting (Cat. No. 02CH37344)*, vol. 3. IEEE, 2002, pp. 1586–1591.
- [69] J. Huh, W. Lee, G.-H. Cho, B. Lee, and C.-T. Rim, "Characterization of novel inductive power transfer systems for on-line electric vehicles," in *2011 Twenty-Sixth Annual IEEE Applied Power Electronics Conference and Exposition (APEC)*. IEEE, 2011, pp. 1975–1979.
- [70] G. A. Covic and J. T. Boys, "Modern trends in inductive power transfer for transportation applications," *IEEE Journal of Emerging and Selected topics in power electronics*, vol. 1, no. 1, pp. 28–41, 2013.
- [71] S. Li and C. C. Mi, "Wireless power transfer for electric vehicle applications," *IEEE journal of emerging and selected topics in power electronics*, vol. 3, no. 1, pp. 4–17, 2014.
- [72] J. Shin, S. Shin, Y. Kim, S. Ahn, S. Lee, G. Jung, S.-J. Jeon, and D.-H. Cho, "Design and implementation of shaped magnetic-resonance-based wireless power transfer system for roadway-powered moving electric vehicles," *IEEE Transactions on Industrial electronics*, vol. 61, no. 3, pp. 1179–1192, 2013.
- [73] O. C. Onar, J. M. Miller, S. L. Campbell, C. Coomer, C. P. White, and L. E. Seiber, "A novel wireless power transfer for in-motion ev/phev charging," in *2013 Twenty-Eighth Annual IEEE Applied Power Electronics Conference and Exposition (APEC)*. IEEE, 2013, pp. 3073–3080.
- [74] J. M. Miller, O. C. Onar, C. White, S. Campbell, C. Coomer, L. Seiber, R. Sepe, and A. Steyerl, "Demonstrating dynamic wireless charging of an electric vehicle: The benefit of electrochemical capacitor smoothing," *IEEE Power Electronics Magazine*, vol. 1, no. 1, pp. 12–24, 2014.

- [75] A. N. Azad, A. Echols, V. A. Kulyukin, R. Zane, and Z. Pantic, "Analysis, optimization, and demonstration of a vehicular detection system intended for dynamic wireless charging applications," *IEEE Transactions on Transportation Electrification*, vol. 5, no. 1, pp. 147–161, 2018.
- [76] V. Z. Barsari, D. J. Thrimawithana, and G. A. Covic, "An inductive coupler array for in-motion wireless charging of electric vehicles," *IEEE Transactions on Power Electronics*, vol. 36, no. 9, pp. 9854–9863, 2021.
- [77] K. Song, C. Zhu, K.-E. Koh, D. Kobayashi, T. Imura, and Y. Hori, "Modeling and design of dynamic wireless power transfer system for ev applications," in *IECON 2015-41st Annual Conference of the IEEE Industrial Electronics Society*. IEEE, 2015, pp. 005 229–005 234.
- [78] X. Zhang, Z. Yuan, Q. Yang, Y. Li, J. Zhu, and Y. Li, "Coil design and efficiency analysis for dynamic wireless charging system for electric vehicles," *IEEE Transactions on Magnetics*, vol. 52, no. 7, pp. 1–4, 2016.
- [79] Y. Li, J. Hu, T. Lin, X. Li, F. Chen, Z. He, and R. Mai, "A new coil structure and its optimization design with constant output voltage and constant output current for electric vehicle dynamic wireless charging," *IEEE Transactions on Industrial Informatics*, vol. 15, no. 9, pp. 5244–5256, 2019.
- [80] T. Campi, S. Cruciani, F. Maradei, and M. Feliziani, "Magnetic field mitigation by multicoil active shielding in electric vehicles equipped with wireless power charging system," *IEEE Transactions on Electromagnetic Compatibility*, vol. 62, no. 4, pp. 1398–1405, 2020.
- [81] W. Li, H. Zhao, J. Deng, S. Li, and C. C. Mi, "Comparison study on ss and double-sided lcc compensation topologies for ev/phev wireless chargers," *IEEE Transactions on Vehicular Technology*, vol. 65, no. 6, pp. 4429–4439, 2015.
- [82] V.-B. Vu, D.-H. Tran, and W. Choi, "Implementation of the constant current and constant voltage charge of inductive power transfer systems with the double-sided lcc compensation topology for electric vehicle battery charge applications," *IEEE Transactions on Power Electronics*, vol. 33, no. 9, pp. 7398–7410, 2017.
- [83] Y. Chen, H. Zhang, C.-S. Shin, C.-H. Jo, S.-J. Park, and D.-H. Kim, "An efficiency optimization-based asymmetric tuning method of double-sided lcc compensated wpt system for electric vehicles," *IEEE Transactions on Power Electronics*, vol. 35, no. 11, pp. 11 475–11 487, 2020.
- [84] D. McRobbie, "Concerning guidelines for limiting exposure to time-varying electric, magnetic, and electromagnetic fields (1 hz–100 khz)," *Health physics*, vol. 100, no. 4, p. 442, 2011.
- [85] U. K. Madawala, M. Neath, and D. J. Thrimawithana, "A power–frequency controller for bidirectional inductive power transfer systems," *IEEE Transactions on Industrial Electronics*, vol. 60, no. 1, pp. 310–317, 2011.

- [86] H. H. Wu, A. Gilchrist, K. D. Sealy, and D. Bronson, "A high efficiency 5 kw inductive charger for evs using dual side control," *IEEE Transactions on Industrial Informatics*, vol. 8, no. 3, pp. 585–595, 2012.
- [87] Z. U. Zahid, Z. M. Dalala, C. Zheng, R. Chen, W. E. Faraci, J.-S. J. Lai, G. Lisi, and D. Anderson, "Modeling and control of series-series compensated inductive power transfer system," *IEEE Journal of Emerging and Selected Topics in Power Electronics*, vol. 3, no. 1, pp. 111–123, 2014.
- [88] J.-Y. Lee and B.-M. Han, "A bidirectional wireless power transfer ev charger using self-resonant pwm," *IEEE Transactions on Power Electronics*, vol. 30, no. 4, pp. 1784–1787, 2014.
- [89] B. X. Nguyen, D. M. Vilathgamuwa, G. H. B. Foo, P. Wang, A. Ong, U. K. Madawala, and T. D. Nguyen, "An efficiency optimization scheme for bidirectional inductive power transfer systems," *IEEE Transactions on Power Electronics*, vol. 30, no. 11, pp. 6310–6319, 2014.
- [90] K. Colak, E. Asa, M. Bojarski, D. Czarkowski, and O. C. Onar, "A novel phase-shift control of semibridgeless active rectifier for wireless power transfer," *IEEE Transactions on Power Electronics*, vol. 30, no. 11, pp. 6288–6297, 2015.
- [91] R. Bosshard *et al.*, "Modeling and η - α -pareto optimization of inductive power transfer coils for electric vehicles," *IEEE Journal of Emerging and Selected Topics in Power Electronics*, vol. 3, no. 1, pp. 50–64, 2014.
- [92] S. Bandyopadhyay *et al.*, "Multi-objective optimisation of a 1-kw wireless ipt systems for charging of electric vehicles," in *2016 IEEE Transportation Electrification Conference and Expo (ITEC)*. IEEE, 2016, pp. 1–7.
- [93] R. Bosshard *et al.*, "Multi-objective optimization of 50 kw/85 khz ipt system for public transport," *IEEE Journal of Emerging and Selected Topics in Power Electronics*, vol. 4, no. 4, pp. 1370–1382, 2016.
- [94] M. Lu *et al.*, "A fast method to optimize efficiency and stray magnetic field for inductive-power-transfer coils using lumped-loops model," *IEEE Transactions on Power Electronics*, vol. 33, no. 4, pp. 3065–3075, 2017.
- [95] T. Guillod, P. Papamanolis, and J. W. Kolar, "Artificial neural network (ann) based fast and accurate inductor modeling and design," *IEEE Open Journal of Power Electronics*, vol. 1, pp. 284–299, 2020.
- [96] C. Serpico *et al.*, "Magnetic hysteresis modeling via feed-forward neural networks," *IEEE Transactions on Magnetics*, vol. 34, no. 3, pp. 623–628, 1998.
- [97] S. Cincotti *et al.*, "A neural network model of parametric nonlinear hysteretic inductors," *IEEE transactions on magnetics*, vol. 34, no. 5, pp. 3040–3043, 1998.
- [98] S. Li *et al.*, "A double-sided lcc compensation network and its tuning method for wireless power transfer," *IEEE transactions on Vehicular Technology*, vol. 64, no. 6, pp. 2261–2273, 2014.

- [99] A. Kamineni, G. A. Covic, and J. T. Boys, "Analysis of coplanar intermediate coil structures in inductive power transfer systems," *IEEE Transactions on Power Electronics*, vol. 30, no. 11, pp. 6141–6154, 2014.
- [100] C. C. Mi, G. Buja, S. Y. Choi, and C. T. Rim, "Modern advances in wireless power transfer systems for roadway powered electric vehicles," *IEEE Transactions on Industrial Electronics*, vol. 63, no. 10, pp. 6533–6545, 2016.
- [101] A. A. Mohamed, C. R. Lashway, and O. Mohammed, "Modeling and feasibility analysis of quasi-dynamic wpt system for ev applications," *IEEE transactions on transportation electrification*, vol. 3, no. 2, pp. 343–353, 2017.
- [102] J. M. Miller, P. T. Jones, J.-M. Li, and O. C. Onar, "Ornl experience and challenges facing dynamic wireless power charging of ev's," *IEEE Circuits and Systems Magazine*, vol. 15, no. 2, pp. 40–53, 2015.
- [103] L. Hutchinson, B. Waterson, B. Anvari, and D. Naberezhnykh, "Potential of wireless power transfer for dynamic charging of electric vehicles," *IET intelligent transport systems*, vol. 13, no. 1, pp. 3–12, 2019.
- [104] S. Inoue, R. Nimri, A. Kamineni, and R. Zane, "High-resolution design optimization for ipt including stray field and coupling coefficient," in *2021 IEEE Applied Power Electronics Conference and Exposition (APEC)*. IEEE, 2021, pp. 1573–1579.
- [105] H. Li, Y. Liu, K. Zhou, Z. He, W. Li, and R. Mai, "Uniform power ipt system with three-phase transmitter and bipolar receiver for dynamic charging," *IEEE Transactions on Power Electronics*, vol. 34, no. 3, pp. 2013–2017, 2018.
- [106] H. Feng, T. Cai, S. Duan, J. Zhao, X. Zhang, and C. Chen, "An lcc-compensated resonant converter optimized for robust reaction to large coupling variation in dynamic wireless power transfer," *IEEE Transactions on Industrial Electronics*, vol. 63, no. 10, pp. 6591–6601, 2016.
- [107] D. M. Vilathgamuwa and J. Sampath, "Wireless power transfer (wpt) for electric vehicles (evs)—present and future trends," in *Plug in electric vehicles in smart grids*. Springer, 2015, pp. 33–60.
- [108] Z. Zhang, H. Pang, A. Georgiadis, and C. Cecati, "Wireless power transfer—an overview," *IEEE Transactions on Industrial Electronics*, vol. 66, no. 2, pp. 1044–1058, 2018.
- [109] G. Di Capua, A. Maffucci, K. Stoyka, G. Di Mambro, S. Ventre, V. Cirimele, F. Freschi, F. Villone, and N. Femia, "Analysis of dynamic wireless power transfer systems based on behavioral modeling of mutual inductance," *Sustainability*, vol. 13, no. 5, p. 2556, 2021.
- [110] Y. J. Jang, E. S. Suh, and J. W. Kim, "System architecture and mathematical models of electric transit bus system utilizing wireless power transfer technology," *IEEE Systems Journal*, vol. 10, no. 2, pp. 495–506, 2015.

- [111] S. Inoue, R. Nimri, A. Kamineni, and R. Zane, “A new design optimization method for dynamic inductive power transfer systems utilizing a neural network,” in *2021 IEEE Energy Conversion Congress and Exposition (ECCE)*. IEEE, 2021, pp. 1496–1501.
- [112] M. Lu and K. D. Ngo, “Circuit models and fast optimization of litz shield for inductive-power-transfer coils,” *IEEE Transactions on Power Electronics*, vol. 34, no. 5, pp. 4678–4688, 2018.
- [113] G. Tsekouras, S. Kiartzis, A. Kladas, and J. Tegopoulos, “Neural network approach compared to sensitivity analysis based on finite element technique for optimization of permanent magnet generators,” *IEEE Transactions on Magnetics*, vol. 37, no. 5, pp. 3618–3621, 2001.
- [114] A. Sadeghian and J. Lavers, “Implementation of knowledge-based system for iron core inductor design,” *IEEE transactions on magnetics*, vol. 40, no. 6, pp. 3495–3504, 2004.
- [115] S. Shimokawa, H. Oshima, K. Shimizu, Y. Uehara, J. Fujisaki, A. Furuya, and H. Igarashi, “Fast 3-d optimization of magnetic cores for loss and volume reduction,” *IEEE transactions on magnetics*, vol. 54, no. 11, pp. 1–4, 2018.
- [116] E. Waffenschmidt, “Homogeneous magnetic coupling for free positioning in an inductive wireless power system,” *IEEE journal of emerging and selected topics in power electronics*, vol. 3, no. 1, pp. 226–233, 2014.
- [117] M. Lu *et al.*, “Synergetic optimization of efficiency and stray magnetic field for planar coils in inductive power transfer using matrix calculation,” in *2017 IEEE Applied Power Electronics Conference and Exposition (APEC)*. IEEE, 2017, pp. 3654–3660.
- [118] I. Goodfellow, Y. Bengio, and A. Courville, *Deep Learning*. MIT Press, 2016, <http://www.deeplearningbook.org>.
- [119] J. Kamruzzaman and S. M. Aziz, “A note on activation function in multilayer feedforward learning,” in *Proceedings of the 2002 International Joint Conference on Neural Networks. IJCNN'02 (Cat. No. 02CH37290)*, vol. 1. IEEE, 2002, pp. 519–523.
- [120] J. H. Holland, *Adaptation in natural and artificial systems: an introductory analysis with applications to biology, control, and artificial intelligence*. MIT press, 1992.
- [121] S. Katoch, S. S. Chauhan, and V. Kumar, “A review on genetic algorithm: past, present, and future,” *Multimedia Tools and Applications*, vol. 80, no. 5, pp. 8091–8126, 2021.
- [122] A. J. Umbarkar and P. D. Sheth, “Crossover operators in genetic algorithms: a review.” *ICTACT journal on soft computing*, vol. 6, no. 1, 2015.
- [123] T. Guillod, J. Huber, F. Krismer, and J. W. Kolar, “Litz wire losses: Effects of twisting imperfections,” in *2017 IEEE 18th Workshop on Control and Modeling for Power Electronics (COMPEL)*. IEEE, 2017, pp. 1–8.

- [124] J.-G. Cho, J.-W. Baek, C.-Y. Jeong, and G.-H. Rim, "Novel zero-voltage and zero-current-switching full-bridge pwm converter using a simple auxiliary circuit," *IEEE Transactions on Industry applications*, vol. 35, no. 1, pp. 15–20, 1999.
- [125] S. International, "SAE TIR J2954/2: Wireless Power Transfer and Alignment for Heavy Duty Applications," SAE International, Technical Information Report Appendix A, 2022. [Online]. Available: <https://www.sae.org/standards/content/j2954/2.202212/>
- [126] S. Inoue, C. R. Teeneti, D. Goodrich, J. Larsen, A. Kamineni, and R. Zane, "High-power field-focusing circuit for dynamic wireless power transfer systems," in *2022 Wireless Power Week (WPW)*. IEEE, 2022, pp. 699–704.
- [127] S. Inoue, D. Goodrich, S. Saha, R. Nimri, A. Kamineni, N. S. Flann, and R. A. Zane, "Fast design optimization method utilizing a combination of artificial neural networks and genetic algorithms for dynamic inductive power transfer systems," *IEEE Open Journal of Power Electronics*, 2022, [DOI: 10.1109/OJPEL.2022.3224422].
- [128] S. Inoue, S. Kiguthi, J. Newman, T. Goodale, C. R. Teeneti, B. Hesterman, A. Kamineni, and R. A. Zane, "A 50 kw dynamic inductive power transfer system with reflexive tuning networks," *IEEE Transaction on Power Electronics*, 2022, [Under review process].

APPENDICES

APPENDIX A

Python code for the ANN-based design optimization

A.1 User input

```
1 # Import libraries
2 import torch
3 from torch import tensor
4 from torch import nn
5 from torch import sigmoid
6 from torch import atan
7 from torch import tanh
8 import pandas as pd
9 import numpy as np
10 import torch.optim as optim
11 from sklearn.metrics import mean_squared_error
12 from sklearn.model_selection import train_test_split
13
14 # Import FEM data
15 from google.colab import drive
16 drive.mount('/content/drive')
17 foldername = '/content/drive/MyDrive/2021_Fall/
18     OptimizationPipeline_DoubleLCCL3kW/2_FEM/8parameters_gap250mm/'
19
20 filename = 'result_all'
21
22 df = pd.read_csv(foldername+filename+'.csv')
23
24 df.to_csv(foldername+'/alldata.csv')
25 df
```

A.2 Define training and validation data

```

1 # Initialize RNG except to PyTorch
2 import random
3 import statistics
4 seed = 111
5 random.seed(seed)
6 np.random.seed(seed)
7 # Initialize RNG of PyTorch
8 torch.manual_seed(seed)
9
10 # Defining Training data
11 x_df = df.loc[:, 'ax[mm]':'ys4[mm]']
12 y1_df = df.loc[:, 'k_xs0_ys0':'Ls_xs1_ys0[nH]']
13 y2_df = df.loc[:, 'Bx_p_xs0_0deg[uT]':'Bz_s_xs1_90deg[uT]']
14 y_df = pd.concat([y1_df, y2_df], axis=1)
15
16 x_np=0
17 y_np=0
18 dtype = torch.float
19 device = torch.device("cuda:0" if torch.cuda.is_available() else "cpu")
20 x_np = x_df.values
21 y_np = y_df.values
22
23 def min_max(x_sample, x, axis=0):# axis=0 is vertical direction.
24     min_x = x_sample.min(axis=axis, keepdims=True)
25     max_x = x_sample.max(axis=axis, keepdims=True)
26     result = (x-min_x)/(max_x-min_x)
27     return result
28
29 def inv_min_max(x_sample, x_std, axis=0):
30     min_x = x_sample.min(axis=axis, keepdims=True)
31     max_x = x_sample.max(axis=axis, keepdims=True)
32     result = x_std*(max_x-min_x)+min_x
33     return result
34
35 x_np_std = min_max(x_np, x_np)

```

```

36 y_np_std = min_max(y_np, y_np)
37
38 cls=['k_xs0_ys0','k_xs0_ys1', 'k_xs0_ys2', 'k_xs0_ys3', 'k_xs0_ys4', '
      k_xs1_ys0',\
39 'Lp_xs0_ys0[nH]', 'Lp_xs0_ys1[nH]', 'Lp_xs0_ys2[nH]', 'Lp_xs0_ys3[nH]', '
      Lp_xs0_ys4[nH]',\
40 'Ls_xs0_ys0[nH]', 'Ls_xs0_ys1[nH]', 'Ls_xs0_ys2[nH]', 'Ls_xs0_ys3[nH]', '
      Ls_xs0_ys4[nH]',\
41 'Lp_xs1_ys0[nH]', 'Ls_xs1_ys0[nH]',\
42 'Bx_p_xs0_0deg[uT]', 'By_p_xs0_0deg[uT]', 'Bz_p_xs0_0deg[uT]',\
43 'Bx_p_xs0_90deg[uT]', 'By_p_xs0_90deg[uT]', 'Bz_p_xs0_90deg[uT]',\
44 'Bx_s_xs0_0deg[uT]', 'By_s_xs0_0deg[uT]', 'Bz_s_xs0_0deg[uT]',\
45 'Bx_s_xs0_90deg[uT]', 'By_s_xs0_90deg[uT]', 'Bz_s_xs0_90deg[uT]',\
46 'Bx_p_xs1_0deg[uT]', 'By_p_xs1_0deg[uT]', 'Bz_p_xs1_0deg[uT]',\
47 'Bx_p_xs1_90deg[uT]', 'By_p_xs1_90deg[uT]', 'Bz_p_xs1_90deg[uT]',\
48 'Bx_s_xs1_0deg[uT]', 'By_s_xs1_0deg[uT]', 'Bz_s_xs1_0deg[uT]',\
49 'Bx_s_xs1_90deg[uT]', 'By_s_xs1_90deg[uT]', 'Bz_s_xs1_90deg[uT]']
50
51 df_y_std      = pd.DataFrame(y_np_std[:, :42], columns=cls)
52
53 df_y_std.to_csv(foldername+'/alldata_std.csv')
54
55 df_y_std
56
57 x_tensor=torch.tensor(x_np_std)
58 y_tensor=torch.tensor(y_np_std)
59
60 # Deviding to training and validation data
61 n_samples = x_tensor.shape[0]#Get the shape of the data, [150, 1] and output
      first one, 150.
62 n_val = int(0.022*n_samples)
63 shuffled_indices = torch.randperm(n_samples)
64
65 train_indices = shuffled_indices[:n_samples-n_val]
66 val_indices = shuffled_indices[n_samples-n_val:]

```

```

67
68 x_train = x_tensor[train_indices]
69 y_train = y_tensor[train_indices]
70 x_val = x_tensor[val_indices]
71 y_val = y_tensor[val_indices]
72
73 x_train = x_train.to(device)
74 x_train = x_train.to(dtype)
75 x_val = x_val.to(device)
76 x_val = x_val.to(dtype)
77
78 y_train = y_train.to(device)
79 y_train = y_train.to(dtype)
80 y_val = y_val.to(device)
81 y_val = y_val.to(dtype)
82 # shape(y_val)

```

A.3 Neural network process

STEP 1: Design a model

```

1 # STEP 1: Design your model using class
2 class Model(nn.Module):
3     def __init__(self):
4         #In the constructor, we instantiate nn.Linear module.
5         super(Model, self).__init__()
6         self.linear1 = nn.Linear(13, 100, bias=True).cuda()
7         self.linear2 = nn.Linear(100,100, bias=True).cuda()
8         self.linear3 = nn.Linear(100, 42, bias=True).cuda()
9
10    def forward(self, x):
11        x = atan(self.linear1(x))
12        x = atan(self.linear2(x))
13        x = atan(self.linear2(x))
14        y_pred = self.linear3(x)

```

```

15     return y_pred
16 # our model
17 model=Model()

```

STEP 2: Define loss function and optimizer

```

1 # STEP 2: Construct loss and optimizer
2 # Construct our loss function and an Optimizer. The call to model.
   parameters()
3 # in the SGD constructor will contain the learnable parameters of the two
4 # nn.Linear moduled which are members of the model.
5 criterion_L2 = nn.MSELoss(reduction='mean')
6 #size_avarage define whethere devide by bach-size or not.
7 optimizer = optim.SGD(model.parameters(), lr=0.5, momentum=0.9, dampening
   =0.0, weight_decay=0.0,nesterov=False)# atan

```

STEP 3: Training cycle

```

1 # STEP 3: Training cycle (forward, backward, update)
2 import math
3 n_epochs = 170000
4 loss_train_history=[]
5 loss_val_history=[]
6 loss_val_2_history=[]
7 loss_val_3_history=[]
8 loss_val_MAPE_history=[]
9
10 loss_val_k_xs0_ys0_history=[]
11 loss_val_k_xs0_ys1_history=[]
12 loss_val_k_xs0_ys2_history=[]
13 loss_val_k_xs0_ys3_history=[]
14 loss_val_k_xs0_ys4_history=[]
15 loss_val_k_xs1_ys0_history=[]
16
17 loss_val_Lp_xs0_ys0_history=[]

```

```
18 loss_val_Lp_xs0_ys1_history=[]
19 loss_val_Lp_xs0_ys2_history=[]
20 loss_val_Lp_xs0_ys3_history=[]
21 loss_val_Lp_xs0_ys4_history=[]
22 loss_val_Lp_xs1_ys0_history=[]
23
24 loss_val_Ls_xs0_ys0_history=[]
25 loss_val_Ls_xs0_ys1_history=[]
26 loss_val_Ls_xs0_ys2_history=[]
27 loss_val_Ls_xs0_ys3_history=[]
28 loss_val_Ls_xs0_ys4_history=[]
29 loss_val_Ls_xs1_ys0_history=[]
30
31 loss_val_Bp_xs0_ys0_history=[]
32 loss_val_Bs_xs0_ys0_history=[]
33 loss_val_Bp_xs1_ys0_history=[]
34 loss_val_Bs_xs1_ys0_history=[]
35
36 loss_val_kdiff_history=[]
37 loss_val_Pripple_history=[]
38 loss_val_Pave_history=[]
39 loss_val_CoilLoss_history=[]
40 loss_val_Bstray_history=[]
41
42 loss_val_Bx_p_xs0_0deg_history = []
43 loss_val_By_p_xs0_0deg_history = []
44 loss_val_Bz_p_xs0_0deg_history = []
45 loss_val_Bx_p_xs0_90deg_history = []
46 loss_val_By_p_xs0_90deg_history = []
47 loss_val_Bz_p_xs0_90deg_history = []
48
49 loss_val_Bx_s_xs0_0deg_history = []
50 loss_val_By_s_xs0_0deg_history = []
51 loss_val_Bz_s_xs0_0deg_history = []
52 loss_val_Bx_s_xs0_90deg_history = []
```

```

53 loss_val_By_s_xs0_90deg_history = []
54 loss_val_Bz_s_xs0_90deg_history = []
55
56 loss_val_Bx_p_xs1_0deg_history = []
57 loss_val_By_p_xs1_0deg_history = []
58 loss_val_Bz_p_xs1_0deg_history = []
59 loss_val_Bx_p_xs1_90deg_history = []
60 loss_val_By_p_xs1_90deg_history = []
61 loss_val_Bz_p_xs1_90deg_history = []
62
63 loss_val_Bx_s_xs1_0deg_history = []
64 loss_val_By_s_xs1_0deg_history = []
65 loss_val_Bz_s_xs1_0deg_history = []
66 loss_val_Bx_s_xs1_90deg_history = []
67 loss_val_By_s_xs1_90deg_history = []
68 loss_val_Bz_s_xs1_90deg_history = []
69
70 def MAPE(x_true, x_pred, axis=0):
71     result = (x_pred-x_true).abs()/torch.max(x_true.abs(), x_pred.abs())
72     return result
73
74 loss_val_Bstray=[]
75 m = len(y_train[:,0])
76 for epoch in range(n_epochs+1):
77     # Forward pass: Compute predicted y by passing x to the model
78     y_pred_train = model(x_train)
79     loss_train = criterion_L2(y_pred_train[:,0:42], y_train[:,0:42])
80     loss_train_history.append(loss_train.item())
81     y_pred_val =model(x_val)
82     loss_val = criterion_L2(y_pred_val[:,0:42], y_val[:,0:42])
83     loss_val_history.append(loss_val.item())
84     loss_val_MAPE = torch.mean(MAPE(y_pred_val[:,42], y_val[:,42]))
85     loss_val_MAPE_history.append(loss_val_MAPE.item())
86
87     if epoch ==1 or epoch % 10000 ==0:

```

```

88
89     print(f'Epoch {epoch}/{n_epochs} | Training L2 error [%]: {(loss_train.
90         item())**0.5*100: .4f} | Validation L2 error [%]: {(loss_val.item())
91         **0.5*100: .4f} \
92         | Validation MAPE [%]: {(loss_val_MAPE.item())*100: .4f}')
93
94     # Zero gradients, perform a backward pass, and update the weights.
95     optimizer.zero_grad()
96     loss_train.backward()
97
98     optimizer.step()

```

STEP 4: Check accuracy

```

1 !pip install SciencePlots
2 # User input
3 # Setting for academic papers
4
5 import matplotlib
6 import matplotlib.pyplot as plt
7 from matplotlib import rc
8 import scienceplots
9
10 # User input
11 # Setting for paper
12 fig_width = 8 #cm
13 fig_height = 3 #cm
14 font_size = 10 # pt
15 from matplotlib import rc
16 %matplotlib inline
17 from pylab import *
18
19
20 path = '/content/drive/My Drive/Improving/Python_cards/matplot/SciencePlots-
    master/styles/'

```

```
21 plt.style.use('seaborn-whitegrid')
22 plt.style.use([path+'misc/grid.mplstyle'])
23 plt.style.use([path+'journals/ieee.mplstyle'])
24 plt.style.use(['science','no-latex'])# ref: https://github.com/garrettj403/
    SciencePlots
25
26 matplotlib.rcParams.update({'font.size': font_size, 'font.family': '
    STIXGeneral', 'mathtext.fontset': 'stix'})
27
28 def cm2inch(value):
29     return value/2.54
30 fig1=plt.figure(figsize=(cm2inch(fig_width),cm2inch(fig_height)), dpi=300)
31
32 epoch=[]
33 for i in range(n_epochs+1):
34     epoch.append(i/1000)
35
36 arr_loss_train = np.array(loss_train_history)
37 arr_loss_val = np.array(loss_val_history)
38 arr_loss_val_MAPE = np.array(loss_val_MAPE_history)
39
40 train_loss=[]
41 val_loss=[]
42 val_loss_k_xs0_ys0=[]
43 val_loss_k_xs0_ys1=[]
44 val_loss_k_xs0_ys2=[]
45 val_loss_k_xs0_ys3=[]
46 val_loss_k_xs0_ys4=[]
47 val_loss_k_xs1_ys0=[]
48
49 val_loss_Lp_xs0_ys0=[]
50 val_loss_Lp_xs0_ys1=[]
51 val_loss_Lp_xs0_ys2=[]
52 val_loss_Lp_xs0_ys3=[]
53 val_loss_Lp_xs0_ys4=[]
```

```

54
55 val_loss_Ls_xs0_ys0=[]
56 val_loss_Ls_xs0_ys1=[]
57 val_loss_Ls_xs0_ys2=[]
58 val_loss_Ls_xs0_ys3=[]
59 val_loss_Ls_xs0_ys4=[]
60
61 val_loss_Lp_xs1_ys0=[]
62 val_loss_Ls_xs1_ys0=[]
63
64 val_loss_Bp_xs0_ys0=[]
65 val_loss_Bs_xs0_ys0=[]
66 val_loss_Bp_xs1_ys0=[]
67 val_loss_Bs_xs1_ys0=[]
68
69 val_loss_CoilLoss=[]
70 val_loss_kdiff=[]
71 val_loss_Prippl=[]
72 val_loss_Pave=[]
73 val_loss_Bstray=[]
74
75 lw = 0.5
76 p3,=plt.plot(epoch,(arr_loss_val_MAPE)*100, "g-", linewidth=1, label="
    Validation error")
77 plt.xlabel(r"Number of calculation iterations ( $\times 10^3$ )")
78 plt.ylabel(r"Validation error [%]")
79 plt.axis([0, n_epochs/1000, 0, 20])
80 plt.tick_params(axis = 'both', which = 'major', length = 4, direction = 'in')
81 plt.tick_params(axis = 'both', which = 'minor', length = 2, direction = 'in')

```

A.4 Save the created model

```

1 torch.save(model.state_dict(), '/content/drive/MyDrive/2022_Summer/Python/
    GA_for_OpenPE/saved_model_for_8parameters_V2.pt')

```

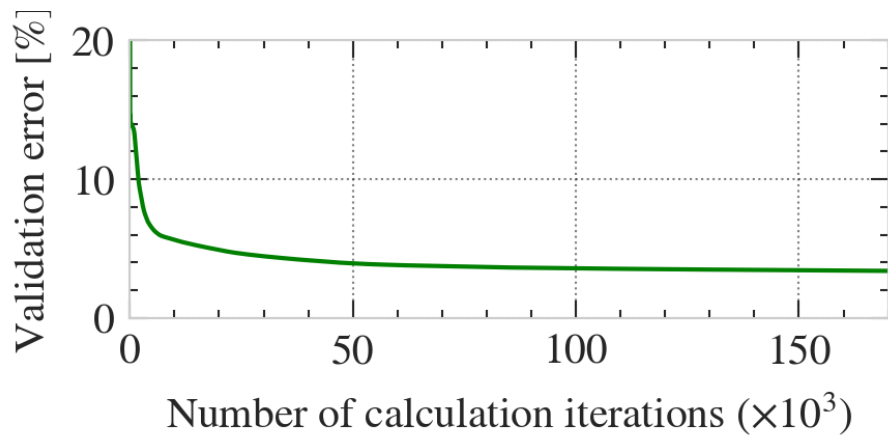


Fig. A.1: Output of the source code: Prediction error with respect to the number of iterative calculations

```
2 model.load_state_dict(torch.load('/content/drive/MyDrive/2022_Summer/Python/
  GA_for_OpenPE/saved_model_for_8parameters_V2.pt'))
```

A.5 Generate random input

```
1 #Load FEM data again
2
3 df = pd.read_csv(foldername+filename+'.csv')
4 import random
5 seed = 7777
6 random.seed(seed)
7 np.random.seed(seed)
8 torch.manual_seed(seed)
9
10 ##### Plot #####
11 #Make spec data in equal intervals
12 import pandas as pd
13 import numpy as np
14
15 N=1000000
16 dp=6.6 #mm
17 ds=6.6 #mm
18
```

```
19 Np_min = 3 #turn
20 Np_max = 7 #turn
21 Ns_min = 3 # 6 #turn
22 Ns_max = 7 # 10 #turn
23
24 lpy_min = 50 #mm
25 lpy_max = 2050 #mm
26 lpx_min = 50 #mm
27 lpx_max = 650 #mm
28 wpy_min = 25 # mm wpy = dp*Np
29 wpy_max = 325 # mm
30 wpx_min = 25 # mm wpx = dp*Np ~ 325
31 wpx_max = 325 # mm
32 ax_min = 0 # mm
33 ax_max = 200 # mm
34 ay_min = 0 # mm
35 ay_max = 0 # mm
36 p_min = 0 # mm
37 p_max = 200 # mm
38 ls_min = 50 # mm
39 ls_max = 450 # mm
40 ws_min = 25 # mm
41 ws_max = 225 # mm
42 Ip_min = 30 # 20 # A rms
43 Ip_max = 70 # 50 # A rms
44 Ip=[]
45 Np=[]
46 Ns=[]
47 ax=[]
48 lpx=[]
49 lpy=[]
50 ls=[]
51 p=[]
52 wpx=[]
53 wpy=[]
```

```

54 ws=[]
55 ys0=[]
56 ys1=[]
57 ys2=[]
58 ys3=[]
59 ys4=[]
60
61 df_x_N = pd.DataFrame(index=[], columns=[])
62
63 import math
64 for i in range(N):
65
66     Np_i = round(random.uniform(Np_min, Np_max),0)
67     Ns_i = round(random.uniform(Ns_min, Ns_max),0)
68     Ip_i = random.uniform(Ip_min, Ip_max) #A(rms)
69     # wpy_i = random.uniform(dp * Np_i, wpy_max)
70     wpy_i = dp * Np_i
71     wpx_i = random.uniform(wpy_i, wpx_max)
72     ax_i = random.uniform(ax_min, ax_max)
73     ay_i = random.uniform(ay_min, ay_max)
74     p_i = random.uniform(p_min, p_max)
75     lpx_i = 0
76     while (lpx_i < lpx_min or lpx_max < lpx_i):
77         lpx_i = round(random.uniform(lpx_min+2*ax_min+2*wpx_min, lpx_max+2*
78             ax_max+2*wpx_max)/25,0)*25-2*ax_i-2*wpx_i
79
80     lpy_i = 0
81     while (lpy_i < lpy_min or lpy_max < lpy_i):
82         lpy_i = round(random.uniform(lpy_min+2*ay_min+2*wpy_min, lpy_max+2*
83             ay_max+2*wpy_max)/25,0)*25-2*ay_i-2*wpy_i
84
85     ws_i = 0
86     while (ws_i < ws_min):
87         ws_i = random.uniform(ds*Ns_i, ws_max)

```

```
87 ls_i = random.uniform(ls_min, ls_max)
88
89 y0_i = (lpy_i+wpy_i)/2
90 y1_i = 3/2*lpy_i+5/2*wpy_i+2*ay_i+p_i
91 ys_min = y1_i # mm
92 ys_max = y1_i+(y1_i-y0_i)/2 # mm
93 ys = np.linspace(ys_min, ys_max,num=5)
94 ys0_i = ys[0]
95 ys1_i = ys[1]
96 ys2_i = ys[2]
97 ys3_i = ys[3]
98 ys4_i = ys[4]
99 Ip.append(Ip_i)
100 Np.append(Np_i)
101 Ns.append(Ns_i)
102 ax.append(ax_i)
103 lpx.append(lpx_i)
104 lpy.append(lpy_i)
105 ls.append(ls_i)
106 p.append(p_i)
107 wpx.append(wpx_i)
108 wpy.append(wpy_i)
109 ws.append(ws_i)
110 ys0.append(ys0_i)
111 ys1.append(ys1_i)
112 ys2.append(ys2_i)
113 ys3.append(ys3_i)
114 ys4.append(ys4_i)
115
116 if i % 200000 ==0:
117     print(f'Calculating... {i}/{N} ')
118
119 df_x_N.insert(0, 'ys4[mm]', ys4)
120 df_x_N.insert(0, 'ys3[mm]', ys3)
121 df_x_N.insert(0, 'ys2[mm]', ys2)
```

```

122 df_x_N.insert(0, 'ys1[mm]', ys1)
123 df_x_N.insert(0, 'ys0[mm]', ys0)
124 df_x_N.insert(0, 'ws[mm]', ws)
125 df_x_N.insert(0, 'wpy[mm]', wpy)
126 df_x_N.insert(0, 'wpx[mm]', wpx)
127 df_x_N.insert(0, 'p[mm]', p)
128 df_x_N.insert(0, 'ls[mm]', ls)
129 df_x_N.insert(0, 'lpy[mm]', lpy)
130 df_x_N.insert(0, 'lpx[mm]', lpx)
131 df_x_N.insert(0, 'ax[mm]', ax)
132 df_x_N.insert(0, 'Ns[turn]', Ns)
133 df_x_N.insert(0, 'Np[turn]', Np)
134 df_x_N.insert(0, 'Ip[A(rms)]', Ip)
135 df_x_N
136 import torch
137 torch.cuda.empty_cache()

```

A.6 Generate prediction data for random input data

```

1 x_df = df.loc[:, 'ax[mm]':'ys4[mm]']
2 y1_df = df.loc[:, 'k_xs0_ys0':'Ls_xs1_ys0[nH]']
3 y2_df = df.loc[:, 'Bx_p_xs0_0deg[uT]':'Bz_s_xs1_90deg[uT]']
4 y_df = pd.concat([y1_df, y2_df], axis=1)
5 x_N_df = df_x_N.loc[:, 'ax[mm]':'ys4[mm]']
6 y_cls = df.columns.values
7
8 import torch
9 import numpy as np
10 x_np = x_df.values
11 y_np = y_df.values
12 x_np_new = x_N_df.values
13
14 dtype = torch.float
15 device = torch.device("cuda:0" if torch.cuda.is_available() else "cpu")
16

```

```

17 def min_max(x_sample, x, axis=0):# axis=0 is vertical direction.
18     min_x = x_sample.min(axis=axis, keepdims=True)
19     max_x = x_sample.max(axis=axis, keepdims=True)
20     result = (x-min_x)/(max_x-min_x)
21     return result
22 def inv_min_max(x_sample, x_std, axis=0):
23     min_x = x_sample.min(axis=axis, keepdims=True)
24     max_x = x_sample.max(axis=axis, keepdims=True)
25     result = x_std*(max_x-min_x)+min_x
26     return result
27
28 x_np_new_std = min_max(x_np, x_np_new)
29 x_tensor=torch.tensor(x_np_new_std)
30
31 #-----
32
33 n_samples = x_tensor.shape[0] #Get the shape of the data, [150, 1] and
    output first one, 150.
34 n_val = int(1.0*n_samples)
35
36 x_val = x_tensor
37
38 x_val = x_val.to(device)
39 x_val = x_val.to(dtype)
40
41 y_std_pred = model(x_val)
42 y_pred = inv_min_max(y_np, y_std_pred.cpu().detach().numpy())
43 x_val_final = inv_min_max(x_np, x_val.cpu().detach().numpy())
44
45 cls=['k_xs0_ys0', 'k_xs0_ys1', 'k_xs0_ys2', 'k_xs0_ys3', 'k_xs0_ys4', '
    k_xs1_ys0',\
46 'Lp_xs0_ys0 [nH]', 'Lp_xs0_ys1 [nH]', 'Lp_xs0_ys2 [nH]', 'Lp_xs0_ys3 [nH]', '
    Lp_xs0_ys4 [nH]',\
47 'Ls_xs0_ys0 [nH]', 'Ls_xs0_ys1 [nH]', 'Ls_xs0_ys2 [nH]', 'Ls_xs0_ys3 [nH]', '
    Ls_xs0_ys4 [nH]',\

```

```

48 'Lp_xs1_ys0[nH]', 'Ls_xs1_ys0[nH]',\
49 'Bx_p_xs0_0deg[uT]', 'By_p_xs0_0deg[uT]', 'Bz_p_xs0_0deg[uT]',\
50 'Bx_p_xs0_90deg[uT]', 'By_p_xs0_90deg[uT]', 'Bz_p_xs0_90deg[uT]',\
51 'Bx_s_xs0_0deg[uT]', 'By_s_xs0_0deg[uT]', 'Bz_s_xs0_0deg[uT]',\
52 'Bx_s_xs0_90deg[uT]', 'By_s_xs0_90deg[uT]', 'Bz_s_xs0_90deg[uT]',\
53 'Bx_p_xs1_0deg[uT]', 'By_p_xs1_0deg[uT]', 'Bz_p_xs1_0deg[uT]',\
54 'Bx_p_xs1_90deg[uT]', 'By_p_xs1_90deg[uT]', 'Bz_p_xs1_90deg[uT]',\
55 'Bx_s_xs1_0deg[uT]', 'By_s_xs1_0deg[uT]', 'Bz_s_xs1_0deg[uT]',\
56 'Bx_s_xs1_90deg[uT]', 'By_s_xs1_90deg[uT]', 'Bz_s_xs1_90deg[uT]' #,\
57 df_y_pred=pd.DataFrame(y_pred, columns=cls)
58 df_x_final=pd.DataFrame(x_val_final, columns=['ax[mm]', 'lpx[mm]', 'lpy[mm]',
59      'ls[mm]',\
60      'p[mm]', 'wpx[mm]', 'wpy[mm]', 'ws[mm]', 'ys0[mm]', 'ys1[mm]', 'ys2[mm]',
61      'ys3[mm]', 'ys4[mm]'])
62
63
64 #Calculate B field from the prediction
65 df_pred = pd.concat([df_x_N.loc[:, 'Ip[A(rms)]': 'Ns[turn]'], df_x_final,
66      df_y_pred], axis=1)
67
68 Bx_p_xs0_0deg = []
69 By_p_xs0_0deg = []
70 Bz_p_xs0_0deg = []
71
72 Bx_p_xs0_90deg = []
73 By_p_xs0_90deg = []
74 Bz_p_xs0_90deg = []
75
76 Bx_p_xs1_0deg = []
77 By_p_xs1_0deg = []
78 Bz_p_xs1_0deg = []
79
80 Bx_p_xs1_90deg = []
81 By_p_xs1_90deg = []

```

```
80 Bz_p_xs1_90deg = []
81
82 Bx_s_xs0_0deg = []
83 By_s_xs0_0deg = []
84 Bz_s_xs0_0deg = []
85
86 Bx_s_xs0_90deg = []
87 By_s_xs0_90deg = []
88 Bz_s_xs0_90deg = []
89
90 Bx_s_xs1_0deg = []
91 By_s_xs1_0deg = []
92 Bz_s_xs1_0deg = []
93
94 Bx_s_xs1_90deg = []
95 By_s_xs1_90deg = []
96 Bz_s_xs1_90deg = []
97
98 import math
99 f = 85*10**3 #[Hz]
100 w =2*math.pi*f #[rad/s]
101 Pout=3300#1500 #W 50000 #W
102 Vdc = 100 # V 800 # V
103 Vbat = 100 # V 400 #V
104 Ip = []
105 Is = []
106 VLp = []
107 VLs = []
108 n1 = []
109 n2 = []
110 Np = []
111 Ns = []
112 Lp_xs0_ys0=[]
113 Lp_xs0_ys1=[]
114 Lp_xs0_ys2=[]
```

```

115 Lp_xs0_ys3=[]
116 Lp_xs0_ys4=[]
117 Ls_xs0_ys0=[]
118 Ls_xs0_ys1=[]
119 Ls_xs0_ys2=[]
120 Ls_xs0_ys3=[]
121 Ls_xs0_ys4=[]
122 Lp_xs1_ys0=[]
123 Ls_xs1_ys0=[]
124 k_xs0_ys0=[]
125 k_xs0_ys1=[]
126 k_xs0_ys2=[]
127 k_xs0_ys3=[]
128 k_xs0_ys4=[]
129 k_xs1_ys0=[]
130 kdiff=[]
131 Pdiff = []
132 df_pred_Bx_p_xs0_0deg=df_pred['Bx_p_xs0_0deg[uT]'] # uT(0-Peak)
133 df_pred_By_p_xs0_0deg=df_pred['By_p_xs0_0deg[uT]'] # uT(0-Peak)
134 df_pred_Bz_p_xs0_0deg=df_pred['Bz_p_xs0_0deg[uT]'] # uT(0-Peak)
135 Bx_p_xs0_0deg =df_pred_Bx_p_xs0_0deg.values
136 By_p_xs0_0deg =df_pred_By_p_xs0_0deg.values
137 Bz_p_xs0_0deg =df_pred_Bz_p_xs0_0deg.values
138
139 df_pred_Bx_p_xs0_90deg=df_pred['Bx_p_xs0_90deg[uT]']
140 df_pred_By_p_xs0_90deg=df_pred['By_p_xs0_90deg[uT]']
141 df_pred_Bz_p_xs0_90deg=df_pred['Bz_p_xs0_90deg[uT]']
142 Bx_p_xs0_90deg =df_pred_Bx_p_xs0_90deg.values
143 By_p_xs0_90deg =df_pred_By_p_xs0_90deg.values
144 Bz_p_xs0_90deg =df_pred_Bz_p_xs0_90deg.values
145
146 df_pred_Bx_p_xs1_0deg=df_pred['Bx_p_xs1_0deg[uT]']
147 df_pred_By_p_xs1_0deg=df_pred['By_p_xs1_0deg[uT]']
148 df_pred_Bz_p_xs1_0deg=df_pred['Bz_p_xs1_0deg[uT]']
149 Bx_p_xs1_0deg =df_pred_Bx_p_xs1_0deg.values

```

```
150 By_p_xs1_0deg =df_pred_By_p_xs1_0deg.values
151 Bz_p_xs1_0deg =df_pred_Bz_p_xs1_0deg.values
152
153 df_pred_Bx_p_xs1_90deg=df_pred['Bx_p_xs1_90deg[uT]']
154 df_pred_By_p_xs1_90deg=df_pred['By_p_xs1_90deg[uT]']
155 df_pred_Bz_p_xs1_90deg=df_pred['Bz_p_xs1_90deg[uT]']
156 Bx_p_xs1_90deg =df_pred_Bx_p_xs1_90deg.values
157 By_p_xs1_90deg =df_pred_By_p_xs1_90deg.values
158 Bz_p_xs1_90deg =df_pred_Bz_p_xs1_90deg.values
159
160 df_pred_Bx_s_xs0_0deg=df_pred['Bx_s_xs0_0deg[uT]']
161 df_pred_By_s_xs0_0deg=df_pred['By_s_xs0_0deg[uT]']
162 df_pred_Bz_s_xs0_0deg=df_pred['Bz_s_xs0_0deg[uT]']
163 Bx_s_xs0_0deg =df_pred_Bx_s_xs0_0deg.values
164 By_s_xs0_0deg =df_pred_By_s_xs0_0deg.values
165 Bz_s_xs0_0deg =df_pred_Bz_s_xs0_0deg.values
166
167 df_pred_Bx_s_xs0_90deg=df_pred['Bx_s_xs0_90deg[uT]']
168 df_pred_By_s_xs0_90deg=df_pred['By_s_xs0_90deg[uT]']
169 df_pred_Bz_s_xs0_90deg=df_pred['Bz_s_xs0_90deg[uT]']
170 Bx_s_xs0_90deg =df_pred_Bx_s_xs0_90deg.values
171 By_s_xs0_90deg =df_pred_By_s_xs0_90deg.values
172 Bz_s_xs0_90deg =df_pred_Bz_s_xs0_90deg.values
173
174 df_pred_Bx_s_xs1_0deg=df_pred['Bx_s_xs1_0deg[uT]']
175 df_pred_By_s_xs1_0deg=df_pred['By_s_xs1_0deg[uT]']
176 df_pred_Bz_s_xs1_0deg=df_pred['Bz_s_xs1_0deg[uT]']
177 Bx_s_xs1_0deg =df_pred_Bx_s_xs1_0deg.values
178 By_s_xs1_0deg =df_pred_By_s_xs1_0deg.values
179 Bz_s_xs1_0deg =df_pred_Bz_s_xs1_0deg.values
180
181 df_pred_Bx_s_xs1_90deg=df_pred['Bx_s_xs1_90deg[uT]']
182 df_pred_By_s_xs1_90deg=df_pred['By_s_xs1_90deg[uT]']
183 df_pred_Bz_s_xs1_90deg=df_pred['Bz_s_xs1_90deg[uT]']
184 Bx_s_xs1_90deg =df_pred_Bx_s_xs1_90deg.values
```

```
185 By_s_xs1_90deg =df_pred_By_s_xs1_90deg.values
186 Bz_s_xs1_90deg =df_pred_Bz_s_xs1_90deg.values
187
188 df_pred_Np = df_pred['Np[turn]']
189 df_pred_Ns = df_pred['Ns[turn]']
190 Np = df_pred_Np.values
191 Ns = df_pred_Ns.values
192
193 df_pred_Lp_xs0_ys0 = df_pred['Lp_xs0_ys0[nH]']
194 df_pred_Lp_xs0_ys1 = df_pred['Lp_xs0_ys1[nH]']
195 df_pred_Lp_xs0_ys2 = df_pred['Lp_xs0_ys2[nH]']
196 df_pred_Lp_xs0_ys3 = df_pred['Lp_xs0_ys3[nH]']
197 df_pred_Lp_xs0_ys4 = df_pred['Lp_xs0_ys4[nH]']
198 pred_Lp_xs0_ys0 = df_pred_Lp_xs0_ys0.values
199 pred_Lp_xs0_ys1 = df_pred_Lp_xs0_ys1.values
200 pred_Lp_xs0_ys2 = df_pred_Lp_xs0_ys2.values
201 pred_Lp_xs0_ys3 = df_pred_Lp_xs0_ys3.values
202 pred_Lp_xs0_ys4 = df_pred_Lp_xs0_ys4.values
203
204 df_pred_Ls_xs0_ys0 = df_pred['Ls_xs0_ys0[nH]']
205 df_pred_Ls_xs0_ys1 = df_pred['Ls_xs0_ys1[nH]']
206 df_pred_Ls_xs0_ys2 = df_pred['Ls_xs0_ys2[nH]']
207 df_pred_Ls_xs0_ys3 = df_pred['Ls_xs0_ys3[nH]']
208 df_pred_Ls_xs0_ys4 = df_pred['Ls_xs0_ys4[nH]']
209 pred_Ls_xs0_ys0 = df_pred_Ls_xs0_ys0.values
210 pred_Ls_xs0_ys1 = df_pred_Ls_xs0_ys1.values
211 pred_Ls_xs0_ys2 = df_pred_Ls_xs0_ys2.values
212 pred_Ls_xs0_ys3 = df_pred_Ls_xs0_ys3.values
213 pred_Ls_xs0_ys4 = df_pred_Ls_xs0_ys4.values
214
215 df_pred_Lp_xs1_ys0 = df_pred['Lp_xs1_ys0[nH]']
216 df_pred_Ls_xs1_ys0 = df_pred['Ls_xs1_ys0[nH]']
217 pred_Lp_xs1_ys0 = df_pred_Lp_xs1_ys0.values
218 pred_Ls_xs1_ys0 = df_pred_Ls_xs1_ys0.values
219
```

```

220 df_pred_k_xs0_ys0 = df_pred['k_xs0_ys0']
221 df_pred_k_xs0_ys1 = df_pred['k_xs0_ys1']
222 df_pred_k_xs0_ys2 = df_pred['k_xs0_ys2']
223 df_pred_k_xs0_ys3 = df_pred['k_xs0_ys3']
224 df_pred_k_xs0_ys4 = df_pred['k_xs0_ys4']
225 df_pred_k_xs1_ys0 = df_pred['k_xs1_ys0']
226 k_xs0_ys0 = df_pred_k_xs0_ys0.values
227 k_xs0_ys1 = df_pred_k_xs0_ys1.values
228 k_xs0_ys2 = df_pred_k_xs0_ys2.values
229 k_xs0_ys3 = df_pred_k_xs0_ys3.values
230 k_xs0_ys4 = df_pred_k_xs0_ys4.values
231 k_xs1_ys0 = df_pred_k_xs1_ys0.values
232
233 df_pred_Ip = df_pred['Ip[A(rms)]']
234 Ip = df_pred_Ip.values # A(rms)
235
236 for i in range(len(df_pred.loc[:, 'Bx_p_xs0_0deg[uT]'])):
237
238     Lp_xs0_ys0.append(pred_Lp_xs0_ys0[i]*Np[i]**2)# The datatype is list.
239     Lp_xs0_ys1.append(pred_Lp_xs0_ys1[i]*Np[i]**2)
240     Lp_xs0_ys2.append(pred_Lp_xs0_ys2[i]*Np[i]**2)
241     Lp_xs0_ys3.append(pred_Lp_xs0_ys3[i]*Np[i]**2)
242     Lp_xs0_ys4.append(pred_Lp_xs0_ys4[i]*Np[i]**2)
243
244     Ls_xs0_ys0.append(pred_Ls_xs0_ys0[i]*Ns[i]**2)
245     Ls_xs0_ys1.append(pred_Ls_xs0_ys1[i]*Ns[i]**2)
246     Ls_xs0_ys2.append(pred_Ls_xs0_ys2[i]*Ns[i]**2)
247     Ls_xs0_ys3.append(pred_Ls_xs0_ys3[i]*Ns[i]**2)
248     Ls_xs0_ys4.append(pred_Ls_xs0_ys4[i]*Ns[i]**2)
249
250     Lp_xs1_ys0.append(pred_Lp_xs1_ys0[i]*Np[i]**2)
251     Ls_xs1_ys0.append(pred_Ls_xs1_ys0[i]*Ns[i]**2)
252
253     if i % 200000 ==0:
254         print(f'Calculating Is... {i}/{N}')

```

```

255
256 for i in range(len(Ip)):
257     n1_i = math.pi*w*Lp_xs0_ys0[i]*10**(-9)*Ip[i]*math.sqrt(2)/(4*Vdc) # Note
        that Ip is rms value.
258     n2_i = (math.pi)**2*w*(Lp_xs0_ys0[i]*10**(-9)*Ls_xs0_ys0[i]*10**(-9))
        **0.5*Pout/(8*k_xs0_ys0[i]*n1_i*Vdc*Vbat)
259     Is_i = 4*n2_i*Vbat/(math.pi*w*Ls_xs0_ys0[i]*10**(-9))/math.sqrt(2) # A(rms
        )
260     VLp_i = ( (((4*(Lp_xs0_ys0[i])**0.5*Vbat*k_xs0_ys0[i]*n2_i)/(math.pi*(
        Ls_xs0_ys0[i])**0.5))**2 + (4*Vdc *n1_i/math.pi)**2)**0.5 )/(2**0.5) #
        Vrms
261     VLs_i = ( (((4*(Ls_xs0_ys0[i])**0.5*Vdc *k_xs0_ys0[i]*n1_i)/(math.pi*(
        Lp_xs0_ys0[i])**0.5))**2 + (4*Vbat*n2_i/math.pi)**2)**0.5 )/(2**0.5) #
        Vrms
262
263     n1.append(n1_i)
264     n2.append(n2_i)
265     Is.append(Is_i)
266     VLp.append(VLp_i)
267     VLs.append(VLs_i)
268
269 Pout_xs0=[]
270 Pout_xs1=[]
271 Pave=[]
272 Pripple=[]
273 Pout = []
274
275 Bx_xs0=[]
276 By_xs0=[]
277 Bz_xs0=[]
278 Bx_xs1=[]
279 By_xs1=[]
280 Bz_xs1=[]
281 Bstray=[]
282 CoilLoss_xs1=[]

```

```

283 Qcoil=400
284
285 for i in range(len(Bx_p_xs0_0deg)):
286     Bx_xs0.append(((Bx_p_xs0_0deg[i]*Ip[i]*Np[i]+ Bx_s_xs0_0deg[i]*Is[i]*Ns[i]
                )**2 +(Bx_p_xs0_90deg[i]*Ip[i]*Np[i]+ Bx_s_xs0_90deg[i]*Is[i]*Ns[i] )
                **2)**0.5) #[uT(rms)]
287     By_xs0.append(((By_p_xs0_0deg[i]*Ip[i]*Np[i]+ By_s_xs0_0deg[i]*Is[i]*Ns[i]
                )**2 +(By_p_xs0_90deg[i]*Ip[i]*Np[i]+ By_s_xs0_90deg[i]*Is[i]*Ns[i] )
                **2)**0.5)
288     Bz_xs0.append(((Bz_p_xs0_0deg[i]*Ip[i]*Np[i]+ Bz_s_xs0_0deg[i]*Is[i]*Ns[i]
                )**2 +(Bz_p_xs0_90deg[i]*Ip[i]*Np[i]+ Bz_s_xs0_90deg[i]*Is[i]*Ns[i] )
                **2)**0.5)
289     Bx_xs1.append(((Bx_p_xs1_0deg[i]*Ip[i]*Np[i]+ Bx_s_xs1_0deg[i]*Is[i]*Ns[i]
                )**2 +(Bx_p_xs1_90deg[i]*Ip[i]*Np[i]+ Bx_s_xs1_90deg[i]*Is[i]*Ns[i] )
                **2)**0.5)
290     By_xs1.append(((By_p_xs1_0deg[i]*Ip[i]*Np[i]+ By_s_xs1_0deg[i]*Is[i]*Ns[i]
                )**2 +(By_p_xs1_90deg[i]*Ip[i]*Np[i]+ By_s_xs1_90deg[i]*Is[i]*Ns[i] )
                **2)**0.5)
291     Bz_xs1.append(((Bz_p_xs1_0deg[i]*Ip[i]*Np[i]+ Bz_s_xs1_0deg[i]*Is[i]*Ns[i]
                )**2 +(Bz_p_xs1_90deg[i]*Ip[i]*Np[i]+ Bz_s_xs1_90deg[i]*Is[i]*Ns[i] )
                **2)**0.5)
292
293     Pout_xs0.append(w*k_xs0_ys0[i]*(Lp_xs0_ys0[i]*10**(-9)*Ls_xs0_ys0[i]
                )*10**(-9)**0.5*Ip[i]*Is[i] ) #[W]
294     Pout_xs1.append(w*k_xs1_ys0[i]*(Lp_xs1_ys0[i]*10**(-9)*Ls_xs1_ys0[i]
                )*10**(-9)**0.5*Ip[i]*Is[i] )#[W]
295     Pout_xs0_ys0_i = w*k_xs0_ys0[i]*(Lp_xs0_ys0[i]*10**(-9)*Ls_xs0_ys0[i]
                )*10**(-9)**0.5*Ip[i]*Is[i] #[W]
296     Pout_xs0_ys1_i = w*k_xs0_ys1[i]*(Lp_xs0_ys1[i]*10**(-9)*Ls_xs0_ys1[i]
                )*10**(-9)**0.5*Ip[i]*Is[i] #[W]
297     Pout_xs0_ys2_i = w*k_xs0_ys2[i]*(Lp_xs0_ys2[i]*10**(-9)*Ls_xs0_ys2[i]
                )*10**(-9)**0.5*Ip[i]*Is[i] #[W]
298     Pout_xs0_ys3_i = w*k_xs0_ys3[i]*(Lp_xs0_ys3[i]*10**(-9)*Ls_xs0_ys3[i]
                )*10**(-9)**0.5*Ip[i]*Is[i] #[W]

```

```

299 Pout_xs0_ys4_i = 2*w*k_xs0_ys4[i]*(Lp_xs0_ys4[i]*10**(-9)*Ls_xs0_ys4[i
    ]*10**(-9))*0.5*Ip[i]*Is[i] #[W]
300 Pave_i = (Pout_xs0_ys0_i+2*Pout_xs0_ys1_i+2*Pout_xs0_ys2_i+2*
    Pout_xs0_ys3_i+Pout_xs0_ys4_i)/8 #[W]/m
301 Pave.append(Pave_i)
302 Pmax_i = max(abs(Pout_xs0_ys0_i), abs(Pout_xs0_ys1_i), abs(Pout_xs0_ys2_i)
    , abs(Pout_xs0_ys3_i), abs(Pout_xs0_ys4_i))
303 Pmin_i = min(abs(Pout_xs0_ys0_i), abs(Pout_xs0_ys1_i), abs(Pout_xs0_ys2_i)
    , abs(Pout_xs0_ys3_i), abs(Pout_xs0_ys4_i))
304 Pripple_i = (Pmax_i-Pmin_i)/Pmax_i*100 # %
305 Pripple.append(Pripple_i)
306
307 if i % 200000 ==0:
308     print(f'Calculating Bstray... {i}/{N}')
309 B_xs0 = [(x**2 + y**2 + z**2)**0.5 for (x,y,z) in zip(Bx_xs0,By_xs0,Bz_xs0)]
    #[uT(rms)]
310 B_xs1 = [(x**2 + y**2 + z**2)**0.5 for (x,y,z) in zip(Bx_xs1,By_xs1,Bz_xs1)]
    #[uT(rms)]
311 Bstray = max(B_xs0, B_xs1)
312
313 df_pred_processed=df_pred
314 df_pred_processed.insert(0, 'Is[A(rms)]', Is)
315 df_pred_processed.insert(0, 'VLp[V(rms)]', VLp)
316 df_pred_processed.insert(0, 'VLs[V(rms)]', VLs)
317 df_pred_processed.insert(0, 'n1', n1)
318 df_pred_processed.insert(0, 'n2', n2)
319 df_pred_processed.insert(0, 'Bxs0[uT(rms)]', B_xs0)
320 df_pred_processed.insert(0, 'Bxs1[uT(rms)]', B_xs1)
321 df_pred_processed.insert(0, 'Bstray[uT(rms)]', Bstray)
322 df_pred_processed.insert(0, 'Pout_xs0[W]', Pout_xs0)
323 df_pred_processed.insert(0, 'Pout_xs1[W]', Pout_xs1)
324 df_pred_processed.insert(0, 'Pave[W/m]', Pave)
325 df_pred_processed.insert(0, 'Pripple[%]', Pripple)
326

```

```

327 kdiff = [abs(x1 - x2)/max(abs(x1), abs(x2)) *100 for (x1, x2) in zip(
        k_xs0_ys0, k_xs1_ys0)]
328 CoilLoss_xs0 = [w*x1*10**(-9)*y1**2/Qcoil + w*x2*10**(-9)*y2**2/Qcoil for (
        x1,y1,x2,y2) in zip(Lp_xs0_ys0, Ip, Ls_xs0_ys0, Is)]
329
330 lpy_df_pred = df_pred.loc[:, 'lpy[mm]']
331 lpx_df_pred = df_pred.loc[:, 'lpx[mm]']
332 wpx_df_pred = df_pred.loc[:, 'wpx[mm]']
333 wpy_df_pred = df_pred.loc[:, 'wpy[mm]']
334 ax_df_pred = df_pred.loc[:, 'ax[mm]']
335 p_df_pred = df_pred.loc[:, 'p[mm]']
336 ls_df_pred = df_pred.loc[:, 'ls[mm]']
337 ws_df_pred = df_pred.loc[:, 'ws[mm]']
338 b = 50 # mm
339 # Core volume
340 V_PriCore_temp = []
341 V_PriCore = []
342 V_SecCore_temp = []
343 V_SecCore = []
344 V_PriCore_ave_temp = []
345 V_PriCore_ave = []
346 num_temp = []
347 num = []
348 for i in range(len(lpy_df_pred)):
349     # Primary
350     lpx_i = lpx_df_pred.values[i]
351     lpy_i = lpy_df_pred.values[i]
352     wpx_i = wpx_df_pred.values[i]
353     wpy_i = wpy_df_pred.values[i]
354     ax_i = ax_df_pred.values[i]
355     ay_i = 0
356     p_i = p_df_pred.values[i]
357     V_PriCore_temp = (lpy_i+2*wpy_i+2*ay_i)*(lpx_i+2*wpx_i+2*ax_i)*5/(10**3) #
        cm3
358     V_PriCore.append(V_PriCore_temp)

```

```

359 V_PriCore_ave_temp = V_PriCore_temp/(lpy_i+2*wpy_i+2*ay_i+p_i)*10**3 # cm3
    /m
360 V_PriCore_ave.append(V_PriCore_ave_temp)
361 # Secondary
362 ls_i = ls_df_pred.values[i]
363 ws_i = ws_df_pred.values[i]
364 V_SecCore_temp = (ls_i+2*ws_i+2*b)**2*5/(10**3) # cm3
365 V_SecCore.append(V_SecCore_temp)
366 # Number of inverter
367 num_temp = 1/(lpy_i+2*wpy_i+2*ay_i+p_i)*10**3 # 1/m
368 num.append(num_temp)
369 if i % 200000 ==0:
370     print(f'Calculating Vcore... {i}/{N}')
371
372 # Windings volume
373 V_PriWind_temp=[]
374 V_PriWind = []
375 V_SecWind_temp=[]
376 V_SecWind = []
377 V_PriWind_ave_temp = []
378 V_PriWind_ave = []
379 wout=[]
380 len_p_temp = []
381 len_p = []
382 wid_p_temp = []
383 wid_p = []
384 len_s_temp = []
385 len_s = []
386 Coil_Interval = []
387
388 for i in range(len(wpx_df_pred)):
389     # Primary
390     lpx_i = lpx_df_pred.values[i]
391     lpy_i = lpy_df_pred.values[i]
392     wpx_i = wpx_df_pred.values[i]

```

```

393 wpy_i = wpy_df_pred.values[i]
394 ax_i = ax_df_pred.values[i]
395 ay_i = 0
396 p_i = p_df_pred.values[i]
397 V_PriWind_temp = (2*(lpx_i+wp_x_i)+2*(lpy_i+wpy_i))*6.6*6.6/(10**3)*Np[i]
398 V_PriWind.append(V_PriWind_temp)
399 V_PriWind_ave_temp = V_PriWind_temp/(lpy_i+2*wpy_i+2*ay_i+p_i)*10**3 # cm3
    /m
400 V_PriWind_ave.append(V_PriWind_ave_temp)
401 len_p_temp = lpy_i + 2*wpy_i
402 len_p.append(len_p_temp)
403 Coil_Interval.append(len_p_temp+p_i)
404 wid_p_temp = lpx_i + 2*wp_x_i + 2*ax_i
405 wid_p.append(wid_p_temp)
406 #Secondary
407 ls_i = ls_df_pred.values[i]
408 ws_i = ws_df_pred.values[i]
409 V_SecWind_temp = 4*(ls_i+ws_i)*6.6*6.6/(10**3)*Ns[i]
410 V_SecWind.append(V_SecWind_temp)
411 len_s_temp = ls_i + 2*ws_i + 100
412 len_s.append(len_s_temp)
413
414 if i % 200000 ==0:
415     print(f'Calculating Vwind... {i}/{N}')
416 df_pred_processed.insert(0, 'kdiff[%]', kdiff)
417 df_pred_processed.insert(0, 'V_PriCore_ave[cm3/m]', V_PriCore_ave)
418 df_pred_processed.insert(0, 'V_PriWind_ave[cm3/m]', V_PriWind_ave)
419 df_pred_processed.insert(0, 'V_SecCore[cm3]', V_SecCore)
420 df_pred_processed.insert(0, 'V_SecWind[cm3]', V_SecWind)
421 df_pred_processed.insert(0, 'Inverter[1/m]', num)
422 df_pred_processed.insert(0, 'CoilLoss_xs0[W]', CoilLoss_xs0)
423 df_pred_processed.insert(0, 'Length of primary core[mm]', len_p)
424 df_pred_processed.insert(0, 'Coil interval[mm]', Coil_Interval)
425 df_pred_processed.insert(0, 'Width of primary core[mm]', wid_p)
426 df_pred_processed.insert(0, 'Length of secondary core[mm]', len_s)

```

```
427
428 df_pred_processed
```

A.7 Extraction process

```
1 df_pred_direct = []
2 df_pred_direct = df_pred_processed
3 df_pred_direct
4 df_pred_1 = df_pred_direct
5 # User input
6 # Setting for academic papers
7 !pip install SciencePlots
8 import matplotlib
9 import matplotlib.pyplot as plt
10 # User input
11 # Setting for paper
12 fig_width = 8 #cm
13 fig_height = 3 #cm
14 font_size = 10 # pt
15 marker_size = 5
16 x_tick_pad = 2
17 y_tick_pad = 2
18 x_label_pad = 0.5
19 y_label_pad = 1
20
21 import matplotlib
22 from matplotlib import rc
23 import matplotlib.pyplot as plt
24 %matplotlib inline
25 from pylab import *
26 import scienceplots
27
28 path = '/content/drive/My Drive/Improving/Python_cards/matplot/SciencePlots-
      master/styles/'
29 plt.style.use('seaborn-whitegrid')
```

```

30 plt.style.use([path+'misc/grid.mplstyle'])
31 plt.style.use([path+'journals/ieee.mplstyle'])
32 plt.style.use(['science','no-latex'])# ref: https://github.com/garrettj403/
    SciencePlots

```

Plot 1

```

1 x = df_pred_1.loc[:, 'Coil interval [mm]'] #Length of primary core [mm]
2 y = df_pred_1.loc[:, 'CoilLoss_xs0 [W]']
3 z = df_pred_1.loc[:, 'Bstray [uT(rms)]']
4
5 fig1=plt.figure(figsize=(cm2inch(fig_width),cm2inch(fig_height)), dpi=300)
6 xlim = 800 # [mm]
7 ylim = 140 #Coil loss [W]
8
9 # lower right
10 x1 = np.arange(xlim,xlim*10,0.1)
11 y1 = ylim
12 plt.fill_between(x1,y1,facecolor='r',alpha=0.3) #alpha is transparency
13 plt.plot([xlim, xlim], [0, ylim], 'r--', lw=0.5) # draw vertical line
14 plt.plot([xlim, xlim*10], [ylim, ylim], 'r--', lw=0.5) # draw horizontal
    line
15
16 plt.scatter(x, y, c=z, s=marker_size, cmap = 'viridis', vmin = 0, vmax=100,
    rasterized=True)
17 plt.colorbar(label=r"$B_{stray}$ [\u03bcT]") #Show color bar at the right side
18 plt.xlabel(r"Coil interval [mm]", labelpad = x_label_pad)
19 plt.ylabel(r"Coil loss [W]", labelpad = y_label_pad)
20 plt.axis([0, 2000, 0, 300])
21 df_pred_2=df_pred_1[(df_pred_1['Coil interval [mm]']>xlim)&(df_pred_1['
    CoilLoss_xs0 [W]']<ylim) ]
22 print(len(df_pred_2))

```

Plot 2

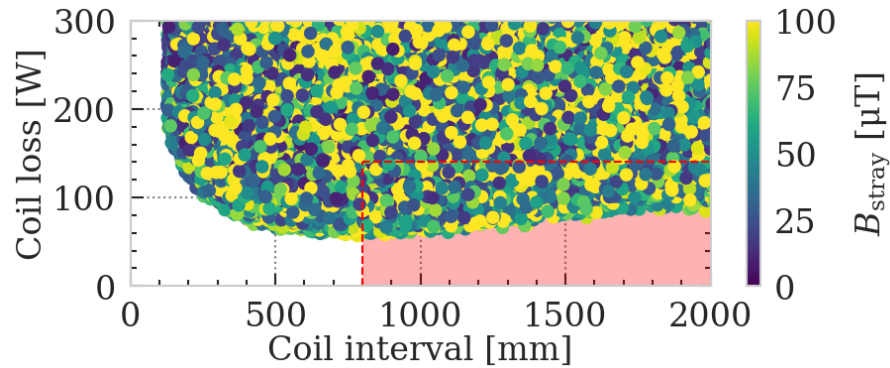


Fig. A.2: Output of the source code: Plot 1

```

1 x = df_pred_2.loc[:, 'Bstray[uT(rms)]']
2 y = df_pred_2.loc[:, 'kdiff [%]']
3 z = df_pred_2.loc[:, 'V_PriCore_ave [cm3/m]']
4 fig1=plt.figure(figsize=(cm2inch(fig_width),cm2inch(fig_height)), dpi=300)
5 xlim = 20 #Bstray[uT]
6 ylim = 50 #kdiff [%]
7 x1 = np.arange(0,xlim+1,1)
8 y1 = ylim
9 plt.fill_between(x1,y1,facecolor='r',alpha=0.3)#alpha is transparency
10 # Ref: https://www.kite.com/python/docs/matplotlib.pyplot.fill_between
11 plt.scatter(x, y, c=z, s=marker_size, cmap = 'viridis', vmin = 0, vmax=6000,
12            rasterized=True)
13 plt.colorbar(label=r'V_PriCore [cm3/m]')#Show color bar at the right side
14 plt.xlabel(r"Bstray [μT]",labelpad = x_label_pad) # not shown
15 plt.ylabel(r"kdiff [%]",labelpad = y_label_pad)
16 plt.axis([0, 100, 0, 60])
17 # draw vertical line
18 plt.plot([xlim, xlim], [0, ylim], 'r--', lw=0.5)
19 # draw horizontal line
20 plt.plot([0, xlim], [ylim, ylim], 'r--', lw=0.5)
21 plt.show()
22 df_pred_3=df_pred_2[(df_pred_2['Bstray[uT(rms)]']<xlim)&(df_pred_2['kdiff [%]']<ylim) ]
23 print(len(df_pred_3))

```

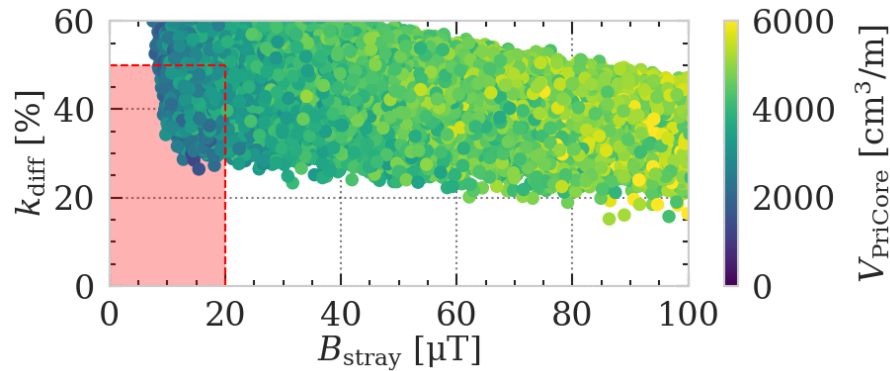


Fig. A.3: Output of the source code: Plot 2

Plot 3

```

1 from matplotlib.cbook import get_sample_data
2 y = (df_pred_3.loc[:, 'Pave[W/m]'])/1000
3 x = df_pred_3.loc[:, 'V_PriCore_ave [cm3/m]']
4 z = df_pred_3.loc[:, 'V_PriWind_ave [cm3/m]']
5 fig1=plt.figure(figsize=(cm2inch(fig_width),cm2inch(fig_height)), dpi=300)
6 xlim = 3500 #_VPriCore[cm3]
7 ylim = 2.5 #Pave[kW]
8 # Upper left
9 x1 = np.arange(0,xlim+0.1,0.1)
10 y1 = ylim
11 y2 = ylim*10
12 x1 = np.arange(0,xlim+1,1)
13 y1 = ylim
14 y2 = ylim*10
15 plt.fill_between(x1,y1, y2 ,facecolor='r',alpha=0.3)#alpha is transparency
16 # Ref: https://www.kite.com/python/docs/matplotlib.pyplot.fill_between
17 # draw vertical line
18 plt.plot([xlim, xlim], [ylim, ylim*10], 'r--', lw=0.5)
19 # draw horizontal line
20 plt.plot([0, xlim], [ylim, ylim], 'r--', lw=0.5)
21 plt.scatter(x, y, c=z, s=marker_size, cmap = 'viridis', vmin = 0, vmax=800,
22            rasterized=True)
23 plt.colorbar(label=r'V_PriWind [cm³/m]')#Show color bar at the right side

```

```

23 plt.xlabel(r"$V_{PriCore}$ [cm3/m]",labelpad = x_label_pad)
24 plt.ylabel(r"$P_{ave}$ [kW/m]",labelpad = y_label_pad)
25 plt.axis([0, 5000, 0, 4])
26 df_pred_4=df_pred_3[(df_pred_3['Pave [W/m]']>yylim)&(df_pred_3['V_PriCore_ave [
    cm3/m]']<xlim) ]
27 df_pred_4
28 plt.show()
29 print(len(df_pred_4))
30 fig_update = True

```

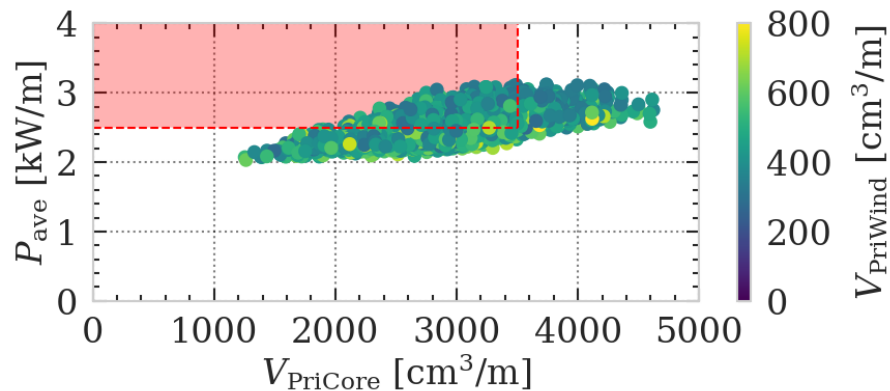


Fig. A.4: Output of the source code: Plot 3

Plot 4

```

1 import matplotlib.pyplot as plt
2 from matplotlib.cbook import get_sample_data
3 matplotlib.rcParams.update({'font.size': font_size, 'font.family': '
    STIXGeneral', 'mathtext.fontset': 'stix'})
4 x = df_pred_4.loc[:, 'V_SecCore [cm3]']
5 y = (df_pred_4.loc[:, 'PriPple [%]'])
6 z = df_pred_4.loc[:, 'V_SecWind [cm3]']
7 fig1=plt.figure(figsize=(cm2inch(fig_width),cm2inch(fig_height)), dpi=300)
8 xlim = 2400 #V_SecCore [cm3]
9 ylim = 40 #Pdiffer [%]
10 x1 = np.arange(0,xlim+1,1)

```

```

11 y1 = 0
12 y2 = ylim
13 plt.fill_between(x1,y1, y2 ,facecolor='r',alpha=0.3)#alpha is transperancy
14 # Ref: https://www.kite.com/python/docs/matplotlib.pyplot.fill_between
15 plt.scatter(x, y, c=z, s=marker_size, cmap = 'viridis', vmin = 0, vmax=800,
    rasterized=True)
16 plt.colorbar(label=r'$V_{SecWind}$ [cm3'])#Show colar bar at the right side
17 plt.ylabel(r"$P_{ripple}$ [%]",labelpad = y_label_pad) # not shown
18 plt.xlabel(r"$V_{SecCore}$ [cm3]",labelpad = x_label_pad) # not shown
19 plt.axis([0, 5000, 0, 100])
20 plt.plot([xlim, xlim], [0, ylim], 'r--', lw=0.5)
21 # draw horizontal line
22 plt.plot([0, xlim], [ylim, ylim], 'r--', lw=0.5)
23 # draw vertical line
24 df_pred_5=df_pred_4[(df_pred_4['Pripple [%]']<ylim)&(df_pred_4['V_SecCore[cm3]']<xlim) ]
25 df_pred_5.to_csv('/content/drive/My Drive/2021_Fall/
    OptimizationPipeline_DoubleLCCL3kW/3_NeuralNetwork/
    candidate_v7_0_seed_7777.csv')
26 plt.show()
27 print(len(df_pred_5))
28 df_pred_5

```

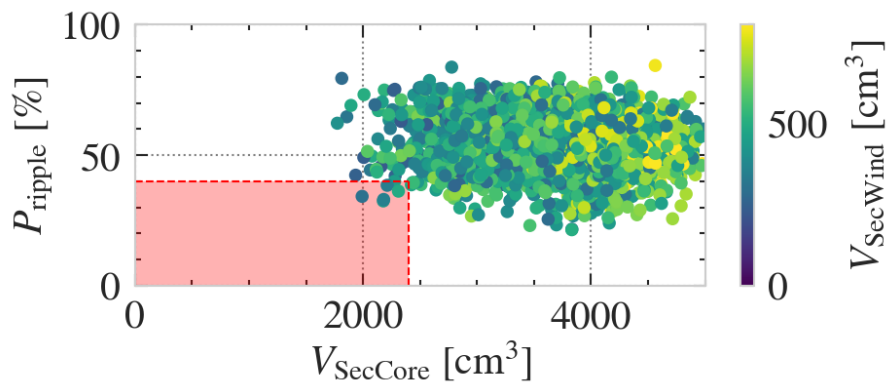


Fig. A.5: Output of the source code: Plot 4

CURRICULUM VITAE

Personal Information



Name: Shuntaro Inoue

Place of Birth: Osaka, Japan

Citizen of: Aichi, Japan

Contact: shuntaro0628@gmail.com

Education

2019 - 2022 Ph.D. Electrical Engineering at the Power Electronics Laboratory, Utah State University, Logan, Utah, USA

2011 - 2013 M.S. Precision Engineering at the University of Tokyo, Bunkyo-ku, Tokyo, Japan

2007 - 2011 B.S. Mechanical, Materials and Manufacturing Science at Osaka University, Suita, Osaka, Japan

Work Experience

2013 - Present Power Electronics Researcher at Toyota Central R&D Labs., Inc., Nagakute, Aichi, Japan